UNIVERSITY OF SOUTHAMPTON

Control Systems for Capacitive Micromachined Inertial Sensors with High-Order Sigma-Delta Modulators

by

Yufeng Dong

A thesis submitted in partial fulfillment for the degree of Doctor of Philosophy

in the

Faculty of Engineering, Science and Mathematics

School of Electronics and Computer Science

June 2006

PUBLICATION LISTS

JOURNAL PAPERS

[1] Y. Dong, M. Kraft, and W. Redman-White, "Micromachined vibratory gyroscopes controlled by a high order bandpass sigma delta modulator," *IEEE Sensors Journal*, accepted and to be published in 2006.

[2] Y. Dong, M. Kraft, and W. Redman-White, "Force feedback linearization for higher-order electromechanical sigma-delta modulators," *Journal of Micromechanics and Microengineering*, vol. 16, no. 6, pp. S54–S60, 2006.

[3] Y. Dong, M. Kraft, C. Gollasch, and W. Redman-White, "A high-performance accelerometer with a fifth-order sigma-delta modulator," *Journal of Micromechanics and Microengineering*, vol. 15, no. 7, pp. S22–S29, 2005.

[4] Y. Dong, M. Kraft, and W. Redman-White, "Higher-order noise-shaping filters for high performance micromachined inertial sensors," *IEEE Transactions on Instrumentation and Measurement*, submitted in March 2004.

CONFERENCE PAPERS

[1] Y. Dong, M. Kraft, and W. Redman-White, "High order band-pass sigma delta interface for gyroscopes," in *Proc. IEEE Sensors 2005 Conference*, Irvine, California, USA, Oct. 31st - Nov. 3rd, 2005, pp. 1080–1083. (One of ten finalists of the best student paper competition at the IEEE SENSORS 2005, absence due to the fire).

[2] Y. Dong, M. Kraft, and W. Redman-White, "Force feedback linearization for higher-order electromechanical sigma-delta modulators," in *Proc. 16th Workshop on Micromachining, Micromechanics and Microsystems*, Goteborg, Sweden, September 4-6, 2005, pp. 1080–1083.

[3] Y. Dong, M. Kraft, and W. Redman-White, "Noise analysis for high order eelectromechanical sigma-delta modulators," in *Proc. 5th International Conference on Advanced A/D and D/A Conversion Techniques and their Applications*, Limerick, Ireland, July 24-27, 2005, pp. 147–152.

[4] M. Kraft, Y. Dong, and W. Redman-White, "Using higher order sigma delta modulators as interface for closed loop micromachined sensors," in *Proc. 5th International Conference on Advanced A/D and D/A Conversion Techniques and their Applications*, Limerick, Ireland, July 24-27, 2005, pp. 293–298.

[5] M. Kraft and Y. Dong, "Higher order sigma-delta modulator interfaces for MEMS capacitive sensors," in *Proc. NSTI Nanotech*, vol. 3, Anaheim, USA, May 8-12, 2005, pp. 459–462.

[6] Y. Dong, M. Kraft, and C. Gollasch, "A high performance accelerometer with fifth-order sigma-delta modulator," in *Proc. 15th Workshop on Micromachining, Micromechanics and Microsystems*, Leuven, Belgium, September 5-7, 2004, pp. 41–44.

[7] Y. Dong and M. Kraft, "Simulation of micromachined inertial sensors with higher-order single loop sigma-delta modulators," in *Proc. 6th Conf. on Modeling and Simulation of Microsystems*, vol. 1, Boston, USA, March 7-11, 2004, pp. 414–417.

UNIVERSITY OF SOUTHAMPTON

ABSTRACT

FACULTY OF ENGINEERING, SCIENCE AND MATHEMATICS
SCHOOL OF ELECTRONICS AND COMPUTER SCIENCE

Doctor of Philosophy

by Yufeng Dong

This work, for the first time, systematically presents a design methodology of the control system for micromachined inertial sensors with a high-order electromechanical ΣΔM. The methodology is based on relatively mature design techniques for high-order ΣΔ ADC. Different loop topologies, including multi-feedback, multi-feedback with resonators and feed-forward with resonators, were investigated and the noise levels at different stages of the high-order ΣΔM was analyzed. The behaviour of noise shaping for Brownian noise, quantization noise and electronic noise was discussed in detail. Monte-Carlo analysis was performed to investigate the sensitivity to fabrication tolerances of the sensing element and circuits, which showed that the single loop ΣΔM had a good immunity to fabrication tolerances. Using a displacement dependent feedback, a linearization scheme was proposed to cancel the nonlinear conversion from the voltage to electrostatic feedback force and, as result the output signal harmonic distortion was considerably suppressed. The mechanical quality factor Q of the sensing element has a remarkable effect on noise shaping, and phase lead compensator influences the loop stability. In a high-order electromechanical ΣΔM, non-idealities due to dead-zone and idle tones were greatly alleviated compared with a second-order ΣΔM. Special issues in continuous-time ΣΔM were addressed, including inter-symbol effects and excess loop delay. Non-idealities in the interface and control circuits were investigated. Furthermore, the approach was extended to apply to vibratory gyroscopes. The control system using a high-order bandpass ΣΔM leads to a much lower oversampling frequency and more flat signal response. A high performance fully differential accelerometer is designed with a mechanical noise floor below $1\mu g/\sqrt{Hz}$. Detailed FEM analysis were performed using CoventorWare to design key parameters. Two fabrication processes based on silicon on glass (SOG) and silicon on insulator (SOI) were explored. A preliminary prototype of a continuous-time fifth-order electromechanical ΣΔM was built using SMT components on a six-layer PCB. A SNR of the PCB prototype using fully differential circuits of about 90dB was achieved in a 1kHz signal band with a sampling frequency 125kHz.

Contents

List of Figures iv

List of Tables x

List of Abbreviations xi

List of Symbols xiv

Acknowledgements xvi

1 Introduction 1
- 1.1 Motivation . . . 2
- 1.2 Thesis Organization . . . 3

2 Fundamental Principles 5
- 2.1 The Principles of Micromachined Accelerometers . . . 5
  - 2.1.1 Mechanical Lumped Model . . . 5
  - 2.1.2 Dynamic Responses . . . 6
  - 2.1.3 Thermal Noise Equivalent Acceleration . . . 7
- 2.2 The Principles of MEMS Vibratory Gyroscopes . . . 9
  - 2.2.1 Vibratory Gyroscopes . . . 9
- 2.3 The Principles of A ΣΔM . . . 13
  - 2.3.1 Noise Shaping . . . 13
  - 2.3.2 SQNR . . . 15
  - 2.3.3 Quantizer Model . . . 18
  - 2.3.4 High-Order Single Loop ΣΔM . . . 21
  - 2.3.5 MASH . . . 22
  - 2.3.6 Multi-Bit ΣΔM . . . 24
  - 2.3.7 Lowpass to Bandpass Transformation . . . 25
  - 2.3.8 Continuous-Time ΣΔM vs Discrete-Time ΣΔM . . . 27
- 2.4 Performance Metric . . . 29

3 Background: Closed-loop Micromachined Capacitive Inertial Sensors 30
- 3.1 Interface to Micromachined Capacitive Inertial Sensors . . . 31
- 3.2 Microfabrication . . . 33
  - 3.2.1 Surface Micromachining . . . 33
  - 3.2.2 Bulk Micromachining . . . 34
  - 3.2.3 LIGA . . . 35

3.3 ΣΔM Micromachined Capacitive Inertial Sensors . . . 35
3.3.1 Analog Closed-Loop Sensors . . . 35
3.3.2 Second-Order Electromechanical ΣΔM . . . 36
3.3.3 MASH Electromechanical ΣΔM . . . 38
3.3.4 High-Order Single Loop Electromechanical ΣΔM . . . 40
3.4 Summary . . . 42

4 High-Order Single Loop Electromechanical ΣΔM **43**
4.1 Design Methodology of High-Order Electromechanical ΣΔM . . . 44
4.2 Loop Topologies and Performance . . . 48
4.2.1 Multi-Feedback Topology . . . 48
4.2.2 Conditional Stability . . . 51
4.2.3 Topology: Feed-Forward Loops with Resonators . . . 54
4.2.4 Topology: Multi-Feedback Loops with Resonators . . . 59
4.3 Noise Analysis . . . 62
4.3.1 Noise Analysis of A Second-Order Electromechanical ΣΔM . . . 63
4.3.2 Noise Analysis of A High-Order Electromechanical ΣΔM . . . 66
4.4 SQNR Sensitivity to Fabrication Tolerances . . . 69
4.5 Dead-Zone and Idle Tones . . . 71
4.6 Effects of The Mechanical Quality Factor Q on Noise Shaping . . . 75
4.7 Electrostatic Force Feedback Delay . . . 76
4.8 High-Order Continuous-Time Electromechanical ΣΔM . . . 79
4.9 Circuit Non-Idealities . . . 80
4.10 Summary . . . 82

5 Force Feedback Linearization **84**
5.1 Nonlinear Electrostatic Feedback Force . . . 84
5.2 Feedback Electrostatic Force Linearization . . . 89
5.2.1 Linearized Voltage to Force Conversion in Feedback Loop . . . 89
5.2.2 Nonlinear Displacement to Voltage Conversion in Forward Path . . . 91
5.3 Summary . . . 93

6 High-Order Bandpass ΣΔM for Vibratory Gyroscopes **94**
6.1 Introduction . . . 94
6.2 System Level Model of A Vibratory Gyroscope . . . 95
6.3 High-Order Lowpass ΣΔM Vibratory Gyroscopes . . . 98
6.4 Second-Order Bandpass ΣΔM for Sense Mode Control System . . . 100
6.5 High-Order Bandpass ΣΔM Vibratory Gyroscopes . . . 103
6.5.1 High-Order Bandpass ΣΔM Using A MFLR Topology . . . 103
6.5.2 High-Order Bandpass ΣΔM Using A FFLR Topology . . . 104
6.6 Discussions . . . 107
6.6.1 Properties of Signal and Noise Transfer Functions . . . 107
6.6.2 Effects of Quadrature Force on System Performance . . . 110
6.6.3 Effects of Resonant Frequency Mismatch on System Performance . . . 111
6.6.4 Effects of $1/f$ Noise and White Electronic Noise . . . 111
6.7 Summary . . . 115

7 Experimental Results: A Fifth-Order Lowpass Electromechanical CT ΣΔM **116**
7.1 Sensing Element Used in the Prototype 116
7.2 Front-End Circuits 117
7.2.1 Pickoff Interface Circuit 117
7.2.2 Synchronous Demodulation 119
7.2.3 Diode Demodulator 123
7.2.4 Force Feedback Schemes 124
7.3 First PCB Prototype Experimental Results 127
7.4 Second PCB Prototype Experimental Results 130
7.5 Summary 131

8 Microfabrication of A Prototype Accelerometer **134**
8.1 Motivation 134
8.2 Sensing Element Design and Analysis 135
8.2.1 Fully Differential Structure 135
8.2.2 Spring Design 136
8.2.3 Damping Optimization 137
8.2.4 Modal Analysis 140
8.2.5 Sensitivity and TNEA 142
8.3 Fabrication Process 144
8.3.1 Silicon on Glass (SOG) 144
8.3.2 Silicon on Insulator (SOI) 147
8.4 Summary 149

9 Conclusions **150**
9.1 Conclusions 150
9.2 Future Work 151

A MatLab Source Code for the PSD Simulation **154**

B OrCAD Schematic of PCB Prototype (1st version) **158**

C Block Diagram of PCB Prototype (2nd version) **160**

D OrCAD Schematic of PCB Prototype (2nd version) **162**

Bibliography **164**

List of Figures

2.1 General capacitive accelerometer structure and its mechanical lumped model. 5
2.2 Bode diagram of a sensing element with different quality factor Q. 7
2.3 Operation principle of a vibratory gyroscope. 10
2.4 Coriolis force and quadrature force due to imperfections of mechanical structure microfabrication. 12
2.5 Schematic spectrum comparison between the Nyquist sampling converters, oversampling converters and noise shaping and oversampling converters. . . 14
2.6 Structures of a ΣΔM. 14
2.7 A linearized quantizer model of a ΣΔM. 18
2.8 General block diagram of a single loop ΣΔM. 20
2.9 Theoretical SNR limits for one-bit lowpass ΣΔMs. 22
2.10 A MASH ΣΔM. 23
2.11 A multi-bit ΣΔM. 24
2.12 Pole/zero map of the quantization noise transfer functions for a fourth-order lowpass ΣΔM with OSR=64. 26
2.13 Pole/zero map of the quantization noise transfer functions for a eighth-order bandpass ΣΔM with OSR=64. 26
2.14 Inter-symbol interference of a CT ΣΔM. 28
2.15 Performance metric: output bitstream spectrum of a fifth-order lowpass ΣΔM. 29

3.1 A charge amplifier used for capacitive inertial sensors. 31
3.2 Typical surface micromachining process (Boser [36]). 34
3.3 Block diagram of a sensing element embedded in a second-order ΣΔM. . . . 37
3.4 Linearized block diagram of the micromachined accelerometer incorporated in a MASH ΣΔM (Kraft et al [11]). 39
3.5 SQNR with the sensing element incorporated in the MASH ΣΔM compared with a single loop approach (Kraft et al [11]). 40
3.6 System diagram of a third-order electromechanical ΣΔM (Smith et al [8]). . 41
3.7 A fourth-order electromechanical ΣΔM for vibratory gyroscopes (Petkov et al [12]). 41
3.8 Measured in-band gyroscope response (Petkov et al [12]). 42

4.1 Block diagram of a high-order electromechanical ΣΔM. 43
4.2 Design flow of a high-order electromechanical ΣΔM. 45
4.3 Conversion of a high-order ΣΔ ADC into a high-order electromechanical ΣΔM with the equivalent topology. 45
4.4 Relationship between the SQNR (dB) vs. K_{po} and α in a high-order electromechanical ΣΔM. 47
4.5 A fifth-order electromechanical ΣΔM with multi-feedback loops. 48

4.6 Bode diagram of STF, QNTF and ENTF of the system shown in Figure 4.5. 50
4.7 Noise shaping comparison: a fifth-order vs. a second-order electromechanical ΣΔM with OSR=256 and SBW=1024Hz. 51
4.8 Root locus of the loop filter of the system shown in Figure 4.5. 52
4.9 Bode diagram of the loop filter of the system shown in Figure 4.5. 52
4.10 Full view: Nyquist diagram of the loop filter of the system shown in Figure 4.5. 53
4.11 Zoom on (-1, 0): Nyquist diagram of the loop filter of the system shown in Figure 4.5. 53
4.12 A fifth-order electromechanical ΣΔM with feed-forward loops and resonators. 55
4.13 Bode diagram of STF, QNTF and ENTF of the system shown in Figure 4.12. 56
4.14 Pole-zero map of the loop filter of the system shown in Figure 4.12. 56
4.15 Root locus of the loop filter of the system shown in Figure 4.12. 57
4.16 Bode diagram of the loop filter of the system shown in Figure 4.12. 57
4.17 Nyquist diagram of the loop filter of the system shown in Figure 4.12. . . . 58
4.18 FFLR topology: integrator output number of occurrence vs. integrator output voltage (maximum 1V). 58
4.19 Output bitstream spectrum of the system shown in Figure 4.12 with a 1g, 128Hz sinusoidal input signal. 59
4.20 A fifth-order electromechanical ΣΔM with multi-feedback loops and resonators. 59
4.21 Bode diagram of STF, QNTF and ENTF of the system shown in Figure 4.20. 61
4.22 Root locus of the loop filter of the system shown in Figure 4.20. 61
4.23 MFLR topology: integrator output number of occurrence vs. integrator output voltage (maximum 1V). 62
4.24 Output bitstream spectrum of the system shown in Figure 4.20 with a 1g, 128Hz sinusoidal input signal. 62
4.25 Block diagram of a second-order electromechanical ΣΔM for noise analysis. 63
4.26 Effects of electronic noise on SNR in a second-order electromechanical ΣΔM with different OSR. 65
4.27 Block diagram for noise analysis of a fifth-order electromechanical ΣΔM. . 66
4.28 Noise transfer functions at different stage in a fifth-order electromechanical ΣΔM. 68
4.29 Effects of electronic noise on SNR in a fifth-order electromechanical ΣΔM with different OSR. 69
4.30 A second order electromechanical ΣΔM control loop. 70
4.31 Monte Carlo analysis: SNR sensitivity to microfabrication tolerance in a second-order electromechanical ΣΔM control loop. 71
4.32 Monte Carlo analysis: SNR sensitivity to microfabrication tolerance in a fifth-order electromechanical ΣΔM control loop. 71
4.33 Equivalent block diagram of Figure 4.12, illustrating the origin of a dead-zone in a high-order electromechanical ΣΔM. 72
4.34 Bode diagram of the electronic filter of the high-order electromechanical ΣΔM shown in Figure 4.12. 73
4.35 Power spectral density of the output bitstream assuming a full scale sensor dynamic range of 1g, OSR=64 and 1024Hz signal bandwidth: (a) shows a second-order ΣΔM with a sinusoidal input signal of 1 Hz and an amplitude of -54dB; (b) the amplitude is reduced to -60dB; (c) shows a fifth-order ΣΔM force feedback loop with an input signal amplitude of -120dB; (d) the amplitude is reduced to 0. 74

4.36 SNR comparison among sensors with different Q. 76
4.37 Waveform of the feedback electrostatic force and definitions [53], [54]. . . . 76
4.38 Bode diagram of the open-loop filter vs. the delay τ_d. 78
4.39 QNTF vs. the delay τ_d in a fifth-order ΣΔM Figure 4.5. 78
4.40 Continuous-time implementation of the FFLR ΣΔM shown in Figure 4.12. 79
4.41 Output bitstream spectrum of the the FFLR ΣΔM shown in Figure 4.40. . 79
4.42 Continuous-time implementation of the MFLR ΣΔM shown in Figure 4.20. 80
4.43 Output bitstream spectrum of the MFLR ΣΔM shown in Figure 4.42. . . . 80
4.44 A fifth-order electromechanical SC ΣΔM model to analyze the effects of non-idealities of circuits. 81
4.45 Influence of circuit non-idealities on the performance of a high-order electromechanical ΣΔM: (a) with GBW=10MHz; (b) with slew rate=0.8V/us. 82

5.1 Generic block diagram of a high-order electromechanical ΣΔM for nonlinearity analysis. 85
5.2 Common electrode arrangement of the force feedback path in an electromechanical ΣΔM. 86
5.3 Systematic level model of a fifth-order electromechanical ΣΔM. 87
5.4 Output spectrum of a fifth-order electromechanical ΣΔM with a conventional force feedback DAC. 88
5.5 Variation of the feedback force magnitude due to residual proof mass motion. 88
5.6 Residual proof mass displacement. 89
5.7 Modified electrostatic force feedback arrangement of the electromechanical ΣΔM. 90
5.8 Output spectrum of a fifth-order electromechanical ΣΔM with a linear feedback force DAC. 90
5.9 Feedback nonlinearity on the electromechanical DAC waveform with different feedback loop linearization. 92
5.10 ΣΔM spectrum of the output bitstream with a linear feedback DAC and considering the nonlinearity of the pickoff interface. 92

6.1 Vibratory gyroscope diagram consisting drive mode control loop and sense mode control loop. 95
6.2 Drive mode control loop block of Figure 6.1. 96
6.3 Y-displacement of the gyroscope in the sense mode control system. 97
6.4 Sense mode control loop based on a fifth-order lowpass multi-feedback ΣΔM and local resonators. 98
6.5 Bode diagram of the transfer functions of the signal, quantization noise and electronic noise of the sense mode control system based on a fifth-order ΣΔM depicted in Figure 6.4. 100
6.6 Output bitstream spectrum of the control system based on a fifth-order lowpass ΣΔM depicted in Figure 6.4. 100
6.7 Sense mode control loop based on a second-order bandpass ΣΔM. 101
6.8 Bode diagram of the compensator, sensing element and the product of the sensing element and compensator for the sense mode control system using a bandpass ΣΔM. 102
6.9 Output bitstream spectrum of the control system using a second-order bandpass ΣΔM, showing significant tonal behaviour. 102

6.10 Sense mode control system based on a eighth-order bandpass ΣΔM with multi-feedback loops and local resonators. 103
6.11 Bode diagram of the transfer functions of the signal, quantization noise and electronic noise of the eighth-order bandpass ΣΔM with multi-feedback loops and local resonators. 104
6.12 Root locus of the open-loop filter of the eighth-order bandpass ΣΔM with multi-feedback loops and local resonators. 105
6.13 Output bitstream spectrum of the eighth-order bandpass ΣΔM with multi-feedback loops and local resonators. 106
6.14 Sense mode control system based on a eighth-order bandpass ΣΔM with feed-forward loops and a local resonator. 107
6.15 Bode diagram of the transfer functions of the signal, quantization noise and electronic noise of the eighth-order bandpass ΣΔM with feed-forward loops and a local resonator. 108
6.16 Output bitstream spectrum of the eighth-order bandpass ΣΔM with feed-forward loops and a local resonator. 108
6.17 Root locus of the open-loop filter of the eighth-order bandpass ΣΔM with feed-forward loops and a local resonator. 109
6.18 Quadrature force effects on the output bitstream spectrum of the eighth-order bandpass ΣΔM with feed-forward loops and a local resonator (shown in Figure 6.14). 111
6.19 Resonant frequency mismatch effects on the output bitstream spectrum of the fifth-order lowpass ΣΔM (compared with Figure 6.6(b)). 112
6.20 Resonant frequency mismatch effects on the output bitstream spectrum of the eighth-order bandpass ΣΔM (shown in Figure 6.10). 112
6.21 Model of the sense mode control system depicted in Figure 6.10 including the effects of $1/f$ noise. 113
6.22 Spectrum of the preamplifier color noise, including the $1/f$ noise and white noise. 113
6.23 Output bitstream spectrum of the system depicted in Figure 6.21 with the PSD of $16\text{nV}/\sqrt{Hz}$ at the second corner frequency in the color noise model. 114

7.1 Bode diagram of the sensing element provided by Qinetiq. 116
7.2 Sensing capacitance with parasitic components. 118
7.3 Pickoff configuration: a charge amplifier. 118
7.4 Synchronous demodulation for a fully differential capacitive interface. . . . 119
7.5 Spectrum of amplitude modulated signal containing two sidebands and the carrier. 120
7.6 Signal emulating 10ppm to 20ppm capacitance variation due to acceleration variation. 121
7.7 Pspice model of the pickoff circuit using the AD630 as a demodulator. . . . 122
7.8 Pickoff circuit output with the AD630 as a demodulator. 122
7.9 Pspice model of the pickoff circuit using the AD734 as a demodulator. . . . 122
7.10 Pickoff circuit output with the AD734 as a demodulator. 123
7.11 The schematic of a diode envelope detector. 123
7.12 Diode envelope demodulation for a fully differential capacitive interface. . . 123
7.13 Pspice model using a diode envelope as demodulator. 125
7.14 Pickoff output with a diode envelope as demodulator. 125

7.15 Capacitor electrode arrangement for force feedback. 126
7.16 Connection diagram between the electrodes and surrounding circuits. 126
7.17 Timing diagram of the control signals for the analog switches of the two DACs. 126
7.18 Pspice simulation: output spectrum of a fifth-order CT electromechanical ΣΔM using single-ended circuits: the pink solid line is without windowing, while the blue line is with Hanning window. 127
7.19 PCB of a fifth-order electromechanical ΣΔM. 127
7.20 Prototype test environment. 128
7.21 Spectrum of the output bitstream measured by ADVANTEST R9211B FFT servo analyzer for high-order electromechanical ΣΔM. 129
7.22 Inter-symbol effect on a fully differential CT ΣΔM. 130
7.23 Pspice simulation: output spectrum of a fifth-order CT electromechanical ΣΔM using fully differential circuits. 131
7.24 Simulations: spectrum of the output bitstream of the fifth-order electromechanical ΣΔM (2nd version). 132
7.25 The spectrum of the output bitstream measured by ADVANTEST R9211B FFT servo analyzer for the fifth-order electromechanical ΣΔM (2nd version). 133

8.1 Schematic diagram of an accelerometer with a fully differential structure. . 135
8.2 Layout of a fully differential microaccelerometer. 136
8.3 Structure of the spring (1/4). 137
8.4 Mechanical spring simulated using the AutoSpring solver (CoventorWare). . 137
8.5 Squeeze-film damping simulated using the MemDamping Solver. 139
8.6 Modal analysis: mode=1, resonant frequency 323Hz. 140
8.7 Modal analysis: mode=2, resonant frequency 3.01kHz. 141
8.8 Modal analysis: mode=3, resonant frequency 3.96kHz. 141
8.9 Cross sensitivity analysis, output displacement response to: (a) input Y-1g/X-1g acceleration; (b) input Y-1g/X-2g acceleration; (c)input Y-1g/Z-1g acceleration; (d) input Y-1g/Z-2g acceleration. 143
8.10 Capacitance including fringe effects (one array comb fingers=30). 144
8.11 SOG fabrication process for the high performance accelerometer. 145
8.12 SEM pictures of the fabricated sensor. 146
8.13 Anodic bonding (silicon wafer to Pyrex 7740 glass). 147
8.14 SOI fabrication process of the high performance accelerometer. 148

9.1 A multi-bit high-order electromechanical ΣΔM. 152
9.2 An electromechanical ΣΔM with quadrature force feedback cancellation. . . 152
9.3 High-order parasitic modal frequencies of a micromachined sensing element. 153

List of Tables

2.1 Performance requirements for different classes of gyroscopes (Yazdi et al [13]). 9

3.1 Typical specifications of accelerometers for automotive and inertial navigation applications (Yazdi et al [13]). 30

4.1 Performance comparison among second-order, third-order, fourth-order and fifth-order electromechanical $\Sigma\Delta$M with multi-feedback loops. 51
4.2 Simulation conditions of the system shown in Figure 4.44. 81
4.3 Simulation results of the system shown in Figure 4.44. 81

6.1 Parameters of the gyroscope used for simulations 97

8.1 Parameters of the μg micro-accelerometer 144
8.2 Wafer parameters of the SOG process. 145
8.3 Wafer parameters of the SOI process 147

List of Abbreviations

ac	alternating current
ADC	analog-to-digital converter
A/D	analog-to-digital
AM	amplitude-modulated
ASIC	application specific integrated circuit
CDS	correlate double sampling
CMOS	complementary metal-oxide semiconductor
CMP	chemical mechanical polishing
CT	continuous-time
CVC	capacitance to voltage converter
DAC	digital-to-analog converter
dc	direct current
D/A	digital-to-analog
DR	dynamic range
DRIE	deep reactive ion etching
DSP	digital signal processor
DT	discrete-time
ENTF	electronic noise transfer function
EMI	electromagnetic interference
FEM	finite elements method
FF	feed-forward

FFLR	feed-forward loops with resonators
FFT	fast Fourier transform
FPGA	field programmable gate array
GAL	gate array logic
GBW	gain bandwidth
GPS	global positioning system
INA	instrumentation amplifier
LF	low frequencies
LIGA	the German acronym for X-ray lithography (X-ray Lithographie), electro-deposition (Galvanoformung), and molding (Abformtechnik)
IC	integrated circuits
ICP	inductance coupling plasma
MASH	multi stage noise shaping
MEMS	micro electrical mechanical system
MF	multi-feedback
MFLR	multi-feedback loops with resonators
NRZ	non-return to zero
op-amp	operational amplifier
OSR	oversampling ratio
PCB	printed circuit board
PSD	power spectrum density
ppm	parts per million
QNTF	quantization noise transfer function
RC	resistor-capacitor
RTZ	return to zero
SBW	signal bandwidth
SC	switched capacitor
SDM	sigma-delta modulation

SEM	scanning electron microscope
$\Sigma\Delta$M	sigma-delta modulator
SMT	surface mounted technology
SNR	signal-to-noise ratio
SNDR	signal-to-(noise plus distortion) ratio
SOG	silicon-on-glass
SOI	silicon-on-insulator
SQNR	signal-to-quantization noise ratio
SR	slew rate
STF	signal transfer function
TF	transfer function
THD	total harmonic distortion
TNEA	thermal noise equivalent acceleration

List of Symbols

A	effective capacitor area
a	applied acceleration
a_{BN}	input-referred acceleration generated by Brownian noise
a_{dead2}	input-referred dead-zone acceleration of a second-order electromechanical $\Sigma\Delta$M
a_{dead5}	input-referred dead-zone acceleration of a fifth-order electromechanical $\Sigma\Delta$M
b	damping coefficient of a sensing element
C_0	nominal sensing capacitance
$C(s)$	phase compensator transfer function in continuous-time domain
$C(z)$	phase compensator transfer function in discrete-time domain
d_0	nominal gap between the sensing capacitors
Δf	bandwidth of interest in Hz
D_0	quantizer output bitstream
ε_0	the permittivity of free space (8.85×10^{-12} F/m)
E	the Young's modulus ($1.65 \times 10^{11} N/m^2$)
f_b	signal bandwidth
f_0	resonant frequency (unit: Hz)
F_{BN}	force generated by Brownian noise
$F_{Coriolis}$	force generated by Coriolis force
$f_{Nyquist}$	Nyquist frequency
$F_{Quad.}$	force generated by quadrature force

f_s	sampling frequency
$\mathscr{F}$	Fourier transform
$H(s)$	continuous-time transfer function
$H(z)$	discrete-time transfer function
k	spring stiffness of a sensing element
K_B	Boltzmann constant (1.38×10^{-23} N·m/K)
K_{fb}	electrostatic force feedback conversion gain
K_{po}	pickoff gain
K_q	quantizer gain
K_{xc}	gain of displacement to capacitance conversion
λ_{min}	minimum quantizer gain to keep high-order loop stable
m	mass of a sensing element
$\mathcal{L}^{-1}$	inverse Laplace transform
$M(s)$	transfer function of a sensing element in continuous-time domain
$M(z)$	transfer function of a sensing element in discrete-time domain
μ	air dynamic viscosity (1.86×10^{-5} Kg/(m·s) at 1atm, 300K)
μ_{eff}	effective dynamic viscosity of air
ω_r	resonant frequency (unit: rad)
Ω_N	minimum detectable angular rotation signal
Q	quality factor
$R(z)$	electronic resonator transfer function
T	absolute temperature in Kelvin
τ_d	loop delay time
θ	misalignment angle between the orthogonal x-axis and y-axis
T_S	sampling period
V_s	excitation carrier voltage
V_{fb}	electrostatic force feedback voltage
$\mathcal{Z}_T$	z-transform

Acknowledgements

Foremost I would like to thank my supervisor, Dr Michael Kraft for his helpful support during these years. This work would not have been possible without his perfect guidance and insight.

I especially thank Prof Bill Redman-White, my co-supervisor, for his excellent advice and valuable feedback.

Thanks to Dr Graham J Ensell for his continuous support on the MEMS fabrication.

I would acknowledge with gratitude the useful discussion and collaboration with the friendly PhD fellows in Rm.2043 of Mountbatten Building: Manouchehr Bahrami, Chien Fat Chau, Lit Ho Chong, Badin Damrongsak, Dr Huda El-Mubarek, Enrico Gili, Dr Mircea Gindila, Carsten Gollasch, Christoph Haas, Dr Ruth Houlihan, Ben Husband, Man N Kham, Pat Kittidachachan, Xiaoli Li, Dr Mir Mokhtari, Tao Sun, Dr Huabing Yin and Wen Zhang.

I also greatly appreciate the cleanroom staff for the fabrication of the device: Dr Nasser Afshar, Brain Ault, Tony Blackburn, Dr Janet Bonar, Sally Croucher, Mohamad Hadrun, Corry Krotochvila, and Dr Becky Neal.

Finally, I thank the wonderful group secretaries, Glenys Howe, Lucia Hewett and Christine Foster who always gave me generous help.

This work was fully supported by the Overseas Research Students Awards Scheme (ORSAS)[1] and the School of Electronics and Computer Science at Southampton University[2].

[1] http://www.orsas.ac.uk/
[2] http://www.ecs.soton.ac.uk/

To

雯晴　欣桐　高峰

WenQing, XinTong, GaoFeng

Chapter 1

Introduction

Micromachined inertial sensors, primarily consisting of accelerometers and gyroscopes, have been the focus in the Micro Electromechanical Systems (MEMS) research for over two decades since Roylance et al [1] reported the first prototype of a micromachined accelerometer in 1978. Now micromachined accelerometers are regarded as one of the most successful commercialized micro sensors ever developed for automotive applications and have the second largest market after pressure sensors. On the other hand, micromachined gyroscopes are a relatively new technology, and there are some devices available, but commercial gyroscopes lag behind by about one decade.

Since MEMS utilize modern semiconductor fabrication technology, miniaturized mechanical structures can be batch-fabricated and even integrated with the interface electronics on the same silicon chip or same package. The integration has the potential to make the sensors smart or intelligent. Surface micromachining uses compatible CMOS processes to fabricate the silicon mechanical structures and can monolithically integrate electronics on the same chip to reduce parasitic capacitance and series resistance. For bulk micromachining, the silicon mechanical structures and electronics interface can be fabricated on two separated dies and packaged together.

The attractive features of micromachined inertial sensors are their potentially low cost, significantly reduced size and light weight, and low power dissipation. This impact will also open up new applications by improving the overall performance of systems with large arrays of devices.

For low to medium performance applications, micromachined accelerometers can be found in large-volume products, such as automotive airbag and rollover detection system, jitter stabilization in camcorders, Parkinson disease monitoring and shipment monitoring, etc. However, there is an increasing demand for high performance (μg accuracy) micromachined accelerometers that comes from inertial navigation/guidance systems for airplanes and missiles (e.g. multi-axis accelerometers and gyroscopes on the same chip as a back-up

for global positioning systems (GPS)), intelligent weapons, space micro-gravity, unmanned aerial vehicles, and distributed battery-powered seismometers.

High performance inertial sensors usually take the advantages of a closed-loop control strategy to increase the dynamic range, linearity and bandwidth of the sensors. However, purely analog force feedback closed-loop schemes suffer from electrostatic pull-in problems in which electrostatic forces can lead the proof mass to latch to one set of electrodes. In the last 15 years, closed-loop force feedback control schemes with sigma-delta modulation have become very attractive for capacitive micromachined inertial sensors, which can not only preserve all advantages of closed-loop sensors but also produce digital output in the format of a pulse density bitstream, which can directly interface to a microprocessor or digital signal processor (DSP) for further signal processing.

1.1 Motivation

Previous work mainly focused on using the sensing element only to form a second-order single loop sigma-delta modulator ($\Sigma\Delta$M) [2], [3], [4], [5], [6], [7] and rarely used additional electronic integrators to form a high-order $\Sigma\Delta$M [8], [9], [10]. In the context of this work, a **high-order** $\Sigma\Delta$M is considered as a control system with an order greater than two. For such a control system, **high-order** also implies that there is one or more electronic integrators (resonators) in the loop. Kraft et al [11] presented a third-order multi-stage noise shaping (MASH) electromechanical $\Sigma\Delta$M, but the MASH loop architecture has been found to be more sensitive to gain variations due to microfabrication tolerance. Recently, Petkov et al [12] put forward a fourth-order single loop interface for inertial sensors, which greatly reduce the interaction between the quantization noise and electronic noise, but there was no detailed design methodology and the loop topology for gyroscopes was based on a lowpass $\Sigma\Delta$M. So far, the advantages of high-order single loop electromechanical $\Sigma\Delta$M have not been fully explored, especially for inertial sensors, which leads to higher signal to noise ratio (SNR) in a wide signal bandwidth. This thesis presents systematic design, simulation, fabrication and prototype of a control system for a high-order $\Sigma\Delta$M using a high performance inertial accelerometer. The research work mainly focussed on the following issues:

- Systematic design, analysis and simulation of the electromechanical high-order single loop $\Sigma\Delta$Ms. To investigate the loop stability, the loop coefficients have to be optimized for different topologies. The noise-shaping performance for quantization noise, electronic noise and signal are analyzed and compared.
- The electrostatic force feedback, or one-bit electromechanical DAC is inherently nonlinear, which results in harmonic distortion in bitstream output and therefore considerably reduce signal to noise plus distortion ratio (SNDR). The research proposes an effective linearization approach which can be easily implemented in circuitry.

- Application of a high-order bandpass ΣΔM instead of a lowpass ΣΔM to micromachined vibratory gyroscopes.
- A PCB prototype (not ASIC chip) of a fifth-order electromechanical ΣΔM to demonstrate the design methodology.
- Design and fabrication of an in-plane accelerometer (micro-g mechanical noise floor, high sensitivity 10pF/g and high modal frequencies) with a fully differential structure.

Optimizing coefficients of the control loop lead to stable closed loop systems with improved SNR. The single loop high-order ΣΔM can accommodate relatively large microfabrication tolerance from both the mechanical structure and analog circuits. Both simulations and prototyping show that high-order ΣΔM force feedback loops can get better dynamic range (DR) than a second order loop and tonal behaviour is greatly alleviated. The topologies investigated are applicable not only to accelerometers, but also to other inertial sensors such as gyroscopes.

1.2 Thesis Organization

Chapter 2 briefly describes the operating principles of accelerometers and vibratory gyroscopes. A mechanical lumped model is described, and several parameters including dynamic performance, thermal noise equivalent acceleration (TNEA) and the SNR are defined. The principles of a ΣΔM are described with the concept of noise shaping, calculation of SQNR and linear quantizer model. The performance of different topology, including high-order single loop ΣΔM, MASH and multi-bit ΣΔM are compared. The Chapter also gives the lowpass to bandpass transformation and the advantages and disadvantages of continuous-time ΣΔM vs discrete-time ΣΔM. The bitstream output spectrum is the performance metric of a ΣΔM. Not only the SQNR can be derived, but also it can be used to check if the noise shaping has the correct order.

In Chapter 3, a comprehensive backgrounds is given on the closed-loop ΣΔ micromachined capacitive inertial sensors. First, the interface to micromachined capacitive inertial sensors is analyzed. For present microfabrication techniques, surface micromachining, bulk micromachining and LIGA are described. The second-order single loop, MASH and high-order single loop are reviewed for micromachined capacitive inertial sensors using ΣΔMs.

In Chapter 4, a detailed design methodology and simulation results of a high-order single loop electromechanical ΣΔM are presented. The performance and design with the different topologies, including multi-feedback loops, multi-feedback loops with resonators, and feed-forward loops with resonators, are simulated and compared. Noise sources are analyzed in detail and methods are proposed for suppression of the electronic noise. Monte-Carlo simulation is used to verify performance variation due to microfabrication tolerance for

both high-order single loop and second-order loop. Some special phenomena of a high-order electromechanical ΣΔM are also investigated in detail, including the dead-zone and idle tones, the effect of the mechanical quality factor on noise shaping, electrostatic force feedback delay, and non-ideal circuit implementation.

In Chapter 5, an effective force linearization is put forward to reduce the harmonic distortion in the bitstream of the electromechanical ΣΔM. The non-linearity coming from the charge amplifier is also discussed.

In Chapter 6, a control system with a high-order bandpass ΣΔM is applied to micromachined vibratory gyroscopes. The sense mode is described in detail. The oversampling frequency is greatly reduced compared with a lowpass ΣΔM. The low frequency $1/f$ noise and drift are removed in the signal band.

In Chapter 7, experimental results are given. A fifth-order lowpass electromechanical CT ΣΔM is prototyped using a PCB. Front interface circuits are analyzed in detail, including preamplifier, demodulation and force feedback schemes. Experimental results show the SNR of the control system is about 90dB using a fully-differential circuits.

In Chapter 8, a high performance micromachining capacitive accelerometer is designed with a fully differential structure. Key parameters, such as spring stiffness constant, damping coefficient, modal analysis, cross axis sensitivity, static sensitivity and TNEA are simulated and calculated. Two practical fabrication processes are outlined and some fabrication results are shown.

In the final chapter, the major achievements of the resaerch are summarized and further work for investigation is outlined.

Chapter 2

Fundamental Principles

2.1 The Principles of Micromachined Accelerometers

2.1.1 Mechanical Lumped Model

An accelerometer comprises a proof mass suspended by a spring to a fixed frame and converts the signal from the mechanical to the electrical domain. A schematic diagram of a second-order mass-spring-damper system is shown in Figure 2.1.

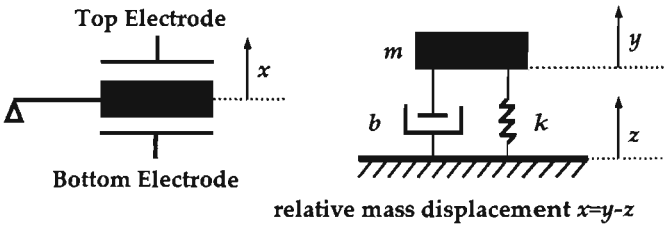

FIGURE 2.1: General capacitive accelerometer structure and its mechanical lumped model.

m is the mass of the proof mass, k is the effective spring stiffness constant of the suspension spring and b is the damping factor which affects the dynamic characteristics of the proof mass. The input acceleration is exerted on the proof mass by the relative motion of the suspended proof mass to the fixed frame; the suspended spring and the damper dissipate the energy in the system. The differential equation for the displacement as a function of external acceleration is:

$$m\frac{d^2y}{dt^2} = -b\frac{d(y-z)}{dt} - k(y-z) \tag{2.1}$$

$$m\frac{d^2x}{dt^2} + b\frac{dx}{dt} + kx = -m\frac{d^2z}{dt^2} = -ma = -F \tag{2.2}$$

where x is the movement of the proof mass, F is the external force, and a is the external acceleration.

2.1.2 Dynamic Responses

By applying Laplace transform for Equation 2.2, the transfer function for the sensing element is of the form:

$$H(s) = \frac{x(s)}{a(s)} = \frac{1}{s^2 + \frac{b}{m}s + \frac{k}{m}} = \frac{1}{s^2 + \frac{\omega_r}{Q}s + \omega_r^2} \tag{2.3}$$

where $\omega_r = \sqrt{\frac{k}{m}}$ is the resonant frequency. Q is the quality factor and is defined as:

$$Q = \frac{m\omega_r}{b} = \frac{\sqrt{mk}}{b} : \begin{cases} < 0.5 & \text{overdamped} \\ = 0.5 & \text{critical damped} \\ > 0.5 & \text{underdamped} \end{cases} \tag{2.4}$$

In the frequency domain, the transfer function Equation 2.3 of the sensing element is of the form:

$$H(\omega) = \frac{x(\omega)}{a(\omega)} = \frac{1}{(\omega_r^2 - \omega^2) + j\frac{\omega_r \omega}{Q}} \tag{2.5}$$

The response magnitude and phase:

$$\text{magnitude} : \quad \left|\frac{x(\omega)}{a(\omega)}\right| = \frac{1}{\sqrt{(\omega_r^2 - \omega^2)^2 + (\frac{\omega_r \omega}{Q})^2}} = \begin{cases} \frac{1}{\omega_r^2} & \text{if } \omega \ll \omega_r \\ \frac{Q}{\omega_r^2} & \text{if } \omega = \omega_r \\ \frac{1}{\omega^2} & \text{if } \omega \gg \omega_r \end{cases} \tag{2.6}$$

$$\text{phase} : \quad \Phi = \arctan\left(\frac{\frac{\omega_r \omega}{Q}}{\omega_r^2 - \omega^2}\right) \tag{2.7}$$

From Equation 2.6, it can be seen that, for low frequencies, the response is inversely proportional to the resonant frequency squared. At the resonant frequency, the response is the quality factor divided by the resonant frequency squared. For frequencies higher than the resonant frequency, the response is inversely proportional to the acceleration frequency squared. Figure 2.2 shows the response of an accelerometer: under-damped (black line, upper), critically damped (blue line, middle) and over-damped (red line, bottom). The bandwidth of the sensor is determined by the resonant frequency. The resonant frequency

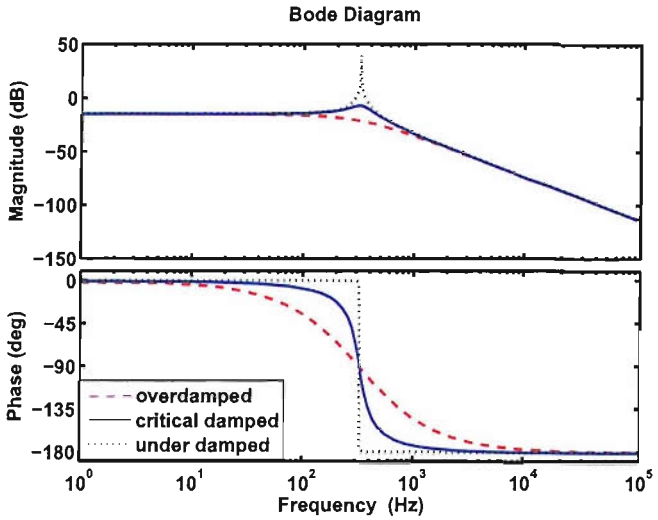

FIGURE 2.2: Bode diagram of a sensing element with different quality factor Q.

of the mechanical structure can be increased by increasing the spring stiffness constant and decreasing the proof mass, while the quality factor of the device can be increased by reducing damping and by increasing proof mass and spring stiffness constant. For maximum bandwidth, the sensing element should be critically damped, which is determined by the quality factor Q. The static sensitivity of the device can be improved by reducing its resonant frequency. The static sensitivity (dc gain) of a sensing element is a metric for a dc input and given by:

$$\mathbb{S}_{static} = \frac{m}{k} = \frac{1}{\omega_r^2} \tag{2.8}$$

2.1.3 Thermal Noise Equivalent Acceleration

Mechanical noise is normally called Brownian noise, which is a random force generated by the Brownian motion of ambient molecules surrounding the proof mass and the Brownian motion of the proof mass suspension or anchors. The power spectral density (PSD) of the Brownian noise force is given by:

$$\overline{F^2}_{BN} = 4K_B \times T \times b \tag{2.9}$$

where K_B=1.38e-23 Nm/K is Boltzmann constant, and T is the absolute temperature in Kelvin and b is the damping coefficient. The PSD of the input-referred Brownian noise for

accelerometers is defined as:

$$\overline{a^2}_{BN} = \frac{\overline{F^2}_{BN}}{(m \times g)^2} = \frac{4K_B \times T \times b}{9.8^2 \times m^2} \mathrm{g}^2/\mathrm{Hz} \tag{2.10}$$

and the thermal noise equivalent acceleration (TNEA) [13] is defined as:

$$TNEA = \sqrt{\overline{a^2}_{BN}} = \frac{\sqrt{4K_B \times T \times b}}{9.8 \times m} = \frac{1}{9.8}\sqrt{\frac{4K_B \times T \times \omega_r}{m \times Q}} \ (\mathrm{g}/\sqrt{Hz}) \tag{2.11}$$

In order to lower the mechanical noise floor, from Equation 2.11 it is desirable to reduce air damping and increase the sensing element mass. TNEA mainly depends on the structure of the sensor and also the micromachining fabrication process. The associated noise response in the bandwidth of interest Δf (Hz) referred to the proof mass displacement of an accelerometer is given by:

$$|x_{BN}| = \frac{|F_{BN}|}{k} = \frac{\sqrt{4K_B \times T \times b \times \Delta f}}{k} = \sqrt{\frac{4K_B \times T \times b \times \Delta f}{m \times Q \times \omega_r^3}} \tag{2.12}$$

The static proof mass displacement of an accelerometer is given by:

$$|x_{signal}| = \frac{|F_{Signal}|}{k} = \frac{ma}{k} = \frac{ma}{m\omega_r^2} = \frac{a}{\omega_r^2} \tag{2.13}$$

Equation 2.12 shows that the Brownian noise sets the minimum detectable displacement, and therefore the minimum detectable acceleration. The SNR of an accelerometer is another measure of the minimum detectable acceleration, and is defined by the ratio of the signal power to the noise (only Brownian noise considered) power:

$$SNR = \frac{|x_{signal}|^2}{|x_{BN}|^2} = a^2 \times \frac{m \times Q}{4K_B \times T \times b \times \omega_r \times \Delta f} \tag{2.14}$$

It can be seen in Equation 2.14 that in order to increase the SNR, the parameters mass m and quality factor Q should be designed with as large as possible while the parameters damping b and resonant frequency ω_r should be designed with as small as possible.

Parameters	Rate Grade	Tactical Grade	Inertial Grade
Angle Random Walk, $^o/\sqrt{h}$	>0.5	0.5-0.05	<0.001
Bias Drift, $^o/h$	10-1000	0.1-10	<0.01
Scale Factor Accuracy, %	0.1-1	0.01-0.1	<0.001
Full Scale Range, $(^o/sec)$	500-1000	>500	>400
Max. Shock in 1msec, g's	10^3	10^3-10^4	10^3
Bandwidth, Hz	> 70	~100	~100

TABLE 2.1: Performance requirements for different classes of gyroscopes (Yazdi et al [13]).

2.2 The Principles of MEMS Vibratory Gyroscopes

A gyroscope is an angular rate sensor and has traditionally been exclusively regarded as being a core component of navigation system (INS), which can complement GPS. There are three kinds of gyroscopes: optical gyroscopes (including ring laser gyroscopes and optical fibre gyroscopes), spinning gyroscopes and vibration gyroscopes. The fundamental consideration for performance is zero drift rate, which means the smaller the drift the higher the cost of the gyroscope. For example, the accuracy of a ring laser sensor has a drift of a rate of $0.01^o/h$, one of most accurate gyroscopes ever made (cost about $10k) [14]. The applications require different performance sensors and their parameters are shown in Table 2.1.

However, optical gyros are expensive and optical components are difficult to be miniaturized and integrated mainly due to the optical path cannot be shrunk. Moreover, spinning-mass gyros need large inertial mass to increase sensitivity, so they are also not suitable for microfabrication. In fact, vibratory gyroscopes, which operate due to the Coriolis force, are the main-stream type so far for MEMS implementation.

2.2.1 Vibratory Gyroscopes

A simplified operating principle for a vibratory gyroscope is shown in Figure 2.3. The mechanical system is a mass-damped-spring system in two degrees of freedom. The proof mass can vibrate in two orthogonal directions: along the x-axis (drive mode) by an electrostatic actuation force F_{drive}; along the y-axis (sense mode) incurred by the rotation around the z-axis with an angular velocity to be detected.

In operation, the proof mass is driven into vibration in the x-direction and its displacement is given by

$$x = A_x \cos(\omega_x t) \tag{2.15}$$

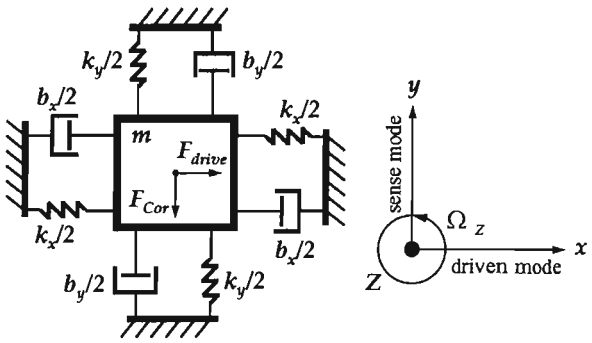

FIGURE 2.3: Operation principle of a vibratory gyroscope.

where A_x is the amplitude and ω_x the driving frequency of the oscillation, respectively. Assuming the system is then rotated around the z-axis with an angular velocity $\vec{\Omega} = \Omega_z \vec{e}_z$ with respect to an inertial system. a Coriolis force acting upon the proof mass:

$$\vec{F}_{Coriolis} = 2mV_x\vec{e}_x \times \vec{\Omega} \tag{2.16}$$

where $v_x\vec{e}_x$ is the velocity relative to the reference frame. Taking the Equation 2.15 into account, the Coriolis force is given by:

$$\vec{F}_{Coriolis} = -2mA_x\omega_x\Omega_z \sin(\omega_x t)\vec{e}_y \tag{2.17}$$

Equation 2.17 indicts that the amplitude of Coriolis force is directly proportional to the rotation rate and the force is along the y-axis. The proof mass oscillation in the y-axis can also be described by a second-order linear system:

$$m\frac{d^2y}{dt^2} + b_y\frac{dy}{dt} + k_y y = -2mA_x\omega_x\Omega_z \sin(\omega_x t) \tag{2.18}$$

The solution of the differential equation, the displacement in the y-axis is given by:

$$y = -A_y \sin(\omega_x t - \varphi) \tag{2.19}$$

where A_y is the magnitude:

$$A_y = \frac{2A_x\omega_x\Omega_Z}{\omega_y^2\sqrt{\left(1 - \frac{\omega_x^2}{\omega_y^2}\right)^2 + 4\xi_y^2\frac{\omega_x^2}{\omega_y^2}}} \tag{2.20}$$

ξ_y damping ratio:

$$\xi_y = \frac{b_y}{2m\omega_y} \tag{2.21}$$

and φ phase lag:

$$\varphi = \arctan \frac{2\xi_y \omega_x \omega_y}{\omega_y^2 - \omega_x^2} \tag{2.22}$$

where ω_y is resonant frequency of the sense mode. Therefore, the displacement in y-axis $A_y$is proportional to the angular rate Ω. Equation 2.20 can be rewritten with the quality factor in the sense mode (x-axis) $Q_y = \frac{1}{2\xi_y}$:

$$A_y = \frac{2A_x\omega_x\Omega_Z}{\omega_y^2\sqrt{\left(1 - \frac{\omega_x^2}{\omega_y^2}\right)^2 + \frac{1}{Q_y^2}\frac{\omega_x^2}{\omega_y^2}}} \tag{2.23}$$

For ω_x equal to ω_y, the maximum sensitivity is achieved as:

$$A_y = \frac{2A_x Q_y \Omega_Z}{\omega_y} \tag{2.24}$$

It can be seen from Equation 2.24 that in order to increase the sensitivity, the drive amplitude A_x and the sense mode quality factor Q_y should be as large as possible, while the vibration frequency of the sense mode ω_y should be small. However, Equation 2.24 applies only for a constant angular rotation and if for a open-loop operation (ω_y should be separated from ω_x)the 3db bandwidth is $0.54(\omega_y - \omega_x)$ [15], but for a closed-loop operation (ω_y can be maintained equal to ω_x for high sensitivity) electrostatic force feedback is used to extend the bandwidth. In micromachined gyroscopes, the Coriolis force is usually far less than the inertial force, so the minimum detectable angular rotation signal is also limited by the thermo mechanical noise as a micro-accelerometer. Combination of Equation 2.9 and Equation 2.17, the thermal mechanical noise equivalent angular rate signal Ω_N can be found by the condition of:

$$2mA_x\omega_x\Omega_N = 4K_B \times T \times b \times \Delta f \tag{2.25}$$

Finally, we have:

$$\Omega_N = \sqrt{\frac{K_B T \omega_y \Delta f}{m A_x^2 \omega_x^2 Q_y}} \tag{2.26}$$

For example, a typical surfaced micromachined gyroscope packaged in vacuum has the following parameters [16]: A_x=0.1μm, m=5×10^{-9} Kg, $\omega_x = \omega_y = 10^5$rad/s, Δf=100Hz and Q=30000, working at T=300K, the equivalent angular rate signal of the thermo mechanical noise is derived from Equation 2.26 to be Ω_N=5.711$^o/h$. This indicates the performance of a MEMS gyroscope still needs to be considerably improved to meet inertial grade applications.

The state-of-art designs of micromachined gyroscopes are still far from the theoretical limits because of the technological constraints and imperfections of microfabrication:

1. misalignment errors of the two orthogonal sense and drive axes.
2. non-uniform etching.
3. parasitic capacitances and series resistances.

1 and 2 will lead to quadrature force errors and mechanical resonant frequency mismatches; while 3 will considerably degrade the performance of the preamplifier. These issues also cause temperature-dependance errors and nonlinearity. Furthermore, air damping in micro structures will result in significant mechanical thermal noise, and can only be reduced by vacuum packaging. All these problems will considerably reduce the SNR. A closed-loop control system is a very effective solution to these problems and a more advanced closed-loop control system based ΣΔM principle will give further benefits, which will be discussed in detail in Chapter 6.

In an ideal implementation of a micromachined gyroscope, the sense and drive mode should be only coupled through the Coriolis force. In practice, the misalignments and non-uniform etching in the microfabrication process usually cause the mechanical mismatches even though the mechanical structure is perfectly symmetrically designed. The microfabrication tolerances produce a coupling force along the sense mode direction as shown in Figure 2.4.

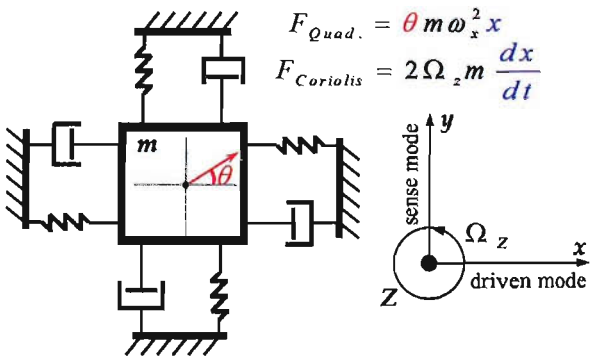

FIGURE 2.4: Coriolis force and quadrature force due to imperfections of mechanical structure microfabrication.

This force $F_{Quad.} = \theta m\omega_x^2 x$ is referred to as quadrature force due to quadrature (90^o out of phase) with Coriolis force. θ is the misalignment angle between the orthogonal x-axis

and y-axis. Since it is proportional to the displacement (x) along the drive direction, which is much larger than that of along the sense direction, quadrature force is typically orders of magnitude larger than the Coriolis force. Therefore, it is necessary to separate the Coriolis force component from the quadrature force using synchronous phase-sensitive demodulation, otherwise it would overload the interface electronics.

2.3 The Principles of A ΣΔM

2.3.1 Noise Shaping

ΣΔM has been applied for over 50 years since Inose et al [17] proposed it in 1962, and Plassche [18] made the first ΣΔ Analog-to-Digital converter (ADC) in replacement of traditional Nyquist-rate ADCs in 1978, but only until the last two decades did the high-density digital VLSI circuits mature sufficiently to manufacture them as inexpensive monolithic integrated circuits [19]. A ΣΔM is the combination of a delta modulator and an additional integrator in the feed-forward (FF) path performing the summation.

A major reason for the popularity of ΣΔM architectures lies in their ability to trade bandwidth for quantization noise. In addition, they have advantages over the traditional Nyquist-rate analog ADCs: relaxed requirements for anti-aliasing filters, relaxed requirements for component matching, and compatibility with digital VLSI technology. The quantization noise property is compared between a Nyquist sampling converter, an oversampling converter and an oversampling and noise shaping converter. Their schematic spectra are shown in Figure 2.5. A ΣΔ ADC is composed of two basic blocks: a modulator and a digital signal processing block for filtering and decimation. The shaped noise is then filtered by an appropriate digital decimation filter. The first-order discrete integrator, $H(z) = z^{-1}/(1 - z^{-1})$ effectively acts as a memory for the modulator, and has a frequency response that decays by 20dB/dec and a constant phase shift of -90^o.

A ΣΔM was originated from the Δ modulator, shown in Figure 2.6(a), in early digital communication applications [20]. The output bitstream of the Δ modulator represents the sign of the difference between the input and feedback integrator, which acts as a decoder to approximate the input analog signal. This is where the meaning of **Delta** or Δ comes from. However, a high frequency input signal will overload the feedback integrator. The solution is to put an additional integrator in the front of the input signal to suppress its amplitude of high frequencies, which leads to the structure shown in Figure 2.6(b). The structure results in encoding the integral of the input signal (summation, **Sigma** or Σ). According to classic control theory, the structure of Figure 2.6(b) can be transformed into the block diagram shown in Figure 2.6(c). Furthermore, the integrator can be modified by using lowpass analog filters to form a high-order lowpass ΣΔM, or by using bandpass analog filters to form a high-order bandpass ΣΔM. The analog filters can either be implemented

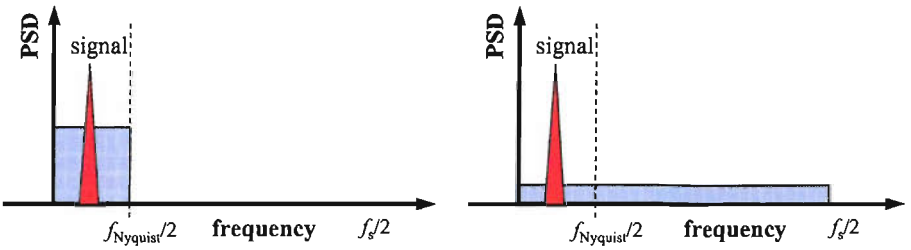

(a) Quantization noise in a Nyquist sampling converter.

(b) Quantization noise in an oversampling converter.

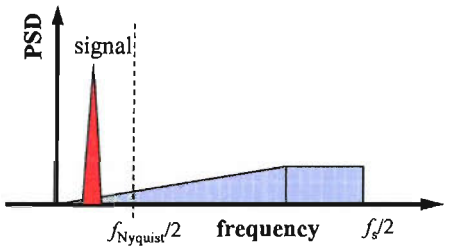

(c) Quantization noise in an oversampling and noise shaping converter.

FIGURE 2.5: Schematic spectrum comparison between the Nyquist sampling converters, oversampling converters and noise shaping and oversampling converters.

in continuous-time or discrete-time circuits, and the quantizer can be configured as one-bit or multi-bit.

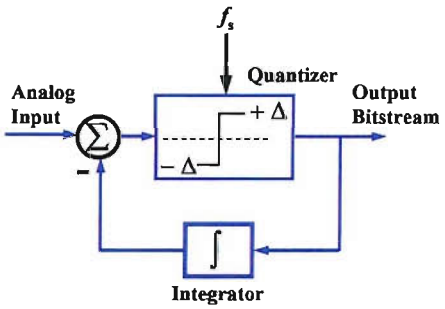

(a) Δ modulator.

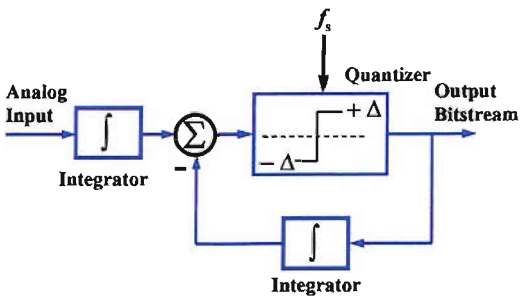

(b) Original structure of a ΣΔM.

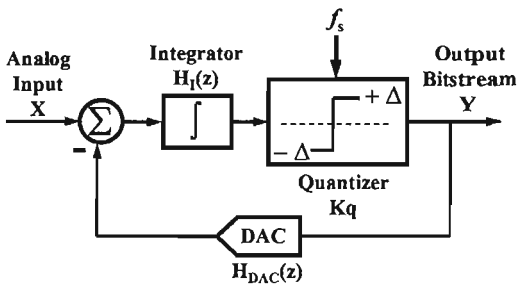

(c) Equivalent structure of a ΣΔM.

FIGURE 2.6: Structures of a ΣΔM.

2.3.2 SQNR

The Fourier transform decomposes a function into a continuous spectrum of the frequencies that comprise that function. In mathematical physics, the Fourier transform of a signal $x(t)$ can be thought of as that signal in the frequency domain. A Fourier transform to the frequency domain, f, is given by the function:

$$X(f) = \int_{-\infty}^{+\infty} x(t)e^{-j2\pi ft}dt \tag{2.27}$$

$j = \sqrt{-1}$ is the imaginary unit and $X(f) = \mathscr{F}\{x(t)\}$ represents the Fourier transform of $x(t)$ and f represents the frequency component (in hertz) of $x(t)$.

The inverse Fourier transform (IFT) is given by:

$$x(t) = \int_{-\infty}^{+\infty} X(f)e^{j2\pi ft}df \tag{2.28}$$

In signal processing, given a signal $x(t)$, the continuous autocorrelation $R_f(\tau)$ is the continuous cross-correlation of $x(t)$ with itself, at lag τ, and is defined as:

$$R_{xx}(\tau) = x^*(-\tau) \otimes x(\tau) = \int_{-\infty}^{+\infty} x(t+\tau)x^*(t)dt = \int_{-\infty}^{+\infty} x^*(t)x(t-\tau)dt \tag{2.29}$$

where x^* represents the complex conjugate and $\otimes$ represents convolution.

The $WienerKhinchin$ theorem defines that power spectral density (PSD) of a signal $x(t)$ is the Fourier transform of the corresponding autocorrelation function.

$$PSD_x(f) = \int_{-\infty}^{\infty} R_{xx}(\tau)e^{-j2\pi f\tau}d\tau \tag{2.30}$$

or,

$$PSD_x(f) = \int_{-\infty}^{+\infty}\left[\int_{-\infty}^{+\infty} x(t+\tau)x^*(t)dt\right]e^{-j2\pi f(t+\tau)}e^{j2\pi ft}d\tau = \mathscr{F}\{x(t)\} \times \mathscr{F}^*\{x(t)\} \tag{2.31}$$

The PSD describes the statistic characteristic of the power (or variance) distribution of a random signal with frequency components. The units of spectral power density are commonly expressed in watts per hertz (W/Hz).

- The PSD of f(t) and the autocorrelation of f(t) form a Fourier transform pair. The spectral density is usually calculated using the Fourier transform.
- PSD is a function of frequency not time.
- PSD is amount of power between frequencies f and $f + df$ divided by df.

The total average power of signal $x(n)$ is represented by its variance:

$$\sigma_x^2 = E[|x(n)|^2] = \frac{1}{2\pi} \int_{-\pi}^{\pi} PSD_x(\omega) d\omega \tag{2.32}$$

where $E[\ ]$ denotes expectation (average) and PSD_x denotes the power spectral density of signal $x(n)$. Integrating the PSD of a random signal over all frequencies yields the total average power of a random signal.

Parseval's theorem [21] states that the area under the spectral density curve is equal to the area under the square of the magnitude of the signal.

$$\int_{-\infty}^{+\infty} PSD_x(f) df = \int_{-\infty}^{+\infty} |x(t)|^2 dt \tag{2.33}$$

Modern interpretation of Parseval's theorem [22] is actually a statement of a physical principle, the conservation of energy: the total energy contained in a waveform $x(t)$ summed across all of time t is equal to the total energy of the waveform's Fourier transform $X(f)$ summed across all of its frequency components f:

$$\int_{-\infty}^{+\infty} |x(t)|^2 dt = \int_{-\infty}^{+\infty} |X(f)|^2 df \tag{2.34}$$

Combination Equation 2.33 with Equation 2.34:

$$\int_{-\infty}^{+\infty} PSD_x(f) df == \int_{-\infty}^{+\infty} |X(f)|^2 df \tag{2.35}$$

Equation 2.35 denotes the power can be calculated by the magnitude spectrum of the signal.

For a linear system, which is described by its transfer function $H(z)$, the PSD of output y in response to input signal x is given by [22]:

$$PSD_y(f) = \left|H(e^{j2\pi f})\right|^2 \times PSD_x(f) \tag{2.36}$$

Equation 2.36 is very useful for understanding the concept of a ΣΔM. The quantization noise is mostly regarded as white noise, which is uniformly distributed over all frequencies, however, it can be transformed or shaped by some transfer function $H(z)$, the QNTF of the ΣΔM.

The output of a ΣΔM is a bitstream in a pulse density format. Supposing the band of interest is $[0, f_b]$, OSR= $f_s/2f_b$, $\omega_b = 2\pi f_b/f_s$, and $Y(e^{j\omega})$ is the PSD of output bitstream. $X(e^{j\omega})$ and $E(e^{j\omega})$ are the PSDs of input signal x and quantization noise e in the output bitstream. The SQNR calculation of a ΣΔM for the signal bandwidth can be calculated in the frequency domain by:

$$SQNR = \frac{Power_{signal}}{Power_{noise}} = \frac{\int_0^{\omega_b} |X(e^{j\omega})|^2 \, d\omega}{\int_0^{\omega_b} |E(e^{j\omega})|^2 \, d\omega} = \frac{\int_0^{\omega_b} |X(e^{j\omega})|^2 \, d\omega}{\int_0^{\omega_b} |Y(e^{j\omega})|^2 \, d\omega - \int_0^{\omega_b} |X(e^{j\omega})|^2 \, d\omega} \tag{2.37}$$

The discrete equivalent of Equation 2.37 is given by:

$$SQNR \approx \frac{\frac{2\pi}{N}}{\frac{2\pi}{N}} \frac{\sum_{k=0}^{M} |X(e^{j\omega_k})|^2}{\sum_{k=0}^{M} |Y(e^{j\omega_k})|^2 - \sum_{k=0}^{M} |X(e^{j\omega_k})|^2} = \frac{\sum_{k=0}^{M} |X(e^{j\omega_k})|^2}{\sum_{k=0}^{M} |Y(e^{j\omega_k})|^2 - \sum_{k=0}^{M} |X(e^{j\omega_k})|^2} \tag{2.38}$$

where N is the length of $y(n)$, $\Delta\omega = \frac{2\pi}{N}$ the frequency spacing, $M = \frac{\omega_b}{\Delta\omega} = \frac{N}{2OSR}$ the bins within the bandwidth of interest, and $\omega_k = \frac{2\pi}{N}k$ the discrete frequency.

Applying the N-bins fast Fourier transform (FFT) for $y(n)$ and $x(n)$,

$$X(e^{j\omega_k}) = FFT[x(n)] = X(k) \tag{2.39}$$

$$Y(e^{j\omega_k}) = FFT[y(n)] = Y(k) \tag{2.40}$$

the SQNR calculation in Equation 2.38 is given by:

$$SQNR = \frac{\sum_{k=0}^{M} |X(k)|^2}{\sum_{k=0}^{M} |Y(k)|^2 - \sum_{k=0}^{M} |X(k)|^2} \tag{2.41}$$

For a sinusoidal single-frequency input signal $x(n)$, there is only one spectral line at $\omega_x = \frac{2\pi}{f_s} f_x$, which corresponds to the bin: $k_1 = \frac{N}{f_s} f_x$ and thus:

$$\sum_{k=0}^{M} |X(k)|^2 = |Y(k_x)|^2 \tag{2.42}$$

Equation 2.41 can be further simplified:

$$SQNR = \frac{|Y(k_x)|^2}{\sum\limits_{\substack{k=0 \\ k \neq k_x}}^{M} |Y(k)|^2} \tag{2.43}$$

In practical calculations, N should be long enough and the length a power of 2, and k_x is chosen as an integer. In order to reduce the spectrum leakage, it is necessary for the output bitstream to be convolved with a window function before doing FFT, such as Hann window.

2.3.3 Quantizer Model

Due to the closed-loop control architecture of a ΣΔM, stability analysis is necessary, but the nonlinear behaviour of the quantizer, embedded in forward path, makes the stability analysis using linear control system theory unapplicable. So far, there are no rigorous analytical solutions to characterize the behaviour of a ΣΔM [23], [24]. A ΣΔM will be referred to as stable when for a certain class of input signals, the states of the system are bounded and the modulator is free of large signal limit cycles. Although several criteria are applied to examine the stability of a ΣΔM, such as Lee's rule (the out-of-band gain of the QNTF should be less than two for zero input [25], [26]), the most popular method is the describing function method [27], which uses an approximate model to qualitatively investigate the dynamic behaviour of a ΣΔM. The approximation enables the stability analysis of a ΣΔM using linear control theory. A quantizer is approximately modeled by a signal $x(n)$ dependent variable gain and plus an additive white quantization noise source $e(n)$: $y(n) = \lambda x(n) + E(n)$. Figure 2.7 shows the linearized model of the quantizer block. λ is the variable gain of the quantizer, and the white noise source implies that the error has statistical probabilities that are independent of the signal.

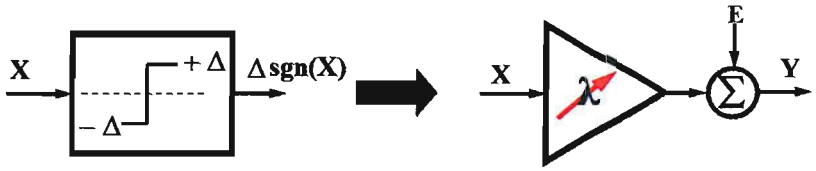

FIGURE 2.7: A linearized quantizer model of a ΣΔM.

For uniform quantization, the dynamic range (-E to $+E$) of the input signal $x(n)$ is equally divided into N steps, each step is $\Delta = 2E/N$. The stationary random quantization error $e(n) = \hat{x}(n) - x(n)$ is uniformly distributed and its probability density is:

$$PSD(e) = \begin{cases} \frac{1}{\Delta} & |e| \leq \frac{\Delta}{2} \\ 0 & \text{otherwise} \end{cases} \tag{2.44}$$

For a not overloaded quantizer, the dc component of the random white noise is represented by its expectation m_e and its average power (subtracting dc) is represented by its variance σ_e^2:

$$m_e = E[e(n)] = \int_{-\infty}^{\infty} ePSD(e)de \tag{2.45}$$

$$\sigma_e^2 = E[(e(n) - m_e)^2] = \int_{-\infty}^{\infty} (e - m_e)^2 PSD(e)de \tag{2.46}$$

Combining Equation 2.44 with Equation 2.45 and Equation 2.46, respectively, yield:

$$m_e = 0 \tag{2.47}$$

$$\sigma_e^2 = \Delta^2/12 = E^2/3N^2 \tag{2.48}$$

Although the assumption that the noise is independent of the input signal may result in serious modeling errors in some cases such as first-order or second-order modulators with low over-sampling ratios, for high-order modulators with high over-sampling ratios this assumption is a good approximation to determine the properties of ΣΔMs [28].

Figure 2.8 shows a general block diagram for a single loop ΣΔM, comprising a loop filter block and a nonlinear quantizer [23]. The $L = 1/QNTF - 1$ is the denominator of QNTF and is referred to the open-loop filter. The zeros of a loop filter is the poles of the QNTF, which determines the fundamental characteristic of the stability of a ΣΔM.

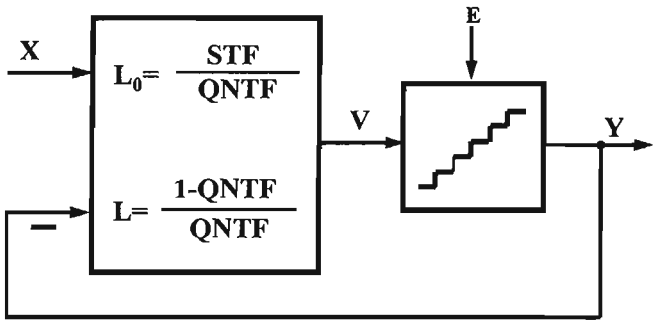

FIGURE 2.8: General block diagram of a single loop ΣΔM.

First, considering a quantizer with constant gain, assuming $\lambda = 1$ in Figure 2.8, the output of the modulator is given by its input $X(z)$ and the quantization error $E(z)$:

$$V(z) = L_0(z)X(z) + L(z)Y(z) \tag{2.49}$$

$$E(z) = Y(z) - V(z) \tag{2.50}$$

$$Y(z) = STF(z)X(z) + QNTF(z)E(z) \tag{2.51}$$

However, if the gain of the quantizer is assumed to be arbitrary and the error $E(z)$ is regarded as independent of the signal, Equation 2.51 can be re-written as:

$$Y(z) = STF'(z)X(z) + QNTF'(z)E(z) \tag{2.52}$$

where

$$STF' = \frac{\lambda STF(z)}{\lambda + (1-\lambda)STF(z)}, \quad QNTF' = \frac{QNTF(z)}{\lambda + (1-\lambda)QNTF(z)}$$

An estimation of the quantizer gain λ can be found from extensive simulations [23], by taking the ratio of the average quantizer input signal power to its output power. Root locus, Nyquist plots and Bode diagrams of the loop filter of a ΣΔM can be used to determine the minimal value of the quantizer gain λ_{min} to keep the ΣΔM loop stable (or not overloaded by the input signal). These methods will be addressed in detail in Chapter 4.

2.3.4 High-Order Single Loop ΣΔM

The transfer function of a theoretical Nth-order ΣΔM is given by [28]:

$$H(z) = (1 - z^{-1})^n \tag{2.53}$$

The PSD of the quantization noise in the output bitstream is given by:

$$PSD_{QN}(\omega) = QNTF(z)QNTF(z^{-1})\sigma_e^2 = 4(1-\cos\omega)^N\sigma_e^2 = \left(2\sin(\frac{\omega}{2})\right)^{2N}\sigma_e^2 \tag{2.54}$$

where $z = e^{j\omega T_s}$, $\omega = \frac{2\pi f}{f_s}$, thus,

$$PSD_{QN}(f) = \left(2\sin(\frac{\pi f}{f_s})\right)^{2N}\frac{2\sigma_e^2}{f_s} \tag{2.55}$$

Equation 2.55 describes the basic concept of a ΣΔM: the uniformly distributed white quantization noise is shaped by $\left(2\sin(\frac{\pi f}{f_s})\right)^{2N}$ and appears as colored noise at the output. This noise shaping technique lowers the noise power at low frequencies and pushes the noise to high frequencies. In the signal bandwidth [0, f_b], for an oversampling ΣΔM, and using the simplification $\sin(\frac{\pi f}{f_s}) \approx \frac{\pi f}{f_s}$, the total quantization noise power is given by:

$$P_{QN}(\omega) = \int_0^{f_b} PSD_N(f)df \approx \frac{\pi^{2N}\sigma_e^2}{2N+1}\left(\frac{2f_b}{f_s}\right)^{2N+1} = \frac{\pi^{2N}\sigma_e^2}{2N+1}OSR^{2N+1} \tag{2.56}$$

For a one-bit quantizer, the power of the random signal $x(n)$ is $\sigma_x^2 = 4\sigma_e^2$, thus the SQNR of a Nth-order ΣΔM can be expressed in (dB):

$$SQNR^N(dB) = 10\lg\frac{\sigma_x^2}{P_{QN}} = 6 + 10\lg(2N+1) + 10(2N+1)\lg OSR - 10N \tag{2.57}$$

Equation 2.57 denotes that the SQNR will increase $3(2N+1)dB$ for every doubling of the sampling frequency, equivalent to increase the resolution by $(N+0.5)$ bits. The theoretical SQNR limit for a one-bit lowpass ΣΔM is shown in Figure 2.9.

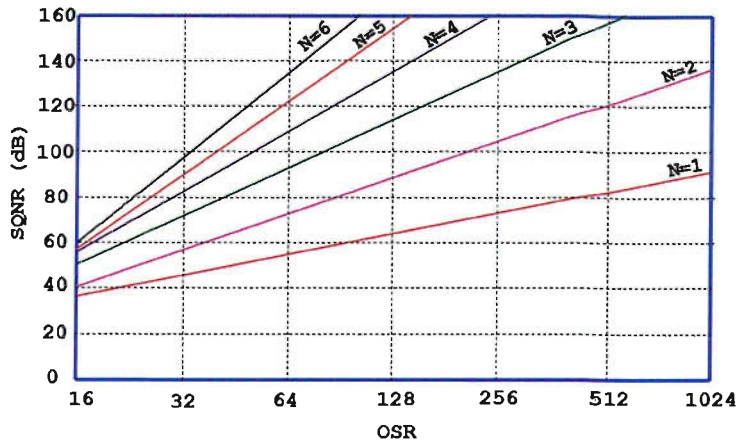

FIGURE 2.9: Theoretical SNR limits for one-bit lowpass ΣΔMs.

Unfortunately, the theoretical value given by Equation 2.57 of a high-order ΣΔM is not achievable in practice due to the nonlinear quantizer in the closed-loop system. Furthermore, it is difficult to keep the loop stable for orders higher than two. For the design of a high-order ΣΔ A/D converters, one of the most successful design procedures is outlined by Norsworthy et al [28], in which a classic analog filter is prototyped and the only design parameter is the filter cutoff frequency which can be determined by extensive simulations. However, high-order one-bit ΣΔMs are particularly prone to instability when the input signal approaches full-scale (set by the quantizer output voltage). A low-pass high order single loop ΣΔM has more integrators in front of the quantizer, and thus a smaller no-overload input range due to integration function. The no-overload input range reduces as the order increases. Some techniques are used for avoiding overload instability, such as clipping and saturation recovery [28].

2.3.5 MASH

A high-order ΣΔM can be designed by cascading independent modulator stages. This methodology does not adversely affect the stability of the overall modulator, provided the individual stages are stable. An example of a second-order modulator obtained by cascading two first-order (1:1) modulators is shown in Figure 2.10.

In this architecture, a primary ΣΔM quantizes the input signal and the associated quantization error is fed to a second ΣΔM. The outputs of these two stages are combined through a digital filter to cancel the quantization error of the first stage. For example, in Figure 2.10, two DAC in feedback loops are ideal one-bit (normalized to unit), the two integrators have the transfer functions of $I_1(z) = k_1 \frac{z^{-1}}{1-z^{-1}}$, $I_2(z) = k_2 \frac{z^{-1}}{1-z^{-1}}$, respectively, and the digital cancellation network have the transfer functions of $H_1(z) = z^{-1}$, $H_2(z) = (1-z^{-1})$, respectively. The quantization errors of the two quantizers are E_1 and E_2, respectively.

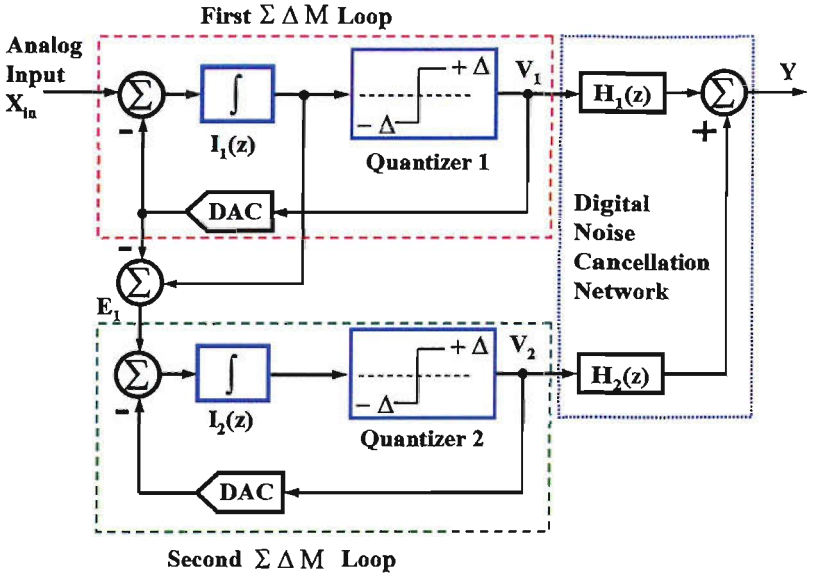

FIGURE 2.10: A MASH ΣΔM.

For the first loop:

$$\begin{aligned} V_1(z) =& \frac{I_1(z)}{1+I_1(z)} X_{in}(z) + \frac{1}{1+I_1(z)} E_1(z) \\ =& \frac{k_1 z^{-1}}{1+(k_1-1)z^{-1}} X_{in}(z) + \frac{(1-z^{-1})}{1+(k_1-1)z^{-1}} E_1(z) \end{aligned} \tag{2.58}$$

and for the second loop:

$$\begin{aligned} V_2(z) =& \frac{I_2(z)}{1+I_2(z)} (-E_1(z)) + \frac{1}{1+I_2(z)} E_2(z) \\ =& -\frac{k_2 z^{-1}}{1+(k_2-1)z^{-1}} E_1(z) + \frac{(1-z^{-1})}{1+(k_2-1)z^{-1}} E_2(z) \end{aligned} \tag{2.59}$$

The total output after the digital cancellation network is:

$$\begin{aligned} Y(z) =& V_1(z)H_1(z) + V_2(z)H_2(z) \\ =& \frac{k_1 z^{-2}}{1+(k_1-1)z^{-1}} X_{in}(z) + \frac{(1-z^{-1})^2}{1+(k_2-1)z^{-1}} E_2(z) \\ &+ \left(\frac{z^{-1}(1-z^{-1})}{1+(k_1-1)z^{-1}} - \frac{k_2 z^{-1}(1-z^{-1})}{1+(k_2-1)z^{-1}} \right) E_1(z) \end{aligned} \tag{2.60}$$

In fact, last term of Equation 2.60 shows the gain mismatch of two integrators leads to a leakage from the previous stage E_1 to the final output. Only the two loops are perfectly

matched, and assumed $k_1 = k_2 = 1$, Equation 2.60 can be re-written as:

$$Y(z) = z^{-2}X_{in}(z) + (1 - z^{-1})^2 E_2(z) \tag{2.61}$$

Equation 2.61 denotes that the final output is the original signal with the high pass filtered replica of the quantization error from the second stage. The two first-order cascaded MASH loops can ideally achieve second-order quantization noise shaping. For example, for a carefully designed MASH, cascading three second-order (2:2:2) ΣΔM loops, the quantization noise shaping can be equivalent to a sixth-order single loop without any stability problems. However, for an electromechanical ΣΔM, the microfabrication tolerance can be large and is difficult to predict precisely, therefore, a MASH structure is not very suitable for the control system.

2.3.6 Multi-Bit ΣΔM

A multi-bit ΣΔM, as shown in Figure 2.11, is formed when the one-bit quantizer is replaced by a multi-bit quantizer, and the feedback DAC also is a multi-bit DAC with the same resolution as the quantizer. For a n bit quantizer, similar to the derivation of Equation 2.57, the SQNR is given by:

$$SQNR^N(dB) = 10\lg\frac{\sigma_e^2}{P_{QN}} = 6n + 10\lg(2N+1) + 10(2N+1)\lg OSR - 10N \tag{2.62}$$

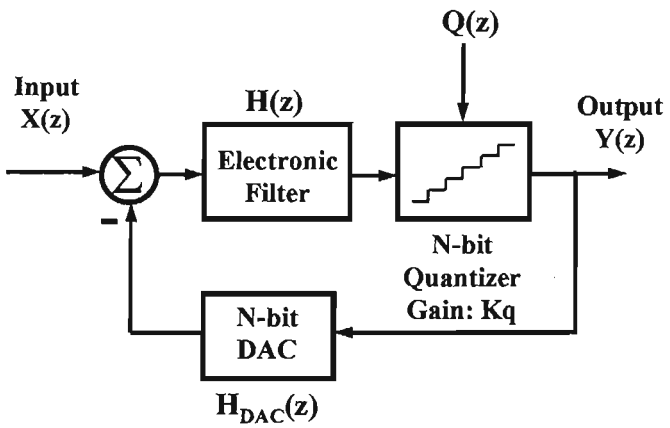

FIGURE 2.11: A multi-bit ΣΔM.

The quantization noise further decreases by 6dB/bit for the quantizer compared with a one-bit quantizer, so a multi-bit ΣΔM has a higher SQNR than a one-bit ΣΔM with the same OSR. Most of all, the non-overload input signal range of the quantizer is increased

due to the relatively well defined gain of the quantizer, in contrast to the arbitrary gain of a one-bit quantizer. The output is given by:

$$Y(z) = \frac{H(z)K_q}{1 + H(z)K_qH_{DAC}(z)}X(z) + \frac{1}{1 + H(z)K_qH_{DAC}(z)}Q(z) \tag{2.63}$$

$$\approx \frac{1}{H_{DAC}(z)}\left(X(z) + \frac{1}{H(z)K_q}Q(z)\right)$$

where $H(z)$ is the TF of the electronic filter (consisting of integrators or resonators), $Q(z)$ is the quantization noise with an approximated gain K_q and $H_{DAC}(z)$ is the transfer function of the multi-bit DAC. The equation shows that nonlinearities of the multi-bit DAC will directly add to the signal and eventually distort the output signal of the loop.

2.3.7 Lowpass to Bandpass Transformation

The design methodology of a high-order bandpass ΣΔM is based on the application of a lowpass to bandpass transformation on a more commonly used lowpass filter topology. One of the standard transformations [28] is:

$$z \rightarrow -z^2 \tag{2.64}$$

A lowpass ΣΔM of order N can be converted to a bandpass modulator of order $2N$ with a center frequency of f_0=$f_s/4$ (f_s is the sampling frequency of both modulators); it preserves both the stability characteristics and the noise-shaping properties of the original modulator [27]. The lowpass ΣΔM has QNTF zeros at or near $z = 1$ (which corresponds to dc), whereas the bandpass ΣΔM has QNTF zeros at or near $z = \pm j$ (which corresponds to $f_0 = f_s/4$). In a bandpass ΣΔM, the equivalent of the integrators in the lowpass ΣΔM is a resonator which has a discrete-time transfer function of:

$$R(z) = \frac{-z^{-2}}{1 + z^{-2}} \tag{2.65}$$

For an electromechanical ΣΔM, Equation 2.65 is only applied to the electronic integrators, but not to the sensing element (such as a gyroscope) as it is already a mechanical resonator.

For illustration, an arbitrary QNTF is generated using the Schreier's toolbox [29] for a fourth-order lowpass and a eighth-order bandpass, respectively. These QNTFs have an OSR of 64 and the maximum out-of-band gain of 1.5. Figure 2.12 shows the pole/zero

map of for a fourth-order lowpass ΣΔM, while Figure 2.13 shows the pole/zero map of a eighth-order bandpass ΣΔM with the center frequency at $f_s/4$.

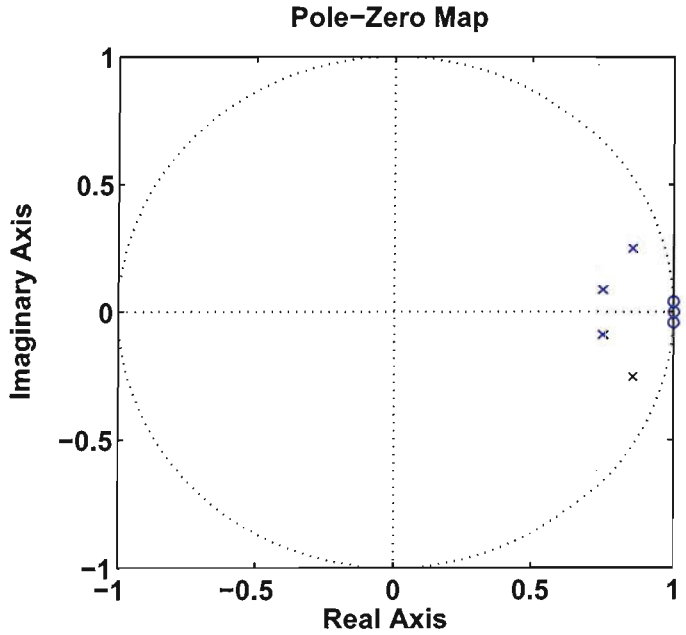

FIGURE 2.12: Pole/zero map of the quantization noise transfer functions for a fourth-order lowpass ΣΔM with OSR=64.

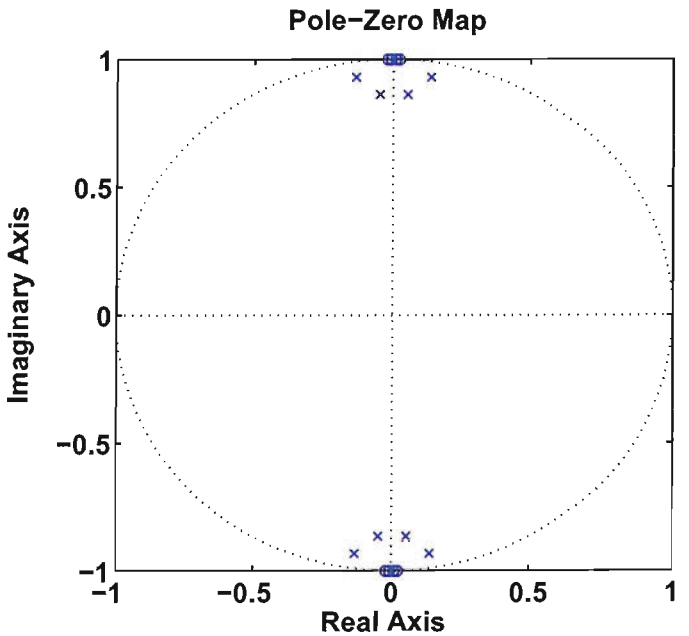

FIGURE 2.13: Pole/zero map of the quantization noise transfer functions for a eighth-order bandpass ΣΔM with OSR=64.

2.3.8 Continuous-Time ΣΔM vs Discrete-Time ΣΔM

Most ΣΔMs are implemented with a discrete-time (DT) circuits such as switched capacitors (SC). The reason is that they are easy to map from a mathematical description into a circuit implementation. In addition, it is not easy to simulate the non-idealities of continuous-time (CT) ΣΔMs [30]. The difference between an electromechanical ΣΔM and an electronic ΣΔM is that both the sensing element, which behaves as the first physical integrator, and electrostatic force feedback unit, operate in the CT domain. It is necessary to compare a CT ΣΔM with a DT ΣΔM:

1. Oversampling frequency. In a DT ΣΔM, opamps with high unity-gain bandwidth (typically at least five times the clock frequency) are required to satisfy the settling accuracy requirements. However, waveforms vary continuously in a CT ΣΔM, and the restrictions on op-amp bandwidth are relaxed.

2. Switch transients. Large switch glitches appear on op amp virtual ground nodes due to switching transients in a DT ΣΔM, while op-amp virtual grounds can be kept very quiet in a CT ΣΔM.

3. Aliasing. In DT domain, signals separated by a multiple of the sampling frequency are indistinguishable. DT ΣΔMs need a separate anti-aliasing filter before the input. However, CT ΣΔMs have an inherent anti-aliasing property, because the input signal is sampled after being filtered through the CT loop filter.

4. Quantizer. In DT ΣΔMs, the sampling accuracy in the front-end is required greater than the full resolution of the entire modulator. But in CT ΣΔMs, the quantizer is inside the noise-shaping loop, any sampling errors, are significantly suppressed by the high gain of the loop filter in the bandwidth of signal.

5. Clock jitter. CT ΣΔMs are more sensitive to clock jitter than DT ΣΔMs [30].

6. Excess loop delay. Excess loop delay is defined as the delay between the quantizer clock and DAC pulse. For CT circuits, if the excess loop delay is too large, it leads to not only the SNR degradation, but also loop instability.

7. Simulation tools. For DT ΣΔMs, there is a natural mapping between the mathematics of the system and its circuit-level implementation. However, in the CT domain, simulations will consume a huge time with a circuit level simulator such as Spice.

For a CT ΣΔM, DAC pulse errors are fed back all the way to the modulator input, and so are not noise-shaped by the action of the loop. Therefore, the shape of the DAC pulse is part of the QNTF expression, the DAC output waveform will affect the noise shaping. The inter-symbol interference [31] results from the unequal rise and fall times in the DAC switching controlled by the quantizer output, as illustrated in Figure 2.14(a). The area under the

pulses is significant due to the pulses are integrated inside the forward modulator loop. The signal-dependent CT ΣΔM introduces harmonic distortion in their output. Several methods are suggested to correct this effect. A Return-to-zero (RTZ) DAC scheme is very effective, which switches according to the quantizer decision for part of the clock cycle and resets to zero for the rest during each clock cycle as illustrated in Figure 2.14(b). In this way, no matter the previous quantizer symbol, a new DAC output starts from the same reset value, including both a rising and a falling edge in the DAC pulse. However, RTZ DACs change the transfer function of the DAC and will ultimately change the noise shaping, and in the worst case, it may lead to an instable loop. A RTZ DAC is also more sensitive to the sampling clock phase jitter than a non-return-to-zero (NRZ) [32].

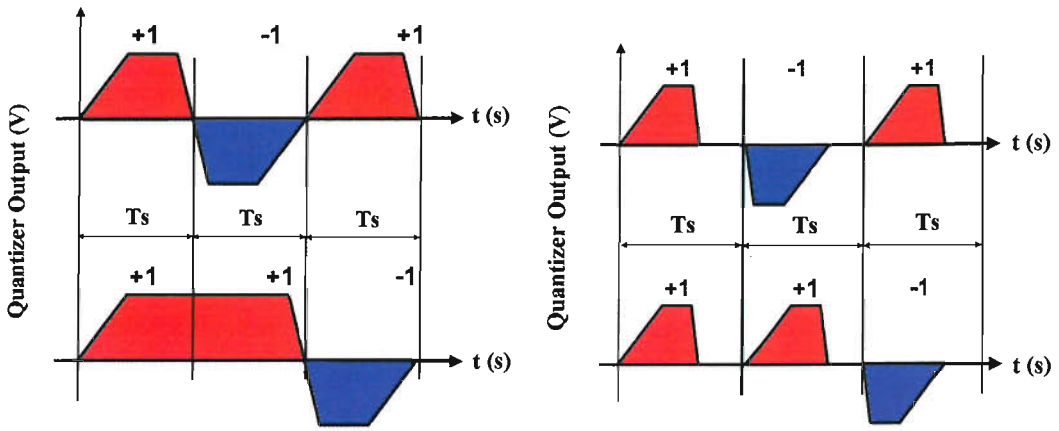

(a) DAC waveform with NRZ (b) DAC waveform with RTZ

FIGURE 2.14: Inter-symbol interference of a CT ΣΔM.

A synthesis methodology of transforming a DT ΣΔM into a CT ΣΔM was defined by [33]:

$$H(z) = (1 - z^{-1})\mathcal{Z}_T \left\{ \mathcal{L}^{-1} \left[\frac{H(s)DAC(s)}{s} \right]_{t=nT_s} \right\} \tag{2.66}$$

where $\mathcal{L}^{-1}$ denotes the inverse Laplace transform, $\mathcal{Z}_T$ the z-transform at sampling period T_s, while DAC(s) represents the feedback DAC transfer function. The electronic integrators in a DT ΣΔM and a CT ΣΔM are given by the transformation pair:

$$\frac{z^{-1}}{1 - z^{-1}} \Leftrightarrow \frac{T_s}{s} \tag{2.67}$$

2.4 Performance Metric

The bitstream output spectrum is the performance metric of a ΣΔM. Not only the SQNR can be derived, but also it can be used to check if the noise shaping has the correct order. The quantization noise raises outside the signal bandwidth according to the loop order [31]. If the order of the loop is L, the slope of the spectrum outside the signal band should be $(20 \times L)dB/decade$. This is very important method to know if the ΣΔ loop filter works well, especially when if the spectrum noise floor is higher than expected. In Chapter 7, the measurement results of a fifth-order electromechanical ΣΔM have relatively higher noise floor than expected which is limited by the mechanical noise of the sensing element used and electronic noise of interface circuits. However, the slope of the output spectrum can be very useful to tell the order of loop filters to make sure the loop works well. For demonstration, a fifth-order lowpass ΣΔM (OSR=64) with optimized NTF zeros is synthesized using Schreier Toolbox [29] and is shown in Figure 2.15. It clearly be seen the spectrum slope outside of signal band is 100dB/decade, which is corresponding to a fifth-order ΣΔM.

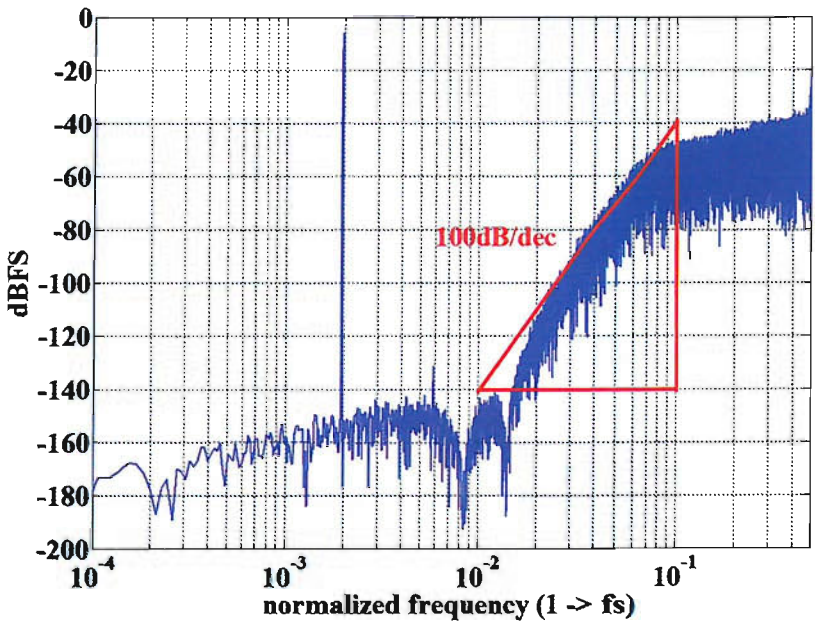

FIGURE 2.15: Performance metric: output bitstream spectrum of a fifth-order lowpass ΣΔM.

Chapter 3

Background: Closed-loop Micromachined Capacitive Inertial Sensors

Since K.Petersen et al [34] reported the first micromachined capacitive accelerometer in 1982, this type of sensor has become one of the most commonly used MEMS sensors, and is also investigated further in this thesis. Micromachined inertial sensors have vast applications in such as automotive systems and inertial navigation instruments, but the requirements of the two categories are quite different. Table 3.1 shows typical specifications of accelerometers for automotive and inertial navigation applications [13]. This kind of sensors has the combined advantages of high sensitivity, good dc response and noise performance, low-drift, low-temperature sensitivity, low-power dissipation, and large bandwidth. However, a capacitive accelerometer has high output impedance, so it is susceptible to electromagnetic interference. A high precision circuitry is necessary for capacitive accelerometers.

Parameters	Automotive	Navigation
Range	±50g (airbag); ±2g (vehicle stab.)	± 1g
Frequency Range	dc-400Hz	dc-100Hz
Resolution	100mg (airbag); 10mg(vehicle stab.)	$< 4\mu g$
Off-axis Sensitivity	$< 5\%$	$< 0.1\%$
Nonlineraity	$< 2\%$	$< 0.1\%$
Max. Shock in 1msec	>2000g	>10g
Temp. Range	-40°C to 85°C	-40°C to 80°C
Temp. Coeff. Offset	< 60mg/°C	$< 50\mu$ g/°C
Temp. Coeff. Sensitivity	< 900ppm/°C	$< \pm$ 50ppm/°C

TABLE 3.1: Typical specifications of accelerometers for automotive and inertial navigation applications (Yazdi et al [13]).

3.1 Interface to Micromachined Capacitive Inertial Sensors

Capacitive accelerometers can be designed in different ways. The most commonly used configurations are vertical and lateral structures. In the vertical (out-of-plane) structure, the proof mass is separated by a narrow gap from a fixed plate, forming a parallel plate sense capacitance. The proof mass moves in a perpendicular direction to its plane and hence changes the air gap. In a lateral (in-plane) structure, a number of moving sense fingers are attached to the proof mass, and the sense capacitances are formed between these moving fingers and parallel fingers fixed to anchors. As a result, the sense direction in a lateral accelerometer is in the proof-mass plane.

When there is a relative movement of the proof mass to the support frame of the accelerometer, there will be capacitance variation between the mobile electrode and the fixed electrode. By measuring the capacitance, the displacement, which is proportional to the acceleration of the body of interest, can be derived by the following equation:

$$C = \varepsilon_0 \frac{A}{d_0 \pm x} \tag{3.1}$$

where C is of the sensing capacitance, ε_0 the permittivity of free space (8.85×10^{-12} F/m), A the overlapping area, d_0 the nominal gap distance between the two electrodes, and x the displacement due to the motion of electrodes.

The displacement of the proof mass can be detected by capacitive sensing, using either gap variation or overlap area variation between the electrodes. However, the relationship between the capacitance and the displacement is non-linear. To improve the linearity, differential capacitive sensors are usually used to cancel the non-linearity error to some extent.

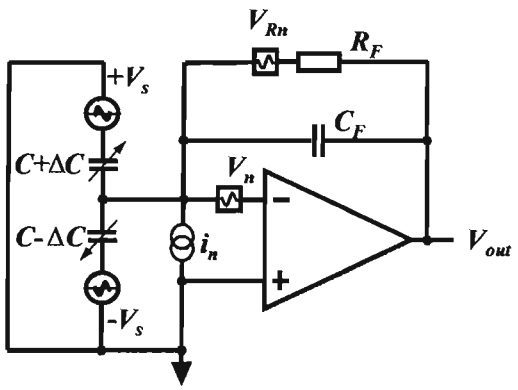

FIGURE 3.1: A charge amplifier used for capacitive inertial sensors.

When an inertial sensing element is at rest, the nominal sensing capacitance is given by:

$$C = \varepsilon \frac{A}{d_0} \tag{3.2}$$

When an inertial force is applied to the sensing element, the variation of the sensing capacitance is:

$$\Delta C = C \frac{x}{d_0 \mp x} \tag{3.3}$$

The capacitance variation is normally detected by a charge amplifier as shown in Figure 3.1. The interface output voltage is given by:

$$V_{out} = -\frac{2\Delta C}{C_F} \times V_s = -\frac{2C}{C_F} \times \frac{x}{d_0 \mp x} \times V_s \tag{3.4}$$

After taking $C_F = 2C$ and assuming a small displacement x compared with the nominal gap d_0, Equation 3.4 can be approximated by:

$$V_{out} \approx -\frac{V_s}{d_0} \times x \tag{3.5}$$

Thus, the conversion gain from the displacement (due to an inertial force) to the interface output voltage is given by:

$$\lambda = \frac{V_{out}}{x} \approx -\frac{V_s}{d_0} \tag{3.6}$$

The gain λ can be increased only by either reducing the nominal gap d_0 or increasing the amplitude of the excitation carrier voltage V_s. After consideration of the electronic input referred voltage noise $\tilde{V}_n$, input-referred current noise $\tilde{i}_n$ and the R_F thermal noise $\tilde{V}_{Rn} = \sqrt{4K_BTR_F}$ in the interface amplifier, their output-referred noise voltage (normalized to 1Hz bandwidth) can be expressed by:

$$\tilde{V}_{nout}^2 = \tilde{V}_{vout}^2 + \tilde{V}_{iout}^2 + \tilde{V}_{rout}^2 = (\frac{2C}{C_F})^2 \times \tilde{V}_n^2 + (\frac{R_F}{1 + j\omega C_F R_F})^2 \times (\tilde{i}_n^2 + \frac{4K_BT}{R_F}) \tag{3.7}$$

taking $C_F = 2C$ and $j\omega C_F R_F \gg 1$, Equation 3.7 can be simplified to:

$$\tilde{V}_{nout}^2 = \tilde{V}_n^2 + (\frac{1}{j\omega C_F})^2 \times (\tilde{i}_n^2 + \frac{4K_BT}{R_F}) \tag{3.8}$$

For low-noise CMOS opamps, the input current noise density is in the order of $fA/\sqrt{HZ}$. Using typical values for the carrier frequency ω=1MHz, the feedback capacitor C_F=2pF and resistor R_F=1M Ω, the second term in Equation 3.8 is not dominant. Therefore, the gain from the voltage noise $\tilde{V}_n$ to the output-referred voltage noise $\tilde{V}_{nout}$ is approximately unity. In the following analysis, when an electronic voltage noise source is embedded in the Simulink models, the noise source will be placed just after the pickoff preamplifier for this reason. The offset and $1/f$ electronic noise in circuits are usually cancelled by autozeroing,

correlated double sampling, and chopper stabilization [35], and therefore are not considered in the following analysis of electronic noise. Usually the noise floor is dominated by the thermal noise and $1/f$ coming from the first stage interface, noise reduction should make effort on the front-end circuits. The prototype discussed in Chapter 7 uses the synchronous demodulation for the front-end pickoff circuits to remove $1/f$ noise, and didn't use the chopper in subsequent circuits.

3.2 Microfabrication

There are three popular types of micromachining processes to fabricate MEMS capacitive accelerometers: surface micromachining, bulk micromachining and LIGA. Silicon-based technology has become the mainstream technology because it is compatible with IC technology, capable of integrating mechanical structures and processing circuits in a single chip, and can be fabricated in batches.

3.2.1 Surface Micromachining

In 1980s U. C. Berkeley invented the surface sacrificial layer technology. Surface micromachining consists of several process steps, such as silicon oxidization and nitrification, polycrystalline silicon deposition and etching, and sacrificial etching. The process is above the silicon substrate, and the substrate is used as a base to build upon and not to implement the structure of the sensor in it. Figure 3.2 shows a typical surface micromachining process [36]. Surface micromachining is compatible with integration of the mechanical sensing element with the electronics on the same chip.

In 1993, Analog Devices successfully commercialized the first integrated accelerometer ADXL50 using surface micromachining. The ADXL50 is the first complete acceleration measurement system on a single monolithic IC. Its control circuitry used a forced-balance analog force feedback loop to improve the performance.

However, surface micromachined accelerometers have a small proof mass due to only several micrometers of the deposition thickness and consequently high mechanical noise unless the device is vacuum packaged [36], [6]. In addition, the suspension system fabricated in polycrystalline silicon suffers from elastic hysteresis. Residual stress of polycrystalline silicon layers inevitably leads to sensitivity drift. Because of fabrication limitations used in surface micromachining technology, the accuracy of the micromachined accelerometers is in the mg range, far away from the requirements of μg and sub-μg resolution for inertial navigation systems.

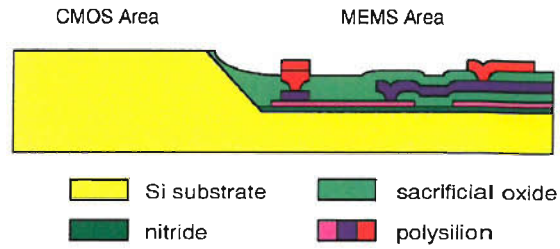

(a) Layer classification and profile

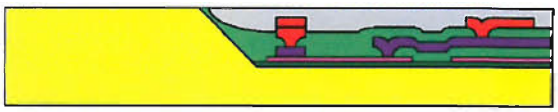

(b) Fill trench with oxide, planarize (CMP)

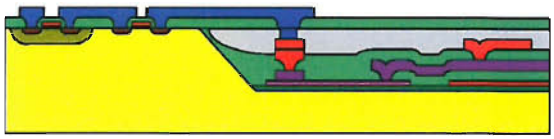

(c) Standard CMOS device fabrication

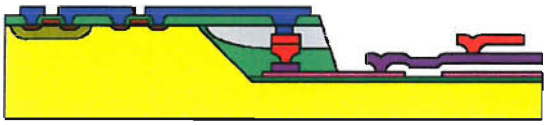

(d) Etch sacrificial oxide in MEMS area - release

FIGURE 3.2: Typical surface micromachining process (Boser [36]).

3.2.2 Bulk Micromachining

Bulk micromachining is designed as a process to remove bulk substrate, and is characterized by subsequent steps of wafer bonding and deep etching. Using bulk micromachining a thick, large proof mass with low stress can be obtained, which can reduce the mechanical Brownian noise floor and consequently improve the resolution of the sensor.

Initially bulk micromachining technology mainly used KOH for wet anisotropic etching [37], [38]. Since the middle of 1990s, bulk micromachining has advanced to a new stage by the invention of DRIE (Deep Reactive Ion Etching), especially the ICP (Inductance Coupling Plasma) technology. Bulk micromachining technologies combine bonding and DRIE technologies. Consequently, a large proof mass can be fabricated by DRIE and multiple layers can be combined by bonding, thus very low stress can be achieved by monocrystalline bulk silicon [39], [40].

Bulk-micromachined accelerometers usually require wafer bonding, and sensors cannot monolithically be integrated with the interface and control electronics [41], [42], [43], [44].

As a result, the electronic interface and control are usually packaged separately to the mechanical structure, which make them more expensive than those using surface micromachining. However, this drawback can turn aside a favorable feature by choosing the most suitable circuitry in designing high performance accelerometers.

Using SOI wafer is an important development in bulk micromachining. The SiO_2 layer between two mono-crystalline silicon layers is very similar to the sacrificial layer in a surface process. A large proof mass can be obtained directly by DRIE and released by etching the oxide sacrificial layer [45]. SOI MEMS is also suitable for integration of integrated circuits and mechanical structures on one chip. The main advantages of a SOI process for MEMS are that it does not require bonding technique and only needs few process steps and masks. However, releasing the proof mass after etching the sacrificial layer is still a problem for SOI MEMS [46], moreover, such sensors have large parasitic capacitance due to the small oxide-Si spacing and hence reduce the sensitivity of a transducer.

3.2.3 LIGA

LIGA is a technique to produce mould for the fabrication of micromachined components. It is a high aspect ratio MEMS technology combining IC lithography with electroplating and moulding to obtain depth. LIGA structures typically have an aspect ratio of greater than 10:1, very precise geometry, and smooth, vertical sidewalls up to 1000μm deep. LIGA allows the use of materials other than silicon such as metals and plastics, opening the door for many different types of structures and devices. Some capacitive accelerometers have been fabricated using LIGA [47], [48], however, LIGA is not widely used technology due to the high cost of lithography.

3.3 $\Sigma\Delta$M Micromachined Capacitive Inertial Sensors

3.3.1 Analog Closed-Loop Sensors

All accelerometers can be divided into two groups: open-loop and closed-loop [49]. The difference between the two groups is based on a simple operational characteristic: open-loop accelerometers have proof masses that are displaced by the inertial force, and that displacement is measured; The proof mass of a closed-loop accelerometer is maintained at a fixed position and the force necessary to maintain that position is providing a measure of the input inertial force.

The open-loop sensitivity of a capacitive accelerometer is proportional to the proof-mass size and capacitance overlap area, and inversely proportional to the spring constant and air gap squared. A system, which is formed by a sensing circuit followed by a pickoff preamplifier and a synchronous demodulator, is an open-loop accelerometer. Open-loop accelerometers

have limited performance in terms of bandwidth, linearity and dynamic range, and also suffer from cross-coupling errors, pickoff nonlinearity and the hysteresis of their mechanical springs [50]. Furthermore, non-linear effects, which are caused by the electrostatic force and the damping, increase with the deflection of the proof mass.

One method to improve the linearity and the performance of an accelerometer is to incorporate the sensing element in a closed-loop control system [13]. In a closed-loop accelerometer system, an electrostatic feedback force is used to keep the proof mass at its rest position by counterbalancing the acceleration force. Since electrostatic forces are always attractive, it is difficult to maintain negative feedback. The most common way to provide a negative feedback is to apply simultaneous two feedback forces on the seismic mass and then the resultant force provides the negative feedback.

Analog closed-loop accelerometers give good results for small deflections of the proof mass but for larger deflections the feedback relationship becomes non-linear, and the feedback gain decreases. Eventually, the feedback force changes sign and the proof mass may be attracted by one of the electrodes and will "latch-up" (or pull-in) [51]. One of the cases, which can lead to large deflections, is when a shock in acceleration occurs. Because the response of the closed-loop system has a delay, for the transient time period, it acts like an open-loop system. After the transient time, the deflection of the proof mass is already so large that the feedback force acts in the same direction as the displacement causing latch-up of the proof mass. Another case is when the acceleration applied to the sensor is larger than the dynamic range of the accelerometer so that, the feedback force applied to the electrodes is not able to return the proof mass back to the central position. Lastly, at the instant, when the accelerometer is switched-on, acceleration can act during this time on the sensor and the initial deflection could be large enough to cause a change of the sign of the feedback force and latch-up of proof-mass. An effective solution to overcome the pull-in problem is the digital control strategy which is based on the principle of $\Sigma\Delta$M, which can preserve all advantages of closed-loop and concurrently produce a digital output in the format of a pulse density modulated bitstream.

3.3.2 Second-Order Electromechanical $\Sigma\Delta$M

In 1990, Henrion et al [2] firstly investigated a digital control strategy for micromachined accelerometers using the principle of $\Sigma\Delta$ modulation. Since 1992, Howe's group and Boser's group at Berkeley have done intensive and extensive research on this digital control strategy and published numerous experimental results from second-order loops to fourth-order loops for micromachined capacitive accelerometers and gyroscopes [52], [3], [4], [53], [54], [10]. One representative work was done by Lemkin [53] in 1997. He reported an integrated three-axis surface micromachined accelerometer with a CMOS position-sense interface and digital offset-trim electronics. It was based on a second-order $\Sigma\Delta$M using switch-capacitor circuits. Another representative work was done by Jiang [6] in 2002. He systematically

investigated the interaction between the quantization noise and electronic noise in a second-order electromechanical ΣΔM. While Najafi's group at Michigan explored on second-order control loop [55], [7] for micro-g micromachined accelerometers.

The system level diagram of such a second-order single-bit loop is shown in Figure 3.3. The transfer function of the mechanical sensing element can be approximated by a second-order mass-damper-spring system and can be regarded as analogous to the two cascaded electronic integrators commonly used in second-order electronic ΣΔM A/D converters. The accelerometer has a direct digital output signal in form of a pulse density modulated bitstream, so that it can be directly interfaced to a digital signal processing system and has higher noise immunity than an analog closed-loop accelerometer. It also retains the usual merits of closed-loop control, such as an increase in bandwidth, dynamic range and linearity, and also reduces cross-coupling errors, pickoff nonlinearity and the hysteresis of their mechanical springs.

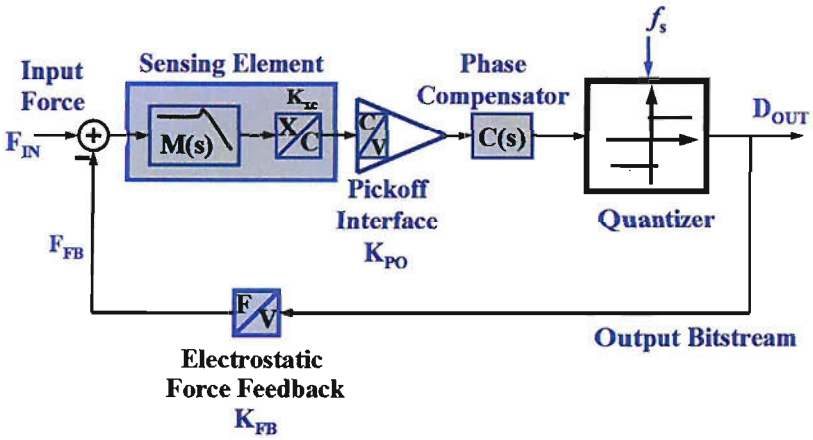

FIGURE 3.3: Block diagram of a sensing element embedded in a second-order ΣΔM.

A major design parameter for such an electromechanical ΣΔ is the SNR. The quantization noise should be made small enough so that it does not limit the minimum detectable signal of the sensor, i.e. appreciably smaller than other noise sources such as Brownian noise, electronic thermal noise and noise introduced by interconnects. The systematic noise analysis of a ΣΔ capacitive silicon micro accelerometer will be discussed later.

In general, if a system is described by a discrete transfer function, $D[z]$, then, the dc gain of the system is going to be $D(1) = \lim_{z \to 1} D(z)$. If a system is described by a continuous-time transfer function, $C[s]$, then, the dc gain of the system is going to be $C(0) = \lim_{s \to 0} C(z)$.

For example, the dc gain of the ideal integrator $H(z) = \frac{z^{-1}}{1 - z^{-1}}$ is infinite. In practice, the actual gain is limited by circuit constraints and in particular by the opamp open-loop gain A_0. The transfer function of the integrator with leakage [56] becomes:

$$H(z) = \frac{z^{-1}}{1 - \alpha z^{-1}}$$

The dc gain becomes therefore:

$$H_0 = H(1) = \frac{1}{1-\alpha}$$

where

$$\alpha = \frac{A_0 - 1}{A_0}$$

Due to the opamp open-loop gain A_0 usually has a very large value, $\alpha \approx 1$ and thus the integrator dc gain H_0 is nearly infinite. Since the equivalent dc gain of the integrator functions Equation 2.3 of a mechanical sensing element is determined by

$$M_{dc} = \lim_{s \to 0} \frac{m}{ms^2 + bs + k} = \frac{m}{k}$$

The mass of proof mass m (most less than $10^{-5}kg$) is considerably lower due to microfabrication and the spring stiffness k is usually between 1 to 1000 N/m; these two mechanical parameters lead to considerably lower dc gain than their electronic counterparts. Furthermore, the quantization noise transfer function QNTF in the system shown in Figure 3.3 is given by

$$QNTF(s) = \frac{1}{1 + K_{FB}M(s)K_{po}C(s)K_q}$$

where K_q is the equivalent gain of quantizer and other symbols are defined in the diagram. In the signal band, or in low frequencies:

$$QNTF_{dc} = \lim_{s \to 0} QNTF(s) \approx \frac{1}{K_{FB}K_{po}C(0)K_q} \frac{k}{m}$$

It can be seen from this expression that $QNTF_{dc}$ is constant proportional to k/m, the limited dc gain at low frequencies reduces the attenuation of the quantization noise in the signal band and consequently result in an increase of the in-band quantization noise.Consequently, this results in a considerably lower SQNR for the electromechanical ΣΔM compared with an electronic ΣΔ A/D converter.

The order of an electromechanical ΣΔM is defined as the total number of the open-loop poles in the modulator loop filter. The mechanical structure of the sensor has two poles and the system without additional integrators is second-order. If the modulator contains L purely electronic integrators, the modulator order is L+2, however this does not represent the real order of noise shaping of the electromechanical ΣΔMs, as the mechanical transfer function is usually far from optimal in signal band as far as noise shaping is concerned.

3.3.3 MASH Electromechanical ΣΔM

The application of MASH to electromechanical loop was first put forward by Kraft et al [11]. The approach is to cascade the electromechanical ΣΔM comprising the capacitive sensing

element with a purely electronic ΣΔM. This results in a modified 'MASH' ΣΔM structure in which the quantization error of the first ΣΔM is fed to a second modulator; this provides further noise shaping of the quantization noise. A simple 2:1 MASH loop topology is chosen and shown in Figure 3.4. The two quantizer gain for the first loop is k_{Q1} and for the second loop is unity. Furthermore, for small proof mass deflections the conversion from a proof mass deflection ($x \ll d_0$) to a voltage can be represented as a simple gain factor, k_{po}. The electrostatic force also can be assumed of constant magnitude, k_{fb}. $D_1(z)$ and $D_2(z)$ are noise cancellation network in digital domain.

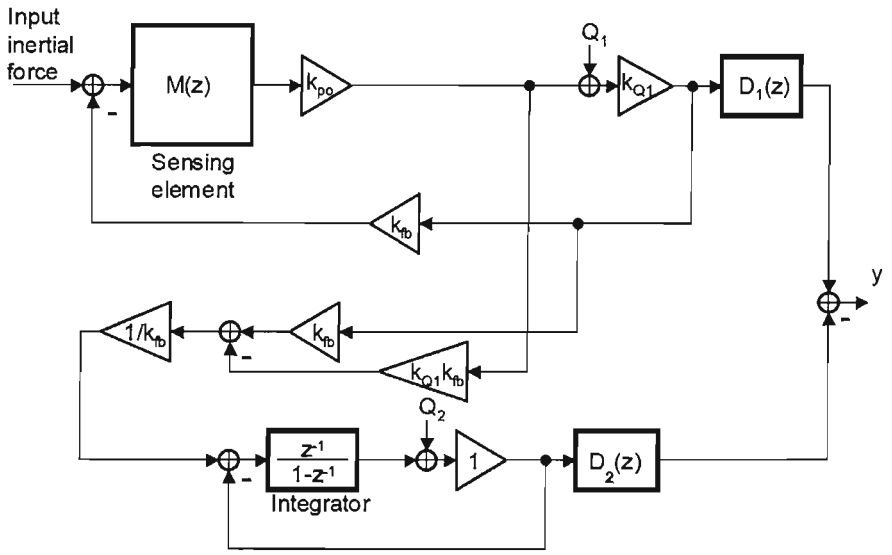

FIGURE 3.4: Linearized block diagram of the micromachined accelerometer incorporated in a MASH ΣΔM (Kraft et al [11]).

It can be shown that noise of the first loop is shaped by:

$$NTF_{Q1} = \left(\frac{k_{Q1} D_1(z)}{1 + M(z) k_{po} k_{Q1} k_{fb}} - k_{Q1} z^{-1} D_2(z) \right) Q_1 \tag{3.9}$$

If $D_1(z) = z^{-1}$ and $D_2(z) = 1/(1 + M(z) k_{fb} k_{po} k_{Q1})$ are chosen, the noise transfer function NTF_{Q1} equals to zero and hence the quantization noise of the first loop is totally cancelled. However, this approach requires the precise knowledge of $M(z)$ and k_{Q1}, but this is not possible in practice. $M(z)$ depends on the absolute values of the spring constant, mass and damping coefficient of the sensing element, the former two are subject to considerable manufacturing tolerances, and the latter is inherently nonlinear due to squeeze film damping effects. k_{Q1} is the effective gain of the quantizer in the first loop and depends on the magnitude of its input signal, thus only an average value can be estimated.

The simulation result is presented in Figure 3.5. Using order L=2 and an OSR=64 for a ΣΔ A/D, the theoretical value of SQNR is nearly 80dB. The ΣΔM with the sensing element only, however, exhibits a nearly 30dB loss in performance. This is due to the low gain of the

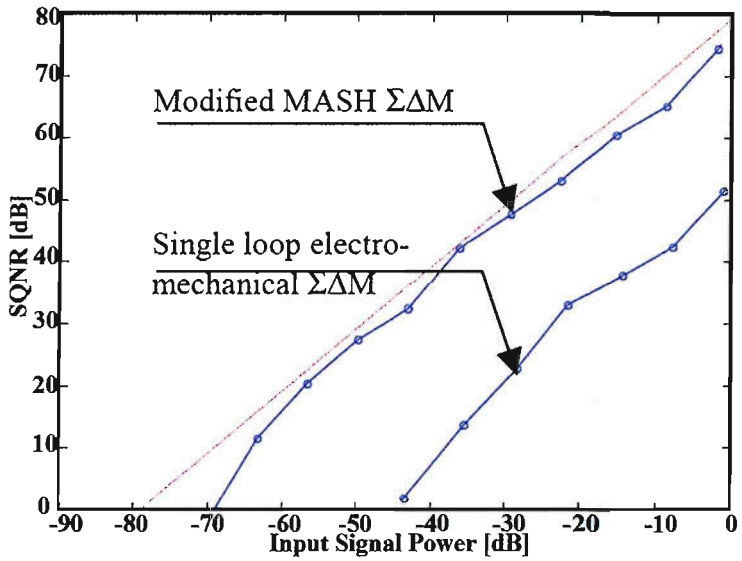

FIGURE 3.5: SQNR with the sensing element incorporated in the MASH ΣΔM compared with a single loop approach (Kraft et al [11]).

integrators at low frequencies and the overdamped characteristics which lead to a SQNR typical for a first-order modulator. The modified MASH ΣΔM control system improves the SQNR ratio by nearly 20dB and makes the noise shaping similar to a second-order ΣΔ A/D converter. This provides considerably better noise shaping compared with a single loop in which the dynamics of the sensing element mainly determine the noise shaping.

3.3.4 High-Order Single Loop Electromechanical ΣΔM

The first third-order electromechanical ΣΔM with single bit quantization was developed by T. Smith et al [8]. The system diagram is shown in Figure 3.6. In previously presented second-order electromechanical ΣΔMs, their dynamics give no noise-shaping at low frequencies and their SNR is determined by the sensor dc gain and resonant frequency. The proposed third-order electromechanical ΣΔM accelerometer enhances the SNR by an additional integrator in the loop. The acceleration sensor is composed of a movable plate (proof mass) suspended by a flexible bar between two fixed electrodes. The half-bridge is used for mass position detection and electrostatic force re-balance. During the force phase, the sensor is disconnected from the measuring interface, and the proof mass is actuated towards the center position. During the position-measuring phase, the capacitive half-bridge is connected to the interface. Its output signal is then fed to the modulator. The system is characterized by three poles: two of the overdamped sensor and one of the electronic integrator, however, the overall electromechanical ΣΔM only provides second-order noise shaping. As the second pole of the sensor (poles at 5Hz and 13kHz) is much higher than the signal bandwidth, it does not influence the noise shaping in the signal band. The two-chip sensor system has a noise floor of $10\mu g/\sqrt{Hz}$ (1Hz bandwidth). The measured static resolution is 15.3bits at a sampling frequency of 80kHz in a 5Hz bandwidth.

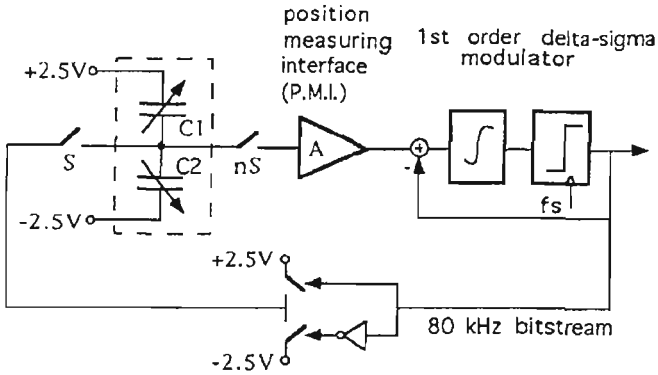

FIGURE 3.6: System diagram of a third-order electromechanical ΣΔM (Smith et al [8]).

In parallel with our research which started in Jan. 2003, Petkov et al investigated a high-order lowpass electromechanical ΣΔM at Berkeley. Most recently, Petkov et al. [12] published a interface chip using a fourth-order ΣΔM for micromachined gyroscopes, which is a lowpass ΣΔM with feed-forward topology (shown in Figure 3.7). Figure 3.8 shows the measured in-band response of the fourth-order gyroscope to an input rotation rate of 25 $^{o}/s$ at 20 Hz. The sinusoidal signal appears amplitude modulated at the drive frequency of the sensor. The spectral component at the drive frequency is due to offset and quadrature error. The system operates at a sampling rate of 850 kHz and achieves a noise floor of $1^{o}/s/Hz$ at atmospheric pressure. However, this is lowpass fourth-order loop and there is no details given on the design methodology of a high-order electromechanical ΣΔM.

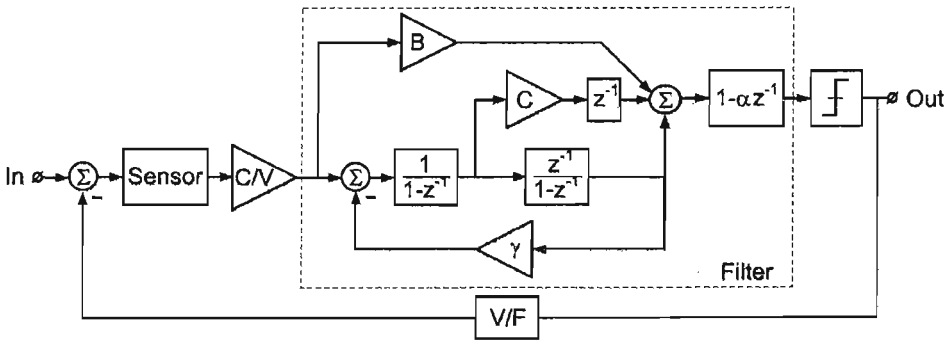

FIGURE 3.7: A fourth-order electromechanical ΣΔM for vibratory gyroscopes (Petkov et al [12]).

In addition, in this field there is trend [57], [9], [58], [59] to investigate on multi-bit noise shaping loops. The first third-order electromechanical ΣΔM with 3-bit quantization was developed by Wu et al [60]. The simulation shows that for a 8kHz resonant frequency, 1MHz sampling frequency and 2kHz signal bandwidth (OSR=256), a second-order modulator with 3-bit quantizer provides 76dB peak SNR. However, only the pickoff preamplifier was verified [61], and so far, there is also no experimental data reported. Tetsuya Kajita et al [9] demonstrated a third-order noise-shaping accelerometer enhancing the SNR by the addition of an integrator in the loop. The main feature of the proposed architecture is an

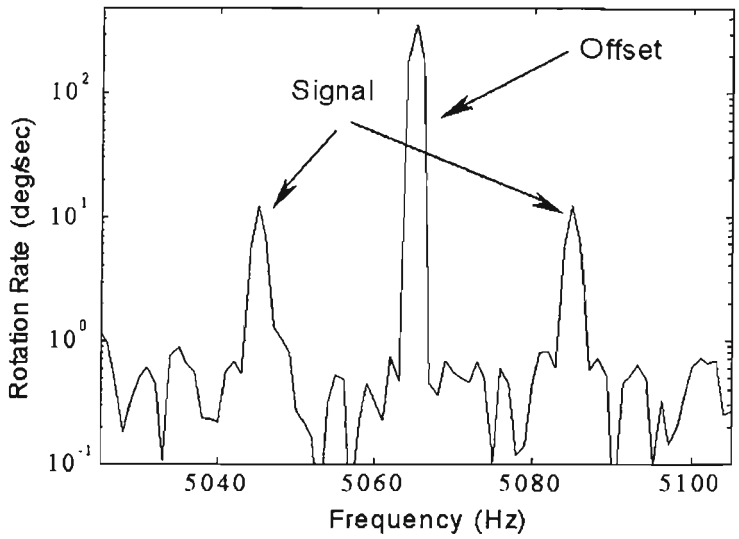

FIGURE 3.8: Measured in-band gyroscope response (Petkov et al [12]).

integrator which is used to replace an amplifier at the input stage of the interface chip. Not only is the noise at low frequencies is shaped, but also the input-referred op-amp noise is first-order shaped by the input integration. Although the inherent multi-bit DAC (including multi-bit force feedback) nonlinear characteristic, which is the main drawback of multi-bit quantizers, can be compensated [62] or further processing in digital domain [63].

3.4 Summary

In this chapter, the state-of-the-art of micromachined capacitive inertial sensors are reviewed. Noise analysis was done for the interface circuit. Surface micromachining technique is compatible with standard IC process, and thus a sensor and circuits can be fully integrated and fabricated in a batch process. Bulk micromachining technique can produce a large proof mass, which is beneficial to increase the electrical sensitivity and decrease the mechanical noise floor. The capacitive sensors using a $\Sigma\Delta$M are one type of closed-loop sensors. So far, the control system using a second-order $\Sigma\Delta$M is a prevailing control technique of such closed sensors. However, due to the low dc gain of the sensing element, the quantization noise is the dominant noise component in a control system using a second-order $\Sigma\Delta$M. A high-order $\Sigma\Delta$M is an effective solution, but it is not well studied, therefore the control for an inertial sensor using a high-order $\Sigma\Delta$M will be thoroughly addressed in next chapters.

Chapter 4

High-Order Single Loop Electromechanical ΣΔM

It is well known closed-loop control operation of a sensing element can improve its linearity, bandwidth and dynamic range. However, as discussed in previous chapter, analog force feedback control systems suffers the electrostatic pull-in problems [51]. A closed-loop digital control strategy is based on the principle of ΣΔM, which can preserve all advantages of closed-loop sensors and concurrently produce a digital output in the format of a pulse density bitstream. Previous work mainly focused on using the sensing element only as a loop filter to form a second-order electromechanical ΣΔM. However, the equivalent dc gain of the mechanical integrator is very low and leads to a much lower SQNR for an electromechanical ΣΔM compared with a second-order ΣΔ A/D converter. It is desirable for high performance inertial sensors to have a quantization noise level at least one order below both the mechanical noise and electronic noise level [64]. Although the SQNR can be somewhat improved by increasing the sampling frequency, the SNQR improvement has limitation due to the coupling between electronic noise and quantization noise in a second-order electromechanical ΣΔM [12]. Furthermore, a second-order electromechanical ΣΔM was found to be particularly prone to idle tones and dead-zones [4].

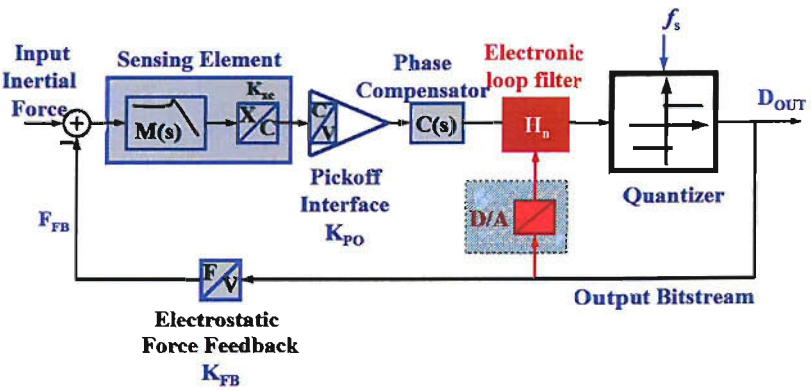

FIGURE 4.1: Block diagram of a high-order electromechanical ΣΔM.

A block diagram of a high-order electromechanical ΣΔM is shown in Figure 4.1, which employ additional electronic filters to further shape the quantization noise in the signal band. In following analysis, it can be seen that not only the SQNR is greatly improved, but also the performance degradation due to micro fabrication tolerances of the inertial sensors is considerably reduced. In fact, higher SQNR can be achieved with high-order electromechanical ΣΔM at lower sampling frequencies. Noise-shaping is determined both by the sensing element and the electronic filter. Additionally, noise shaping of electronic noise is possible in some topologies. The system level design and simulation of such control systems are described in the following.

4.1 Design Methodology of High-Order Electromechanical ΣΔM

The inertial sensing element is equivalent to a second-order mechanical integrator. For the design of a high-order electromechanical ΣΔM, the loop cascades additional electronic integrators to obtain further quantization noise shaping. However, there is no access to the internal nodes of the sensing element incorporated in the ΣΔM loop. In addition, the sensing node, which is at the input of the mechanical integrator, cannot be connected to subsequent electronic integrators to form feed-forward paths or feed back from the later electronic integrators to form local resonators. Therefore, the design methodology of high-order electromechanical ΣΔM is different from conventional ΣΔ A/D converters. However, as the design of high-order ΣΔ A/D converters is relatively mature, the design of a high-order electromechanical ΣΔM should take advantage of these techniques. Interpolative topologies with multi-feedback or feed-forward loops, which have been proven very successful approaches to implement high-order ΣΔ A/D converters [26], [23], can be modified and applied to electromechanical ΣΔM. For a given performance, a high-order ΣΔ A/D converter is designed using existing methods such as mapping the QNTF to an analog Butterworth or Inverse-Chebeyshev filter [28]. The design methodology of a high-order electromechanical ΣΔM combines the design techniques of high-order ΣΔ A/D converters and second-order electromechanical ΣΔMs. The overall procedure of designing a high-order electromechanical ΣΔM is depicted in the flow chart of Figure 4.2.

Choosing a practical topology is the first step to design a high-order electromechanical ΣΔM. Electronic gain constants have to be optimized for stability and performance. The main design procedure of such a loop is aimed at finding find the optimal coefficients for desired lowpass filters. In the same time, a second-order electromechanical ΣΔM is designed and its stability and performance is verified [5]. For example, a fourth-order lowpass ΣΔ A/D converter is shown in Figure 4.3 with feed-forward and resonator topology [65].

In design of a high-order electromechanical ΣΔM, this topology can be adopted. The input of the loop is the mechanical inertial force, which is generated from acceleration

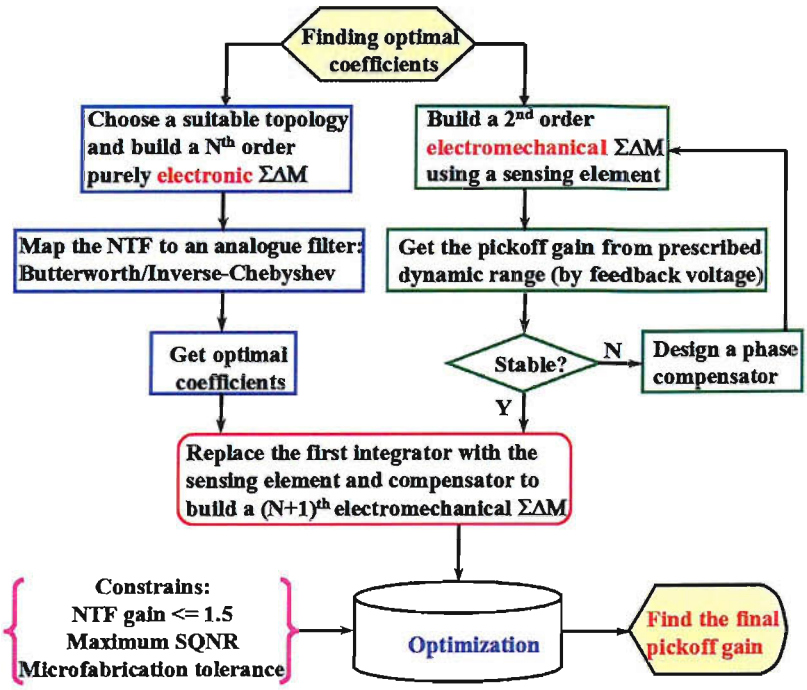

FIGURE 4.2: Design flow of a high-order electromechanical ΣΔM.

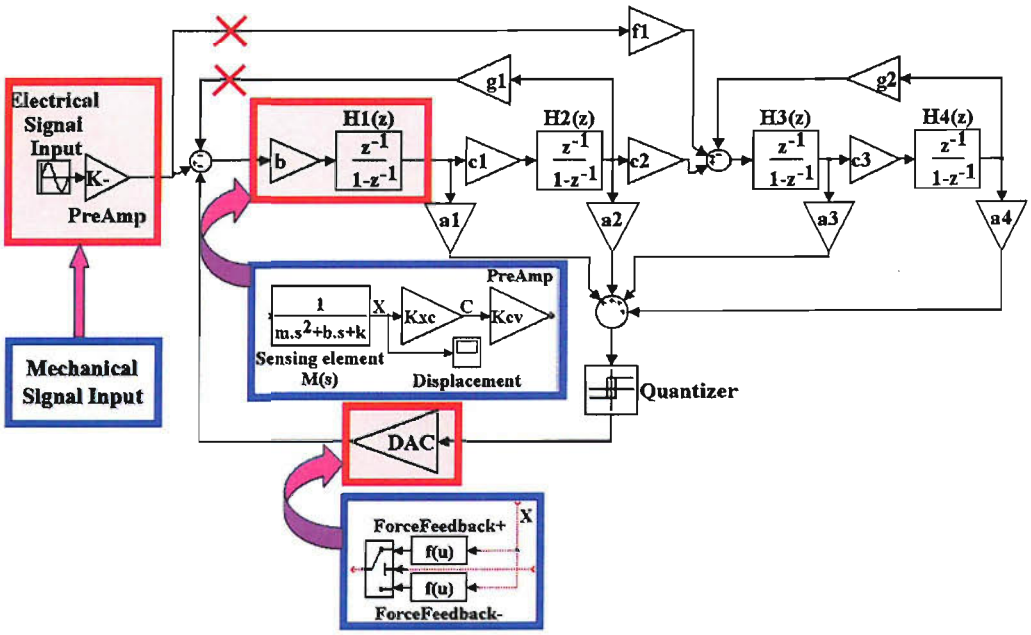

FIGURE 4.3: Conversion of a high-order ΣΔ ADC into a high-order electromechanical ΣΔM with the equivalent topology.

or rotation. In the topology transformation from a high-order ΣΔ A/D converter to a high-order electromechanical ΣΔM, the paths f_1 and g_1 (as indicted in Figure 4.3) should be removed first. The first electronic integrator is replaced by the continuous-time sensing element and pickoff preamplifier. The other coefficients of the high-order ΣΔ A/D converter are kept without change. The DAC in the feedback path in the high-order ΣΔ A/D

converter is replaced by the voltage-to-force converter. An electrostatic feedback force is generated on the proof mass, by applying a voltage to the electrodes of the sensing element. For a given sensing element in a closed-loop control system, the dynamic range is determined by the electrostatic force which can be set by the feedback voltage V_{fb}. K_{fb} is the gain defined by the voltage to electrostatic force conversion on the proof mass in the feedback path and given by:

$$K_{fb} = \mathrm{sgn}(D_{out}) \frac{\varepsilon_0 A_{fb} V_{fb}^2}{2(d_0 + \mathrm{sgn}(D_{out}) \cdot x)^2} \tag{4.1}$$

where ε_0 is the permittivity of free space (8.85×10^{-12} F/m), A_{fb} the area of the feedback electrode, d_0 the nominal gap between proof mass and the electrodes to either side, x the proof mass deflection from its rest position (which is usually negligible compared with the nominal gap) and D_{out} the quantizer output bitstream assumed to be $\pm$1V.

Similar to the design of high-order ΣΔ A/D converters, there is no precise analytic approach to ascertain the stability of a modulator without resorting to simulation due to a highly nonlinear element, the quantizer. For the time being, the most reliable method for verifying stability of a high-order loop is simulation [66]. Throughout this research project, simulation tools developed by P. Malcovati [67], J.M. de la Rosa [68] and R. Schreier [29] were used in Matlab environment. For subsequent simulation, an input sinusoidal signal with an amplitude of -6dB relative to full-scale input signal was used to avoid overloading. The output is measured by its power spectrum density (PSD). The SQNR is calculated using a *Hanning* window 128*1024 bins FFT. The simulations only use a second-order lumped sensing element transfer function, and mechanical high modal responses are omitted and given the future investigation. The sensing element parameters are adopted from the device designed in Chapter 8. Because force feedback greatly increases the sensor's signal bandwidth (SBW) compared with its resonant frequency, a SBW=1024Hz was assumed. As well known, both the loop stability and optimal SQNR depend on the loop coefficients. In fact, if the SQNR drops sharply, it can be regarded as an indication for loop instability. Therefore, the SQNR is a good criterion for loop stability. Although optimization is an effective method for designing a filter [69], the choice of a proper cost function is crucial for convergence. Some sets of coefficients may lead to SQNR with several local maxima, but coefficients are optimal only when a local maxima is chosen having a good quantity degree of stability margin to coefficient variations. After deriving the topology and coefficients of the high-order ΣΔ A/D converter, the multi-dimensional optimization problem is simplified to a two-dimensional optimization problem, i.e. finding the pickoff gain K_{po} and the zero α of phase lead compensator for the high-order electromechanical ΣΔM. Furthermore, K_{po} and α of this second-order electromechanical ΣΔM can be chosen as the initial values for optimization. The essence of the optimization is how to find the relative maximum of

SQNR in a high-order electromechanical ΣΔM: **maximize**$\{SQNR(K_{po}, \alpha)\}$ subjected to the following constraints:

1. $\Delta SQNR(K_{po}, \alpha) \leq 6dB$: SQNR fluctuation due to tolerances of microfabrication:

$$\begin{cases} m = m_0 * (0.95 \sim 1.05) \\ b = b_0 * (0.8 \sim 1.2) \\ k = k_0 * (0.8 \sim 1.2) \end{cases}$$

   and $\pm 2\%$ coefficient mismatch in IC fabrication for electronic integrators. where m_0, b_0 and k_0 are the nominal values of the mass m, damping coefficient b and spring stiffness k of the sensing element $M(s)$.

2. $|\mathrm{NTF}|'s$ gain ≤ 1.5 (stability criteria [26]).

Figure 4.4 shows the SQNR distribution of a fifth-order electromechanical ΣΔM with the pickoff gain K_{po} and the phase lead compensator α. This fifth-order ΣΔM topology used for this simulation will be discussed in the next section. The loop shown in Figure 4.3 is stable and has a maximum SQNR with the compensator only if α is confined to the range from 0.95 to 1.0. K_{po} has much more freedom than α, and its influence on the loop stability is less than α.

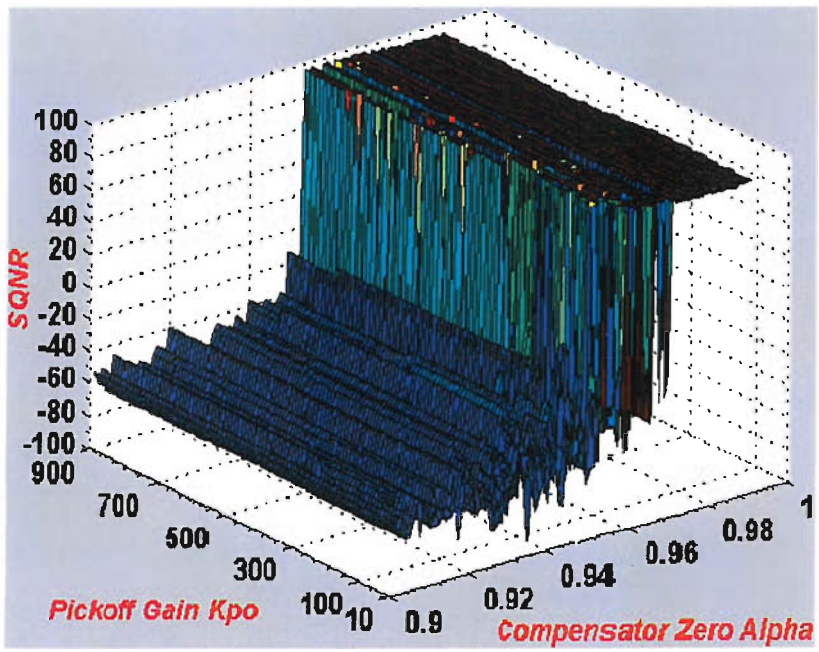

FIGURE 4.4: Relationship between the SQNR (dB) vs. K_{po} and α in a high-order electromechanical ΣΔM.

4.2 Loop Topologies and Performance

4.2.1 Multi-Feedback Topology

For a high-order ΣΔM with a large OSR (usually, ≥32), a linearized quantizer, modeled by a white noise source and a variable gain, is a good approximation to determine the properties of a ΣΔM [28]. A fifth-order electromechanical ΣΔM with multi-feedback (MF) loops is shown in Figure 4.5. The sensing element has the transfer function $M(s)$. The feedback electrostatic conversion has the gain of K_{fb}. K_{po} is the gain of the pickoff pramplifier. K_{bst} is the boosting gain. The coefficients K_1, K_2 and K_3 are used for integrator output scaling. A phase lead compensator C_p is used to stabilize the loop. The input-referred electronic noise source locates in the front of the boosting amplifier.

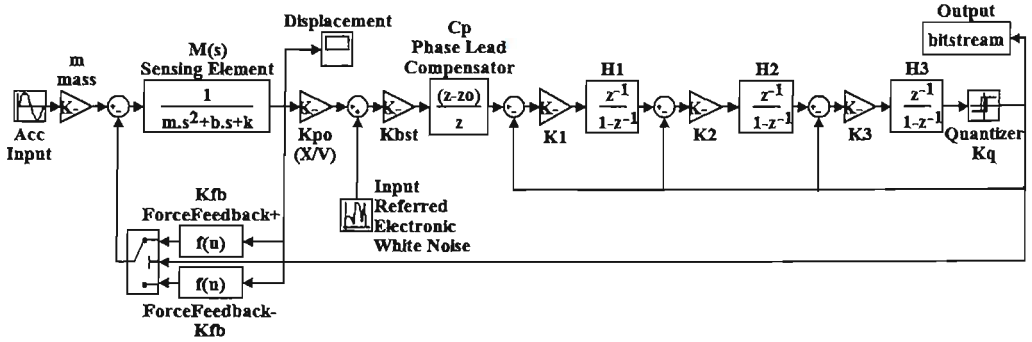

FIGURE 4.5: A fifth-order electromechanical ΣΔM with multi-feedback loops.

Using standard linear control system theory, the signal transfer function (STF), input-referred electronic noise transfer function (ENTF) and quantization noise transfer function (QNTF) of the system shown in Figure 4.5 can be derived as [70]:

$$STF(z) = \frac{m\kappa_m(z)\prod_{i=1}^{3} K_i H_i(z)/K_{fb}}{1+\kappa_m\prod_{i=1}^{3} K_i H_i(z) + K_q\sum_{i=1}^{3}\prod_{j=i}^{3} K_j[H_j(z)]} \tag{4.2}$$

$$ENTF(z) = \frac{\kappa_m(z)\prod_{i=1}^{3} K_i H_i(z)/(K_{fb}M_m(z)K_{po})}{1+\kappa_m\prod_{i=1}^{3} K_i H_i(z) + K_q\sum_{i=1}^{3}\prod_{j=i}^{3} K_j[H_j(z)]} \tag{4.3}$$

$$QNTF(z) = \frac{1}{1 + \kappa_m \prod_{i=1}^{3} K_i H_i(z) + K_q \sum_{i=1}^{3} \prod_{j=i}^{3} K_j [H_j(z)]} \tag{4.4}$$

where $\kappa_m = K_{fb} M(z) K_{po} K_{bst} C_p(z) K_q$ is an effective transfer function comprising the force feedback conversion, sensing element, pickoff preamplifier gain and the compensator; $H_i(z) = \frac{z^{-1}}{1 - z^{-1}}$ (i=1, 2, 3) is the transfer function (TF) of an electronic integrator. M(z) represents the mechanical TF of a sensing element in discrete-time z-domain:

$$M(z) = K_f \frac{(1 - a_f z^{-1}) z^{-1}}{(1 - b_f z^{-1})(1 - c_f z^{-1})} \tag{4.5}$$

where K_f, a_f, b_f and c_f are the gain, zero and two poles of a sensing element, repectively, and all these values are a function of the sampling frequency and the detailed description can be found in [71].

For low frequencies (in the signal band) $f \leq f_b \ll f_s$,

$$z^{-1} = e^{-j2\pi f/f_s} = \cos(\frac{2\pi f}{f_s}) - j \sin(\frac{2\pi f}{f_s}) \approx 1 - j\frac{2\pi f}{f_s}$$

$$\left|1 - z^{-1}\right| \approx \left|j\frac{2\pi f}{f_s}\right| = \left|j\pi \frac{f}{f_b}\frac{2f_b}{f_s}\right| = \left|j\pi \frac{f}{f_b}\frac{1}{OSR}\right| \ll 1$$

where f_b is the signal bandwidth, f_s the sampling frequency, and OSR= $2f_b/f_s$ the over-sampling ratio. Equation 4.4 can consequently be approximated by:

$$QNTF(z) \approx \frac{(1 - z^{-1})^5 + (2 - b_f - c_f)(1 - z^{-1})^4 + (1 - c_f)(1 - b_f)(1 - z^{-1})^3}{K_{fb} K_{po} K_f (1 - a_f) \prod_{i=1}^{4} K_i K_q + (1 - c_f)(1 - b_f) \prod_{i=2}^{4} K_i K_q} \tag{4.6}$$

It can be seen from Equation 4.6 that the noise shaping ability of the fifth-order electromechanical ΣΔM is dependent on the position of the two poles b_f and c_f. Moreover, K_f is very low, which leads to weak noise shaping compared with electronic integrators. Equation 4.6 stimulates the design of a sensing element with ideal second-order integration, i.e. parameters b_f=c_f=1 and a_f=0. Under such a condition, Equation 4.6 can be simplified to:

$$QNTF(z) \approx \frac{(1 - z^{-1})^5}{K_{fb} K_{po} K_f K_q \prod_{i=1}^{4} K_i} \tag{4.7}$$

Equation 4.7 indicates a fifth-order noise shaping ability. However, it requires a sensing element with both extremely low damping and spring stiffness, which would be impossible to fabricate and package. For real sensing elements, the real parts of two poles b_f and c_f are less than unity. For good noise shaping, the real parts of the two poles b_f and c_f should be close to unity, but this will inevitably result in very narrow signal bandwidth (SBW) of the sensor. Therefore, there is a trade-off between SNQR and SBW for the design of a sensor. For a given sensor, Equation 4.7 also indicates that the in-band noise power degrades with increasing the product of the loop gains $K_{fb}K_{po}K_fK_q\prod_{i=1}^{4}K_i$, on the other hand there is an upper limit for this product due to stability requirements for the ΣΔM control loop. Figure 4.6 shows the Bode diagram of STF, QNTF and ENTF of the system shown in Figure 4.5. The quantization noise is considerably shaped and white electronic noise is also shaped favorably.

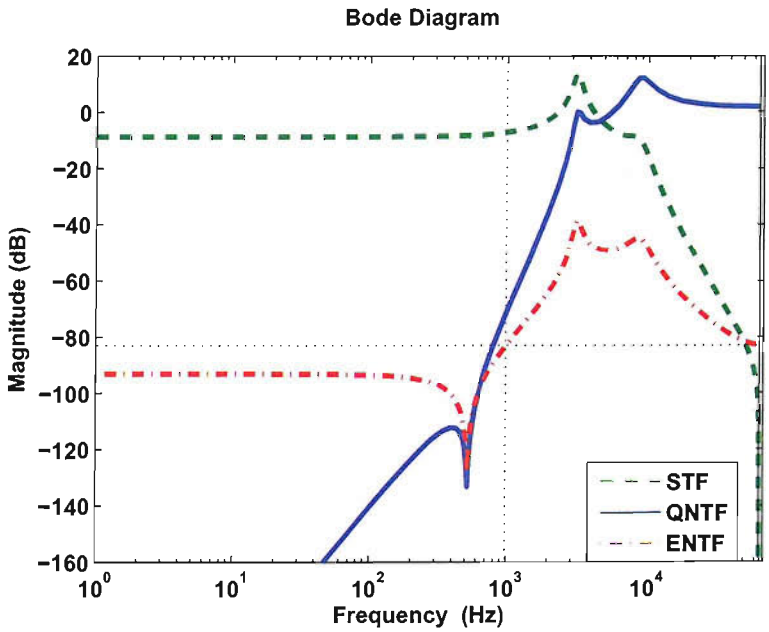

FIGURE 4.6: Bode diagram of STF, QNTF and ENTF of the system shown in Figure 4.5.

A SQNR comparison among different order electromechanical ΣΔM with the same sensing element and similar multi-feedback loops is shown in Table 4.1. DR is the output signal dynamic range, while OL (Overload) is the maximum input signal amplitude for which the SQNR degrades less than 6dB from the DR. It can be concluded that the higher the order of ΣΔM control loop, the wider the DR, and the less the OL. The PSD comparison between a second-order electromechanical ΣΔM and a fifth-order electromechanical ΣΔM is shown in Figure 4.7. The DR difference of the two loops is about 60dB. There is a third harmonic in the fifth-order loop, and limit cycles in the second-order loop. These will be addressed later.

Order	2	3	4	5
OSR	*DR(dB)/OL*	*DR(dB)/OL*	*DR(dB)/OL*	*DR(dB)/OL*
64	49/0.95	69/0.90	79/0.75	87/0.62
128	59/0.93	79/0.85	91/0.70	110/0.57
256	69/0.91	88/0.80	105/0.65	122/0.52

TABLE 4.1: Performance comparison among second-order, third-order, fourth-order and fifth-order electromechanical ΣΔM with multi-feedback loops.

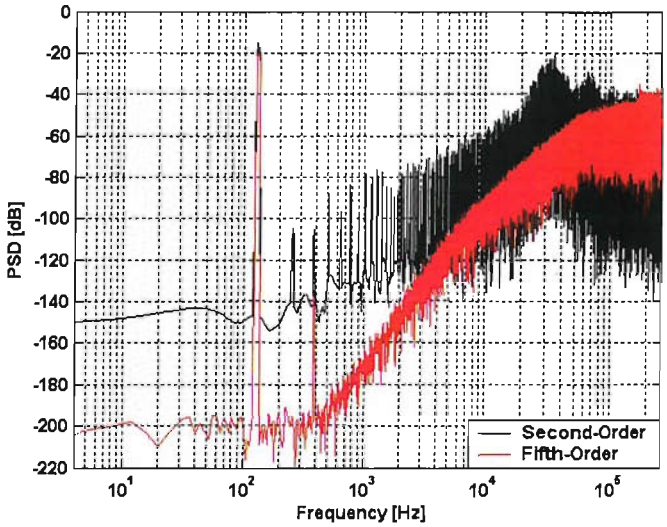

FIGURE 4.7: Noise shaping comparison: a fifth-order vs. a second-order electromechanical ΣΔM with OSR=256 and SBW=1024Hz.

4.2.2 Conditional Stability

According to classic control theory [72], a stable system must has all roots within the unit circle. The open-loop filter transfer function of the system shown in Figure 4.5 is given by:

$$L = 1/QNTF - 1 \tag{4.8}$$

The loop filter root locus is plotted in Figure 4.8. In order to ensure its root locus within the unit circle, the critically minimum gain of the quantizer is $\lambda_{min} = 0.654$. It reveals that one pair pole moves into the unit circle with increasing quantizer gain λ. Moreover, the Bode diagram of the loop filter is plotted in Figure 4.9 with $\lambda = 1$. At low frequencies, the gain is greater than 100dB for frequencies up to 600Hz due to all its poles at or near dc, but at medium frequencies, the gain decreases with frequency at a slope of -100dB/dec to allow for a low unity-gain crossover. Before the unity-gain crossover, two pairs of complex zeros reduce the phase lag to less than 180^o.

However, for a frequency range, the Bode amplitude plot has multiple crossover unity-gain frequencies, and finally the phase lag is above 180^o where the gain is greater than unity

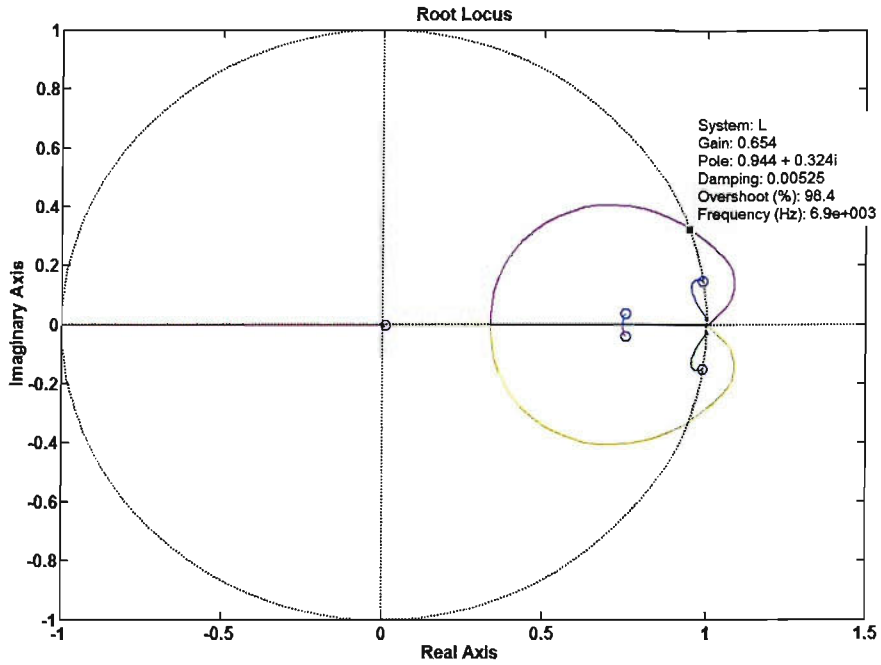

FIGURE 4.8: Root locus of the loop filter of the system shown in Figure 4.5.

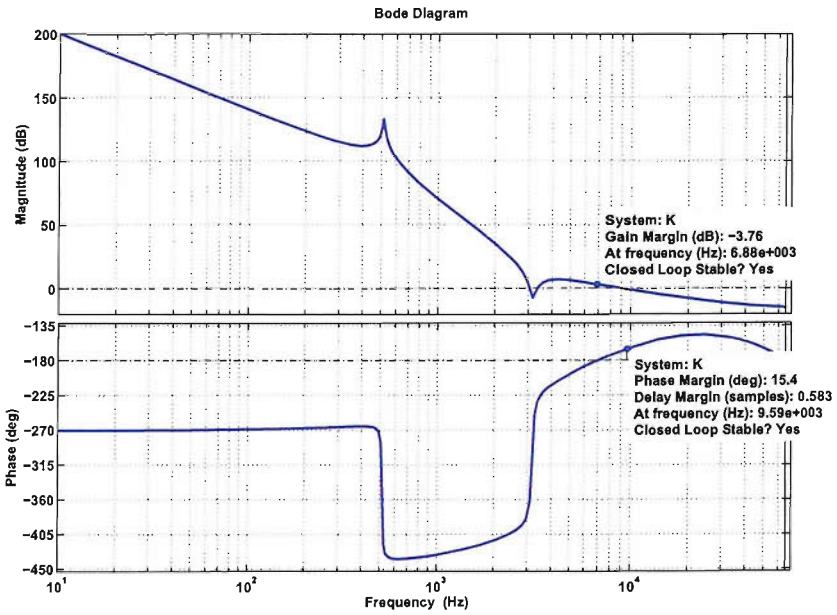

FIGURE 4.9: Bode diagram of the loop filter of the system shown in Figure 4.5.

(above 0dB line). This phenomena contradicts the stability criteria for a system with single unity-gain crossover and is referred as *conditional stability* [73], [74], [75]. Typically, a high-order (> 2) single loop ΣΔM is a conditionally stable control system, which means the quantizer gain must stay above a minimum limit. This also means before the input signal goes into the quantizer, it should not overload each integrator in the forward path

of a ΣΔM. There are some effective mechanism [76], [77], [78] to prevent the saturation of integrators caused by transients and start-up conditions. In the plot shown in Figure 4.9, the stability margins of amplitude and phase are -3.76dB and 15.4°, respectively. It also indicates a minimum quantizer gain of $\lambda_{min} = 10^{-3.76/20} = 0.65$ for a stable loop.

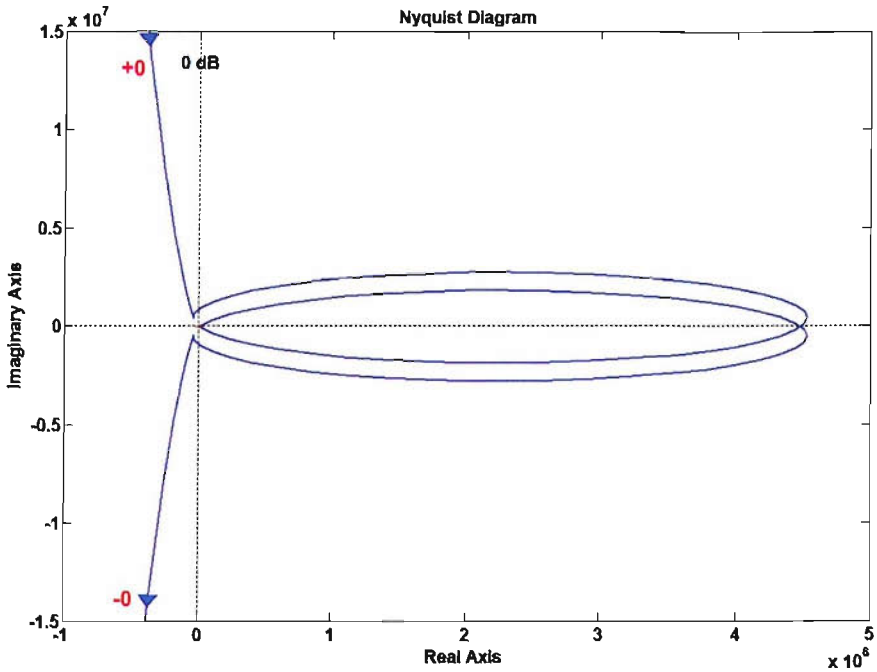

FIGURE 4.10: Full view: Nyquist diagram of the loop filter of the system shown in Figure 4.5.

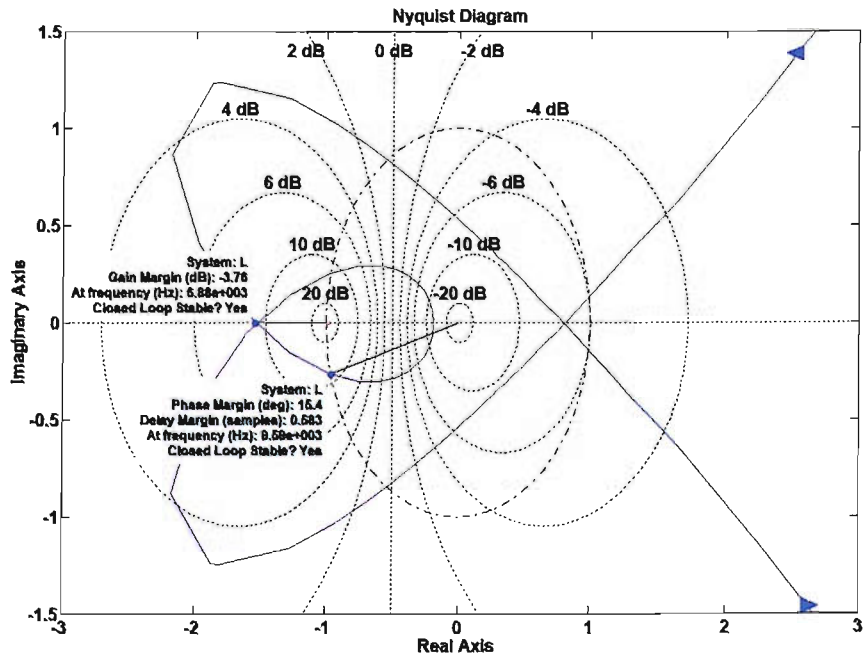

FIGURE 4.11: Zoom on (-1, 0): Nyquist diagram of the loop filter of the system shown in Figure 4.5.

The conditional stability can be also verified by the Nyquist diagram as shown in Figure 4.10. According to classic control theory [72], for a stable system, the net number of clockwise encirclements of the critical point at(-1, j0) equals the number of zeros (closed-loop system roots) outside the unit circle, minus the number of the open-loop poles outside the unit circle. Because there are no poles of this loop filter outside the unit circle, the net number of encirclements of the critical point at(-1, j0) should be zero. The full view of the Nyquist diagram (shown in Figure 4.10) and zoom view on (-1, j0) (shown in Figure 4.11) show the contour clockwise and anticlockwise encircle the critical point twice, respectively, so the net encirclement is zero. The ΣΔM is expected to be conditionally stable with gain λ margin (-3.76dB, or 0.65). In a practical implementation, the stability criteria provided by the root locus, Bode and Nyquist diagram, which are based on linear model of a quantizer, cannot precisely predict the stability of a high-order electromechanical ΣΔM. However, as discussed above, quantizer linear model and classic control theory do provide the insights of characteristic of the nonlinear control system. Each design step must be verified by effective and extensive simulations [23].

4.2.3 Topology: Feed-Forward Loops with Resonators

It can be seen from Figure 4.6 that for a MF topology, the total in-band noise is dominantly determined by the quantization noise at the end of the signal band. Four of five QNTF zeros are placed at dc ($z = 1$). This quasi-*Butterworth* high pass filter severely limits the maximum obtainable signal bandwidth. It is desirable to spread the zeros inside the signal bandwidth and further reduce the QNTF's in-band mean value, thus reducing the total in-band quantization noise power [31]. Unlike a second-order electromechanical ΣΔM, a high-order single loop electromechanical ΣΔM may apply more local feedback paths in the loop filter to shape the end-of-the-band quantization noise [30]. Figure 4.12 shows the topology of a fifth-order electromechanical ΣΔM with feed-forward loops and resonators (FFLR) [79]. The coefficient a_1, a_2, a_3 and a_4 determine the zeros. The coefficient b_1, b_2 and b_3 are used for integrator output scaling. The discrete equivalent transfer function of the sensing element supplies a pair of complex poles and a negative real zero. The phase lead compensator $C_p(z)$ creates a dc pole and a zero near unity circle. The local feedback path g creates a local resonator, or complex pairs of zeros in the QNTF, which produce some notches [80], [28] to cause faster decay in the stop-band and thus further suppress the quantization noise presented here. This makes the QNTF turn out to be a quasi-*inverse-Chebyshev* high pass filter.

The transfer functions STF, ENTF and QNTF are given by:

$$STF(z) = \frac{m\kappa_m(z)[b_1H_1(z)b_2H_2(z)(b_3H_3(z)a_4 + a_3) + (1 + gH_2(z)b_3H_3(z))(b_1H_1(z)a_2 + a_1)]}{L(z) \times K_{fb}} \tag{4.9}$$

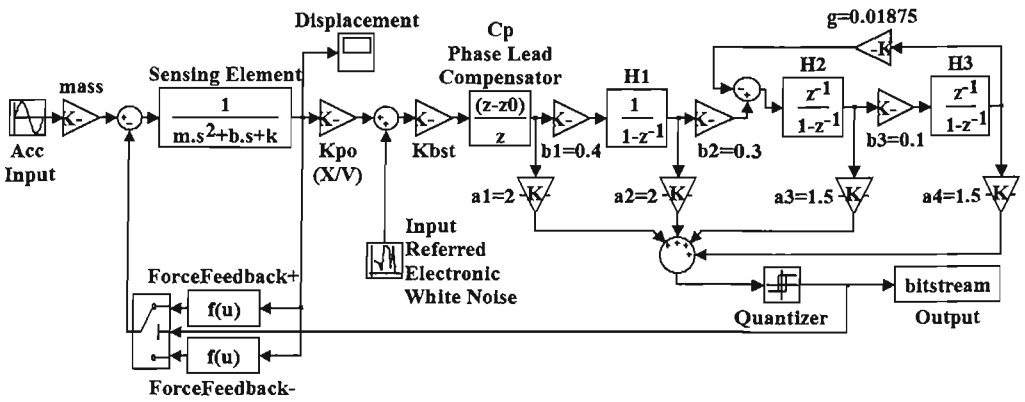

FIGURE 4.12: A fifth-order electromechanical ΣΔM with feed-forward loops and resonators.

$$ENTF(z) = \frac{\kappa_m(z)K_q[b_1H_1(z)b_2H_2(z)(b_3H_3(z)a_4 + a_3) + (1 + gH_2(z)b_3H_3(z))(b_1H_1(z)a_2 + a_1)]}{L(z) \times (K_{fb}M_mK_{po})} \tag{4.10}$$

$$QNTF(z) = \frac{1 + gH_2(z)b_3H_3(z)}{L(z)} \tag{4.11}$$

where $\kappa_m(z) = K_{fb}M_m(z)K_{po}K_{bst}C_p(z)K_q$ is an effective transfer function comprising the force feedback conversion, sensing element, pickoff preamplifier gain, the compensator, quantizer gain; and

$$L(z) = 1 + \kappa_m(z)\sum_{i=1}^{4} a_i \prod_{j=1,j>0}^{i-1} b_jH_j(z) + gH_2(z)b_3H_3(z)[1 - (\kappa_m(z)K_q(a_1 + b_1H_1(z)a_2)]$$

Figure 4.13 shows the Bode diagram of STF, QNTF and ENTF of the system shown in Figure 4.12. In contrast to the MF topology, the electronic noise level in the signal band is nearly same but at high frequencies the noise is amplified considerably. Moreover, there are two notches in the QNTF, while one notch in the QNTF of the MF topology. The first notch frequency is still determined by the poles of the sensing element at f_{no1}=509 Hz. The local resonator formed by $g_1H_2(z)g_4H_3(z)$ contributes a pair of complex poles, and the second notch frequency is determined by the local resonator (the numerator of Equation 4.11) at

$$\omega_{no2} = \sqrt{\omega_2\omega_3gb_3}$$

where ω_2 and ω_3 are the unity-gain frequency of the second and third integrators, respectively. Usually the unity-gain frequency of integrators is chosen as the sampling frequency f_s, and thus f_{no2} is at 903Hz.

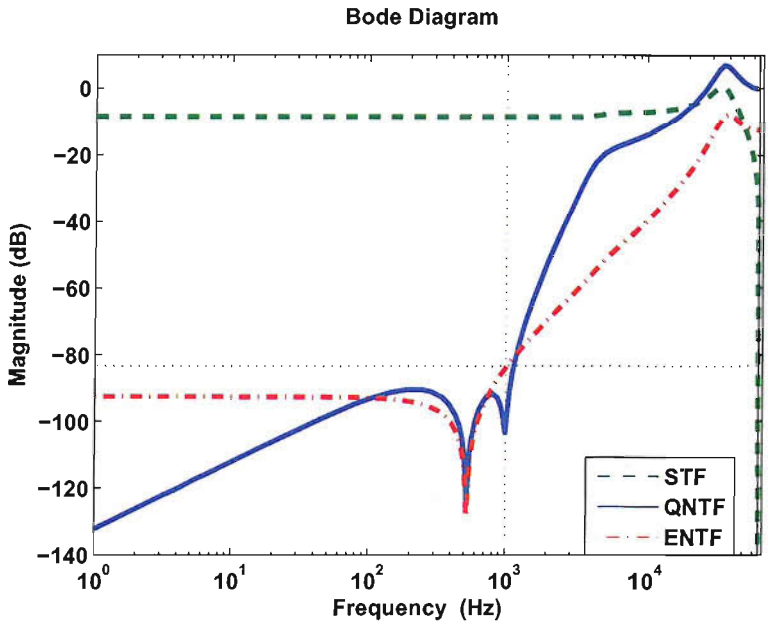

FIGURE 4.13: Bode diagram of STF, QNTF and ENTF of the system shown in Figure 4.12.

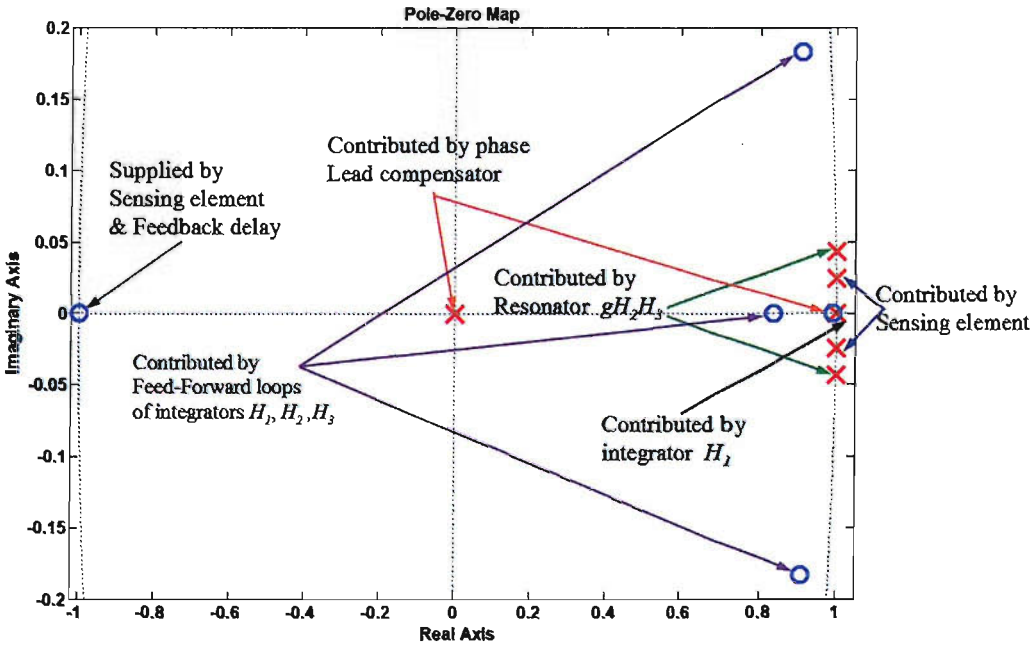

FIGURE 4.14: Pole-zero map of the loop filter of the system shown in Figure 4.12.

Figure 4.14 shows the pole-zero map of the open loop filter. Root locus of the open loop filter of the system shown in Figure 4.12 is plotted in Figure 4.15. The figure indicates that the quantizer gain should stay between $\lambda_{min} = 0.613$ and $\lambda_{max} = 2.69$ for stable operation,

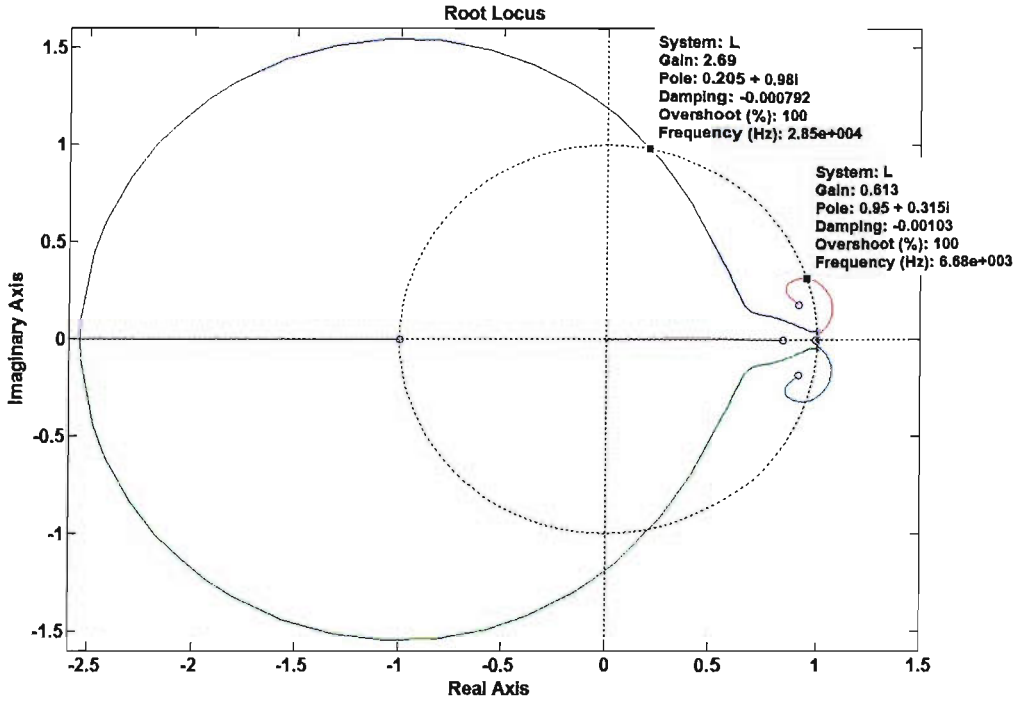

FIGURE 4.15: Root locus of the loop filter of the system shown in Figure 4.12.

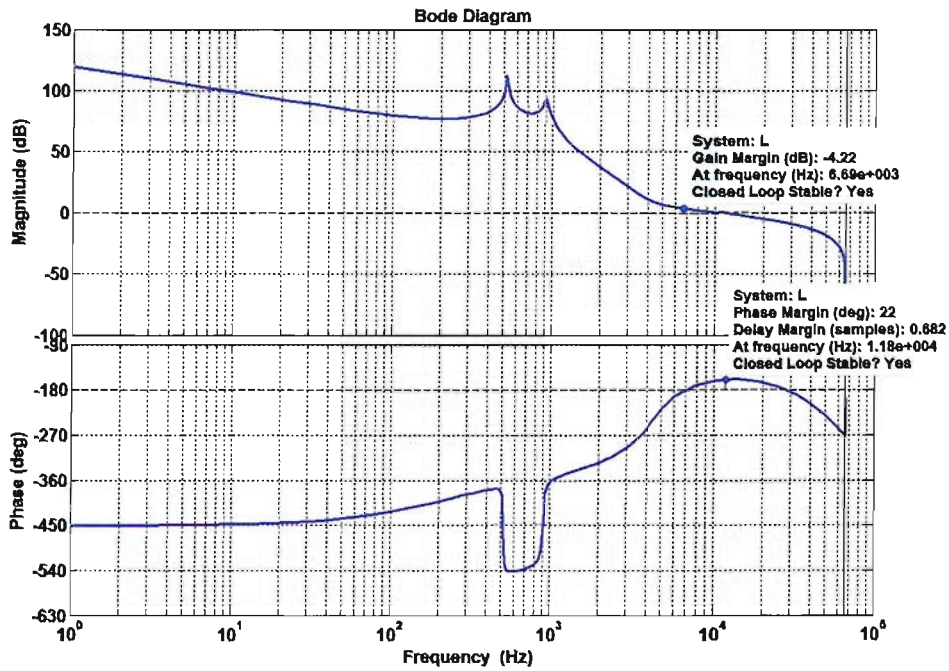

FIGURE 4.16: Bode diagram of the loop filter of the system shown in Figure 4.12.

which can be ensured by avoiding overload instability techniques [81], [82], such as clipping and saturation recovery. This conditionally stable system is also verified by a Bode diagram (shown in Figure 4.16) and Nyquist diagram (shown in Figure 4.17). Figure 4.18 shows the histogram of each integrator output swing. An output bitstream spectrum is shown in

Figure 4.19 with (a) quantization noise only (SQNR=97.3dB) and (b) quantization noise and white electronic noise (SNR=95.4dB, 2dB lower than SQNR) in response to a sinusoidal $1g$, 128Hz input acceleration. The displacement of the sensing element is 0.1nm, which is very small compared with a nominal gap of 3μm.

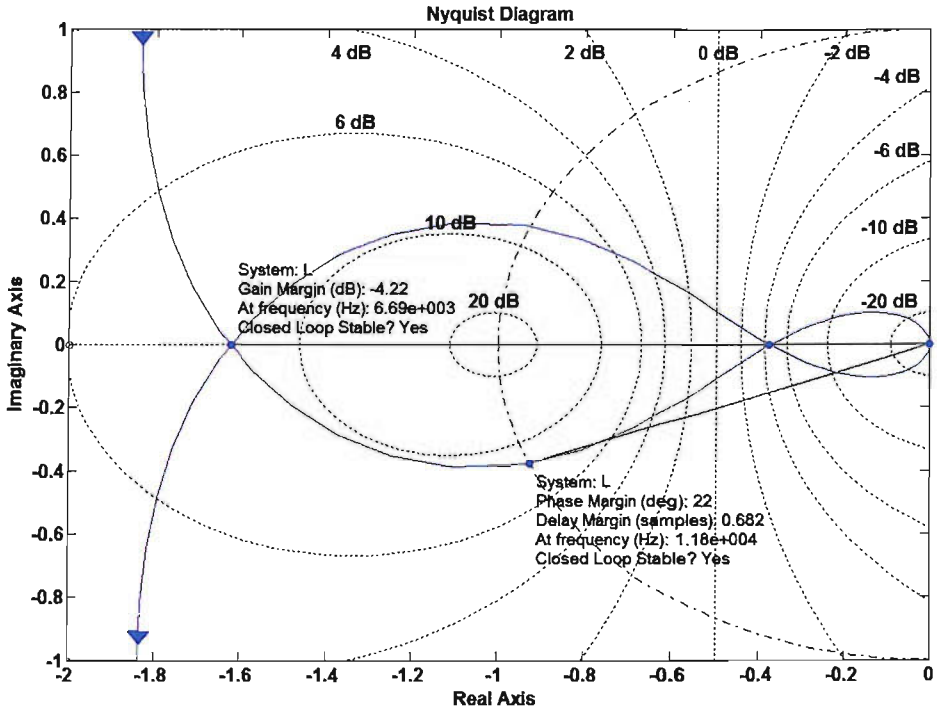

FIGURE 4.17: Nyquist diagram of the loop filter of the system shown in Figure 4.12.

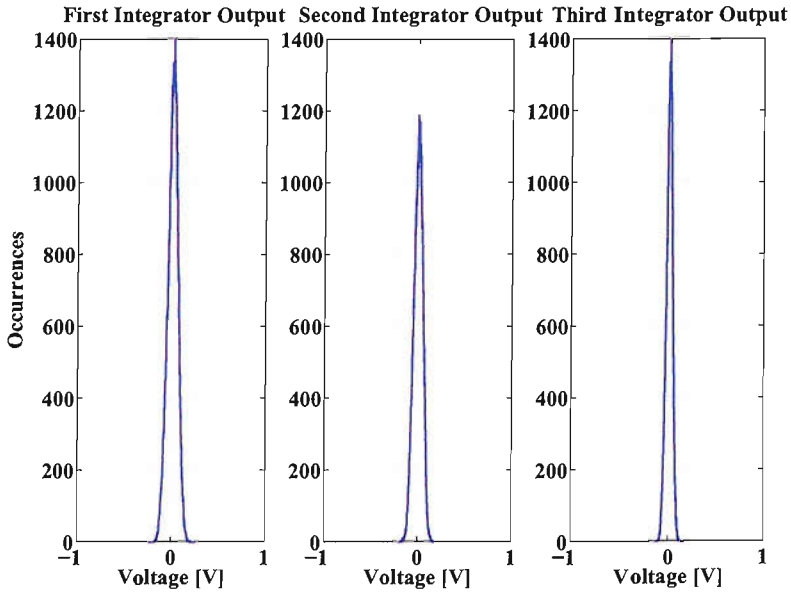

FIGURE 4.18: FFLR topology: integrator output number of occurrence vs. integrator output voltage (maximum 1V).

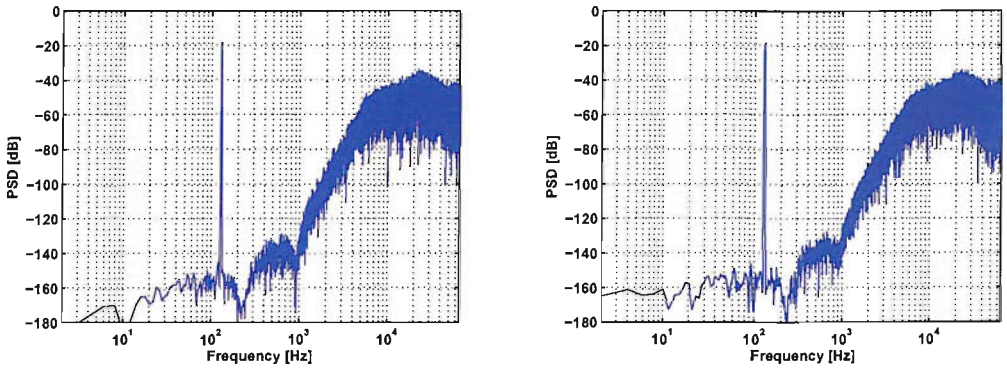

(a) With quantization noise only.

(b) With quantization noise and electronic noise.

FIGURE 4.19: Output bitstream spectrum of the system shown in Figure 4.12 with a 1g, 128Hz sinusoidal input signal.

4.2.4 Topology: Multi-Feedback Loops with Resonators

Figure 4.20 shows the topology of a fifth-order electromechanical ΣΔM with multi-feedback loops and local resonators (MFLR) [83], in which the coefficients a_1, a_2 and a_3 are used for integrator output scaling, the coefficients b_1, b_2 and b_3 determine the poles and loop stability, and the coefficients g_1 and g_2 create complex pairs of zeros. A phase lead compensator $C_p(z)$ is used to stabilize the loop.

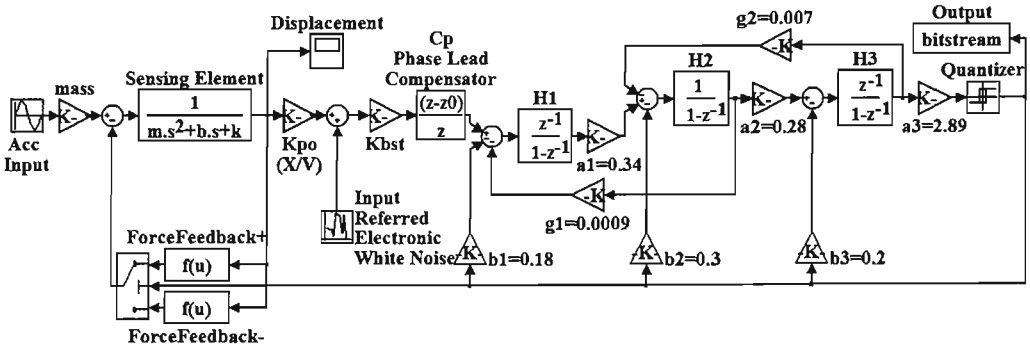

FIGURE 4.20: A fifth-order electromechanical ΣΔM with multi-feedback loops and resonators.

The transfer functions STF, ENTF, and QNTF are given by:

$$STF(z) = \frac{m\kappa_m(z)\prod_{i=1}^{3} H_i(z)a_i}{L(z) \times K_{fb}} \tag{4.12}$$

$$ENTF(z) = \frac{\kappa_m(z)\prod_{i=1}^{3} H_i(z)a_i}{L(z) \times (K_{fb}M_m(z)K_{po})} \tag{4.13}$$

$$QNTF(z) = \frac{1 + H_1(z)a_1H_2(z)g_1 + H_2(z)a_2H_3(z)g_2}{L(z)} \tag{4.14}$$

where

$$L(z) = 1+\kappa_m(z)\prod_{i=1}^{3} H_i(z)a_i+K_q\sum_{i=1}^{3} b_i\prod_{j=i}^{3} H_j(z)a_j+\sum_{i=1}^{2} a_ig_i\prod_{j=i}^{i+1} H_j(z)+H_1(z)a_1H_2(z)g_1a_3H_3(z)b_3K_q$$

Figure 4.21 shows the Bode diagram of STF, QNTF and ENTF of Figure 4.20. The QNTF is mainly determined by the number of integrators in the forward paths of the loop and only slightly by any resonators. Furthermore, the electronic noise level in the signal bandwidth is nearly the same as that of the FFLR topology, but at high frequencies the noise is highly attenuated due to the feedback loops compared with the FFLR topology. There are two notches in the QNTF, the first notch frequency is still determined by the poles of the sensing element (f_{no1} =509Hz) and the second notch frequency is provided by both local resonators (the numerator of Equation 4.14) and given by:

$$\omega_{no2} = \sqrt{\omega_1\omega_2g_1a_1 + \omega_2\omega_3g_2a_2}$$

where ω_1, ω_2 and ω_3 are the unity-gain frequencies of the first, second and third integrators, respectively, and f_{no2}=923 Hz if the unity-gain frequencies of integrators are chosen as the sampling frequency f_s.

However, the outputs of the integrators in any feedback loop topologies, not only contain the filtered quantization noise, but also a substantial part of the input signal [30]. Compared with the FFLR topology, the unity gain frequencies of each integrators in MFLR topology should be kept lower enough not to saturate the integrators. This leads to the relatively low gain of each integrator, the noise and distortion of each stage can not be heavily suppressed. A root locus of the open-loop filter of the system shown in Figure 4.20 is plotted in Figure 4.22, in which the minimum quantizer gain $\lambda_{min} = 0.798$. Figure 4.23 shows the histogram of each integrator output swing. Compared with the FFLR topology (Figure 4.18), the MFLR output voltage amplitude of each integrator is much higher (on average three times higher). Therefore, the FFLR topologies are suitable for low-voltage, low-power applications due to their integrator outputs having a relatively low amplitude [30]. The output bitstream spectrum of the system shown in Figure 4.20 are shown in Figure 4.24 with (a) quantization noise only (SQNR=96.1dB) and (b) quantization noise and white electronic noise (SNR=94.1dB, 2dB lower than SQNR) in response to a 1g, 128Hz sinusoidal acceleration in a 1kHz signal bandwidth. The displacement of the sensing element is 15nm, which is larger than that of the FFLR of Figure 4.20. This larger displacement signal is beneficial to the pickoff interface circuits, but will lead to higher harmonic distortion, which can be cancelled by the linearization proposed in Chapter 5.

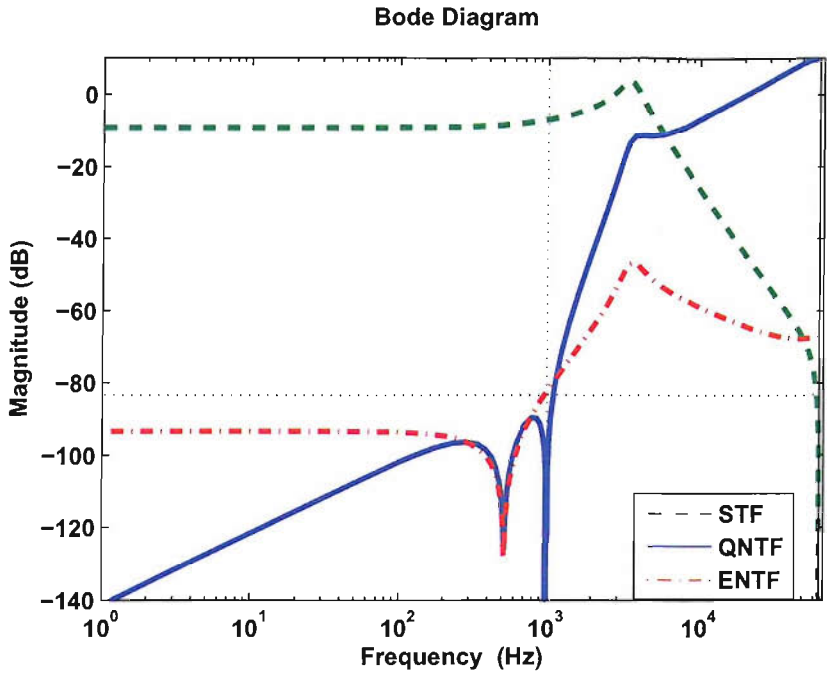

FIGURE 4.21: Bode diagram of STF, QNTF and ENTF of the system shown in Figure 4.20.

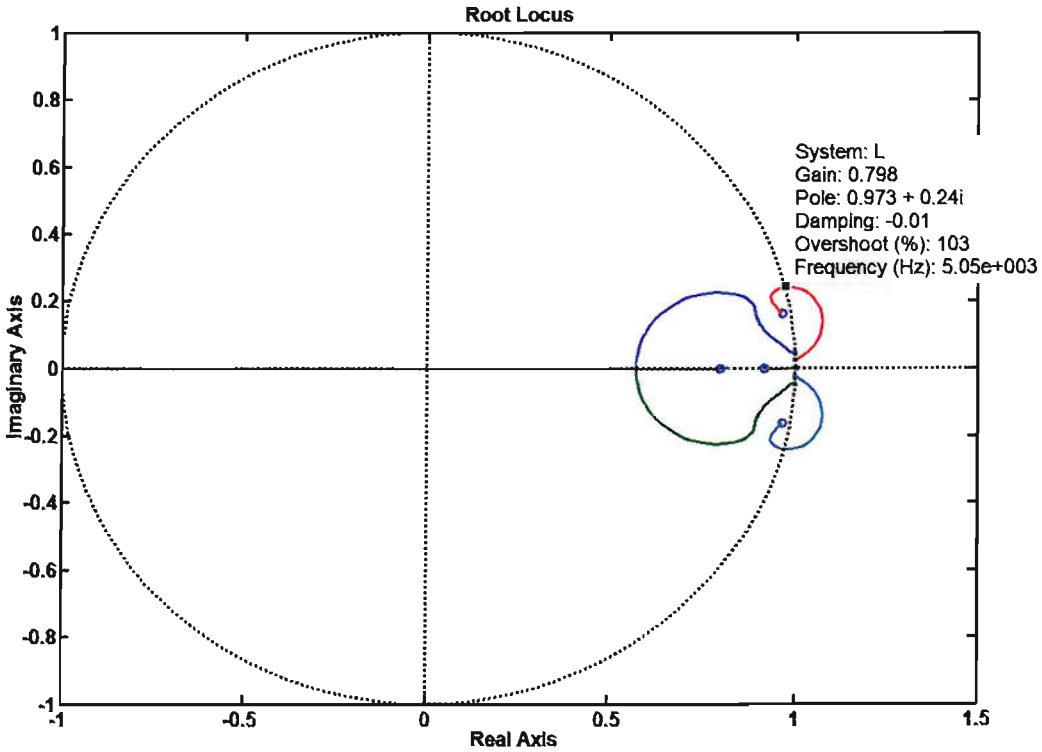

FIGURE 4.22: Root locus of the loop filter of the system shown in Figure 4.20.

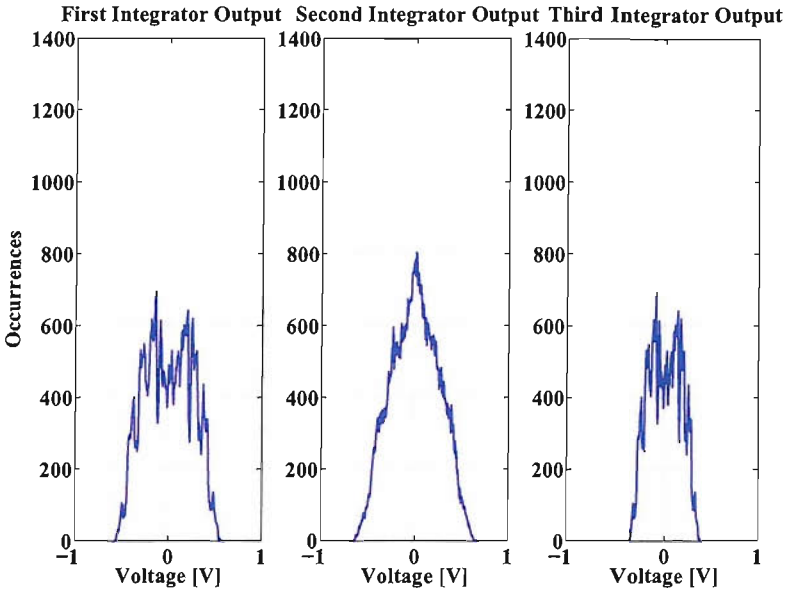

FIGURE 4.23: MFLR topology: integrator output number of occurrence vs. integrator output voltage (maximum 1V).

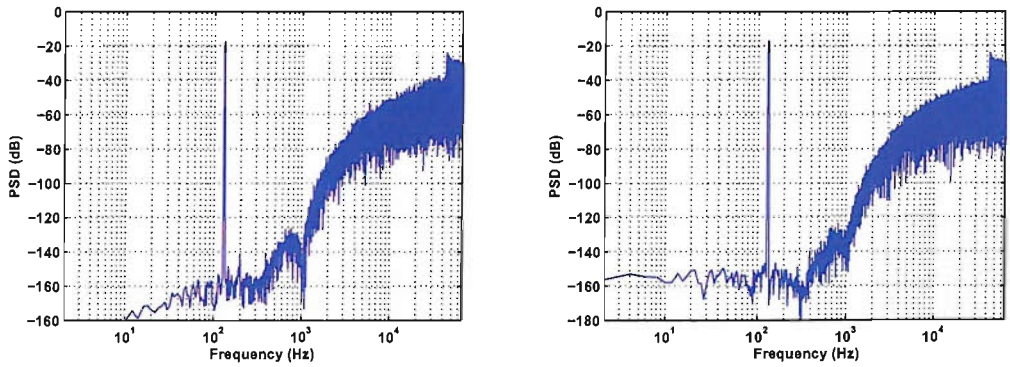

(a) With quantization noise only.

(b) With quantization noise and electronic noise.

FIGURE 4.24: Output bitstream spectrum of the system shown in Figure 4.20 with a 1g, 128Hz sinusoidal input signal.

4.3 Noise Analysis

There are three noise sources in a ΣΔM force feedback control system [7]:

- mechanical noise due to Brownian motion
- electronic noise introduced by the interface circuit due to thermal noise sources in the electronic devices
- quantization noise due to the analog to digital conversion process

It is desirable to design a ΣΔM closed-loop system with considerable lower quantization noise than the other two noise sources. In most applications, the electronic noise is the dominant noise source. Most present control loops for MEMS sensors are second-order electromechanical ΣΔM, in which the inertial sensing element inherently behaves as a physical continuous-time integrator. As discussed in Chapter 3.3.2, although the SQNR can be increased by increasing the over-sampling frequency (similar to a ΣΔ ADC), in a second-order electromechanical ΣΔM loop there is strong interaction between the quantization noise and the electronic noise due to the nonlinear gain of the quantizer. The following analysis shows that the only difference between the quantization transfer function and electronic noise transfer function in a second-order electromechanical is in the effective quantizer gain term. This suggests that increasing the quantizer gain would allow the output-referred quantization noise to be attenuated relative to the electronic noise floor. The effective quantizer gain decreases in the presence of electronic noise. If the electronic noise becomes a significant fraction of the standard deviation of the quantizer input, the effective quantizer gain is thus significantly reduced. This results in higher output-referred quantization noise compared to the ideal value. In this situation, further increase the oversampling frequency can not further increase the SQNR [54], [10].

4.3.1 Noise Analysis of A Second-Order Electromechanical ΣΔM

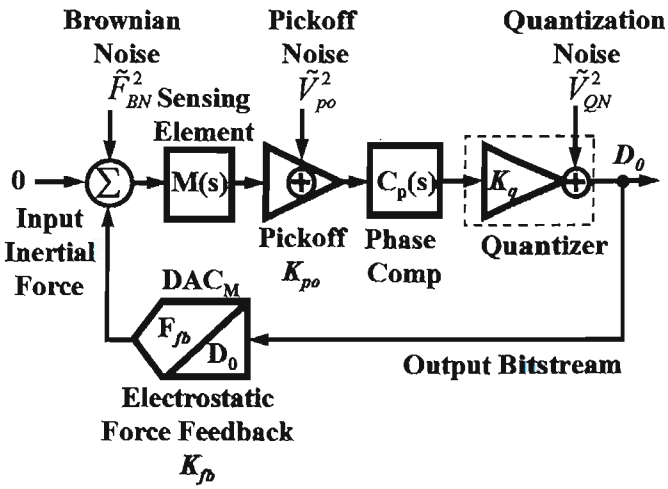

FIGURE 4.25: Block diagram of a second-order electromechanical ΣΔM for noise analysis.

Figure 4.25 shows the diagram of a second-order electromechanical ΣΔ control loop for noise analysis. $M(s)$ represents the mechanical sensing element that converts the input inertial force signal into a displacement and inherently serves as a low pass second-order loop filter. K_{po} is the gain of the pickoff preamplifier that senses the variation of capacitance. Both are approximately constant for small displacement which is ensured by the closed-loop operation. $\overline{V}^2_{po}$ is the input-referred electronic noise of the pickoff preamplifier. If for an under-damped sensing element, a pair of complex poles at the resonant frequency

causes a phase lag of 180^o, so a phase-lead compensator $C_p(s)$ is needed to stabilize the loop with a low-frequency zero z_0 and a high-frequency pole p_0: $C_p(s) = (s + z_0)/(s + p_0)$. It should be noted that the compensator works in the continuous-time domain which has a similar function as the compensator in the discrete-time domain used before. In the following analysis, all transfer functions are assumed in continuous-time for simplifying the derivation. The signal is then digitized by a one-bit quantizer, which is modeled as a variable gain K_q with additive quantization error $\overline{V}^2_{QN}$ and is usually implemented by a clocked comparator. K_{fb} is the gain of the voltage to electrostatic force conversion. From Figure 4.25, the transfer function for the Brownian noise $\overline{F}^2_{BN}$, as defined by Equation 2.9, can be derived as:

$$NTF_{BN}(s) = \frac{D_0(s)}{\overline{F}^2_{BN}(s)} = \frac{mM(s)K_{po}C_p(s)K_q}{1 + K_{fb}M(s)K_{po}C_p(s)K_q}|_{LF} \approx \frac{m}{K_{fb}} \tag{4.15}$$

This is identical to the signal transfer function. For simplicity, Brownian noise is neglected in the forthcoming analysis due to its all-pass property. Flicker noise (or $1/f$ noise) of the electronic circuit is also neglected due to chopper stabilization or correlated double-sampling techniques (CDS) [35]. Only thermal, white electronic noise is considered. The transfer functions for white electronic noise and quantization noise are given by Equation 4.16 and Equation 4.17, respectively:

$$NTF_{EN}(s) = \frac{D_0(s)}{\overline{V}^2_{po}(s)} = \frac{C_p(s)K_q}{1 + K_{fb}M(s)K_{po}C_p(s)K_q}|_{LF} \approx \frac{1}{K_{fb}M(s)K_{po}} \tag{4.16}$$

$$NTF_{QN}(s) = \frac{D_0(s)}{\overline{V}^2_{QN}(s)} = \frac{1}{1 + K_{fb}M(s)K_{po}C_p(s)K_q}|_{LF} \approx \frac{1}{K_{fb}M(s)K_{po}C_p(s)K_q} \tag{4.17}$$

Both the electronic noise and quantization noise exhibit the typical noise shaping characteristic in an electromechanical ΣΔM. However, these two noises are strongly coupled, so an index γ is introduced, as the quantization noise to electronic noise ratio, to indicate the interaction between them:

$$\gamma = \frac{\overline{V}^2_{QN}(s)}{\overline{V}^2_{EN}(s)} = \frac{NTF_{EN}(s)}{NTF_{QN}(s)} = C_p(s)K_q \tag{4.18}$$

Since $\gamma \gg 1$, the electronic noise shaping is not as pronounced as for the quantization noise. The output signal of the sensing element is very low; hence a large gain is required from the pickoff preamplifier and thus leads to a large electronic noise power at the quantizer input. The electronic noise has a strong impact on the performance of an electromechanical

ΣΔM due to its low mechanical dc gain, which is in contrast to a ΣΔ A/D. Equation 4.18 requires that the compensator $C_p(s)$ should have a high in-band gain to minimize in-band quantization noise. However, the $C_p(s)$ only serves as a phase-lead compensator that has low in-band signal gain (z_0/p_0), so a high-order lowpass electronic filter should be inserted between the compensator and quantizer to supply the high gain in the signal band. Nevertheless, the interface for a sensing element which is embedded in an electromechanical ΣΔM has the advantage of suppressing the electronic noise of the pickoff stage. The input-referred PSD_{EN} of the thermal electronic noise at the pickoff preamplifier can be evaluated through some circuit simulation tool, such as Spice. Due to the settling time of the pickoff preamplifier, an empirical value for the amplifier bandwidth is five times the sampling frequency f_s. The electronic noise variance is hence given by:

$$\overline{V}_{po}^2 = (PSD_{EN} \times \sqrt{5f_s})^2 \tag{4.19}$$

Figure 4.26 shows the effect of electronic noise on the SNR in a second-order electromechanical ΣΔM. The degradation of the SNR with the electronic noise is nonlinear. The higher the OSR, the higher the SNR. At very high OSR the quantizer gain will be determined mostly by electronic noise, thus the in-band noise is also dominated by electronic noise.

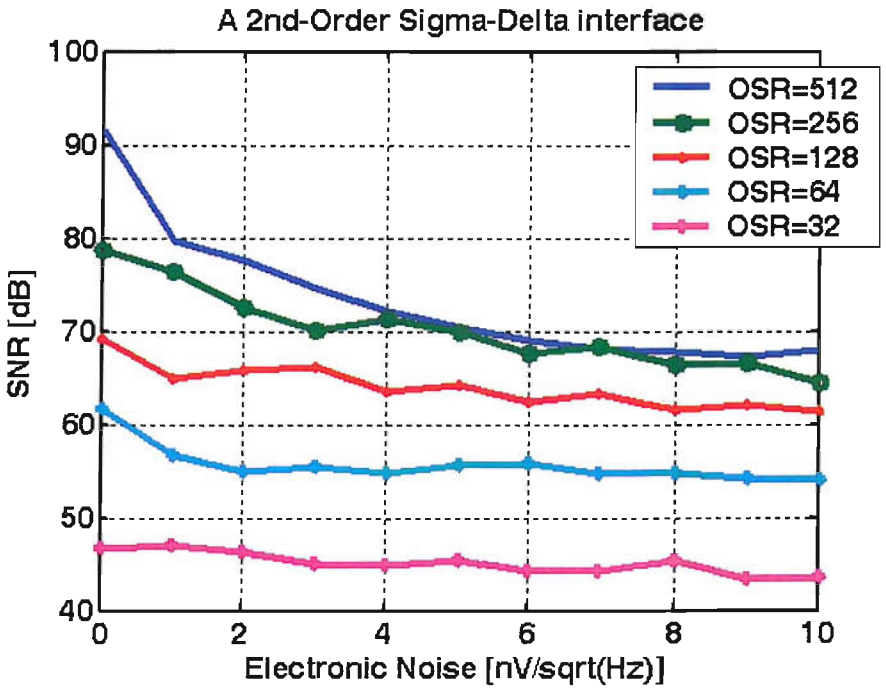

FIGURE 4.26: Effects of electronic noise on SNR in a second-order electromechanical ΣΔM with different OSR.

4.3.2 Noise Analysis of A High-Order Electromechanical ΣΔM

In order to simplify the circuit implementation, a multi-feedback topology is adopted for noise analysis, which has the advantage of the fewest feedback paths. Figure 4.27 shows the block diagram for the noise analysis indicating the various noise contributors at different stages. Most blocks are equivalent to the ones in Figure 4.25, except the electronic integrators have the transfer function given by $H(s)=1/(sT_s)$, where $T_s = 1/f_s$ is the sampling period. K_1, K_2, K_3, K_{F1}, K_{F2} and K_{F3} are gain coefficients, the latter three of the minor feedback loops are required to stabilize the loop. $\overline{V}^2_{en1}$, $\overline{V}^2_{en2}$ and $\overline{V}^2_{en3}$ represent thermal electronic white noise from the first, second and third integrator, respectively.

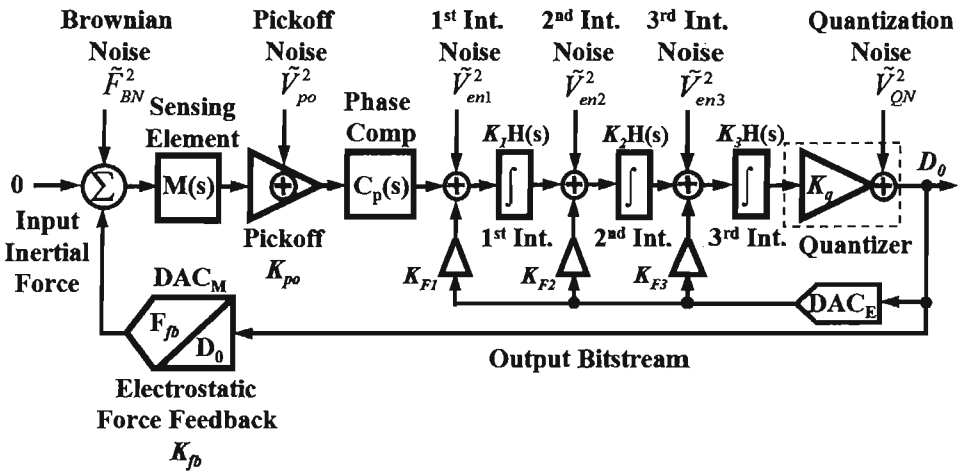

FIGURE 4.27: Block diagram for noise analysis of a fifth-order electromechanical ΣΔM.

The input signal has the same transfer function as the Brownian noise. Input signal and mechanical noise will pass through the system in the signal band without attenuation or shaping, which means that mechanical noise cannot benefit from an electromechanical ΣΔM and can only be reduced by optimizing the mechanical design and vacuum packaging. The transfer function of the electronic noise introduced by the pickoff circuit is given by:

$$NTF_{EN}(s) = \frac{D_0(s)}{\overline{V}^2_{po}(s)} = \frac{C_p(s)K_1\frac{1}{sT_s}K_2\frac{1}{sT_s}K_3\frac{1}{sT_s}K_q}{Loop(s)} \tag{4.20}$$

where

$$\begin{aligned} Loop(s) =& 1 + K_{fb}M(s)K_{po}C_p(s)K_1\frac{1}{sT_s}K_2\frac{1}{sT_s}K_3\frac{1}{sT_s}K_q + \\ &+K_{F1}K_1\frac{1}{sT_s}K_2\frac{1}{sT_s}K_3\frac{1}{sT_s}K_q + K_{F2}K_2\frac{1}{sT_s}K_3\frac{1}{sT_s}K_q + K_{F3}K_3\frac{1}{sT_s}K_q \end{aligned} \tag{4.21}$$

At low frequencies Equation 4.20 can be approximated by:

$$NTF_{EN}(s) = \frac{D_0(s)}{\overline{V}_{po}^2(s)}|_{LF} \approx \frac{1}{K_{fb}M(s)_{LF}K_{po} + \frac{K_{F1}}{C_p(s)}} \tag{4.22}$$

Compared with Equation 4.16, Equation 4.22 reveals that electronic noise of the pickoff circuit in a high-order electromechanical ΣΔM may be further reduced depending on the value of the two terms in the denominator of Equation 4.22, and if the following condition applies:

$$K_{fb}M(s)_{LF}K_{po} \leq \frac{K_{F1}}{C_p(s)} \tag{4.23}$$

This condition is valid for a reduced pickoff gain K_{po}, and, in case of an under-damped sensing element, a compensator with a low signal gain. Although these parameters cannot be arbitrarily chosen due to loop stability constraints, there is still room to modify them to further suppress the electronic noise of the pickoff circuit in a high-order ΣΔM. The impact of the electronic noise of the pickoff preamplifier on the SNR is strongly dependent on the ΣΔM topology and the parameters of sensing element. In contrast, in a second-order electromechanical ΣΔM, the pickoff gain and the signal gain of the compensator $C(s)$ will be cancelled due to the quantizer, hence the SNR cannot be improved by optimizing the pickoff gain and compensator gain. Electronic noise of the first integrator has similar properties as noise of the pickoff circuit, but it is attenuated by the pickoff gain K_{PO} (usually $\gg 1$), which reduces its significance. The noises of the second integrator and the third integrator are not only shaped by the sensing element, but also by the proceeding integrator(s). Noise sources in these stages are greatly attenuated in the signal band and can be negligible. The transfer function of the quantization noise is given by Equation 4.24 and at low frequencies is approximated by Equation 4.25:

$$NTF_{QN}(s) = \frac{D_0(s)}{\overline{V}_{QN}^2(s)} = \frac{1}{Loop(s)} \tag{4.24}$$

$$NTF_{QN}(s) = \frac{D_0(s)}{\overline{V}_{QN}^2(s)}|_{LF} \approx \frac{(sT_s)^3}{K_1K_2K_3K_q \times [K_{fb}M(s)_{LF}K_{po} + \frac{K_{F1}}{C_p(s)}]} \tag{4.25}$$

Equation 4.25 shows that the quantization noise is further shaped by the three additional integrators compared with the second-order loop (Equation 4.18). The transfer functions of

these noise sources are plotted in Figure 4.28 to demonstrate the noise shaping at different stages in a fifth-order electromechanical ΣΔM. In the fifth-order electromechanical ΣΔM, the coupling index between the electronic and quantization noise is given by:

$$\beta = \frac{\overline{V}_{QN}^2(s)}{\overline{V}_{EN}^2(s)} = \frac{NTF_{EN}(s)}{NTF_{QN}(s)} = K_q C_p(s) K_1 K_2 K_3 (sT_s)^3 = \gamma K_1 K_2 K_3 (sT_s)^3 = \gamma\sigma \quad (4.26)$$

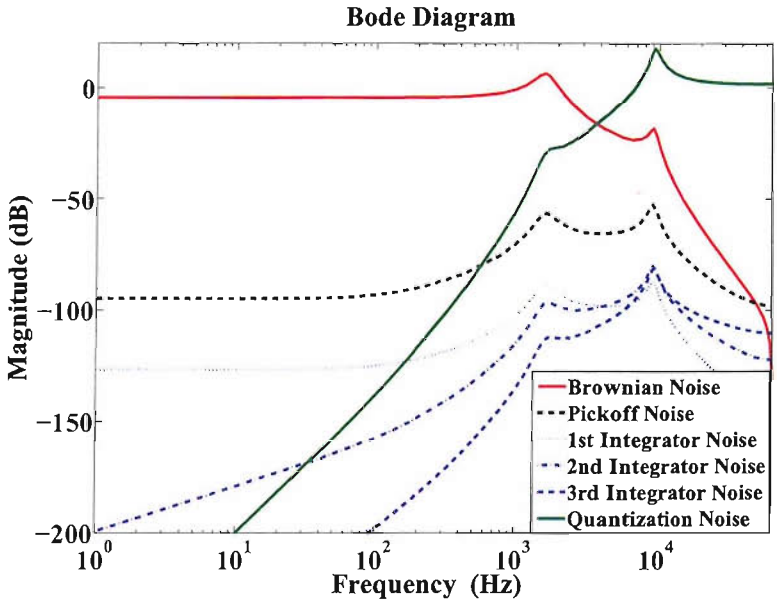

FIGURE 4.28: Noise transfer functions at different stage in a fifth-order electromechanical ΣΔM.

where $\sigma = K_1 K_2 K_3 (sT_s)^3 = K_1 K_2 K_3 (\frac{\pi}{OSR})^3$. Due to oversampling ratio $\gg 1$ and $K_1 K_2 K_3 \ll 1$, and thus $\sigma \ll 1$. Comparing Equation 4.26 with Equation 4.18, the electronic noise in the fifth-order loop has much less impact on the quantization noise due to $\beta \ll 1$ and $\beta \ll \gamma$, therefore the influence of electronic noise is reduced in the signal band and the systems can achieve a lower overall noise floor. Since electronic noise at the pickoff circuit is the dominating noise source in an electromechanical ΣΔM for most applications, the hardware implementation should make a trade-off between the SNR, the complexity of the circuit (i.e. the order of the ΣΔM) and the circuit operating frequency (i.e. the over-sampling ratio). Constraints mostly originate from the thermal electronic noise in the pickoff preamplifier. The typical noise PSD is approximately $4.5nV/\sqrt{Hz}$ in a state-of-the-art CMOS circuit implementation [84]. Providing the electronic noise PSD is around $5nV/\sqrt{Hz}$, a reasonable SNR is about 70dB using an OSR=256 in a second-order electromechanical ΣΔM (as shown in Figure 4.26). However, for a fifth-order electromechanical ΣΔM a reasonable SNR is about 100dB with an OSR=128 (as shown in Figure 4.29).

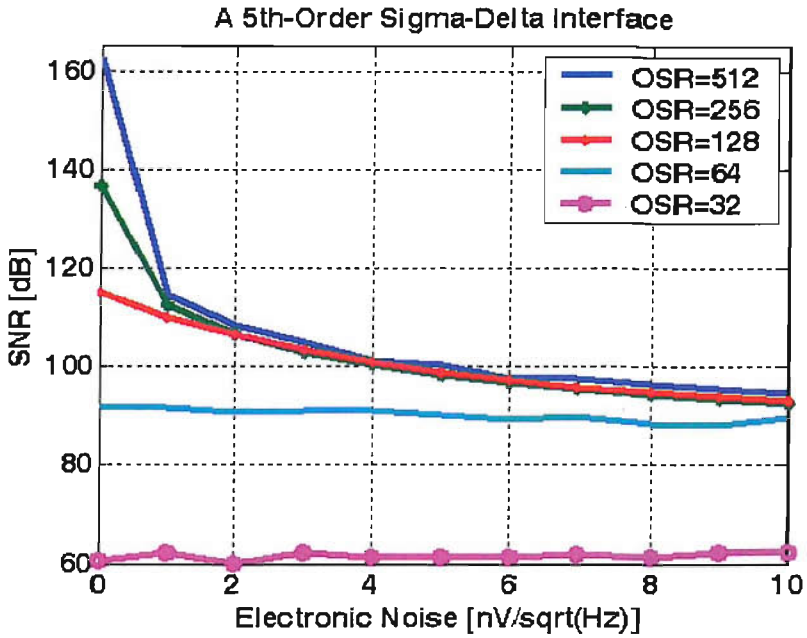

FIGURE 4.29: Effects of electronic noise on SNR in a fifth-order electromechanical ΣΔM with different OSR.

4.4 SQNR Sensitivity to Fabrication Tolerances

Micromachined inertial sensors, despite being fabricated by state-of-the-art micromachining batch-fabricated techniques, inherently suffer from relatively large fabrication tolerances. Both surface and bulk micromachining rely on etching techniques, such as anisotropic etching, isotropic etching and reactive ion etching. The etching processes are not perfect due to chemical or physical reactions with silicon. Furthermore, etch-stops are still not well controlled, therefore micromechanical structures depends strongly on the etching rate and the etchant used; this inevitably results in considerably geometrical feature variations [85]. Consequently, the variations of microstructure geometry will lead to the variation of the lumped parameters of a given sensing element, (which are: m the mass of the proof mass, k the spring stiffness of suspensions, and b the damping coefficient).

It can be seen from Equation 2.3 that for a sensing element, its response varies not only with frequency, but also with parameters $[m, b, k]$. Any coefficient variations lead to changes of the system dynamics, therefore change the desired STF and QNTF. The SQNR may be degraded and in the worst case, the loop may eventually become unstable. Therefore, SQNR is a criterion used to measure the influence of fabrication tolerance on the performance of an electromechanical ΣΔM. Also this criterion can be applied to assess loop stability indirectly, as a sharp drop in SQNR is a reliable indication for loop instability. In the following investigation, each of the nominal values, which are subject to fabrication tolerance, is replaced by its nominal value plus or minus a random number generated with a uniform probability density function. The random fluctuations range from zero to a maximum variation. Relatively high worst case values are assumed: the parameters of a sensing

element have nominal values $[m_0, b_0, k_0]$ (which are given by Chapter 8) with uncertainty ±30%. The electronic gain coefficient tolerance due to variations of the electronic circuits is comparatively small and is assumed to be ±2% [65]. The uncertainty is generated by the Matlab function *unifrnd*. Monte Carlo simulation (200 samples) is used to verify the loop performance sensitivity in terms of SQNR fluctuations. A white noise source is located in the front of the boosting amplifier, with a PSD of $3nV/\sqrt{Hz}$; this models the electronic noise contribution of the pick-off electronic amplifier. While limiting the overall system SNR, the electronic noise has the benefit to dither the ΣΔM loop and thus linearize it. The resultant PSD of the output bitstream includes electronic noise; therefore the metric SQNR is strictly speaking the SNR. The SNR is calculated using a Hanning window 128*1024 bins FFT. A signal bandwidth (SBW) of 1 kHz for the sensor and an OSR of 64 were assumed.

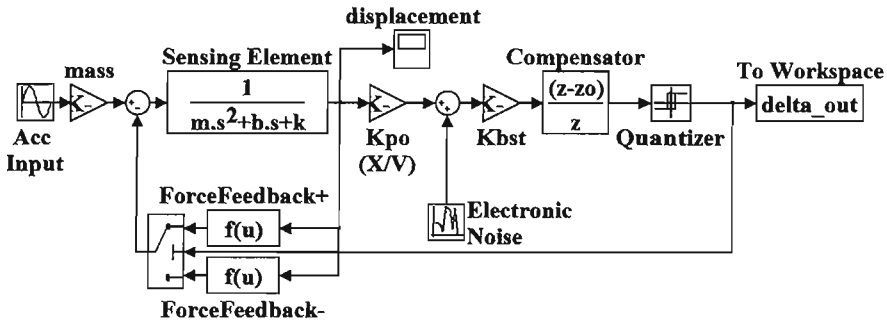

FIGURE 4.30: A second order electromechanical ΣΔM control loop.

A second-order electromechanical ΣΔM is shown in Figure 4.30, which the sensing element only acts as the loop filter. In one simulation run the input signal power is varied from -70dB to full scale and the SNR is calculated from the output bitstream. The result is shown in Figure 4.31; the horizontal length of each bar represents the SNR fluctuation which is approximately 10 dB. The SNR sensitivity to fabrication tolerance was also investigated on the fifth-order control loop shown in Figure 4.12. The SNR fluctuations are shown in Figure 4.32. In one simulation run the input signal power was varied from -105dB to full scale. The maximum SNR fluctuations are within 5dB, which is half of that of the second-order loop. This means that the performance of a fifth-order control loop is on average a factor 2 less sensitive to fabrication tolerance. Another important finding is that the stability of the control loop is not affected by fabrication tolerances. Furthermore, it is worth noting that, being independent of fabrication tolerances, the linearity of the SNR nominal values in the fifth-order loop is considerably improved when comparing with the second-order loop.

In addition, the analysis under the same condition was also done for a third-order (2-1) MASH electromechanical ΣΔM as shown in Figure 3.4, but the SNR average fluctuation was found to be 20dB (not shown here) and is much higher than that of a single loop. If there is no additional intelligent correcting techniques (for example coefficient tuning), a MASH topology may be problematic. This shows that a single loop high-order loop has a better immunity to fabrication tolerance than that of a MASH loop.

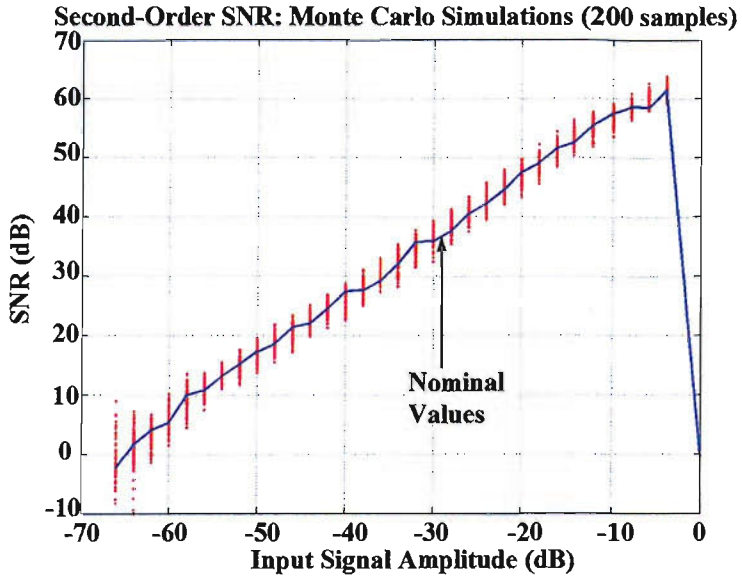

FIGURE 4.31: Monte Carlo analysis: SNR sensitivity to microfabrication tolerance in a second-order electromechanical ΣΔM control loop.

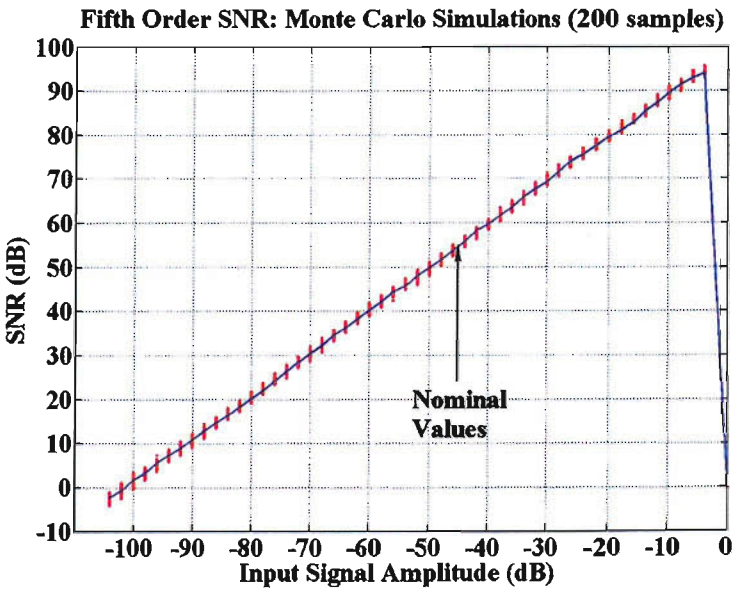

FIGURE 4.32: Monte Carlo analysis: SNR sensitivity to microfabrication tolerance in a fifth-order electromechanical ΣΔM control loop.

4.5 Dead-Zone and Idle Tones

The repetitive patterns that are present in the quantizer output bitstream under zero input conditions are called idle patterns. If the input signal is too small to disturb the idle patterns, this will result in a dead-zone. As discussed in Chapter 3.3.2, ideal ΣΔ A/D converters have an infinite resonant frequency at dc; consequently, dead-zones usually cannot be observed. This is in contrast to a second-order electromechanical ΣΔM. The finite resonant frequency of the sensing element, which corresponds to the filter pole frequencies,

leads to relatively low dc gain at low frequencies (in the signal band). When the external input signal is zero, the digital feedback signal causes the proof mass to move up and down at one quarter of the sampling frequency f_s. If the input signal of a sensing element is to be detected, the displacement must at least equal in amplitude to the idle residual motion generated by the force feedback. Otherwise, a dead-zone occurs in which the output bitstream of the modulator does not change with variations of the input signal [4]. This dead-zone can be greater than other noise sources in a second-order electromechanical ΣΔM, and thus it determines the minimum detectable acceleration. If the input amplitude is smaller than a minimal critical value, in the spectrum of the output bitstream, there will be no visible peak at the input frequency, thus the modulator does not code the input signal any longer. Although increasing the sampling frequency can reduce the dead-zone, this is at the sacrifice of increased circuit noise and higher power consumption. For a second-order electromechanical ΣΔM, assuming a zero input acceleration, the quantizer output bitstream is at the limit cycle frequency of $f_s/4$ and amplitude a_{max} equal to the full scale input range. The amplitude of the residual motion of the proof mass is given by: $\Delta x \approx a_{\max}/s^2 = a_{\max}/(2\pi f_s/4)^2$. Boser [4] derived the dead-zone formula for a second-order electromechanical ΣΔM:

$$a_{dead2} \approx 8a_{\max}(\frac{f_r}{f_s})^2 \tag{4.27}$$

where f_r is the resonant frequency of a sensing element.

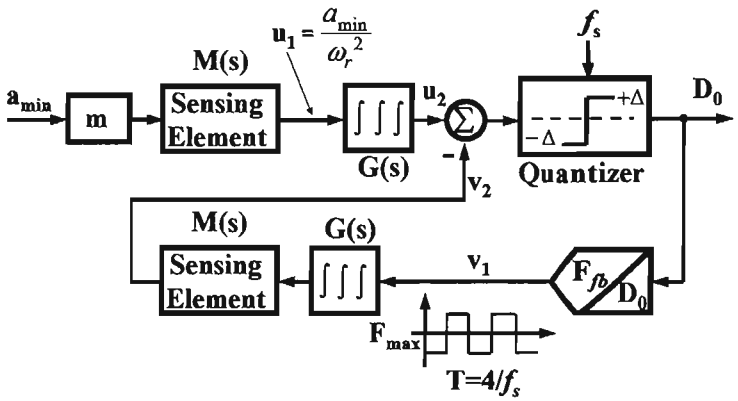

FIGURE 4.33: Equivalent block diagram of Figure 4.12, illustrating the origin of a dead-zone in a high-order electromechanical ΣΔM.

As an example, in the following the FFLR topology (as shown in Figure 4.12) is analyzed. Figure 4.33 shows a re-arranged block diagram of the same system. The figure is used for illustrating the origin of a dead-zone in a high-order electromechanical ΣΔM. $G(s)$ represents the electronic third-order filter, which is formed by three integrators and associated

coefficients (see Figure 4.12) and its transfer function is given by:

$$G(s) = \frac{(a_1 + a_2 b_1 H_1(s)) g H_2(s) H_3(s) b_3 + \sum_{i=1}^{4} a_i \prod_{j=i,j>0}^{i-1} b_j H_j(s)}{1 + g H_2(s) b_3 H_3(s)} \tag{4.28}$$

This transfer function is plotted in Figure 4.34. It can be seen that at low frequencies the electronic filter has a very large gain (=α), while at high frequencies the gain is a constant at 6dB (=β).

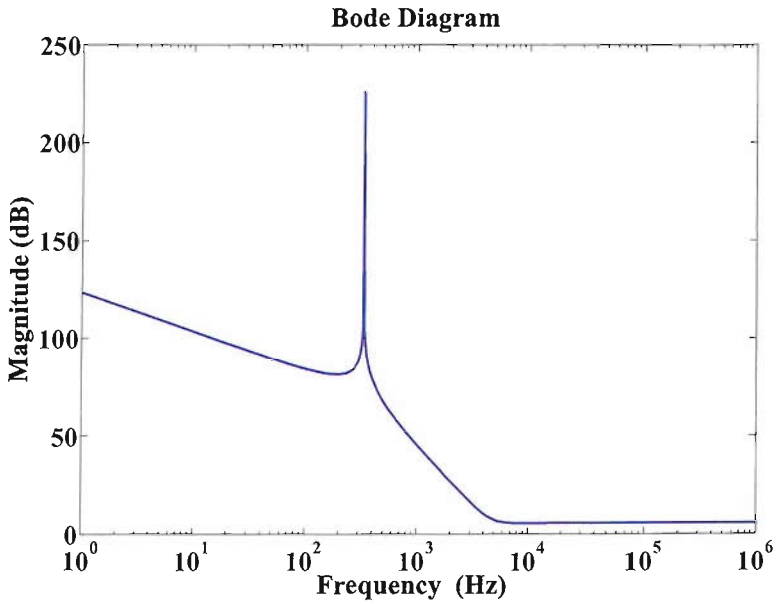

FIGURE 4.34: Bode diagram of the electronic filter of the high-order electromechanical ΣΔM shown in Figure 4.12.

Therefore, when the condition $u_2(=\alpha u_1) \approx v_2/2(=\beta v_1)$ is satisfied, the dead-zone can be derived for a fifth-order electromechanical ΣΔM:

$$a_{dead5} \approx 8(\frac{\beta}{\alpha}) a_{\max} (\frac{f_r}{f_s})^2 \tag{4.29}$$

It can be clearly seen from Equation 4.29 and Equation 4.27 that the dead-zone in a high-order loop is much smaller due to $(\beta/\alpha) << 1$ and thus can be neglected. This phenomenon results from the electronic filter, whose transfer function $G(s)$ has a different behaviour in the forward path and in the feedback path. In the forward path the signal bandwidth is very small compared with the sampling frequency f_s, and the electronic filter has a very large low frequency gain. However, in the feedback path, the bitstream D_0 has relative low gain in high frequencies (around $f_s/4$).

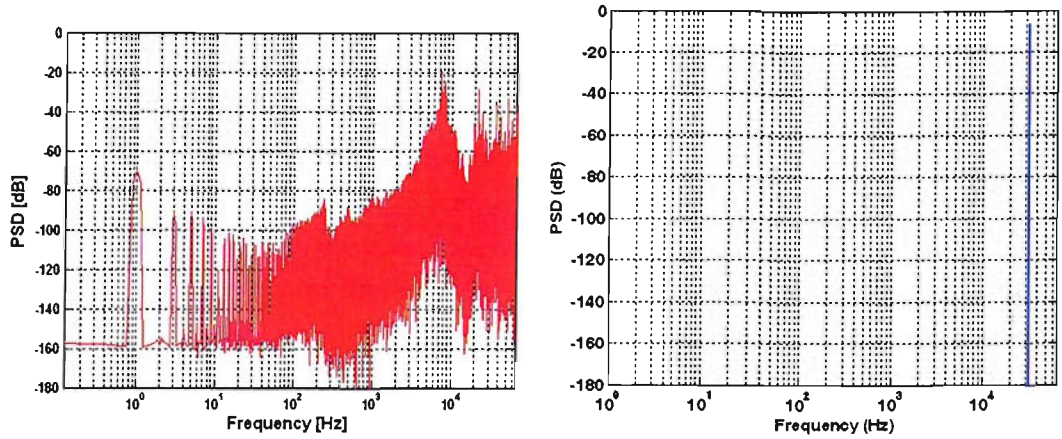

(a) A second-order ΣΔM with an amplitude of -54dB (b) A second-order ΣΔM with an amplitude of -60dB

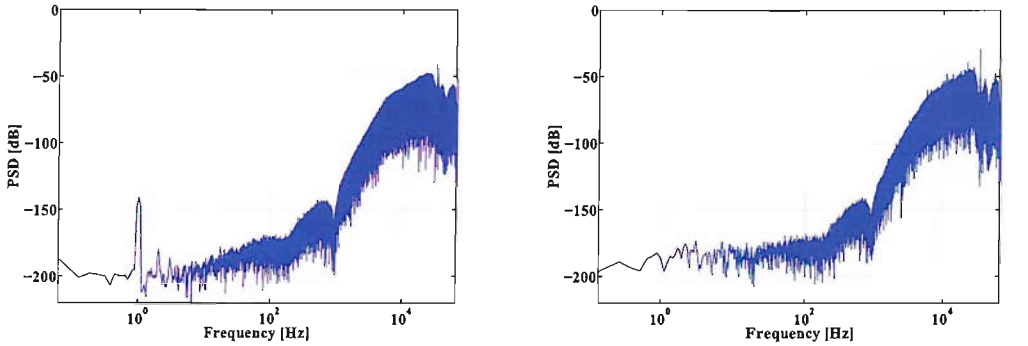

(c) A fifth-order ΣΔM with an amplitude of -120dB (d) A fifth-order ΣΔM with an amplitude of 0dB

FIGURE 4.35: Power spectral density of the output bitstream assuming a full scale sensor dynamic range of 1g, OSR=64 and 1024Hz signal bandwidth: (a) shows a second-order ΣΔM with a sinusoidal input signal of 1 Hz and an amplitude of -54dB; (b) the amplitude is reduced to -60dB; (c) shows a fifth-order ΣΔM force feedback loop with an input signal amplitude of -120dB; (d) the amplitude is reduced to 0.

Figure 4.35(a) shows the power spectral density of the output bitstream in a second-order ΣΔM force feedback loop with a sinusoidal input signal of 1 Hz and an amplitude of 2×10^{-3}g (equivalent to -54dB) and an amplitude of 1×10^{-3}g (equivalent to -60dB) in Figure 4.35(b). If the input amplitude drops below this critical amplitude of 2×10^{-3}g, the signal cannot be seen in the spectrum any longer, this is due to the dead-zone of the control loop. In comparison, Figure 4.35(c) shows the power spectral density of the output bitstream of the fifth-order ΣΔM force feedback loop with the same sinusoidal input signal but an amplitude of 1×10^{-6}g (equivalent to -120dB). The signal can still be clearly seen in the diagram; only when reducing the amplitude further, it disappears due to the dead zone. The minimal critical amplitude for the fifth-order modulator is around -160dB (Figure 4.35(d)). The reduction of the dead zone in a high-order electromechanical ΣΔM is due to the additional electronic integrators in the forward path, which have greater gain at low frequencies.

If the input signal of a ΣΔM is constant, the output signal easily exhibits a tonal behaviour, and in some conditions these tones may be folded into the signal band, thus considerably reducing the SQNR. A low order ΣΔM is particularly prone to exhibit such tonal behaviour [28]. For simulation purposes, the constant input signal is approximated by a very low frequency signal (1Hz). In the Figure 4.35(a), for the second-order electromechanical ΣΔM, such tones can be clearly identified in the spectrum as pronounced peaks in the signal band. As a consequence, the quantization noise cannot be considered as white any longer. In the fifth-order ΣΔM, the additional electronic integrators randomize the quantization error and thus whiten the quantization noise spectrum. There is no evidence of limit cycles in the signal band of Figure 4.35(c), therefore limit cycles are greatly suppressed in the fifth-order electromechanical ΣΔM. In a hardware implementation, there are inevitably additional noise source such as Brownian noise from the sensing element and electronic noise from the interface electronics; these act as a dither signal and further suppress the tonal behaviour.

4.6 Effects of The Mechanical Quality Factor Q on Noise Shaping

The mechanical quality factor Q of a sensing element is defined in Equation 2.4. Not only Q affects the mechanical noise and the dynamic characteristics of inertial sensors, but both electronic noise and quantization noise will be shaped by the sensing element. Sensing elements with different Q will exhibit different noise shaping when embedded in a ΣΔM loop. An under-damped sensing element needs a phase compensator to provide adequate phase margin. For an over-damped sensing element, the first one of two poles is usually lower than the signal bandwidth and the second one is much higher than the signal bandwidth [8], so it is not necessary to add a lead filter to stabilize the loop. The over-damped sensor embedded in a ΣΔM loop is in fact a first-order loop due to the second pole of the sensing element which does not influence noise shaping in the signal band. Using an OSR=256, Figure 4.36(a) shows the SQNR comparison between sensing elements with different Q incorporated in the same loop as shown in Figure 4.5. The parameters of the sensing element are chosen: m=0.97mg and k=48.1 N/m, and b=0.6, 0.04, and 0.006 N/m/s for over-damped, critically damped and under-damped, respectively. It can be seen that the loops with the under-damped and critically damped sensing elements have better quantization noise shaping, while the loop with the over-damped sensing element suffers from a -21dB SQNR degradation.

Electronic noise is not always detrimental to the performance of a ΣΔM loop. They can behave as dithering to improve linearity. An input referred electronic noise of $5nV/\sqrt{Hz}$ is added to the pickoff circuit. The nonlinearity of the SNR shown Figure 4.36(b) is within 0.5dB, which is much lower than that (6dB) of without electronic noise dithering. This is beneficial for control system, but there is a SNR loss due to the electronic noise. For an optimal design of an electromechanical ΣΔM, the level of electronic noise should provide

enough dithering, which sets the lower limit on electronic noise. However, the level of electronic noise should not significantly affect the SNR, which sets the upper limit on electronic noise.

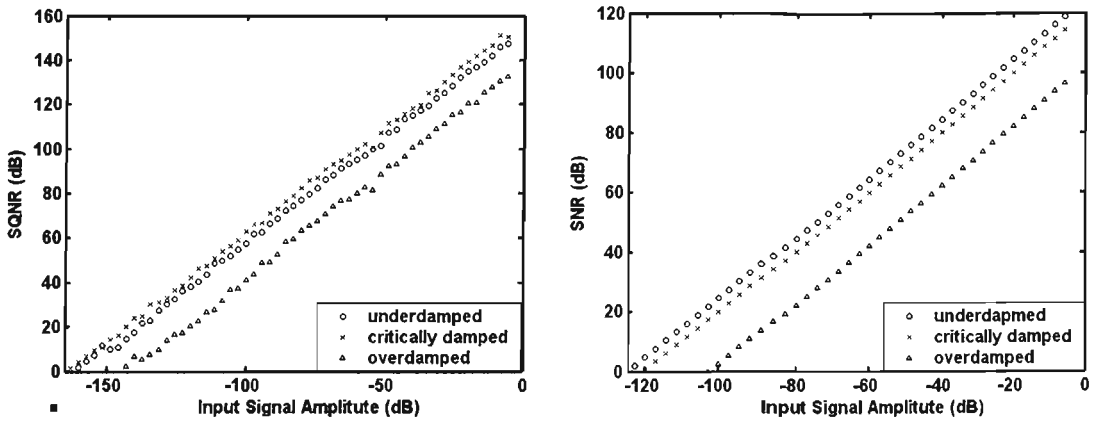

(a) without electronic noise

(b) with input referred electronic noise of $5nV/\sqrt{Hz}$ at pickoff

FIGURE 4.36: SNR comparison among sensors with different Q.

4.7 Electrostatic Force Feedback Delay

There are many methods [86], [87] to map a transfer function in the continuous time domain to an equivalent counterpart in the discrete time domain. The principle is that the impulse responses of the CT and DT should be the same. Using Maple [88], Cherry et al [89] gave a table for calculation of the z-domain equivalents for s-domain transfer functions. The continuous waveform of feedback electrostatic force suffers from a delay between the sensing and feedback phase due to CDS techniques, finite settling time of the charge amplifier and non-ideal feedback pulse. The parameters for the following discussion are defined in Figure 4.37.

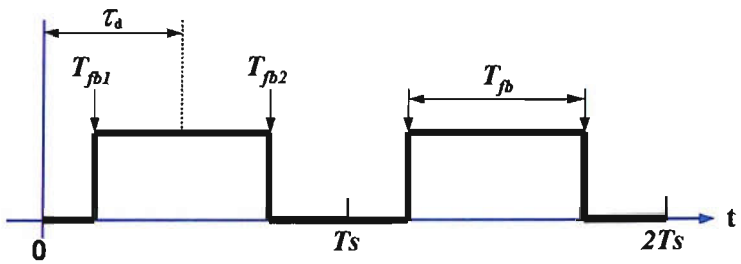

FIGURE 4.37: Waveform of the feedback electrostatic force and definitions [53], [54].

The feedback duration time is $T_{fb} = T_{fb2} - T_{fb1}$, and $\tau_d = (T_{fb2} + T_{fb1})/2$ is the time delay from the center of the feedback pulse to the sampling point. Using the definition τ_d here, instead of the T_{fb1}, as the measure of the loop delay, can provide more information about

feedback duration and delay time. Both Lemkin et al [53] and Jiang et al [54] derived the equivalent transfer function in the discrete time domain of a sensing element as:

$$M(z) = H_M(z)H_{fb}(z)H_d(z) \tag{4.30}$$

where

$$H_M(z) = \frac{T_s^2 z^{-1}}{(1 - z_1 z^{-1})(1 - z_2 z^{-1})}$$

$$H_{fb}(z) = \left(\frac{T_{fb}}{T_s}\right)$$

$$H_d(z) = \left((1 - \frac{\tau_d}{T_s}) + \frac{\tau_d}{T_s} z^{-1}\right) \tag{4.31}$$

$H_M(z)$ is the equivalent transfer function in the discrete time domain of the sensing element. $H_{fb}(z)$ is the effective duration of the feedback force on the proof mass, which is effectively a scale factor of the output amplitude. $H_d(z)$ contains the phase lag $\frac{\tau_d}{T_s} z^{-1}$ due to the delay of feedback force pulse. It is necessary to add some phase lead to compensate the delay in order to keep the loop stable. Equation 4.31 denotes that the loop doesn't suffer from the delay when $T_{fb} = T_s$ and $\tau_d = 0.5T_s$, which is the ideal case.

Simulations were done with the FFLR topology as shown in Figure 4.12. Figure 4.38 shows the Bode diagram of the open-loop filter vs. the delay τ_d, while keeping $T_{fb2} = T_s$. When the delay increases, both the magnitude and phase stability margins decrease. When the delay increases to $\tau_d = 0.85T_s$, the loop becomes critically stable.

In addition, Figure 4.39 gives the relationship of QNTF vs. the delay τ_d. The figure directly demonstrates the effects of $H_{fb}(z)$. The SQNR is calculated to lose 25dB with the delay τ_d increase from 0 to $0.85T_s$ while keeping $T_{fb2} = T_s$.

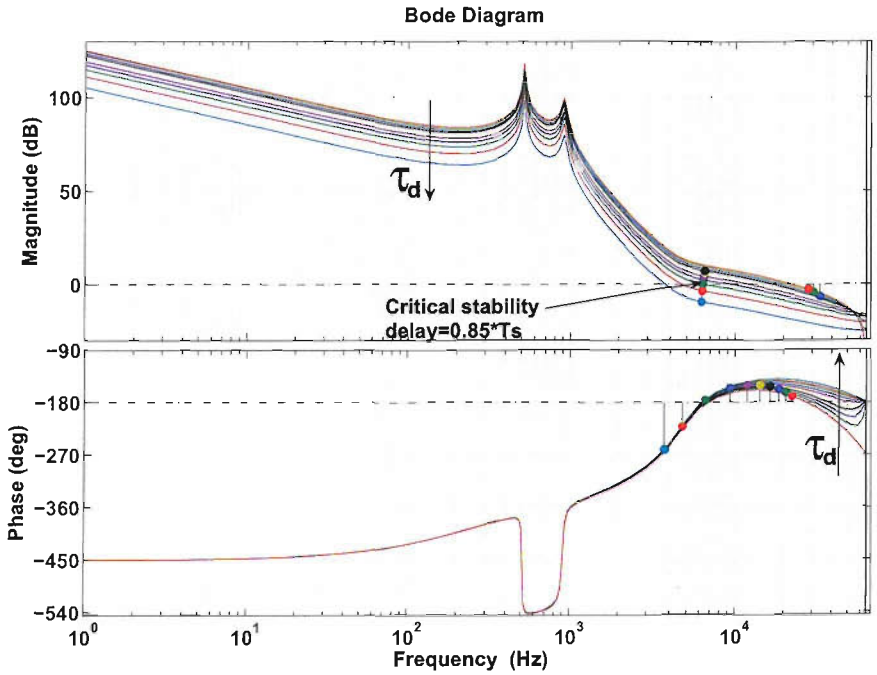

FIGURE 4.38: Bode diagram of the open-loop filter vs. the delay τ_d.

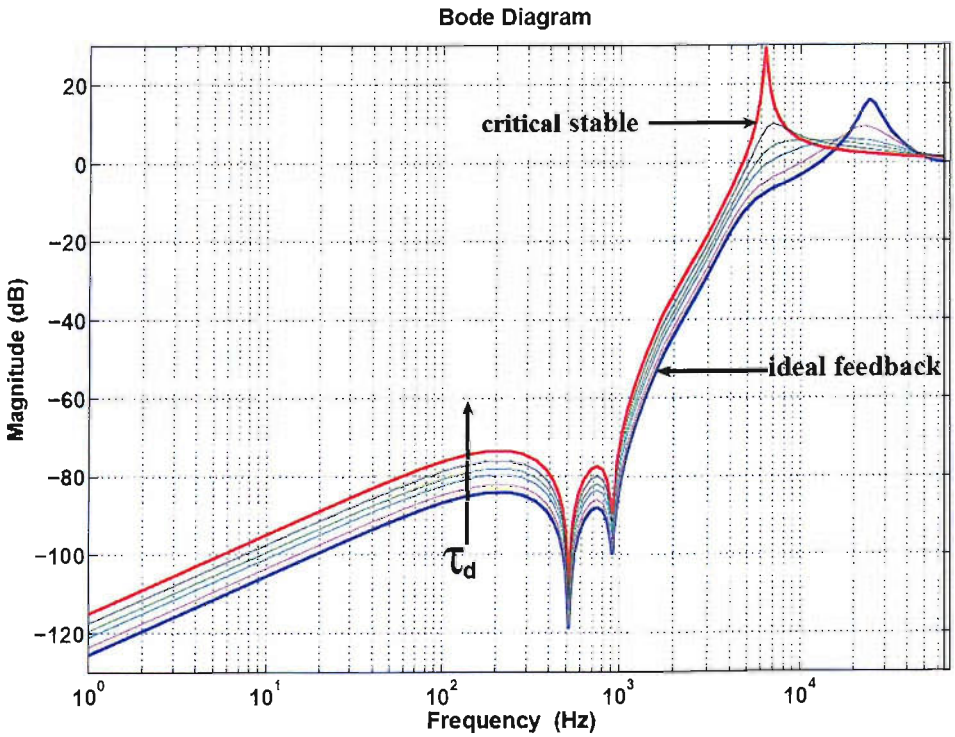

FIGURE 4.39: QNTF vs. the delay τ_d in a fifth-order ΣΔM Figure 4.5.

4.8 High-Order Continuous-Time Electromechanical ΣΔM

Considering the extra loop delay derived by Equation 4.30, Figure 4.12 is mapped into a CT implementation of the FFLR topology as shown in Figure 4.40. The two implementations share the same gain coefficients. With the same simulation conditions (except the loop delay $T_{fb1} = 0.3T_s$ and feedback duration $T_{fb} = 0.7T_s$ for the CT implementation), the output bitstream spectrum is plotted in Figure 4.41(a) with quantization noise only and in Figure 4.41(b) with quantization noise and electronic noise. Comparing with Figure 4.19(a) and Figure 4.19(b), respectively, the CT implementation has nearly the same performance as the DT implementation.

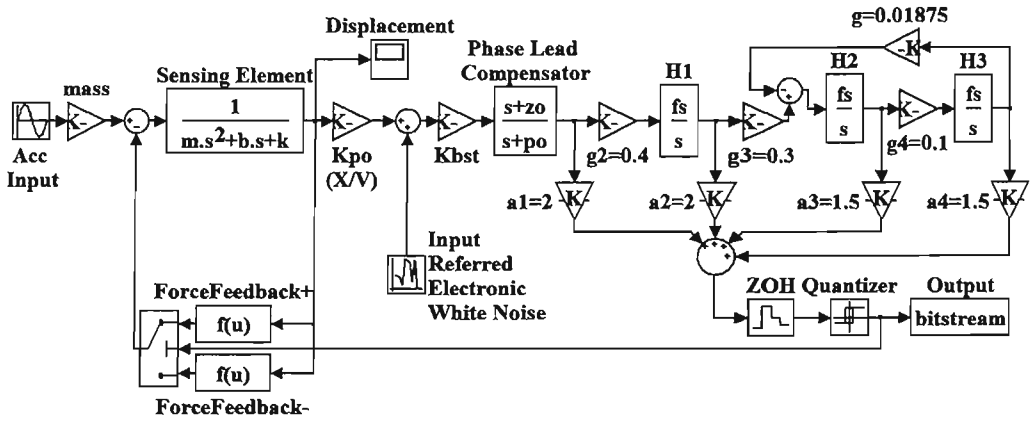

FIGURE 4.40: Continuous-time implementation of the FFLR ΣΔM shown in Figure 4.12.

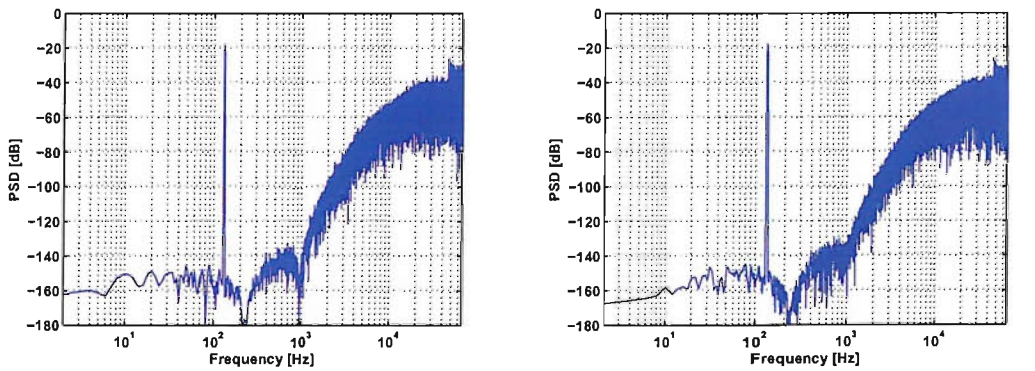

(a) With quantization noise only.

(b) With quantization noise and electronic noise.

FIGURE 4.41: Output bitstream spectrum of the the FFLR ΣΔM shown in Figure 4.40.

Analogously, Figure 4.20 is mapped into a CT implementation of the MFLR topology as shown in Figure 4.42. The two implementation share same gain coefficients. With same simulation conditions (except the loop delay $T_{fb1} = 0.3T_s$ and feedback duration $T_{fb} = 0.7T_s$ for the CT implementation), output bitstream spectrum is plotted in Figure 4.43(a) with quantization noise only and in Figure 4.43(b) with quantization noise and electronic noise.

Comparing with Figure 4.24(a) and Figure 4.24(b), respectively, the CT implementation has nearly the same performance as the DT implementation.

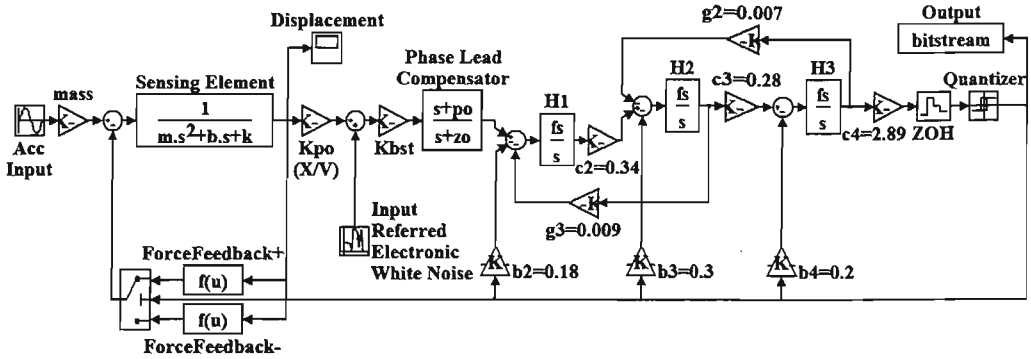

FIGURE 4.42: Continuous-time implementation of the MFLR ΣΔM shown in Figure 4.20.

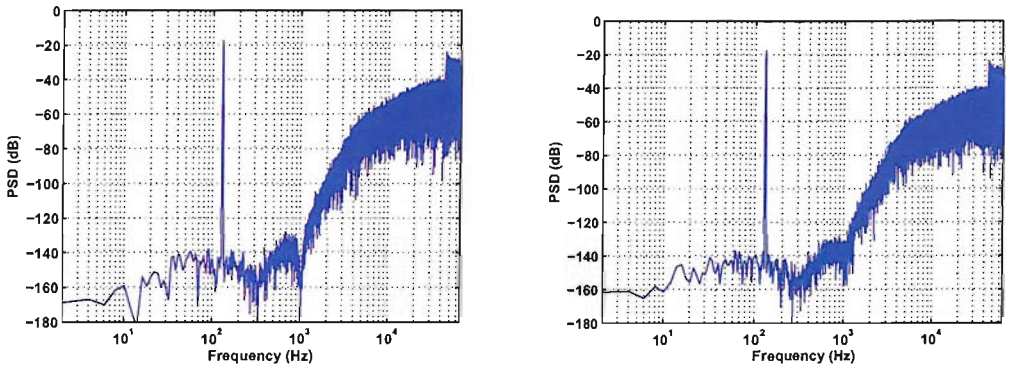

(a) With quantization noise only.

(b) With quantization noise and electronic noise.

FIGURE 4.43: Output bitstream spectrum of the MFLR ΣΔM shown in Figure 4.42.

These simulation results indicate that a CT high-order electromechanical ΣΔM can get a similar performance as that of a DT high-order electromechanical ΣΔM using the same topology and gain coefficients. The extra loop delay is not a significant problem for the control system using a high-order ΣΔM if the sampling frequency is relatively low (usually between 100kHz-500kHz). However, the most attractive property of a CT ΣΔM is that it provides an inherent anti-aliasing filter on the signal path [90].

4.9 Circuit Non-Idealities

For switched-capacitor (SC) ΣΔM, the dominant non-idealities, such as sampling jitter, K_BT/C noise and operational amplifier parameters (white noise, finite dc gain, finite bandwidth, slew rate and saturation voltages), must be taken into account to give overall performance prediction and evaluation. Fortunately, there is a free software toolbox *SDTool* developed by P. Malcovati [67] to simulate all the non-idealities in SC ΣΔM. Figure 4.44 shows the model including the non-idealities: clock jitter, switched thermal noise, op-amp

noise, op-amp finite gain, op-amp bandwidth, op-amp slew rate and op-amp saturation voltages.

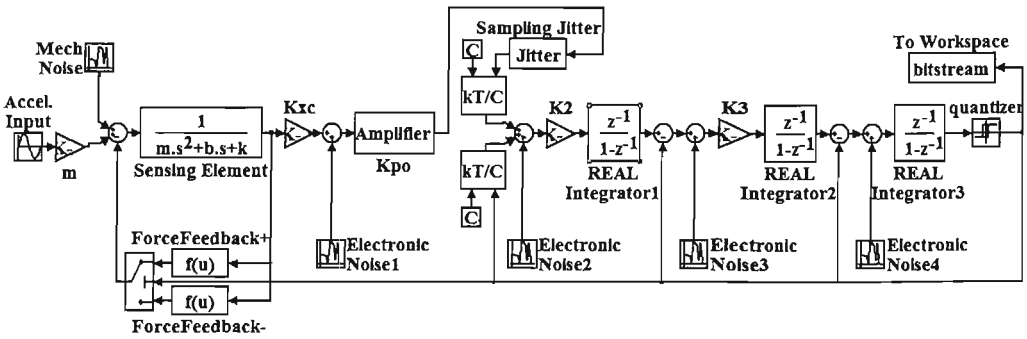

FIGURE 4.44: A fifth-order electromechanical SC ΣΔM model to analyze the effects of non-idealities of circuits.

All these non-idealities are well defined in [56]. The simulation conditions are shown in Table 4.2. These parameters are typically used by a fifth-order ΣΔM to achieve a SNR of about 120dB. This is also the target value for the micromachined sensor, which will be discussed in Chapter 8. The performance of the loop is summarized in Table 4.3 with the conditions of Table 4.2.

Parameters	Value
Signal Bandwidth (SBW)	1024 *Hz*
Sampling Frequency F_s	524288 *Hz*
Oversampling Ratio (OSR)	256
Number of Samples Considered	65536

TABLE 4.2: Simulation conditions of the system shown in Figure 4.44.

Non idealities	SNDR (dB)
Ideal Modulator	143.5
Sampling Jitter (10*ns*)	143
(K_BT/C) *Noise* ($C_s = 5pF$)	126
Input Referred Opamp Noise ($V_n = 10nV/\sqrt{Hz}$)	129
Finite dc Gain ($H_0 = 1000$)	142.6
Finite Bandwidth ($GBW = 10MHz$)	136.9
Slew Rate ($SR = 2V/\mu s$)	140
Saturation Voltages ($V_{max} = \pm 1.1V$)	138

TABLE 4.3: Simulation results of the system shown in Figure 4.44.

It can be seen from the Table 4.3 that switched thermal noise and op-amp noise are the most critical parameters. With modern CMOS technology, for circuits with the sampling frequency below 1MHz, sufficient op-amp bandwidth and slew rate are easily achievable. Figure 4.45(a) and Figure 4.45(b) show the effects of op-amp bandwidth and slew rate, respectively. All non-idealities are included, the SNR (120dB) performance degrades 23.5dB compared with an ideal loop without circuit non-idealities (SNR=143.5dB).

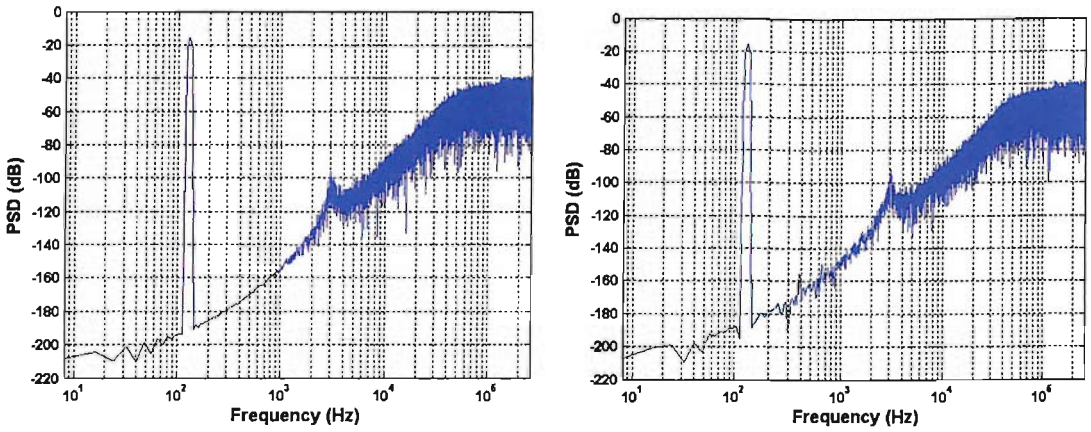

(a) (b)

FIGURE 4.45: Influence of circuit non-idealities on the performance of a high-order electromechanical ΣΔM: (a) with GBW=10MHz; (b) with slew rate=0.8V/us.

In circuit implementation, the loop coefficients obtained by the methodology may not guarantee that the integrators outputs are limited to the maximum signal swing permitted by the circuit realizing the integrators. Coefficient scaling techniques [91] are introduced to scale the integrators output swings, but coefficient scaling must preserve the initial QNTF of a ΣΔM to ensure loop stability. Coefficient scaling methods also may reduce the chip power consumption, but that is different from the power saving from the benefit using different loop topologies (such as FFLR and MFLR) [30].

4.10 Summary

In this chapter, three topologies of fifth-order single loop ΣΔMs for a micromachined accelerometer are presented and discussed in detail. The topologies are adopted from ΣΔ A/D converters. The design methodology utilizes optimization with stability constraints to find the optimum loop coefficients. The design flow starts with a second-order stable electromechanical ΣΔM and a high-order stable electronic ΣΔM. Local resonators are created in the QNTF to further suppress the quantization noise in the signal band. Compared with feedback topologies, the feed-forward topologies are suitable for low-voltage, low-power applications due to their integrator outputs having a relatively low amplitude swing. Noise components at the different stages in the high-order electromechanical ΣΔM have been analyzed and compared with a second-order loop. Due to the large signal gain supplied by additional integrators in the high-order loop, the interaction between electronic and quantization noise is weaker than in a second-order loop. This makes the quantization noise no longer the dominant noise in a high-order electromechanical ΣΔM. Both the electronic noise and quantization noise exhibit more favorable noise shaping characteristic in the signal band in a high-order electromechanical ΣΔM. The electronic noise potentially can be reduced in a high-order loop by optimizing the ΣΔM topology further. However,

an electromechanical ΣΔM of any order can neither reduce nor shape mechanical noise, which can only be lowered by optimization of the mechanical structure and vacuum packaging. Furthermore, the mechanical quality factor has a strong impact on noise shaping. In high-order loops, the dead-zone and tonal behaviour are also considerably suppressed. The electrostatic force feedback delay reduces the output magnitude, which is dependent on the ratio of the delay to sampling clock cycle, but it does not greatly affect the loop stability due to the relatively low sampling frequency when using a high-order ΣΔM. To investigate the stability of the high-order loops, the root locus, Bode diagram and Nyquist plots can be used to find the conditional stability margins (the minimum gain of quantizer). However, so far, the most reliable method to predict the stability margin is system level simulation.

Chapter 5

Force Feedback Linearization

The major advantage of a one-bit DAC in a continuous-time ΣΔM ADC is its linearity, however, this is not true for an electromechanical one-bit ΣΔM. In most analysis of closed-loop micromachined capacitive sensors, the residual motion x of the sensing element proof mass is neglected as it is far smaller than the nominal gap d_0, and thus the resulting nonlinear effect is not considered. This is not a valid assumption for high performance sensors. This chapter analyzes the nonlinearities arising from the conversions between the mechanical and electrical domains in the feedback loop and the forward path. A linearization strategy is put forward to reduce the nonlinearity from electrostatic force feedback on the proof mass to improve the signal-to-noise-and-distortion ratio (SNDR). This linearization strategy is only useful for very high performance inertial sensors not for most state-of-the-art relatively low performance sensors.

5.1 Nonlinear Electrostatic Feedback Force

A modified diagram of a high-order electromechanical ΣΔM is shown in Figure 5.1. $M(s)$ represents the transfer function of the mechanical sensing element that converts the input inertial force signal into a displacement and inherently serves as a second-order low pass filter. V_{fb} represents the feedback voltage, and D_0 the quantizer output, which is either a positive or negative reference voltage (V_{ref}, normalized to 1V). E_{BN} is the intrinsic noise due to Brownian motion. K_{po} is the gain of the pickoff interface that converts the displacement to a voltage. E_{EN} is the input-referred electronic noise of the pickoff interface. $C_p(s)$ is a lead compensator to supply the necessary phase margin to ensure stability of the closed-loop system. $H(s)$ is the electronic filter to boost the noise shaping. The one-bit quantizer is modeled as a variable gain K_q with additive quantization white noise E_{QN}. There are two one-bit DACs in the feedback loop. DAC_E is the conventional electronic DAC within the electronic filter with an error source E_{DAC1}, while DAC_M is the electromechanical DAC, which converts the voltage to an electrostatic feedback force with an error source E_{DAC2}.

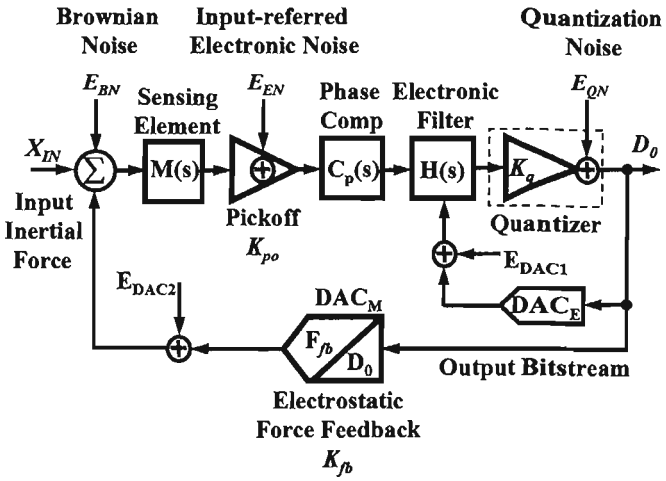

FIGURE 5.1: Generic block diagram of a high-order electromechanical ΣΔM for non-linearity analysis.

Referring to Figure 5.1, the transfer function of the system is given by:

$$\begin{aligned} D_0(s) =& \frac{M(s)K_{po}C_p(s)H(s)K_q}{1+L(s)}(X_{IN}+E_{BN}-E_{DAC2}) \\ &+\frac{H(s)K_q}{1+L(s)}(E_{EN}C_p(s)+E_{DAC1})+\frac{1}{1+L(s)}E_{QN} \end{aligned}$$

or,

$$\begin{aligned} D_0(s) =& STF(s)(X_{IN}+E_{BN}-E_{DAC2})+ \\ &+ ENTF(s)(E_{EN}C(s)+E_{DAC1})+QNTF(s)E_{QN} \end{aligned} \tag{5.1}$$

where $L(s) = K_{fb}M(s)K_{po}C_p(s)H(s)K_q$ is the open-loop filter; and $M(s)$ is the transfer function of sensing element. STF(s), ENTF(s) and QNTF(s) are the signal, electronic noise and quantization noise transfer functions, respectively, and given by:

$$STF(s) = \frac{M(s)K_{po}C_p(s)H(s)K_q}{1+L(s)}$$

$$ENTF(s) = \frac{H(s)K_q}{1+L(s)} \tag{5.2}$$

$$QNTF(s) = \frac{1}{1+L(s)}$$

For an over-sampling system, the signal band is at relatively low frequency, thus Equation 5.1 can be approximated by:

$$D_0(s) = \frac{1}{K_{fb}}(X_{IN} + E_{BN} - E_{DAC2}) + \frac{1}{K_{fb}M(s)K_{po}}(E_{EN}C_p(s) + E_{DAC1}) + \frac{1}{K_{fb}M(s)K_{po}H(s)K_q}E_{QN} \tag{5.3}$$

It can be seen from Equation 5.3 that the electromechanical ΣΔM can shape the quantization noise E_{QN} considerably, depending on the over-sampling frequency and the order of the loop filter. The noise sources E_{EN} and E_{DAC1} are also shaped. However, the Brownian noise E_{BN} and the electromechanical DAC error E_{DAC2} will not be shaped by the ΣΔM and thus add directly to the input of the sensor system. Therefore the electromechanical DAC error $E_{DAC2}$is critical for the sensor system performance. The Brownian noise can be reduced only by mechanical structure optimization and packaging, and thus is not considered in the following analysis. A conventional electrostatic force feedback arrangement of an electromechanical ΣΔM is shown in Figure 5.2.

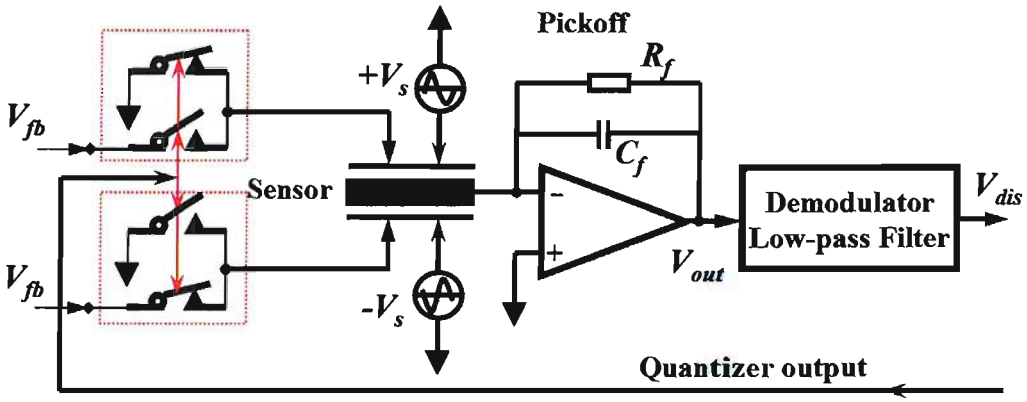

FIGURE 5.2: Common electrode arrangement of the force feedback path in an electromechanical ΣΔM.

For an ideal one-bit electronic DAC, there exists no DAC error due to its inherent linearity, but the conversion of a voltage to an electrostatic feedback force on the proof mass by the DAC_M is nonlinear, as it depends on the residual proof mass motion. Equation 4.1 can be rewritten to:

$$K_{fb} = \mathrm{sgn}(D_0)\frac{K_0}{[1 + \mathrm{sgn}(D_0)(x/d_0)]^2} = \mathrm{sgn}(D_0)K_0[1 - \mathrm{sgn}(D_0)2(\frac{x}{d_0})^1 + 3(\frac{x}{d_0})^2 - 4\mathrm{sgn}(D_0)(\frac{x}{d_0})^3 + ...] \tag{5.4}$$

where $K_0 = \varepsilon_0 A_{fb} V_{fb}^2 / 2d_0^2$ denotes the gain of the electrostatic feedback force without considering the residual proof mass motion. ε_0 is the dielectric constant and A_{fb} the area of the feedback electrodes. The Taylor expansion of Equation 5.4 indicates that the feedback force has higher harmonic content relating to the residual motion x. Therefore, the harmonic distortion will lead to a reduction in the SNDR. To investigate the effects of the nonlinear feedback on electromechanical ΣΔMs, a system level simulation was carried out for a fifth-order electromechanical ΣΔM as shown in Figure 5.3 using Matlab/Simulink.

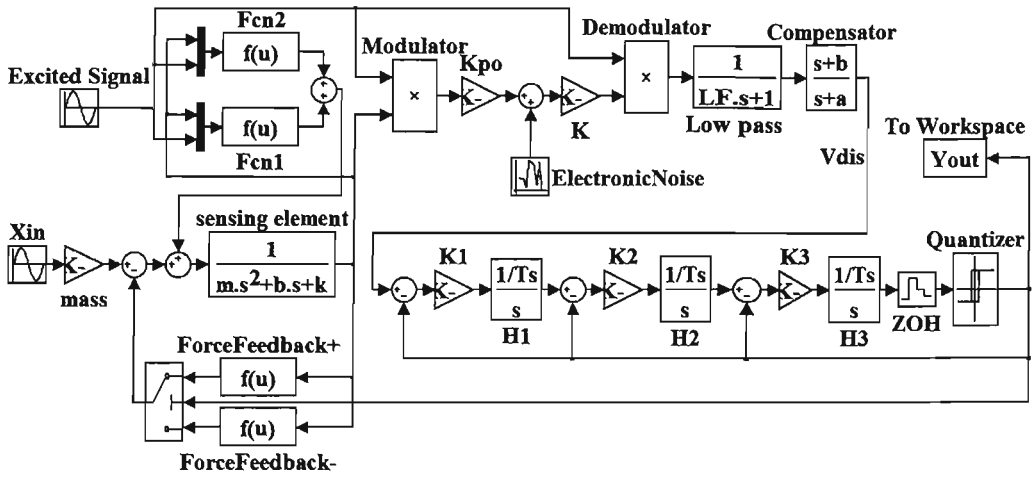

FIGURE 5.3: Systematic level model of a fifth-order electromechanical ΣΔM.

Simulations use a sampling frequency f_s=125kHz and take into account the electronic thermal noise from the pickoff interface assuming a PSD of $10\text{nV}/\sqrt{Hz}$ for the amplifier. The spectrum of the output bitstream D_0 is plotted in Figure 5.4. Obviously, there is a third harmonic distortion peak at three times of the input signal frequency (assumed to be 96Hz) which causes the SNDR to drop by about 20dB in a 300Hz signal bandwidth.

To derive an equation for the signal harmonics all noise sources in Equation 5.1 are omitted. Due to the time-averaging characteristic of the electromechanical ΣΔM output bitstream, the time is virtually identical for the top and bottom electrodes to be energized, thus even harmonics are cancelled. Neglecting the even term of the Taylor expansion of Equation 5.4, the system output can be approximated to:

$$K_{fb} \approx \text{sgn}(D_0) K_0 [1 + 3(\frac{x}{d_0})^2] \tag{5.5}$$

Equation 5.5 denotes that the DAC_M is expected to suffer from third harmonic distortion due to the residual proof mass motion. The amplitude difference Δ between the output signal at the input force signal frequency and the third harmonic can be calculated by $\Delta = 20\log[3(x/d_0)^2]$ (dB). If the proof mass motion x is assumed to be very small and its effect is neglected, the feedback force has a rectangular waveform with amplitude of $|K_0|$

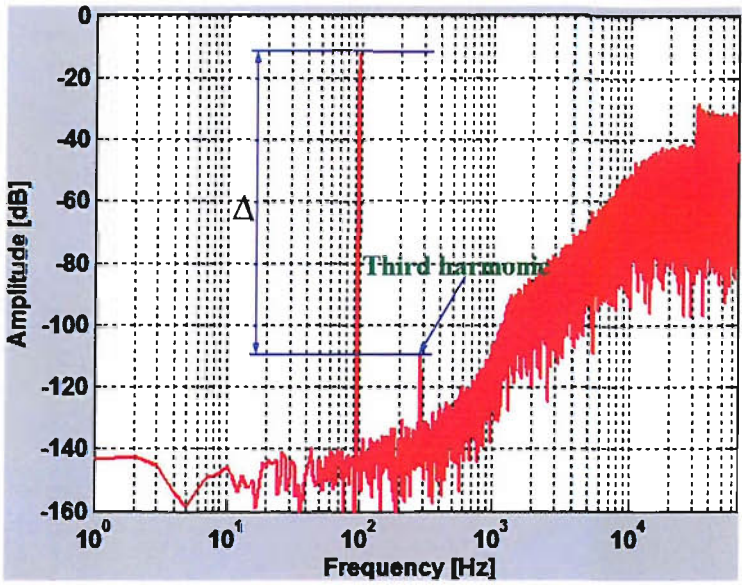

FIGURE 5.4: Output spectrum of a fifth-order electromechanical ΣΔM with a conventional force feedback DAC.

(assuming V_{ref}=1V). However, if the nonlinear feedback effect is considered, the feedback force becomes nonlinear; this is shown in Figure 5.5.

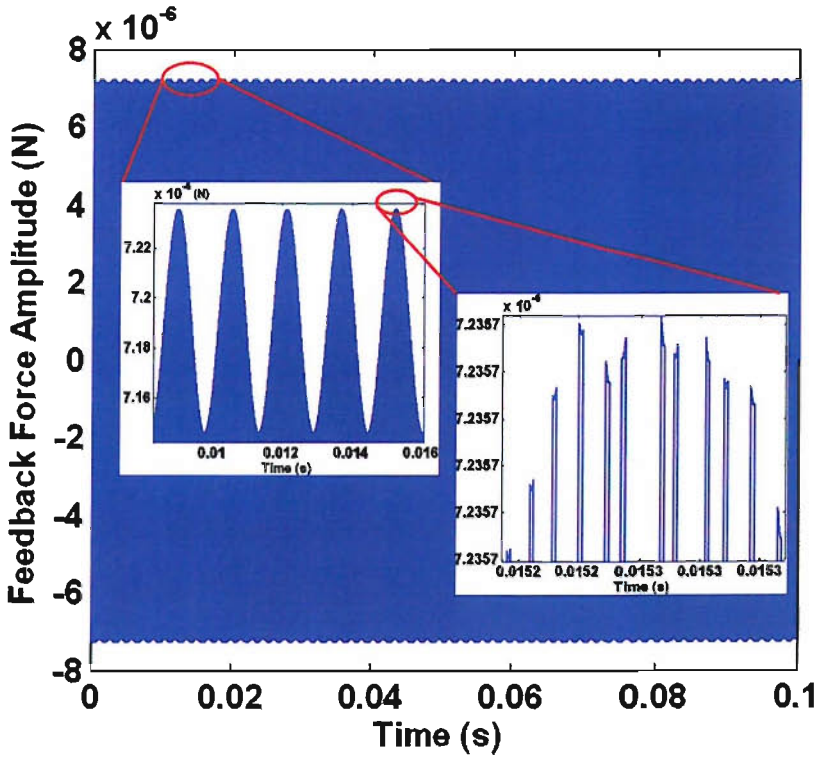

FIGURE 5.5: Variation of the feedback force magnitude due to residual proof mass motion.

The superimposed sinusoidal ripple on the upper and lower waveform edges in Figure 5.5 has the same frequency as the input signal and its amplitude is given by $2(x/d_0)K_0$ according

to Equation 5.4. The amplitude of the third harmonic is given by $(x/d_0)^2 K_0$. Assuming a 50% full scale input signal, the maximum residual proof mass motion x is 0.016μm for a nominal gap of d_0=3μm; this is shown in Figure 5.6.

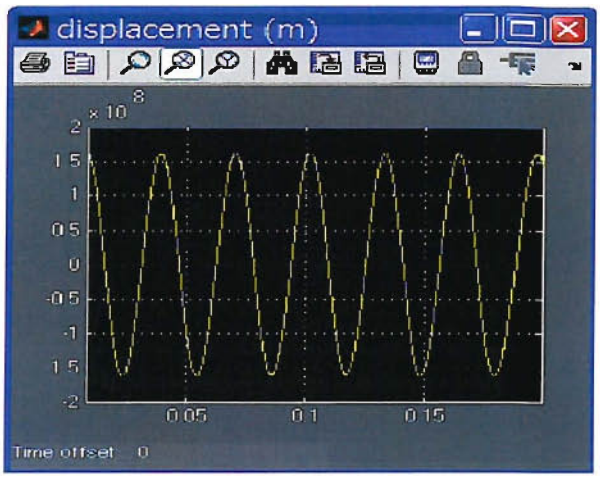

FIGURE 5.6: Residual proof mass displacement.

The SNDR is calculated to be about 82dB with the parameters used for the simulations. For high performance sensing elements with a lower spring constant the residual motion can be considerably higher, thus the maximum achievable SNDR without electrostatic force feedback linearization is even lower.

5.2 Feedback Electrostatic Force Linearization

5.2.1 Linearized Voltage to Force Conversion in Feedback Loop

To circumvent the nonlinear effect due to the proof motion motion, it is necessary to linearize the conversion from voltage to electrostatic force. The feedback voltage is modified to be a function of the residual proof mass motion and is given by:

$$V_{fb}^{*} = V_{fb} + \mathrm{sgn}(D_0) \cdot \ell \tag{5.6}$$

where $\ell = (x/d_0)V_{fb}$ is the linearization factor. The feedback conversion of Equation 5.4 thus becomes:

$$K_{fb}^{*} = \mathrm{sgn}(D_0)\frac{\varepsilon_0 A_{fb}(V_{fb} + \mathrm{sgn}(D_0) \cdot \ell)^2}{2(d_0 + \mathrm{sgn}(D_0) \cdot x)^2} = \mathrm{sgn}(D_0)K_0 \tag{5.7}$$

It should be noted that the force magnitude in Equation 5.7 is independent of the residual proof mass motion x and is equivalent to K_0 in Equation 5.4. The modified feedback arrangement of the electromechanical ΣΔM is shown in Figure 5.7. The additional building blocks consist of an amplifier, an adder and a subtractor.

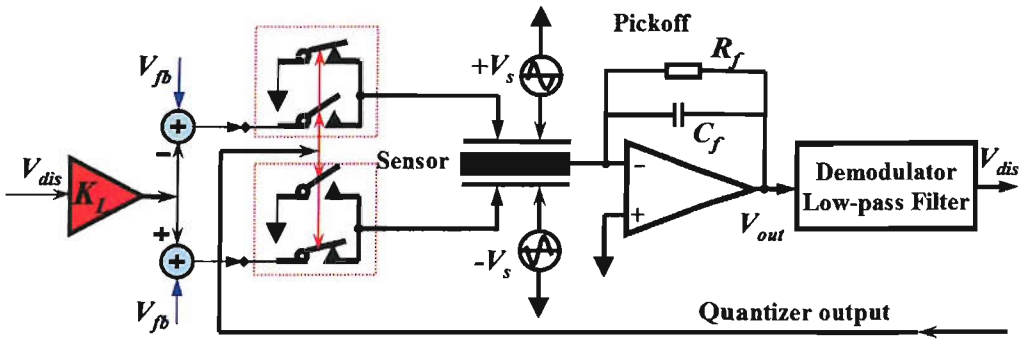

FIGURE 5.7: Modified electrostatic force feedback arrangement of the electromechanical ΣΔM.

Using this force feedback linearization scheme, a simulation was carried out with the system model as shown in Figure 5.3. The spectrum of the output bitstream is shown in Figure 5.8, which has no the third harmonic distortion peak. The SNDR improves about 20dB due to the feedback force linearization.

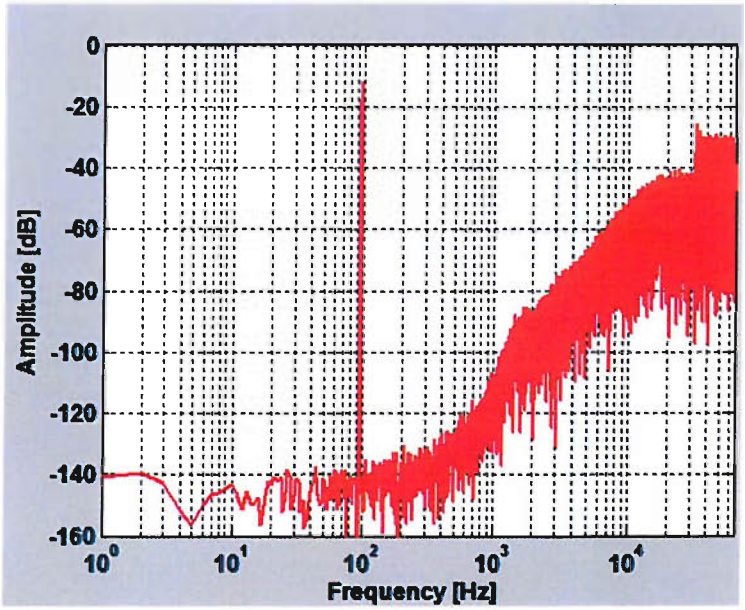

FIGURE 5.8: Output spectrum of a fifth-order electromechanical ΣΔM with a linear feedback force DAC.

Typically, the pickoff interface is implemented with a charge amplifier as shown in Figure 3.1 and its output is given by Equation 3.5. Assuming the gain from the amplifier output V_{out}

to the output V_{dis} of lowpass filter is unity, or

$$V_{dis} = V_{out} = -(x/d_0) \times V_s \tag{5.8}$$

The linearization factor introduced in the previous section can be re-expressed as:

$$\ell = (x/d_0)V_{fb} = V_{dis} \times (-V_{fb}/V_s) = V_{dis} \times K_L \tag{5.9}$$

$$K_{\mathrm{L}} = -V_{fb}/V_s \tag{5.10}$$

K_L is the gain of the linearization amplifier in the modified feedback arrangement shown in Figure 5.7.

5.2.2 Nonlinear Displacement to Voltage Conversion in Forward Path

For high performance sensors, the nonlinear conversion from the sensor motion to voltage of the pickoff interface should be considered. Considering the effect of the residual motion on the transfer function of the pickoff circuit, its output voltage is changed from Equation 3.5 to:

$$V_{dis} \approx -(x/d_0) \times V_s \times [1 - (x/d_0)^2]^{-1} \tag{5.11}$$

Combining Equation 5.6 and Equation 5.11, the electrostatic feedback force conversion factor can be rewritten as:

$$K_{fb}^{**} = \mathrm{sgn}(D_0)K_0 \times \left\{ \frac{d_0 + \mathrm{sgn}(D_0)x[1 - (x/d_0)^2]^{-1}}{d_0 + \mathrm{sgn}(D_0)x} \right\}^2 \tag{5.12}$$

Equation 5.12 indicates the electrostatic force is still a function of the residual motion due to the nonlinear pickoff circuit in the forward path. The feedback force for the three discussed cases (Equation 5.4, Equation 5.7 and Equation 5.12) are plotted in Figure 5.9 with d_0=3μm. The ideal feedback force (Equation 5.7, middle, red line) has a constant absolute magnitude; this is normalized to unity. Consequently, deviations from unity is a measure of the nonlinearity in the feedback path. Without force feedback loop linearization

(Equation 5.4, lower, blue line) a significant harmonic distortion is expected for a residual proof mass deflection x larger than 0.01μm, or 0.33% of the nominal gap. With the proposed linearization (Equation 5.12, upper, green line) noticeable harmonic distortion is only expected for x larger than 0.3μm, or 10% of the nominal gap. For a closed-loop, the proof mass deflection is usually smaller than this. Figure 5.10 shows a simulation result considering the nonlinearity of the pickoff preamplifier in the forward path. It can be seen that the effect of the third harmonic distortion is still visible but considerably reduced.

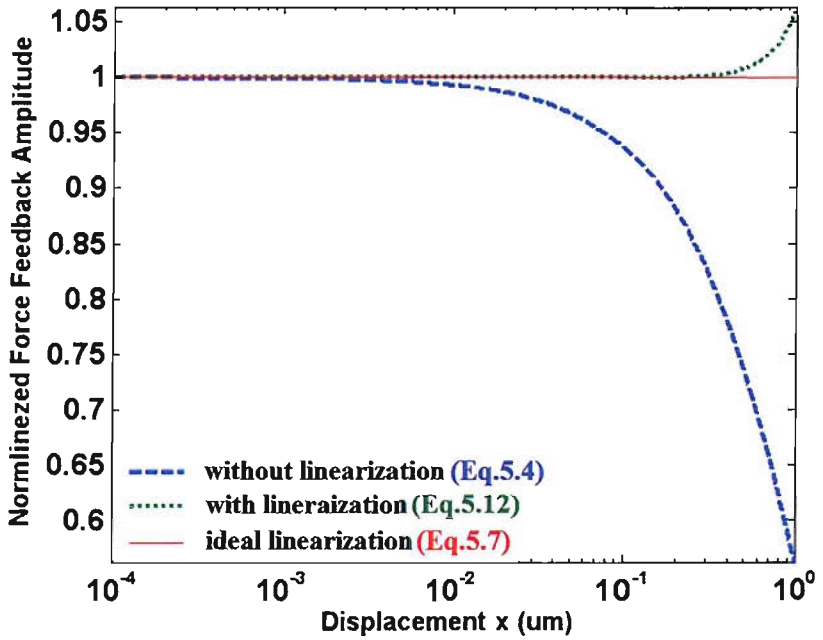

FIGURE 5.9: Feedback nonlinearity on the electromechanical DAC waveform with different feedback loop linearization.

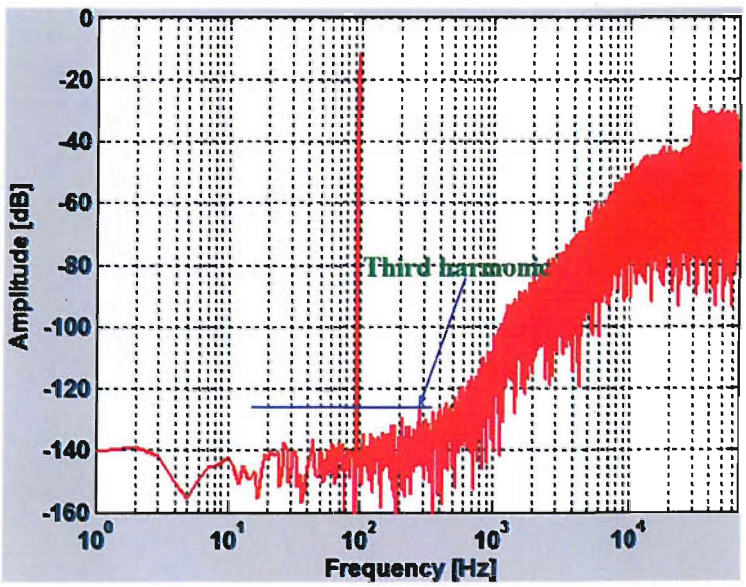

FIGURE 5.10: ΣΔM spectrum of the output bitstream with a linear feedback DAC and considering the nonlinearity of the pickoff interface.

5.3 Summary

In this chapter, the nonlinearity generated by the electromechanical DAC in the feedback loop and the conversion from displacement to voltage in the forward path has been analyzed. An effective linearization scheme is proposed to increase the SNDR. The nonlinearity of the forward path is considerably less significant than that of the feedback loop. The force feedback linearization will be useful for both high performance sensors and very sensitive sensing elements (thus very large displacement of proof mass) in closed-loop operation using a $\Sigma\Delta$M.

Chapter 6

High-Order Bandpass ΣΔM for Vibratory Gyroscopes

6.1 Introduction

As discussed in Chapter 4, the control systems based on a lowpass ΣΔM can not only be applied to micromachined accelerometers, but also to vibratory gyroscopes. The state-of-the-art control system [54] for a vibratory gyroscope is based on a second-order lowpass electromechanical ΣΔM, which has a similar topology as the second-order control system for a micromachined accelerometer as discussed previously.

Usually the sensing element of a vibratory gyroscope is designed with a high quality factor Q to increase the sensitivity, hence can be treated as a mechanical resonator. Furthermore, the output characteristic of vibratory rate gyroscopes is narrow-band amplitude-modulated signal. Therefore, a bandpass ΣΔM is a more appropriate control strategy for a vibratory gyroscope than a lowpass ΣΔM. The design methodology described in Chapter 4 can be applied to vibratory gyroscopes, combined with the mature design techniques of electronic bandpass ΣΔ A/D converters.

The control system using a high-order ΣΔM, as proposed in Chapter 4, can provide much better noise shaping than when using a second-order ΣΔM where the sensing element only constitutes the loop filter in the forward path. The only high-order ΣΔM interface for a gyroscope was recently described by [12] where the sensing element is cascaded by two electronic integrators to form a forth-order loop. However, this is a lowpass ΣΔM and therefore requires a relatively high sampling frequency, which put demanding requirements on the hardware implementation of the interface circuits. A lowpass ΣΔM potentially suffers from $1/f$ noise, dc offset and drift if used without effective circuit cancellation techniques. Some high-order ΣΔM loop topologies have favorable noise shaping characteristics for electronic noise originating from the pickoff circuit. Therefore, the requirements for the electronic circuits can be considerably relaxed.

As a general guideline for the design of electromechanical ΣΔM, it is desirable to implement a control loop with quantization noise level lower than mechanical (Brownian) noise, and electronic noise. Based on a linearized model for the quantizer [28], the signal transfer function (STF), quantization noise transfer function (QNTF), and electronic noise transfer function (ENTF) will be compared between a lowpass fifth-order ΣΔM control loop and two distinct topologies of bandpass ΣΔM control loops. Additionally, extensive system level simulations in Simulink/Matlab are used to investigate their noise shaping abilities.

6.2 System Level Model of A Vibratory Gyroscope

As the sensing element, a typical surface micromachined gyroscope [54] packaged at ambient atmospheric pressure is assumed for simulations (mass, m=2μgram, quality factor, Q=100 and nominal resonant frequency, f_x=2^{14}Hz ($\approx$ 16kHz) for drive mode). $\pm$5% mismatch between the resonance frequencies in two orthogonal directions (drive (x) and sense (y)) is assumed due to fabrication tolerances ($f_y = f_x(1 \pm 5\%)$). The full scale input angular rate is taken to be sinusoidal with an amplitude of $100^o/s$ at f_{in}=128Hz. The continuous-time transfer function of the sensing element in the sense direction is given by:

$$M_m(s) = \frac{1/m}{s^2 + \frac{\omega_y}{Q_y}s + \omega_y^2} \tag{6.1}$$

where ω_y is the resonant frequency, m the mass of the sensing element and Q_y the quality factor of the sense mode. The following analysis uses its equivalent discrete-time transfer function in the z-domain, which can be obtained using an impulse-invariant transformation [54] and already given by Equation 4.30.

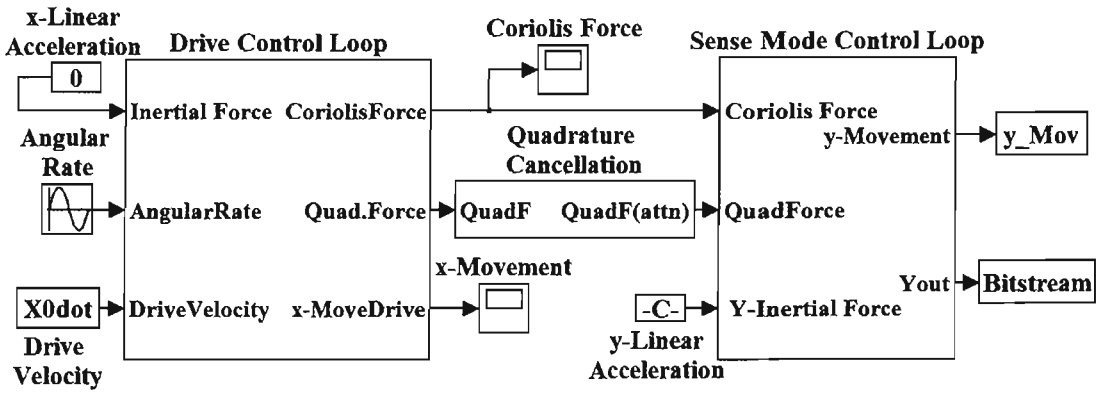

FIGURE 6.1: Vibratory gyroscope diagram consisting drive mode control loop and sense mode control loop.

Figure 6.1 shows a block diagram of a closed-loop vibratory gyroscope, which consists of the drive mode and sense mode control loops. The drive mode control loop is shown in

Figure 6.2, and its main function is to precisely control the drive oscillation at constant frequency (ω_x) and constant amplitude(X_o). The ΣΔM feedback control strategy is not applied to the drive mode, which is usually controlled by phase-locked loops (PLL) [92]. The motion of the vibrating proof mass is described by $x = X_0 \sin(\omega_x t)$. If the sensor is rotated around the z-axis with an angular rate Ω_z, the Coriolis force resulting along the y direction on the proof mass can be given by Equation 2.17. The y-movement in the sense mode control loop generated by the amplitude-modulated Coriolis force is shown in Figure 6.3. The figure is a typical displacement along y-axis in the high-order bandpass ΣΔMs, which will be discussed in the following sections. From Equation 2.26 it can be inferred that the drive frequency ω_x, drive amplitude X_0, proof mass m and quality factor Q_y should be as large as possible.

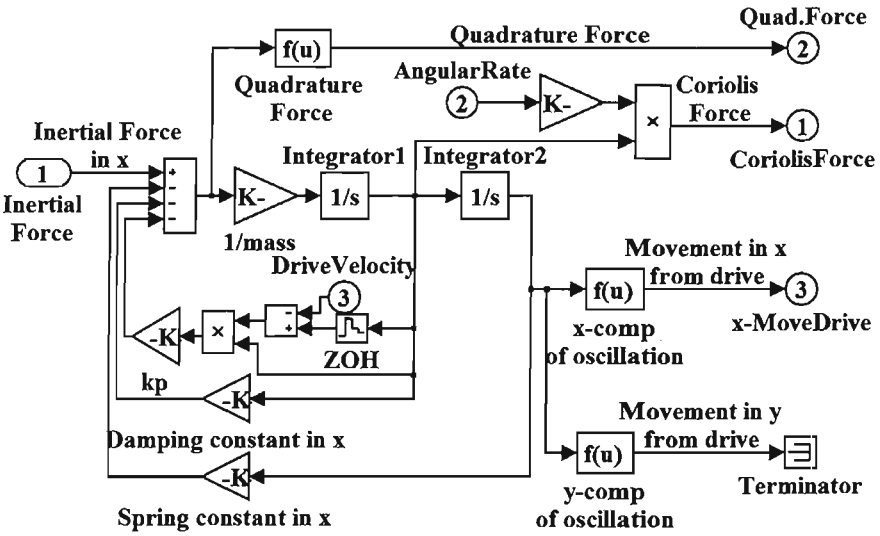

FIGURE 6.2: Drive mode control loop block of Figure 6.1.

Fabrication tolerances can have a considerable impact on the performance of micromachined gyroscopes [93], therefore a quadrature force caused by a misalignment of the sense and drive mode, is also included in the model. The following discussion focuses on the sense mode control system using an electromechanical ΣΔM. There are several possible choices for the sense loop: a) it can be either a low pass or a bandpass ΣΔM, and b) it can be either a second-order (sensing element only as loop filter) or a high-order ΣΔM. Any combination of these choices is also possible. In the case of a high-order, lowpass ΣΔM, the sensing element is cascaded by electronic integrators, whereas in the case of a high-order bandpass ΣΔM the sensing element is cascaded with electronic resonators. Table 6.1 lists the parameters of the micromachined gyroscope used for the simulation throughout this work.

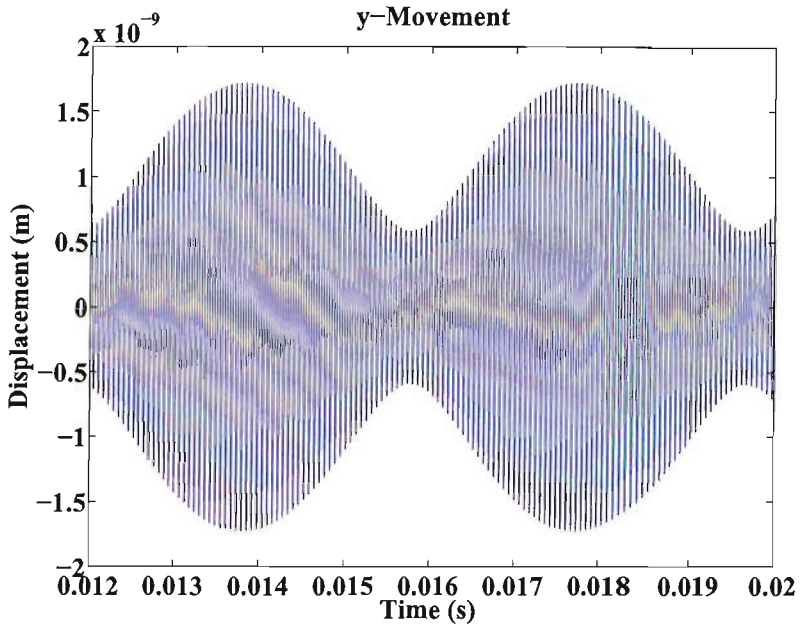

FIGURE 6.3: Y-displacement of the gyroscope in the sense mode control system.

Variable	Value	Unit	Explanations
ε_0	8.85×10^{-12}	F/m	*permittivity constant*
m	2×10^{-9}	kg	*proof mass*
f_s	$2^{16}(BP)$, $2^{23}(LP)$	Hz	*oversampling frequency*
f_{in}	2^7	Hz	*input signal frequency*
Ω_Z	100	deg/sec	*maximum input angular velocity*
f_x	2^{14}	Hz	*X direction drive frequency;* f_x=$f_s/4$
γ	$\pm 5\%$		*resonate frequency mismatch between X and Y*
ω_x	$2\pi f_x$	rad/s	*resonant frequency in X (drive) direction*
ω_y	$2\pi f_x(1+\gamma)$	rad/s	*resonant frequency in Y (drive) direction*
Q_x	100		*quality factor of the drive mode*
Q_y	100		*quality factor of the sense mode*
X_0	2×10^{-6}	m	*amplitude of drive oscillation*
$\dot{X}_0$	$\omega_x \times X_0$	m/s	*velocity of drive oscillation*
Y_{Gap}	1×10^{-6}	m	*gap between sensing capacitors*
K_x	21	N/m	*effective spring constant in X-direction*
K_y	25	N/m	*effective spring constant in Y-direction*
D_x	2.06×10^{-6}	Ns/m	*damping factor in X-direction*
D_y	2.27×10^{-6}	Ns/m	*damping factor in Y-direction*
V_{step}	5	V	*voltage step for signal pickoff*
K_{fb}	3.15×10^{-9}		*gain of the voltage to force conversion in the feedback*
θ	0.001	deg	*misalignment between drive and sense mode*

TABLE 6.1: Parameters of the gyroscope used for simulations

6.3 High-Order Lowpass ΣΔM Vibratory Gyroscopes

A fifth-order lowpass ΣΔM with multi-feedback and two local resonators [83] is investigated as a closed-loop control system for the sense mode of a vibratory gyroscope. The design is shown in Figure 6.4 as a Simulink model. It contains the sensing element $M_m(z)$ in discrete format, a lead phase compensator (transfer function $C_p(z) = (1 - 0.9z^{-1})$ after the pickoff interface (gain K_{po}) and three additional electronic integrators. K_{bst} is the gain of an additional boost amplifier. $H_1(z)$, $H_2(z)$ and $H_3(z)$ are integrators with a transfer function of $H_i(z) = (z^{-1}/1 - z^{-1})$ (i=1, 2, 3). a_1, a_2 and a_3 are gain coefficients used for integrator output scaling. The two local resonators are formed by gain constants g_1 and g_2, which create a notch in the signal band to further suppress the quantization noise. All values of the gain constants are given in the figure. The topology is derived by applying a design methodology based on optimization and stability criteria which is described in more detail in Chapter 4.

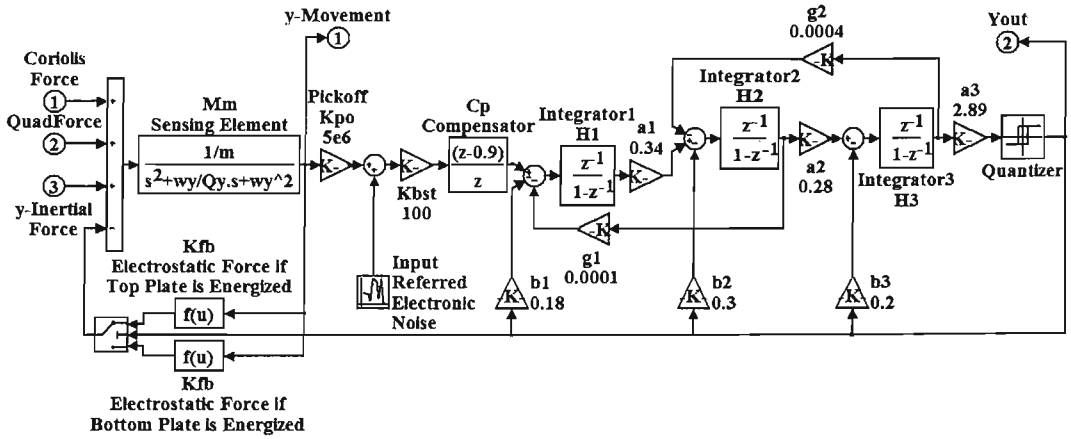

FIGURE 6.4: Sense mode control loop based on a fifth-order lowpass multi-feedback ΣΔM and local resonators.

In most devices, the electronic noise from the interface circuits is the dominant noise source, therefore an input-referred electronic white noise source with a typical value for the power spectral density (PSD) of $6\text{nV}/\sqrt{Hz}$ is placed at the input of the pickoff preamplifier. K_{fb} is the gain defined by the voltage to electrostatic force conversion on the proof mass in the feedback path and given by Equation 4.1.

An oversampling ratio (OSR(= $f_{s1}/2f_y$)) of 256 is chosen as a typical value; this results in a sampling frequency $f_{s1} = 2^{23}$Hz ($\approx$ 8MHz).

The transfer functions STF, ENTF, and QNTF are given by [70]:

$$STF_1(z) = \frac{m\kappa_m(z)\prod_{i=1}^{3} H_i(z)a_i}{L(z) \times K_{fb}} \tag{6.2}$$

$$ENTF_1(z) = \frac{\kappa_m(z) \prod_{i=1}^{3} H_i(z) a_i}{L(z) \times (K_{fb} M_m(z) K_{po})} \tag{6.3}$$

$$QNTF_1(z) = \frac{1 + H_1(z) a_1 H_2(z) g_1 + H_2(z) a_2 H_3(z) g_2}{L(z)} \tag{6.4}$$

where $\kappa_m(z) = K_{fb} M_m(z) K_{po} K_{bst} C_p(z) K_q$ is an effective transfer function comprising the force feedback conversion, sensing element, pickoff preamplifier gain and the compensator; and

$$L(z) = 1 + \kappa_m(z) \prod_{i=1}^{3} H_i(z) a_i + K_q \sum_{i=1}^{3} b_i \prod_{j=i}^{3} H_j(z) a_j + \sum_{i=1}^{2} a_i g_i \prod_{j=i}^{i+1} H_j(z) + H_1(z) a_1 H_2(z) g_1 a_3 H_3(z) b_3 K_q$$

The bode diagram of the transfer functions (STF, QNTF, ENTF) is shown in Figure 6.5. It can be seen that the STF has a sharp peak around the drive resonant frequency f_x due to the quality factor of 100, and therefore the signal bandwidth is very narrow, and there is no flat region in the signal band. The output bitstream spectrum is shown in Figure 6.6(a) with a close-up view around the signal bandwidth (Figure 6.6(b)), which indicates that the signal is symmetrically located at $f_y \pm f_{in}$. The SNR is calculated to be about 90dB in a 256Hz bandwidth. It should be noted that the two signal peaks have 6dB difference, which is due to the signal has a sharp transfer function in the signal band. This further verified the STF Bode diagram shown in Figure 6.5. Bandwidth is a critical factor for the dynamic performance of a micromachined vibratory gyroscope [94]. Thus using a control system based on a lowpass ΣΔM restricts vibratory rate gyroscopes to relatively narrow band signal.

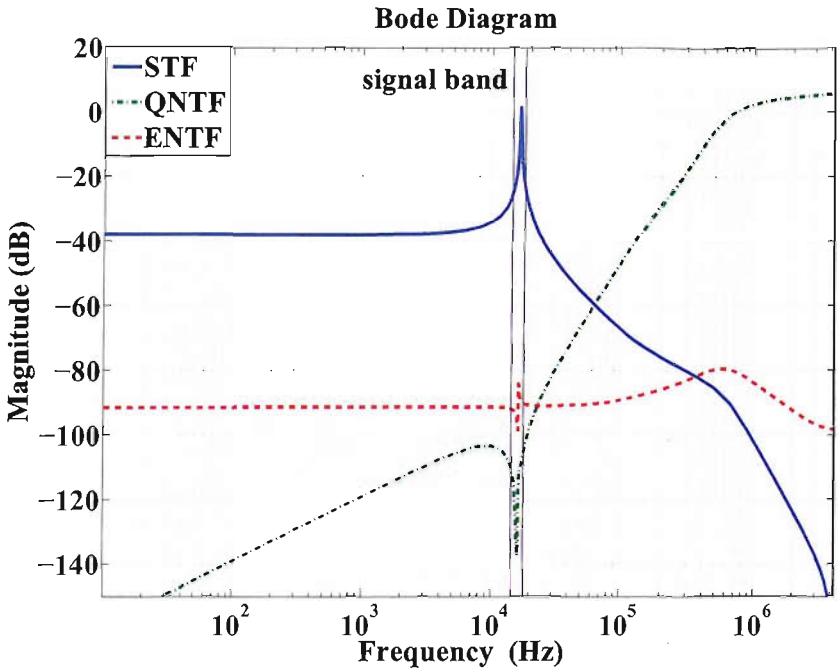

FIGURE 6.5: Bode diagram of the transfer functions of the signal, quantization noise and electronic noise of the sense mode control system based on a fifth-order ΣΔM depicted in Figure 6.4.

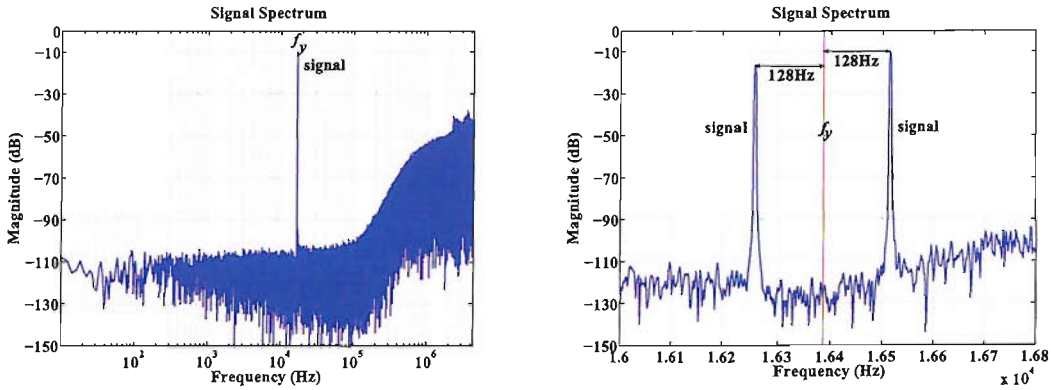

(a) Full view of the output bitstream spectrum

(b) Close-up view of the signal band of Figure 6.6(a)

FIGURE 6.6: Output bitstream spectrum of the control system based on a fifth-order lowpass ΣΔM depicted in Figure 6.4.

6.4 Second-Order Bandpass ΣΔM for Sense Mode Control System

The sensing element of vibratory rate gyroscope is equivalent to a resonator in the electrical domain, therefore it lends itself to be incorporated in a bandpass ΣΔM control loop. A bandpass ΣΔM loop is designed using the sensing element only as the loop filter. This

results in a sense mode control system having a topology of a second-order bandpass ΣΔM, which is shown in Figure 6.7.

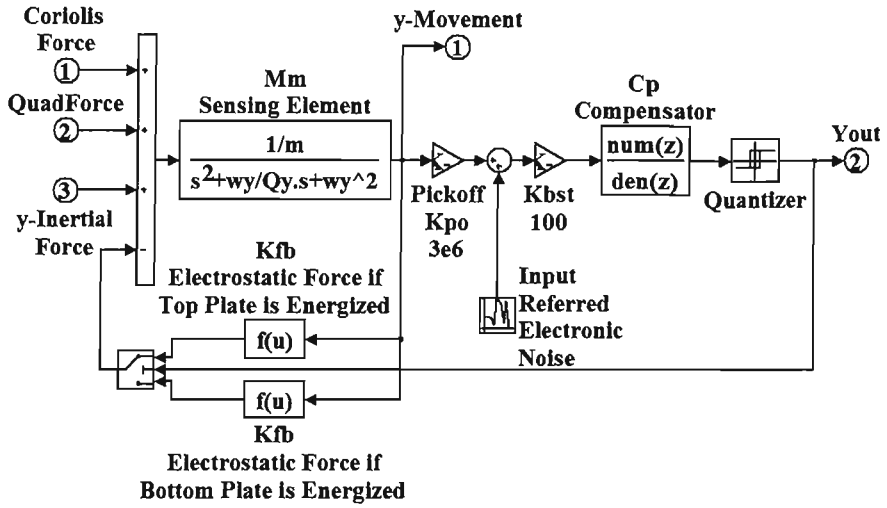

FIGURE 6.7: Sense mode control loop based on a second-order bandpass ΣΔM.

The difference to a second-order lowpass ΣΔM (as described in [54]) is that the sampling frequency can be as low as four times the resonant frequency ($f_s = 4f_y$). Furthermore, the compensator has a different format compared with the compensator for a lowpass ΣΔM interface. It compensates the phase lag of the sensing element at high frequencies to provide sufficient loop phase margin for stable operation. The design of such a compensator using classic control theory [72] is also an initial step toward the design of a high-order bandpass loop addressed subsequently. The compensator used here is given by:

$$C_p(z) = \frac{-22.13}{z + 0.9942} \tag{6.5}$$

The Bode diagram of the compensator and sensing element is plotted in Figure 6.8. With the compensator, the phase lag originating from the sensing element is sufficiently compensated at high frequencies and provides 90^o phase lead at $f_s/2$ compared to without compensation. The output bitstream spectrum is shown in Figure 6.9. If distortion is not included, the signal to noise ratio is about 63dB in a bandwidth of 256Hz. However, there are lots of idle tones in the spectrum, this is due to the quantization noise not being white anymore. Calculating the SNR including harmonic distortion results in a value of about 35dB which unacceptably low for most applications. For a lower order ΣΔM, the additive white noise approximation of the non-linear one-bit quantizer is not a valid assumption. These tones may fold into the signal band and degrade the SNR. In contrast, a high-order ΣΔM suffers less tonal behaviour [28]. Therefore, the control system using a high-order ΣΔM can help to reduce these tones. This is verified in the subsequent sections.

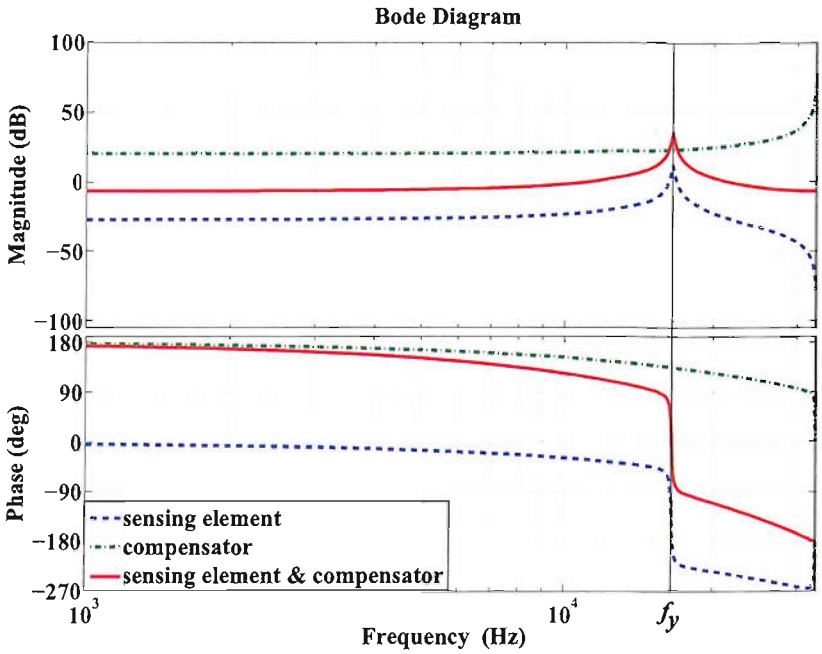

FIGURE 6.8: Bode diagram of the compensator, sensing element and the product of the sensing element and compensator for the sense mode control system using a bandpass ΣΔM.

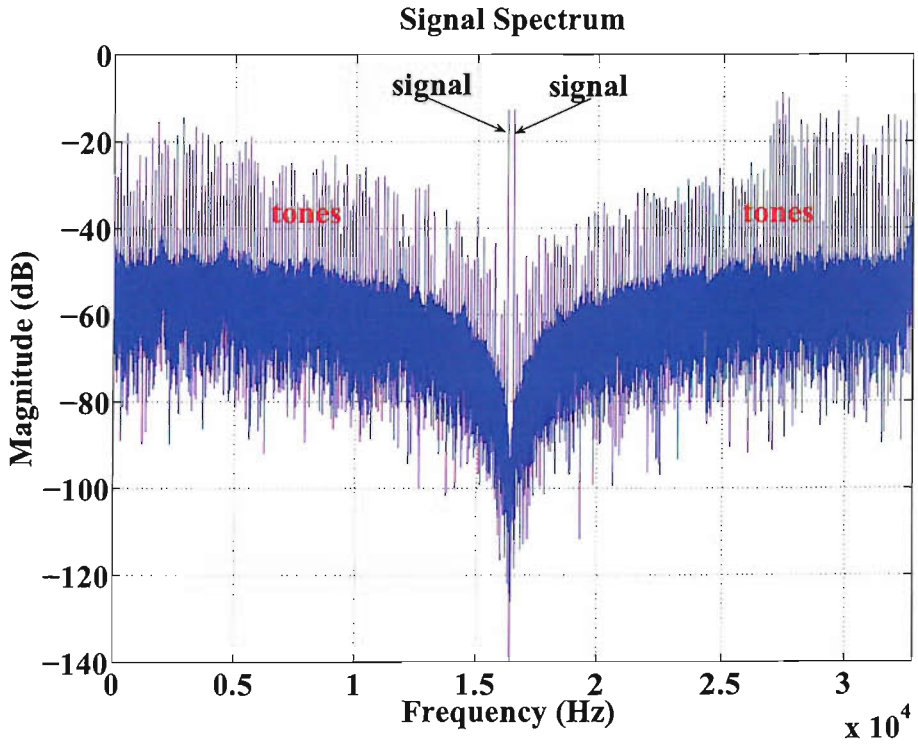

FIGURE 6.9: Output bitstream spectrum of the control system using a second-order bandpass ΣΔM, showing significant tonal behaviour.

6.5 High-Order Bandpass ΣΔM Vibratory Gyroscopes

6.5.1 High-Order Bandpass ΣΔM Using A MFLR Topology

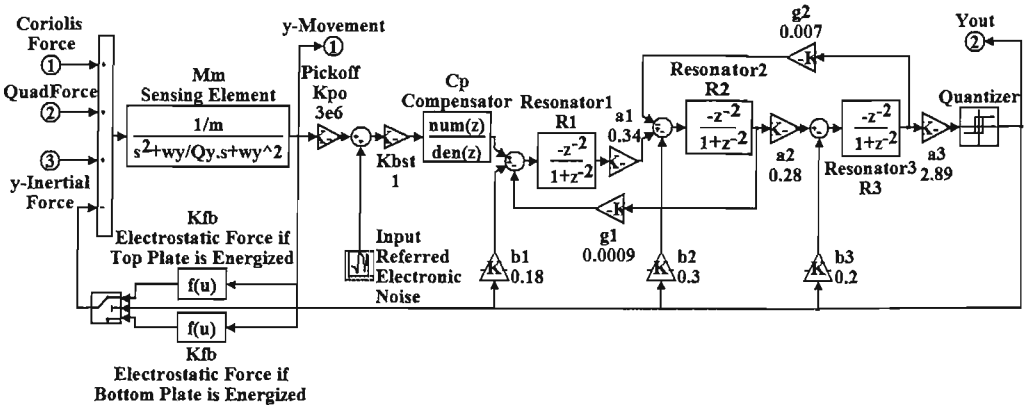

FIGURE 6.10: Sense mode control system based on a eighth-order bandpass ΣΔM with multi-feedback loops and local resonators.

Applying the transformation Equation 2.64 to the fifth-order low pass ΣΔM described above (Figure 6.4) results in an eighth-order bandpass ΣΔM, which is shown in Figure 6.10. This system adopts a topology of multi-feedback loops with two local resonators, which is the same as that used in Chapter 4.2.4. The control loop consists of the same micromachined sensing element $M_m(z)$ (i.e. the first resonator) cascaded with a lead phase compensator $C_p(z)$, and three electronic resonators $R_1(z)$, $R_2(z)$ and $R_3(z)$ which are given by Equation 2.65. a_1, a_2 and a_3 are gain constants used for scaling the resonator output amplitude. The gain constants in the feedback path, g_1 and g_2, are used to generate two local resonators. Thus, a notch is created in the signal band to further suppress the quantization noise. The OSR ($=f_{s2}/2f_{in}$) for a band pass ΣΔM is the ratio between the sampling frequency f_{s2} and twice the input signal frequency f_{in}. Using the same value of the OSR as for the low pass ΣΔM, the sampling frequency f_{s2} is now reduced to 2^{16}Hz ($\approx$ 65kHz) compared with approximately 8 MHz for the lowpass ΣΔM. The transfer functions STF, ENTF and QNTF are given by:

$$STF_2(z) = \frac{m\kappa_m(z)\prod_{i=1}^{3} R_i(z)a_i}{L(z) \times K_{fb}} \tag{6.6}$$

$$ENTF_2(z) = \frac{\kappa_m(z)\prod_{i=1}^{3} R_i(z)a_i}{L(z) \times (K_{fb}M_m(z)K_{po})} \tag{6.7}$$

$$QNTF_2(z) = \frac{1 + R_1(z)a_1R_2(z)g_1 + R_2(z)a_2R_3(z)g_2}{L(z)} \tag{6.8}$$

where

$$L(z) = 1 + \kappa_m(z)\prod_{i=1}^{3} R_i(z)a_i + K_q\sum_{i=1}^{3} b_i\prod_{j=i}^{3} R_j(z)a_j + \sum_{i=1}^{2} a_i g_i\prod_{j=i}^{i+1} R_j(z) + R_1(z)a_1R_2(z)g_1a_3R_3(z)b_3K_q$$

The bode diagram of these transfer functions is shown in Figure 6.11. A high-order

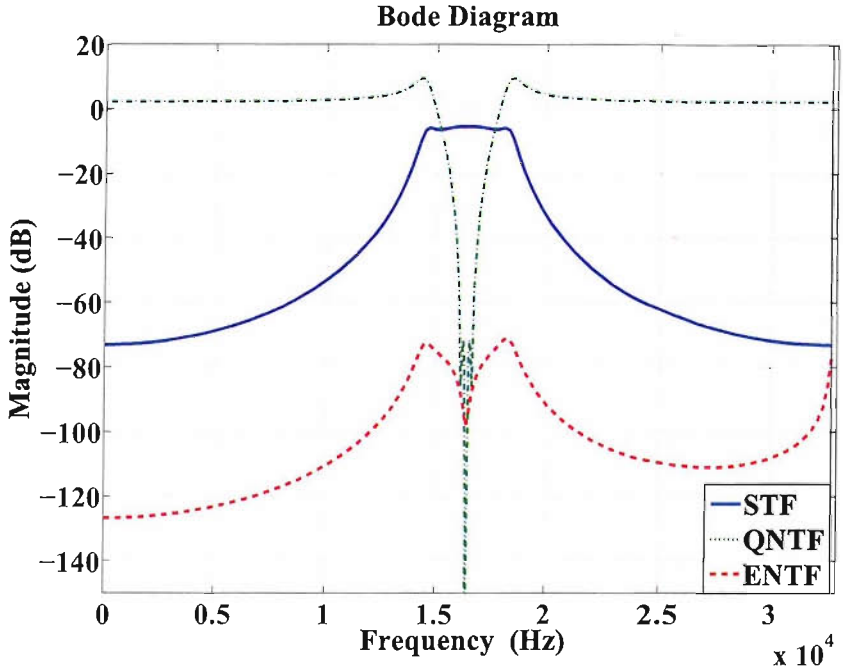

FIGURE 6.11: Bode diagram of the transfer functions of the signal, quantization noise and electronic noise of the eighth-order bandpass ΣΔM with multi-feedback loops and local resonators.

bandpass ΣΔM is also a conditionally stable closed-loop system [28]. The root locus of the open-loop filter is plotted in Figure 6.12(a), with a close-up shown in Figure 6.12(b). In order to ensure that the poles lie within the unit circle, the critical minimum gain of the quantizer should be $K_{qmin} = 0.693$. If the quantizer gain K_q is less than K_{qmin}, one pole pair will move out of the unit circle and finally result in an unstable operation. This could be caused by an input signal overload, therefore instability detection and saturation recovery techniques should be applied to a hardware implementation of a high-order ΣΔM [81], however, this was not considered in this work. The spectrum of the output bitstream is shown in Figure 6.13. The signal is symmetrically located at $f_x \pm f_{in}$. Tones only appear at low or high frequencies, but not in the vicinity of the signal band. The SNR is calculated to be 103dB in a 256Hz signal bandwidth.

6.5.2 High-Order Bandpass ΣΔM Using A FFLR Topology

A second topology of an eighth-order bandpass ΣΔM is presented in Figure 6.14. It consists of feed-forward loops and a local resonator. This topology is the same topology used in

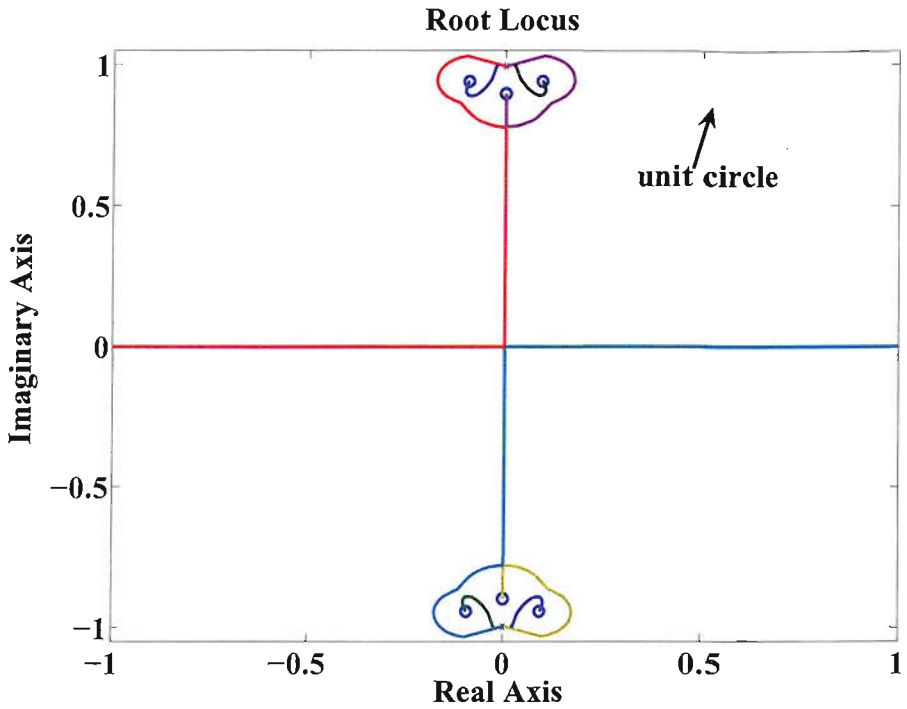

(a) Full view of the root locus of the open-loop filter

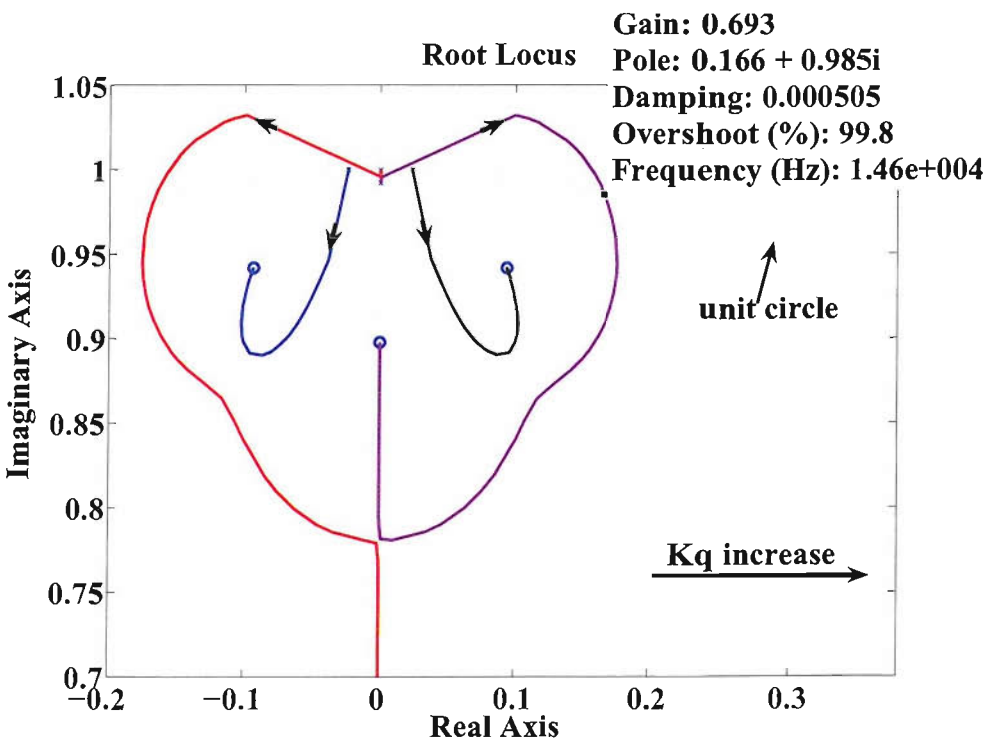

(b) Close-up view of the upper section of Figure 6.12(a)

FIGURE 6.12: Root locus of the open-loop filter of the eighth-order bandpass ΣΔM with multi-feedback loops and local resonators.

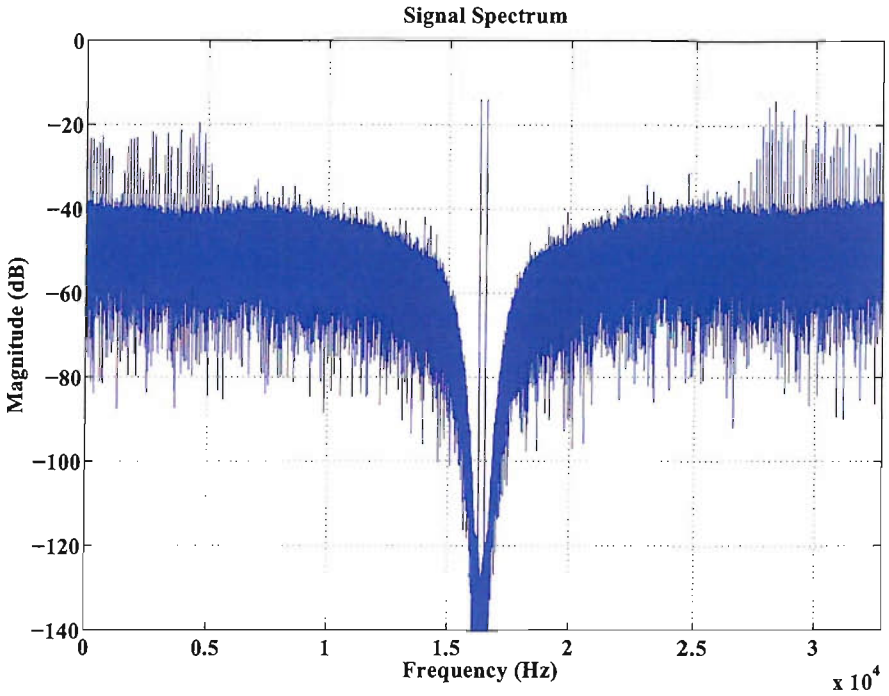

FIGURE 6.13: Output bitstream spectrum of the eighth-order bandpass ΣΔM with multi-feedback loops and local resonators.

Chapter 4.2.3.

Similarly, the control system consists of the micromachined sensing element $M_m(z)$ (as the first resonator) cascaded with a lead phase compensator $C_p(z)$, and three electronic resonators $R_1(z)$, $R_2(z)$ and $R_3(z)$ which are given by Equation 2.65. b_1, b_2 and b_3 are gain constants used for scaling the resonator output amplitude. The feed-forward loops are formed by the gain constants a_1, a_2 and a_3 and a local resonator is formed by the feedback path with gain constant g. Thus, a notch is created in the signal band to further suppress the quantization noise. With a sampling frequency f_{s2}=2^{16}Hz ($\approx$ 65kHz), the OSR ($f_{s2}/2f_{in}$) is equivalent to the lowpass ΣΔM shown in Figure 6.4.

The transfer functions STF, ENTF, and QNTF are given by:

$$STF_3(z) = \frac{m\kappa_m(z)[b_1R_1(z)b_2R_2(z)(b_3R_3(z)a_4 + a_3) + (1 + gR_2(z)b_3R_3(z))(b_1R_1(z)a_2 + a_1)]}{L(z) \times K_{fb}} \tag{6.9}$$

$$ENTF_3(z) = \frac{\kappa_m(z)[b_1R_1(z)b_2R_2(z)(b_3R_3(z)a_4 + a_3) + (1 + gR_2(z)b_3R_3(z))(b_1R_1(z)a_2 + a_1)]}{L(z) \times (K_{fb}M_m(z)K_{po})} \tag{6.10}$$

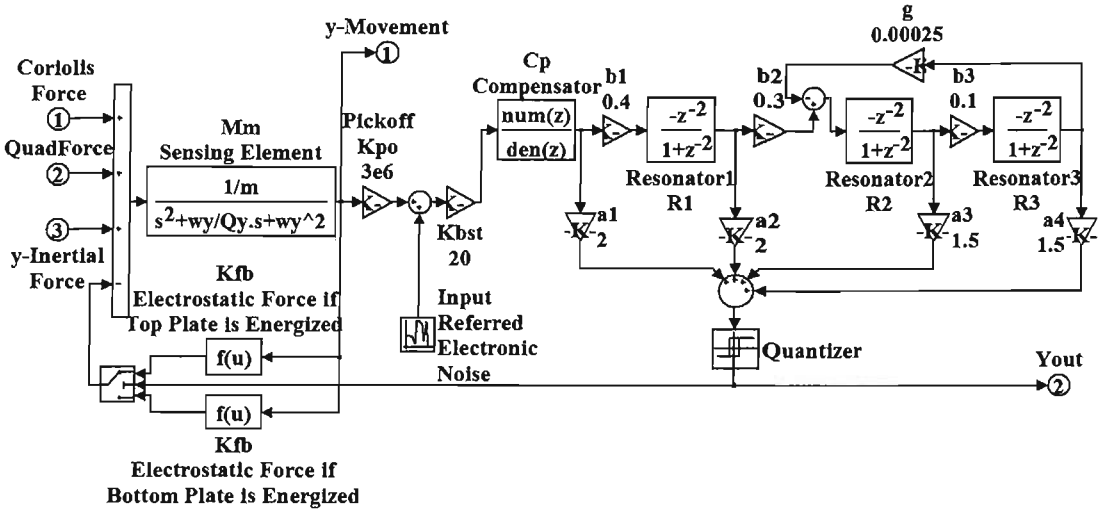

FIGURE 6.14: Sense mode control system based on a eighth-order bandpass ΣΔM with feed-forward loops and a local resonator.

$$QNTF_3(z) = \frac{1 + gR_2(z)b_3R_3(z)}{L(z)} \tag{6.11}$$

where

$$L(z) = 1 + \kappa_m(z)\sum_{i=1}^{4} a_i \prod_{j=1,j>0}^{i-1} b_jR_j(z) + gR_2(z)b_3R_3(z)[1 - (\kappa_m(z)K_q(a_1 + b_1R_1(z)a_2)]$$

The bode diagram of these loop transfer functions is shown in Figure 6.15. The spectrum of the output bitstream is shown in Figure 6.16. The root locus of the open-loop filter is plotted in Figure 6.17(a), with a close-up view shown in (Figure 6.17(b)). In order to ensure the root locus to lie within the unit circle, the critically minimum gain of the quantizer is $K_{qmin} = 0.695$. The SNR is almost same as the control system using a MFLR topology. The tones are located at either low or high frequencies and have no effect on the signal.

6.6 Discussions

6.6.1 Properties of Signal and Noise Transfer Functions

For the signal transfer function, STF, presented in the two high-order bandpass ΣΔMs, the response has a relatively wide (>1kHz) flat all-pass characteristic in the frequency range of interest. This is in contrast to a narrow signal band in a lowpass ΣΔM. Therefore, a vibratory rate gyroscope employing a bandpass ΣΔM intrinsically has a much higher signal bandwidth. Another property is that the discrete time circuit blocks are all located after

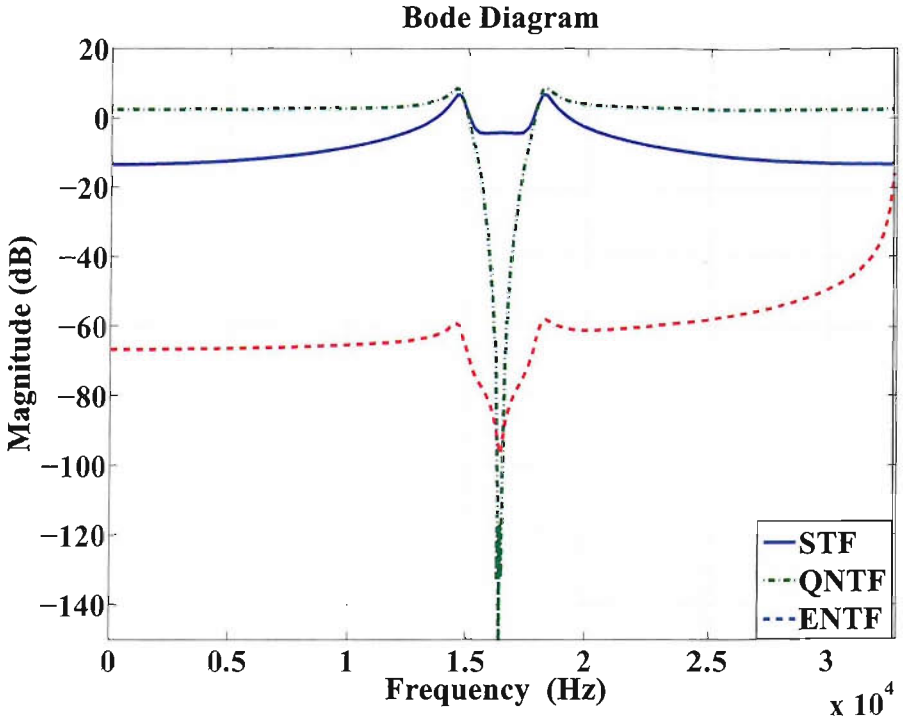

FIGURE 6.15: Bode diagram of the transfer functions of the signal, quantization noise and electronic noise of the eighth-order bandpass ΣΔM with feed-forward loops and a local resonator.

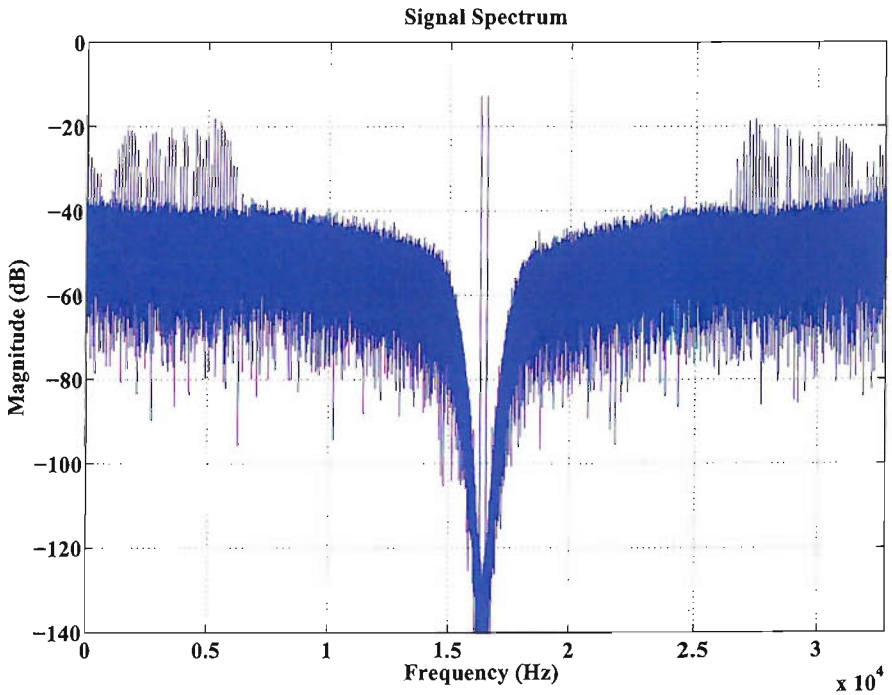

FIGURE 6.16: Output bitstream spectrum of the eighth-order bandpass ΣΔM with feed-forward loops and a local resonator.

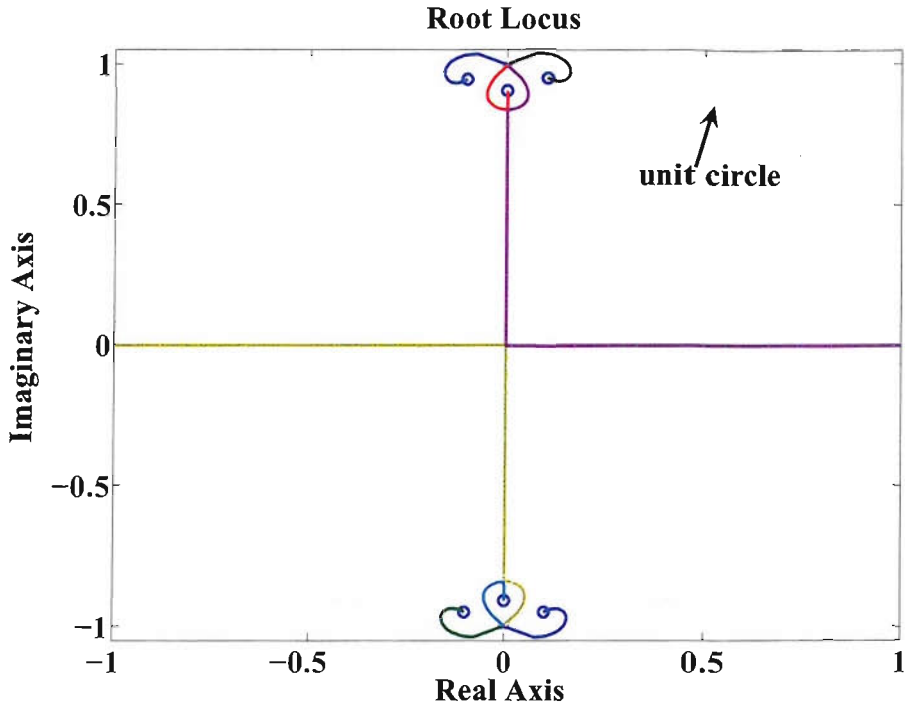

(a) Full view of the root locus of the open-loop filter

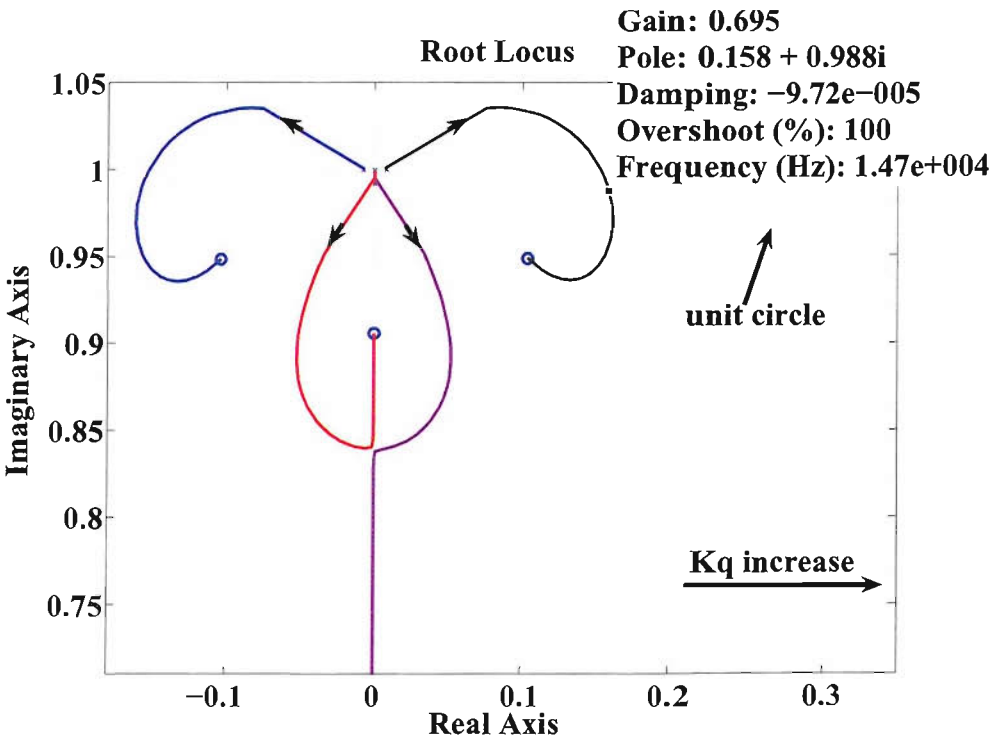

(b) Close-up view of the upper section of Figure 6.17(a)

FIGURE 6.17: Root locus of the open-loop filter of the eighth-order bandpass ΣΔM with feed-forward loops and a local resonator.

the sensing element, therefore the continuous-time sensing element provides an implicit second-order anti-alias filtering. This is an advantageous property of all discussed ΣΔMs control systems.

For all high-order topologies presented in this Chapter, the ratio between the ENTF and the STF is given by:

$$\frac{ENTF_i(z)}{STF_i(z)} = \frac{1}{mM_m(z)K_{po}} \ (i = 1, 2, 3) \tag{6.12}$$

Equation 6.12 is calculated by dividing Equation 6.2 by Equation 6.3, Equation 6.6 by Equation 6.7 and Equation 6.9 by Equation 6.10, respectively. Since the STF has an all-pass characteristic for the two bandpass topologies, Equation 6.12 denotes that the electronic noise is shaped by the inverse transfer function of the sensing element. For a micromachined vibratory gyroscope, the Q is relatively high in order to increase its sensitivity. This leads to a better electronic noise shaping in the signal band for a bandpass ΣΔM. The SNR of the two high-order bandpass ΣΔMs are almost the same; about 100dB in a 256Hz bandwidth, compared with about 90dB for the fifth-order, low pass ΣΔM.

It can be seen from the Bode diagrams and the output bitstream spectra, that electronic noise is dominant noise compared with the quantization noise. Therefore, quantization noise is no longer the limiting factor for the sensor performance. To achieve a comparable noise floor in a control system using a lowpass ΣΔM and a bandpass ΣΔM, the sampling frequency of the former (about 8.4MHz) has to be much higher (256 times) than that of the latter (about 65kHz). This implies a much higher operating frequency of the interface and control circuits for a lowpass ΣΔM; this is a distinct disadvantage. It should be finally noted that, to simplify the analysis in this chapter, the mechanical Brownian noise has not been considered in the simulations because it is directly added to the input signal and is not shaped by any modulator topology.

6.6.2 Effects of Quadrature Force on System Performance

So far quadrature error was not taken into account. Considering a quadrature force due to microfabrication tolerances and assuming a misalignment angle of $\eta = 0.001^o$, the output bitstream spectrum of the system depicted in Figure 6.13 is shown in Figure 6.18. All other simulation parameters were the same as for the simulation result of Figure 6.16. Such a relatively small misalignment angle leads to an output amplitude at the drive resonant frequency, f_x, which is almost equal to the signal amplitude. Therefore, an effective correction mechanism should be adopted to avoid saturating the pickoff preamplifier. The quadrature force can be separated from the Coriolis signal force, since it is out of phase by 90^o with

respect to the input signal. An additional force feedback loop can be used to balance its effects, which will be discussed for future work in Chapter 9.

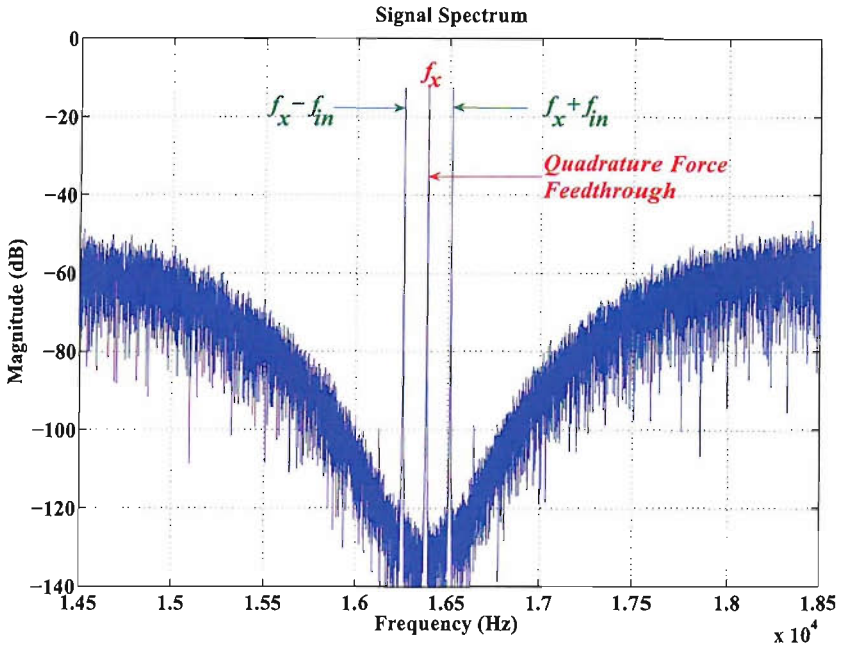

FIGURE 6.18: Quadrature force effects on the output bitstream spectrum of the eighth-order bandpass ΣΔM with feed-forward loops and a local resonator (shown in Figure 6.14).

6.6.3 Effects of Resonant Frequency Mismatch on System Performance

A resonant frequency mismatch between the drive mode and sense mode was not yet considered. Assuming a resonant frequency mismatch ±5% due to microfabrication tolerances, and all other simulation parameters remaining the same, a simulation is done with the fifth-order lowpass ΣΔM (Figure 6.4). The output bitstream spectrum of the system is shown in Figure 6.19. There is a significant signal amplitude loss (15dB) due to the mismatch. While a simulation with the mismatch is done with the control system based on a bandpass ΣΔM (Figure 6.10), the output spectrum (plotted in Figure 6.20) shows that the spectrum is no longer perfectly symmetrically mirrored at f_x and has a slightly higher noise floor compared with the Figure 6.13. Nevertheless, there is no signal amplitude degradation due to the resonant frequency mismatch, this is a major advantage of a bandpass ΣΔM control loop over a lowpass ΣΔM control loop.

6.6.4 Effects of $1/f$ Noise and White Electronic Noise

The circuit implementation of a sensing and control system will inevitably generate noise. Usually, CMOS analog circuits not only generate thermal white noise, but also $1/f$ noise. Chopping modulation and CDS techniques are effective methods to remove $1/f$ noise, drift

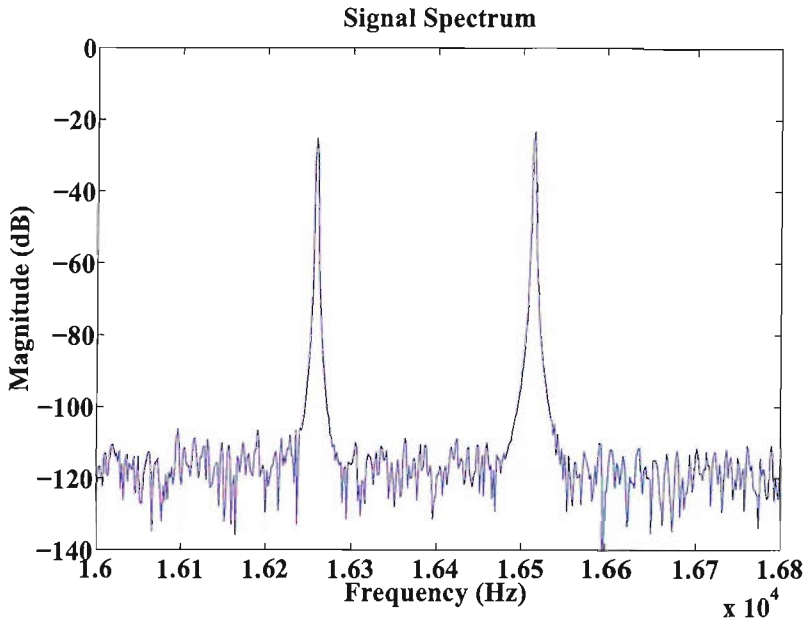

FIGURE 6.19: Resonant frequency mismatch effects on the output bitstream spectrum of the fifth-order lowpass ΣΔM (compared with Figure 6.6(b)).

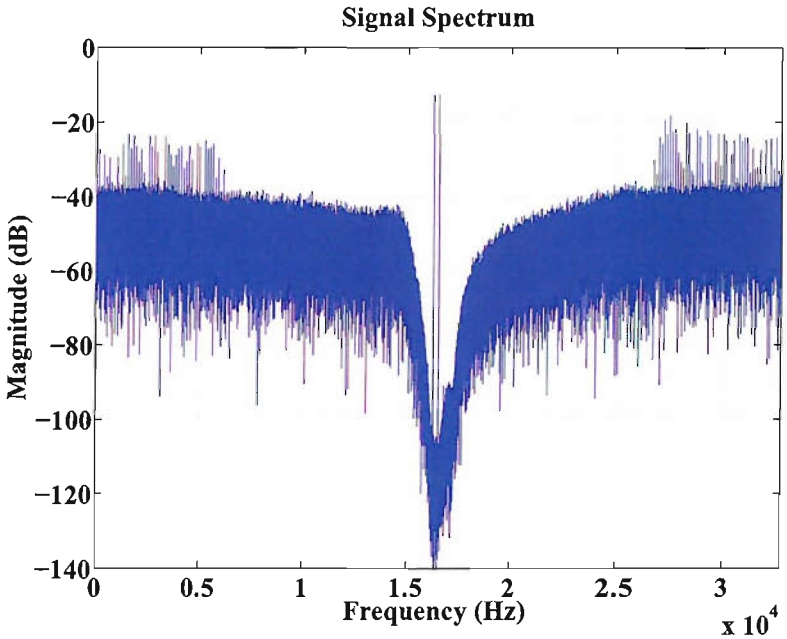

FIGURE 6.20: Resonant frequency mismatch effects on the output bitstream spectrum of the eighth-order bandpass ΣΔM (shown in Figure 6.10).

and offsets [35]. Micromachined vibratory gyroscopes prefer to operate at a high resonant frequency to increase their sensitivity. The mechanical resonant frequency is usually chosen to be several kHz, which is higher than the first corner frequency of $1/f$ noise [95]. This makes it possible to take advantage of a bandpass ΣΔM to remove the low frequency noise components. Malcovati's SDToolbox [67] provides a color noise model for the Matlab environment.

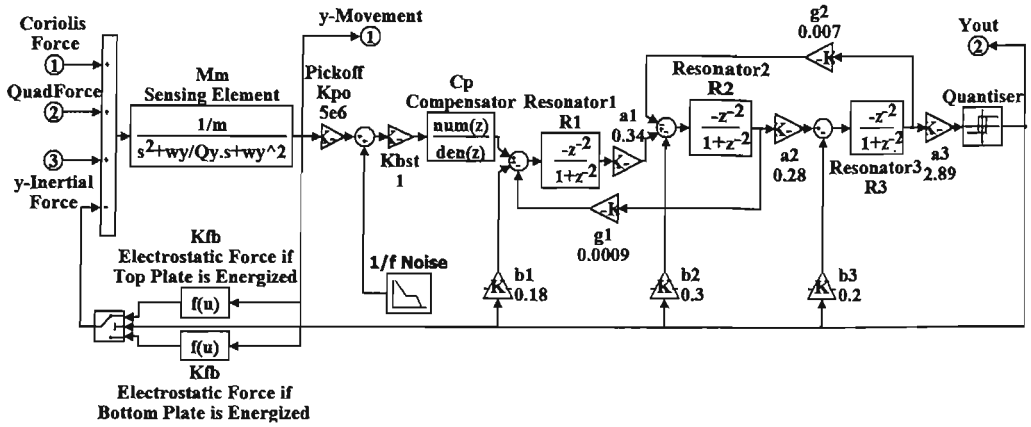

FIGURE 6.21: Model of the sense mode control system depicted in Figure 6.10 including the effects of $1/f$ noise.

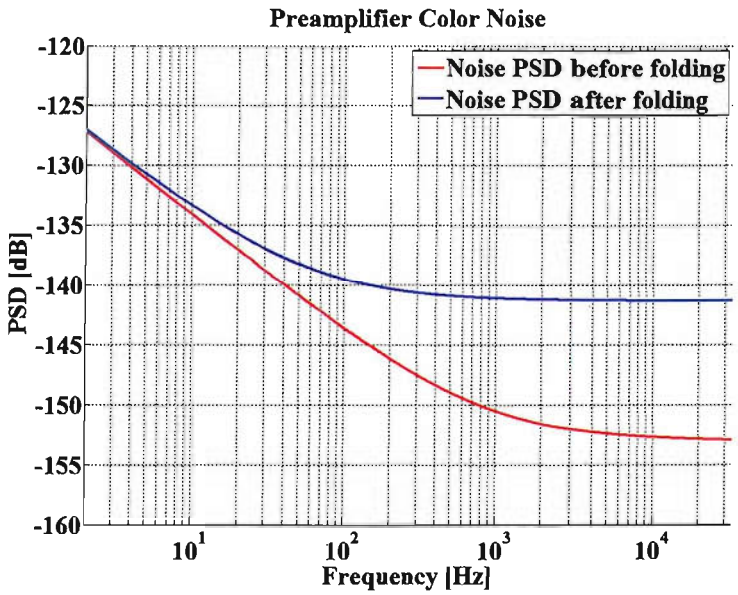

FIGURE 6.22: Spectrum of the preamplifier color noise, including the $1/f$ noise and white noise.

A modified system level model (based on the system shown in Figure 6.10) is depicted in Figure 6.21; it includes the input-referred color noise at the input of the pickoff preamplifier. The parameters in the color noise model, such as the corner frequencies and PSD can be obtained either by transistor-level simulations or from typical values quoted in the literature. Here, the first corner frequency is chosen to be at 1kHz with a conservative value for the PSD of $30\text{nV}/\sqrt{Hz}$ $(1/f)$, and the second corner frequency at five times of the sampling frequency f_{s2} with a PSD of $6\text{nV}/\sqrt{Hz}$ (white noise). Figure 6.22 shows the color noise spectrum.

The output bitstream spectrum in the control system based on a bandpass ΣΔM (shown in Figure 6.21) is same as the previous simulation (shown in Figure 6.13), so there is no penalty from the $1/f$ noise. If the above color noise model is added in the control system

based on a lowpass ΣΔM (shown in Figure 6.4), the output bitstream spectrum is also same as the previous simulation shown in Figure 6.6 and also there is no penalty from the $1/f$ noise. Generally speaking, the $1/f$ noise in closed-loop micromachined gyroscopes do not contribute to overall electronic noise floor due to the vibratory gyroscopes resolve the angular rate signal after synchronous demodulation of the pre-amplified detected sense structure displacement by mixing it with the phase-locked drive signal. Closed-loop operation shifts the preamplifier $1/f$ noise out of the signal band. This $1/f$ noise inherent immunity is another remarkable advantage of an electromechanical ΣΔM, which have no use for any CDS or chopping circuit techniques to remove $1/f$ noise.

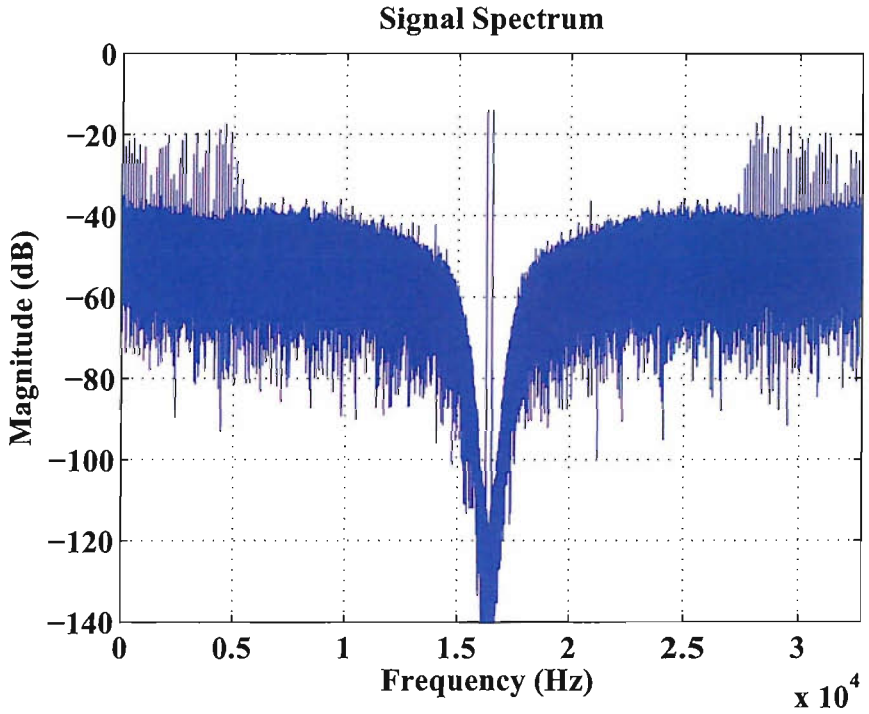

FIGURE 6.23: Output bitstream spectrum of the system depicted in Figure 6.21 with the PSD of 16nV/$\sqrt{Hz}$ at the second corner frequency in the color noise model.

If the PSD at the second corner frequency is raised to 16nV/$\sqrt{Hz}$ in the color noise model, the output spectrum is shown in Figure 6.23. The SNR of the bandpass control system (shown in Figure 6.21) suffers a loss of 6dB. However, if the above color noise model is added in the control system based on a lowpass ΣΔM (shown in Figure 6.4), the system SNR will suffer a loss of 18dB. The discrepancy of the SNR loss comes from the white electronic noise not $1/f$ noise. It should be noted that the higher pickoff preamplifier gain (K_{po}=100) of the lowpass high-order loop is used than that of (K_{po}=1) the bandpass high-order loop. As discussed in Chapter 4, the pickoff gain K_{po} is determined by the loop stability and cannot be arbitrarily chosen. Furthermore, this phenomenon can be explained by the pickoff gain effect on white electronic noise in a high-order electromechanical ΣΔM, which had been discussed in Chapter 4.3: the higher the pickoff gain, the lower the system SNR.

6.7 Summary

This work discusses a range of closed-loop, force feedback control systems based on ΣΔMs for the sense mode of vibratory rate gyroscopes. It was found that a high-order bandpass ΣΔM topology, which cascades several electronic resonators with the micromachined sensing element, has remarkable advantages over other topologies. Compared with a second-order ΣΔM loop (which uses the sensing element only as the loop filter), it provides superior quantization noise shaping and alleviates idle tones. Compared with using a lowpass ΣΔM, a control system using a high-order ΣΔM has advantages: reducing the sampling frequency by about two orders of magnitude, a wider and flat signal transfer function in the frequency range of interest, and an inherent immunity to $1/f$ and other low frequency noise sources. Two novel topologies of an eighth-order, bandpass ΣΔM are discussed: a topology based on multiple feedback loops with two local resonators, and another based on feed-forward loops with one local resonator. The latter has the advantage that it has much reduced internal signal levels hence is suitable for a low power implementation. Both topologies achieve a SNR of about 100dB for typical parameter values for a micromachined sensing element and state-of-the art electronic components.

Chapter 7

Experimental Results: A Fifth-Order Lowpass Electromechanical CT ΣΔM

7.1 Sensing Element Used in the Prototype

According to the inital plan of this research work, a high performance accelerometer would have been fabricated using the University cleanroom for test of the prototype. However, due to the Southampton University fire, these nearly done devices (which discussed in detail in next Chapter) were no longer available. Fortunately, Qinetiq supplied the sensing element for this PCB prototype. The device was fabricated using SOI wafers. Physical parameters of the sensing element are: mass $m = 9.7 \times 10^{-7}$kg, damping coefficient b=0.2N/m/s and spring stiffness k=48N/m. The dynamic frequency response of the sensing element is plotted in Figure 7.1.

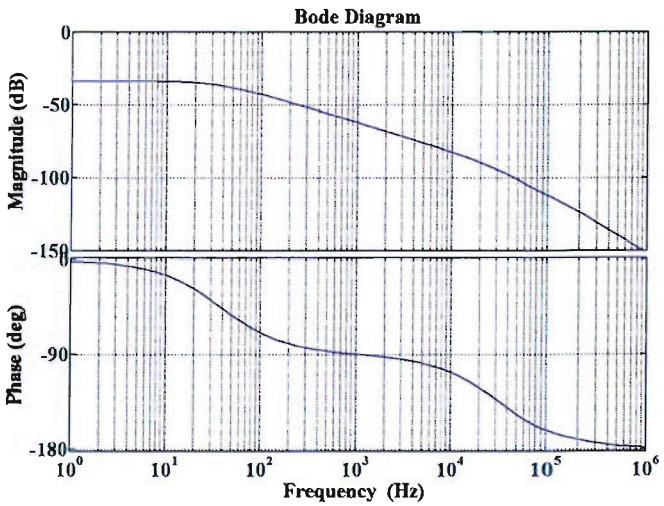

FIGURE 7.1: Bode diagram of the sensing element provided by Qinetiq.

Obviously it is an overdamped sensor and the bandwidth is only 100Hz. The bandwidth needs to be increased by the closed-loop control system. There are two sets of capacitor electrodes: one set electrodes for force feedback which has nominal capacitance value of 2 x 4.45pF and another set electrodes for sensing which has nominal capacitance value of 2 x 1.4pF. Its mechanical noise floor is $10\mu g/\sqrt{Hz}$, which is not so low enough that the ultimate noise floor can not be observed in the following PCB prototype. Therefore, the performance of the fifth-order CT electromechanical ΣΔM reported in this Chapter are only the preliminary measurement results.

7.2 Front-End Circuits

7.2.1 Pickoff Interface Circuit

There are two very effective methods to improve the performance of a pickoff interface circuit: correlated double sampling (CDS) and chopper stabilization, which are applied to suppress low frequency noise (such as $1/f$ noise) and drift in the signal band [35]. However, both methods cannot suppress white noise, which set the ultimate limit for the circuits. Generally speaking, CDS is suitable for SC circuit implementation, while chopper stabilization is usually used for CT circuits. For a PCB prototype using commercial discrete components, a continuous-time ΣΔM is preferred to discrete-time SC ΣΔM, mainly because there are too many analog switches for a SC implementation. In this PCB prototype, the signal is modulated at high frequencies, the dominate $1/f$ noise from pickoff interface circuits is removed after demodulation, and thus a chopper stabilization technique for subsequent circuits is not adopted in the prototype for simplification. High performance capacitance to voltage converters (CVC) are necessary for capacitive accelerometers to measure both statically and dynamically. Several methods have been introduced to convert a capacitance variation into a voltage [96]. However, most of them are not capable of handling very small variations of the order of 1 ppm in the nominal capacitance value. There are two critical parts in the sensor interface: one is the pickoff preamplifier, which is featured with low noise and low distortion. A charge amplifier is one of the best preamplifiers to sense the variation of small capacitance which discussed in Chapter 3.1. Another is the demodulator, which is designed to remove the modulation from the excitation carrier to give the frequency representation of the signal. So far, the dominant demodulation methods include: synchronous demodulation and diode envelope detection, which will be addressed in detail in the following.

For the measurement of small variations in capacitance with high accuracy, a major problem is that parasitic capacitance in most cases has the same order of magnitude as the nominal sensor capacitance; furthermore, capacitances are sensitive to electromagnetic interference. The sensor capacitance C_x and the parasitic capacitances C_{p1}, C_{p2}, and C_{p3} and resistances R_{pp} and R_{ps} are shown in Figure 7.2; all these undesired parasitic components are in parallel

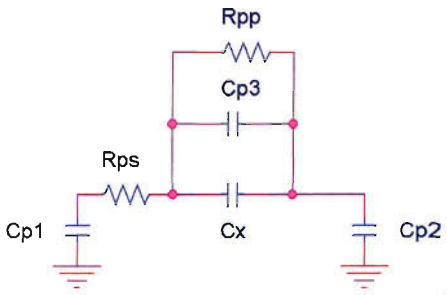

FIGURE 7.2: Sensing capacitance with parasitic components.

or in series with the sensor capacitance. It is desirable that the CVC should be immune to the parasitic impedance, that is its output voltage is only dependent on the sensing capacitance.

Most commonly used capacitive interfaces for accelerometers and vibratory gyroscopes are a single-ended sensing-element output to interface with the sense electronics. A pair of sense capacitors is configured in a capacitive half-bridge; capacitance is measured by driving the ends of the capacitive bridge and taking the output from the center node, as shown in Figure 7.3(a). The affix + or - denotes the capacitance value increasing or decreasing, respectively. High output stability requires the precise generation of the two ac excitation signals which should be insensitive to temperature and power-supply fluctuations. In fact, according to [97], for inertial grade accelerometers and gyroscopes, the bias stability of these voltage amplitude is estimated on the order of 10^{-7} V.

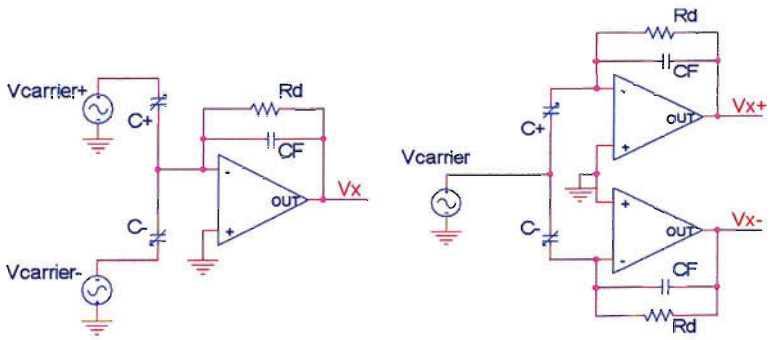

(a) Topology of single-ended interface (b) Topology of differential interface

FIGURE 7.3: Pickoff configuration: a charge amplifier.

This PCB prototype adopts a fully differential interface [5]. By reversing the roles of the center and the end terminals, a differential sense interface can be achieved with the same sense element, as shown in Figure 7.3(b). In this case, an excitation voltage with a carrier frequency $f_{carrier}$ [Hz] and amplitude $V_{carrier}$ [V] is applied to the center of the capacitive half-bridge, while the stationary electrodes are connected to the input of the differential position-sense charge amplifier (which is at virtual ground potential) with very low input impedance. The parasitic capacitances C_{p1} and C_{p2}, as shown in Figure 7.2, are in parallel with the voltage source and the low input impedance of the charge detector, respectively,

thus having virtually no effect on the measurement of the current flowing through. The advantage of this CVC is that circuits are symmetrical, so any undesired common mode interference can be rejected, including improved power-supply rejection ratio and first order rejection of common-mode errors, such as switch charge injection, excitation fluctuations in the magnitude and substrate noise. A final important advantage of driving the proof mass is that multiple sets of sense capacitors in different axes can be simultaneously force balanced. Multi-axis force balancing [5] is achieved using one sense interface for each axis and synchronizing the proof-mass pulses with all three feedback loops. The interface has the following specifications:

1. the frequency range of the change in acceleration is dc to 1kHz;
2. the minimum detectable change in acceleration is expected $10\mu g$, corresponding to a capacitance change 12aF (10ppm of 1.2 pF);
3. the maximum change in acceleration is 1g, corresponding to a capacitance change 12fF (1% of 1.2 pF)

7.2.2 Synchronous Demodulation

Synchronous demodulation is widely used to recover very weak electrical signals from strong noise background. In a capacitive surface-MEMS inertial sensor, for example, synchronous demodulation techniques have the capability of sensing of a sub-angstrom displacement of the inertial proof mass [98]. Synchronous demodulation techniques can attenuate low-frequency error sources such as the input-referred noise and offset of the sensing electronics, substrate coupling, and electromagnetic interference (EMI) by locking the carrier phase.

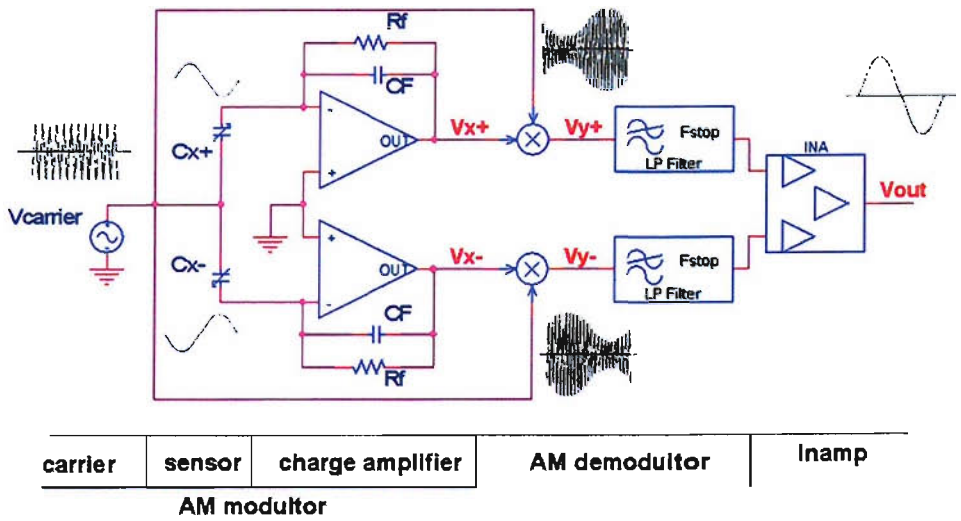

FIGURE 7.4: Synchronous demodulation for a fully differential capacitive interface.

Figure 7.4 shows a common lock-in sensing scheme used for capacitive inertial sensor. The high-frequency carrier voltage is connected to the proof mass. An imbalance in the sensing capacitors, caused by the motion of the proof-mass modulates the carrier to create a modulated signal V_x. An analog multiplier multiplies V_x by a replica of the high-frequency carrier to generate V_y. The subsequent demodulation process interchanges the location of the input signal spectrum and the error spectrum in V_y. Finally, V_y is lowpass filtered to generate V_{out}. The lowpass filtering preserves the input signal in V_{out}, while the low-frequency errors are greatly suppressed.

The output signal of the accelerometer is: $A\sin(\omega_{signal}t)$, where A is the amplitude of the signal and ω_{signal} is the signal frequency. The high frequency carrier is expressed by $B\sin(\omega_{carrier}t)$, where B is the amplitude of the carrier and $\omega_{carrier}$ is the carrier frequency. The modulated signal is $V_x = A\sin(\omega_{signal}t) \times B\sin(\omega_{carrier}t)$. The carrier is used as demodulation but has a small phase shift ϕ (≈ 0) due to delay in the hardware implementation, so the demodulated signal is expressed by Equation 7.1 and its spectrum is shown schematically in Figure 7.5.

$$\begin{aligned} V_y &= A\sin(\omega_{signal}t)\cdot B\sin(\omega_{carrier}t)\cdot B\sin(\omega_{carrier}t+\phi) \\ &= \frac{1}{2}AB^2\sin(\omega_{signal}t)\cos\phi + \frac{1}{4}AB^2\sin[(2\omega_{carrier}-\omega_{signal})t+\phi] \\ &+ \frac{1}{4}AB^2\sin[(2\omega_{carrier}+\omega_{signal})t+\phi] \end{aligned} \tag{7.1}$$

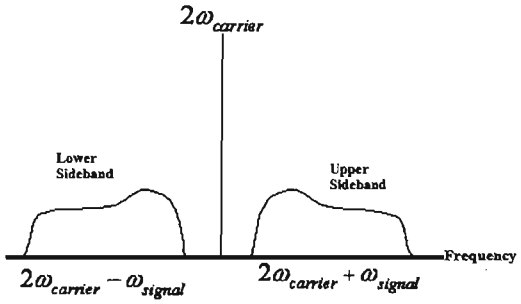

FIGURE 7.5: Spectrum of amplitude modulated signal containing two sidebands and the carrier.

After a fifth-order lowpass filter (with a corner frequency of 67.5kHz, half of the sampling frequency f_s in this prototype), the high frequency carrier is removed and the acceleration signal is recovered as:

$$V_{out} = \frac{1}{2}AB^2\sin(\omega_{signal}t)\cos\phi \tag{7.2}$$

Synchronous demodulators have several advantages. Firstly, noises are all filtered except the noise that is in phase with the excitation carrier. Consequently, the noise level is reduced and the signal to noise ratio is improved. In addition, the level of distortion is less. Unfortunately synchronous detectors are complex, requiring many discrete components to

build. Synchronous demodulation techniques are useful if, and only if, the analog multiplier is functioning within its linear range of operation. If the dc offset in the system is large enough to saturate the multiplier output or to drive it into a nonlinear regime of operation, then the final output will suffer considerable distortion and the benefits of lock-in techniques will start to fade [99].

Pspice simulations are applied to the front-end circuits. A variable capacitance can be represented in Pspice as a variable admittance (YX subcircuit) where the voltage between pin 1 and 2 represents the factor the nominal capacitance (1.2 pF in this case) is multiplied with. The input signal of the Pspice model is a triangle wave as shown in Figure 7.6, which emulates 10ppm to 20ppm capacitance variation due to an acceleration variation.

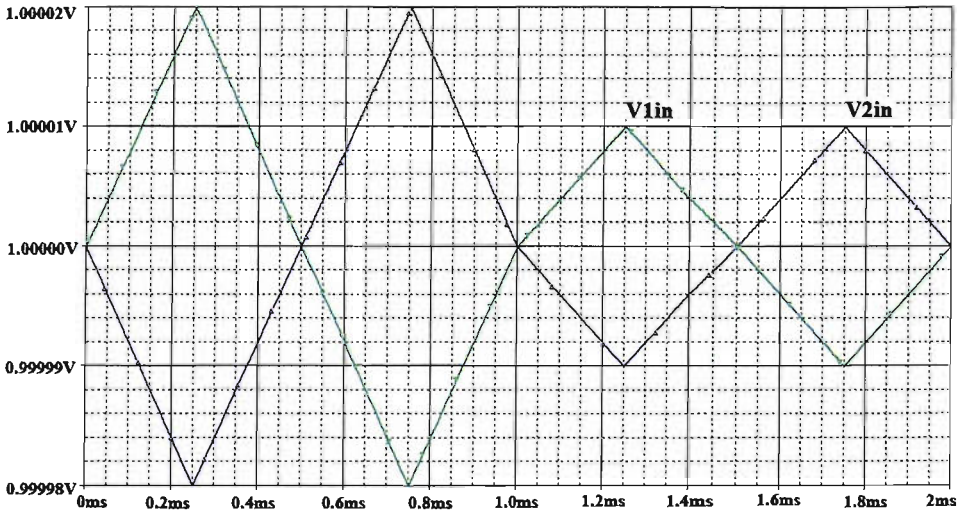

FIGURE 7.6: Signal emulating 10ppm to 20ppm capacitance variation due to acceleration variation.

The performance of a fully differential interface is based on ideally symmetrical conditions, that is all components in the two channels are matched. However, in any real circuits, there is some mismatch, which will lead to an overall performance degradation of the circuit. A precision balanced demodulator AD630 [100] is chosen due to its accuracy and temperature stability. It works like a precision op-amp with two independent differential input stages and a precision comparator which is used to select the active front end. The data sheet shows that AD630 can recover a signal from 100 dB of interfering noise at 1 kHz in a 2MHz channel bandwidth. A Pspice model of the pickoff interface using the AD630 as the demodulator is shown in Figure 7.7. Figure 7.8 shows the simulation result with the ideal matching between the two detection channels except 1% mismatch between sensing capacitors (Cx1 and Cx2).

An analog multiplier can also be used as a demodulator. Figure 7.9 shows a Pspice model of the pickoff interface circuit using the analog multiplier AD734 [100]. Figure 7.10 shows the simulation result with ideal matching between the two channels except 1% mismatch between sensing capacitors (Cx1 and Cx2).

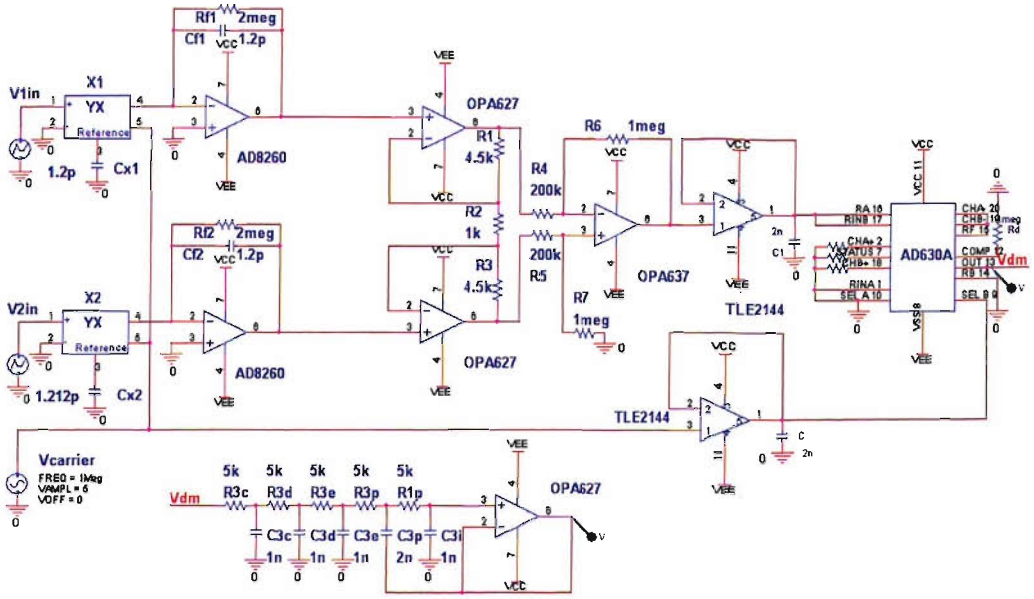

FIGURE 7.7: Pspice model of the pickoff circuit using the AD630 as a demodulator.

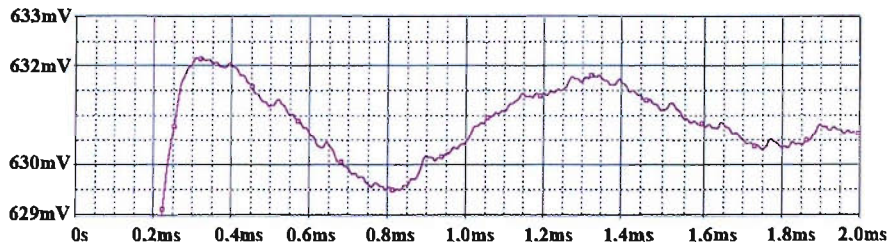

FIGURE 7.8: Pickoff circuit output with the AD630 as a demodulator.

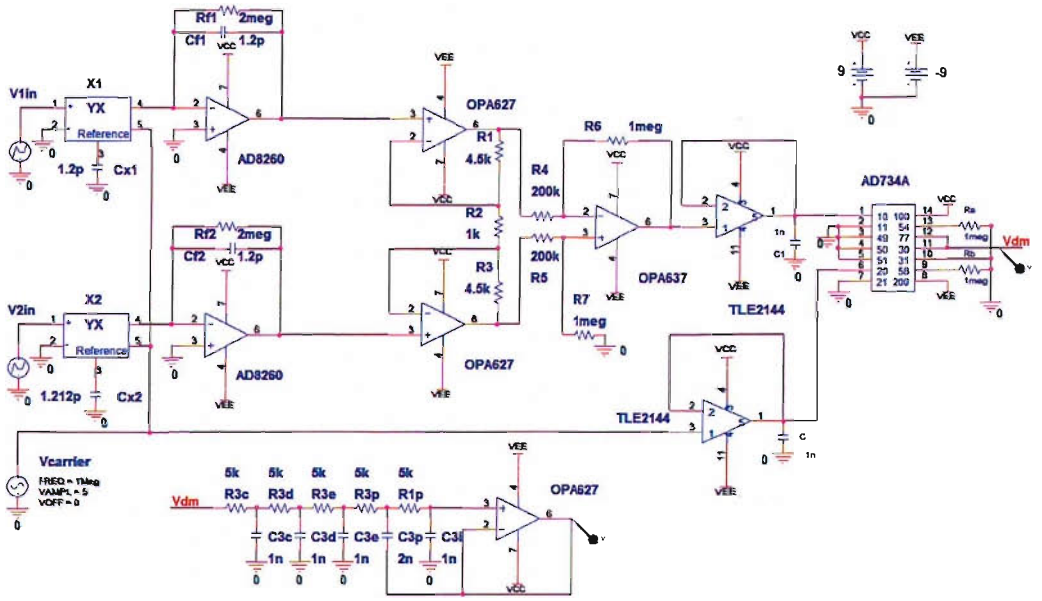

FIGURE 7.9: Pspice model of the pickoff circuit using the AD734 as a demodulator.

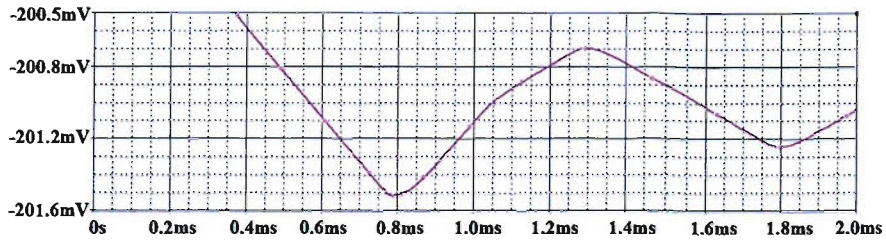

FIGURE 7.10: Pickoff circuit output with the AD734 as a demodulator.

7.2.3 Diode Demodulator

Diode envelope detectors can also be used as a demodulator. The circuit of such a typical detector is shown in Figure 7.11. The diode first rectifies the signal to leave only the positive side of the signal, and then a capacitor removes any of the remaining carrier frequency components to leave the demodulated signal [101]. Unfortunately, diodes are not linear and can cause signal distortion. Its noise performance is not particularly good at low signal levels. Figure 7.12 shows the diode envelope demodulator for the fully differential capacitive interface.

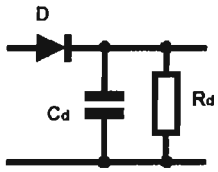

FIGURE 7.11: The schematic of a diode envelope detector.

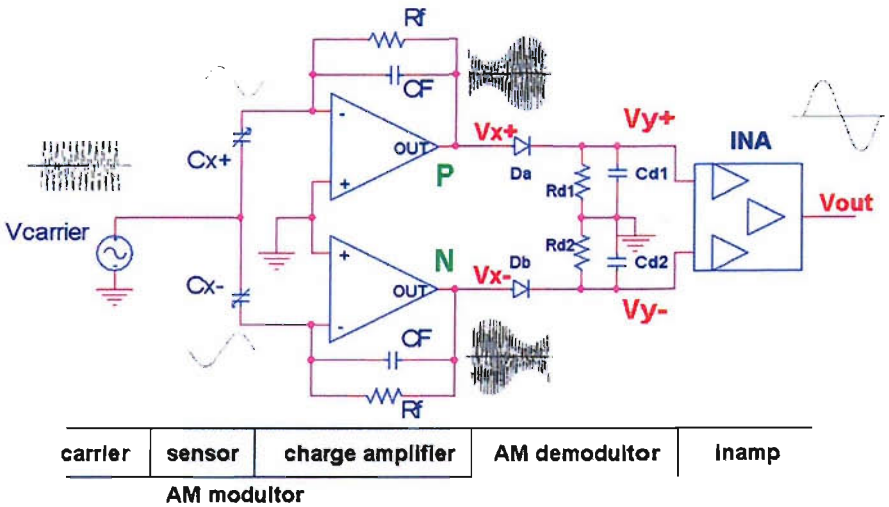

FIGURE 7.12: Diode envelope demodulation for a fully differential capacitive interface.

In order to demodulate the AM signal, the time constant R_dC_d is chosen so that the sensor signal with frequency f_{signal} is transferred unaffectedly and the carrier $f_{carrier}$ is filtered:

$$f_{signal} \ll \frac{1}{2\pi R_d C_d} \ll f_{carrier} \tag{7.3}$$

The signal is then amplified by an instrumentation amplifier (INA) with gain G_{INA}. The output voltage can be calculated by $V_{out} = G_{INA}(V_{x+} - V_{x-})$. Assuming good matching among components and $R_{pp} \gg R_{ps}$,

$$\begin{aligned} V_{out} &= -G_{INA} \times \left(\frac{R_{pp}}{R_{pp} + R_{ps}} \times \frac{(C_{x+} - C_{x-})}{C_f} \times V_{carrier} + (V_{diode+} - V_{diode-}) \right) \\ &\approx -G_{INA} \times (\frac{2\Delta C_x}{C_f}) \times V_{carrier} \end{aligned} \tag{7.4}$$

where V_{diode} is the forward voltage of a diode. However, there will be some offset when the two channels don't match precisely, so offset nulling is needed.

During the demodulation process in one period of the $V_{carrier}$, the diode is reverse biased about 7/8 part of the period and forward biased about 1/8 part of the period [96]. When the diode is reverse biased, both the signal and the noise of the pickoff preamplifier are not transferred by the demodulator due to the high resistance of the diode ($r_{diode} \approx \infty$). When the diode is forward biased, both the signal and the noise of the pickoff preamplifier are transferred by the demodulator due to the very low resistance of the diode ($r_{diode} \approx 0$). A Pspice model using the diode envelope as the demodulator is shown in Figure 7.13. Figure 7.14 shows the simulation result with ideal matching between the two channels except 1% mismatch between sensing capacitors (Cx1 and Cx2). Compared with the other simulations, it can be seen that for a carrier frequency of 1MHz, using the diode envelope as demodulator can achieve a better linearity than with the components AD630 and bigger output amplitude than with the components AD734. The reason might be that the bandwidth of the AD630 is not suitable for demodulating a carrier of 1MHz, and AD734 has a 20dB gain loss due to its design. Although using discrete analog switches and a comparator to build a phase-sensitive demodulator is good solution, the diode envelope was adopted as the demodulator in the PCB prototype due to very simple implementation.

7.2.4 Force Feedback Schemes

The capacitors formed by the electrodes around the proof mass of the sensing element are used for readout and force feedback. There are, in principle, two possible configurations: a) spatial multiplexing as shown in Figure 7.15(a), which use two separate sets of capacitors for readout and force feedback; b) time multiplexing as shown in Figure 7.15(b), which share the same capacitors but a fraction of a cycle is used for readout, the remaining time for force feedback. The advantage of time multiplexing is higher signal amplitude, but

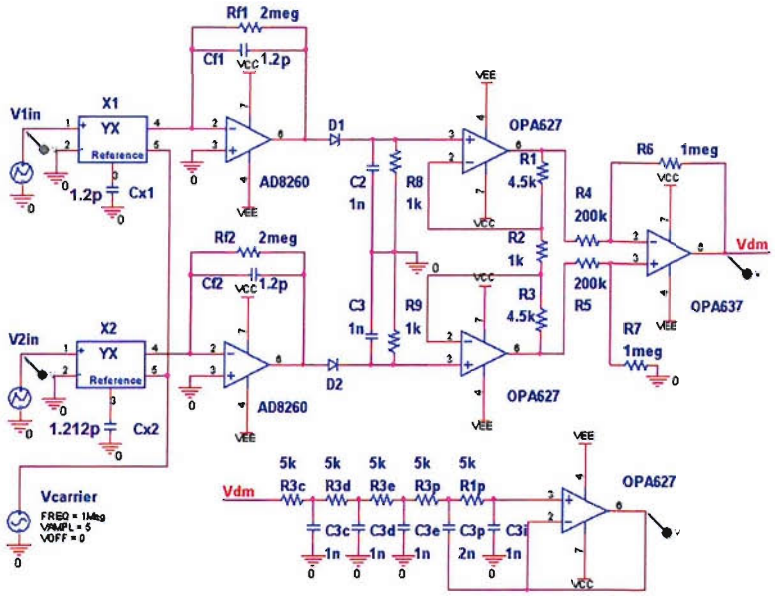

FIGURE 7.13: Pspice model using a diode envelope as demodulator.

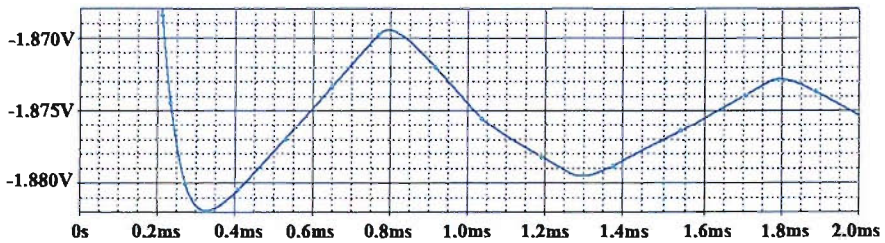

FIGURE 7.14: Pickoff output with a diode envelope as demodulator.

it will increase the requirement for circuit frequency response. The advantage of spatial multiplexing is low requirement for circuit frequency response and common mode rejection, but the signal amplitude will be reduced. In the PCB prototype, a spatial multiplexing strategy is applied and the connection between the electrode of the sensing element and surrounding circuits is shown in Figure 7.16. To avoid any feedback cross-talk effect on the sensor output, there is the need to disconnect the feedback signal from the sensing element during the readout phase. Figure 7.17 shows the control sequence using a GAL6001B. In fact, there are two separate DAC in a high-order electromechanical ΣΔM: a) one DAC for the conversion from a feedback voltage to an electrostatic force on the proof mass, which is called electromechanical DAC; b) another DAC for the electronic feedback to the electronic ΣΔM loop filter. In Figure 7.17, analog switches S1, S2, S3 and S4 are low-active switches for force feedback on the proof mass. In fact, the electromechanical DAC with the timing control is a RTZ DAC. Analog switches S5, S6 and S7 perform a RTZ DAC. INA is the output bitstream and CLKO is the sampling clock with a frequency of 125 kHz, equivalent to an OSR of 62.5 in a 1kHz signal bandwidth. CLK (2MHz) is the main source clock of all other clocks. The ratio of the feedback time to the pickoff cycle is 75%; this leaves $2\mu s$ for the sensing phase.

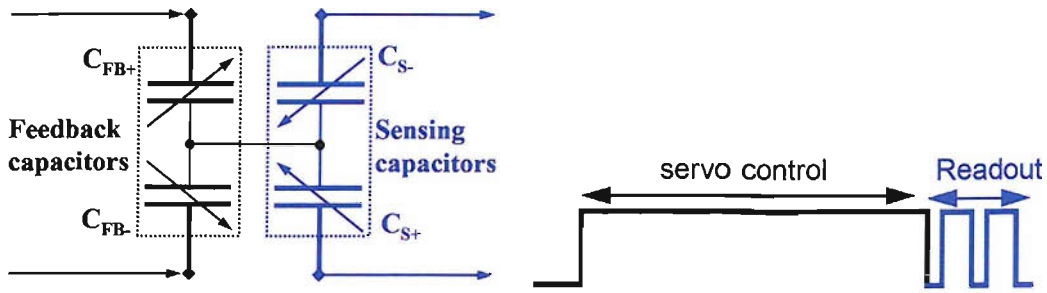

(a) Spatial multiplexing (b) Time multiplexing

FIGURE 7.15: Capacitor electrode arrangement for force feedback.

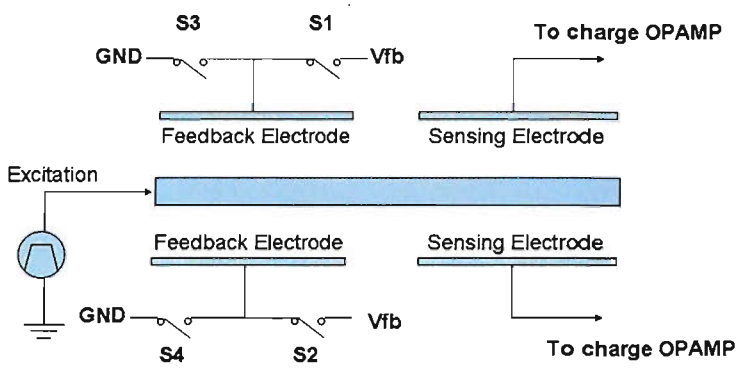

FIGURE 7.16: Connection diagram between the electrodes and surrounding circuits.

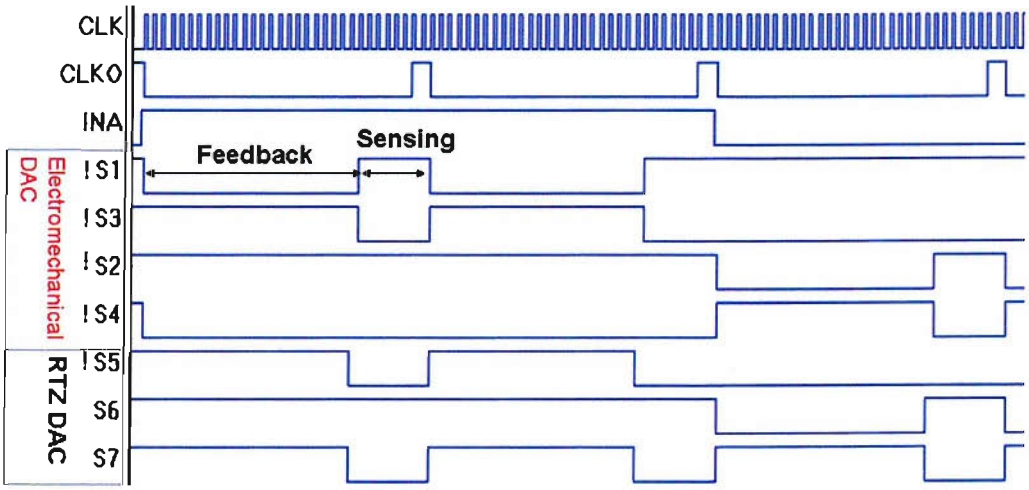

FIGURE 7.17: Timing diagram of the control signals for the analog switches of the two DACs.

To reduce the complexity of a PCB prototype, a simple multi-feedback topology is adopted. The input is a 1 kHz, 1V sinusoidal signal. Figure 7.18 shows the Pspice simulation of the output spectrum in a fifth-order CT electromechanical ΣΔM using single-ended circuits; the lower curve is with a hanning window, the other without any windowing. The noise floor is $200\mu V$, which corresponds to a SNR of 74dB.

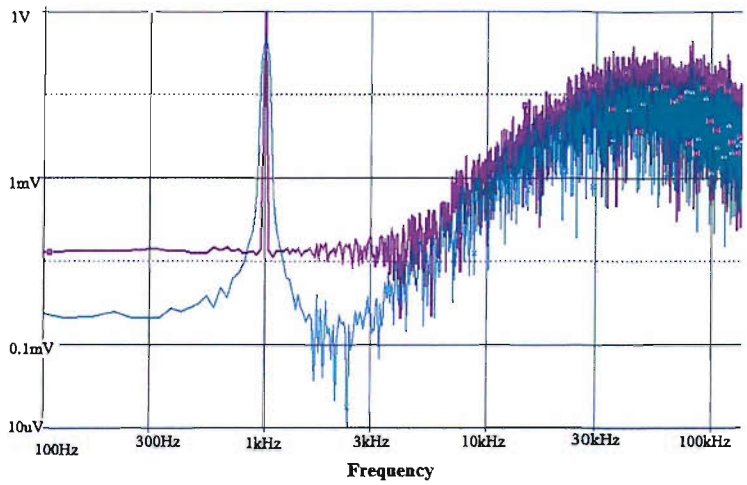

FIGURE 7.18: Pspice simulation: output spectrum of a fifth-order CT electromechanical ΣΔM using single-ended circuits: the pink solid line is without windowing, while the blue line is with Hanning window.

7.3 First PCB Prototype Experimental Results

The system power supply is ±9V volts for the analog circuits and +5V for the digital circuits. The force feedback voltage level is set to 1.5V, while the reference voltage of the DAC for purely electronic ΣΔM is set to 2.5V. The layout principle of the PCB is symmetrical. Most of the components on the four-layer PCB are in SMT packages as shown in Figure 7.19. Appendix 2 shows the schematic of the PCB board. The analog ground and digital ground are connected at the quantizer with a magnet bead. The symmetry of the two detection channels is very important, so the components selected for differential sensing element are all packaged in dual units. The two diodes used for demodulation are Schottky diodes with a forward voltage, V_{diode}=0.25V. After the power supply is switched on, component tuning is critical to get well-matched differential channels. Referring to Figure 7.12, the carrier is turned on, and the two integrating capacitors C_f are adjusted so that V_{x+} and V_{x-} are equal to -$V_{carrier}$ and V_{out} are equal to 0.

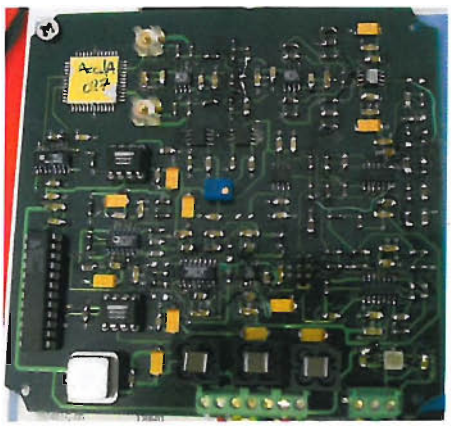

FIGURE 7.19: PCB of a fifth-order electromechanical ΣΔM.

The test environment is illustrated in Figure 7.20. The PCB has been mounted onto a permanent magnet vibration system manufactured by Ling Dynamic System (model V201). Its frequency band operates from dc up to 13 kHz with an input impedance of 6 ohm. The shaker is powered by an audio power amplifier (model Cambridge A1MK3) and a HP 3312A arbitrary waveform generator. A reference accelerometer ADX103 manufactured by Analog Device is soldered on the same PCB board with the sensor to monitor the loop performance. Both R9211B servo analyzer (ADVENTEST) and Marconi 2382/2380 spectrum analyzer are used to measure the spectrum of the output bitstream. Attention should be paid to the impedance matching between the output of the loop and the input of spectrum analyzer. Data acquisition is also performed using a PCI-DIO-32HS card with *LabView* [102]. Output bitstream INA is continuously acquired from a digital input channel. The acquisition rate is controlled by $(CLKO)$. After post-processing with MatLab, the frequency spectrum of the serial bitstream can be obtained.

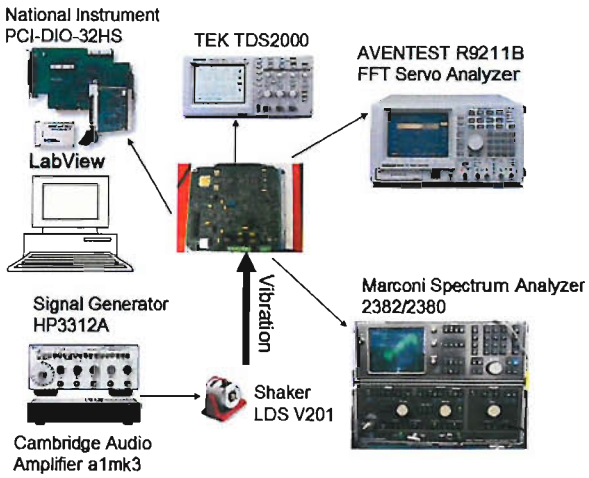

FIGURE 7.20: Prototype test environment.

The order of the ΣΔM on this PCB prototype can easily be chosen from second-order to fifth-order by switching on/off the setting jumper. Figure 7.21 shows a series of spectra of the quantizer output bitstream measured by the ADVANTEST R9211B FFT servo analyzer: (a). second-order noise floor; (b). second-order with 0.1g 1kHz sinusoidal input; (c). third-order noise floor; (d). third-order with 0.1g 1kHz sinusoidal input; (e). fourth-order noise floor; (f). fourth-order with 0.1g 1kHz sinusoidal input; (g). fifth-order noise floor; (h). fifth-order with 0.1g 1kHz sinusoidal input. The maximum SNR of the prototype is about 70dB, which is 20dB below the theoretical simulation due to the electronic noise dominating in the signal band. Moreover, there is little difference between the fourth-order loop and the fifth-order loop, however, as discussed in Chapter 2.4, the spectrum slope of the measurement results are nearly 80dB/decade and 100dB/decade, respectively, which denotes that the control systems are a fourth-order ΣΔM and a fifth-order ΣΔM, respectively. In order to further reduce the electronic noise in the signal band, a second PCB prototype was motivated to implement using a fully differential circuit topology. It consists of a fully differential pickoff and a fully differential continuous-time ΣΔM.

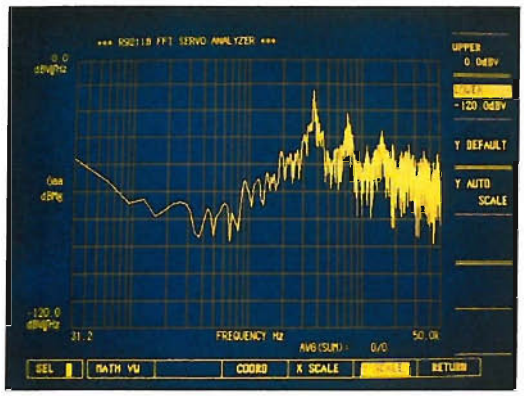

(a) second-order noise floor

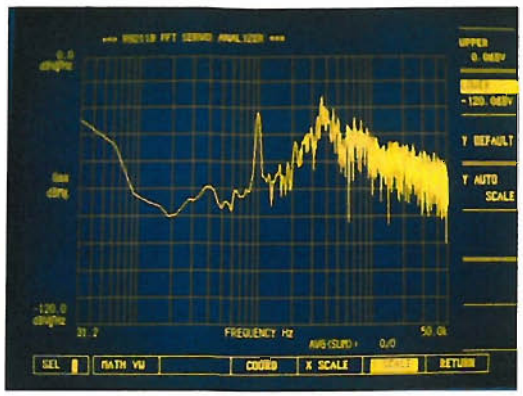

(b) second-order with 0.1g 1kHz sinusoidal input

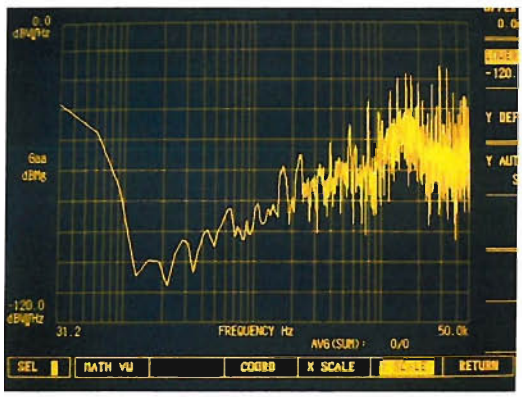

(c) third-order noise floor

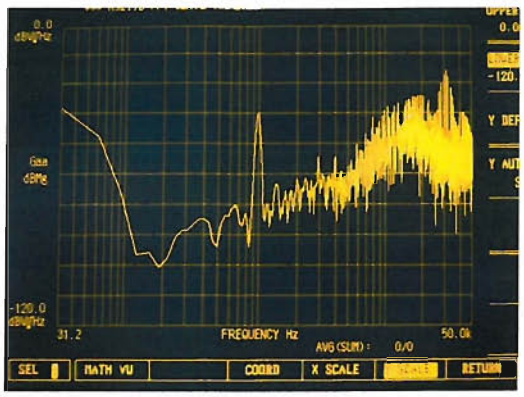

(d) third-order with 0.1g 1kHz sinusoidal input

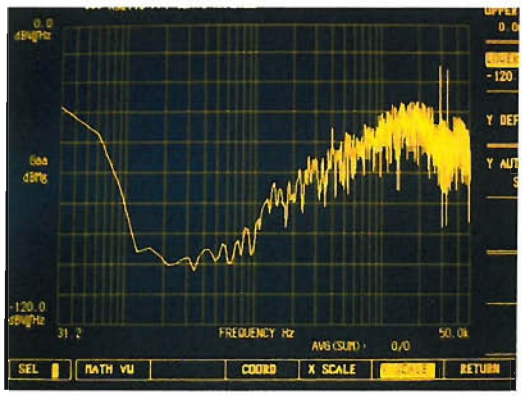

(e) fourth-order noise floor

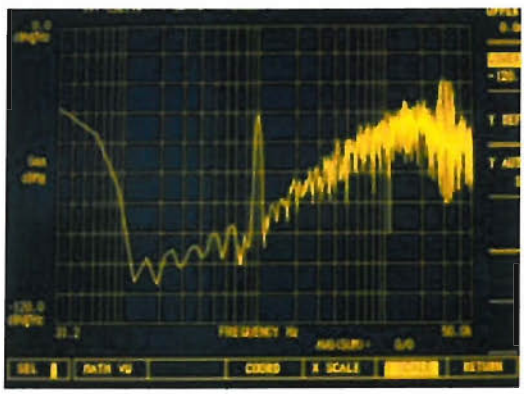

(f) fourth-order with 0.1g 1kHz sinusoidal input

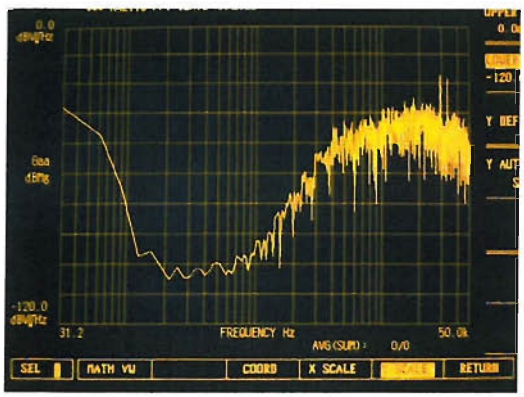

(g) fifth-order noise floor

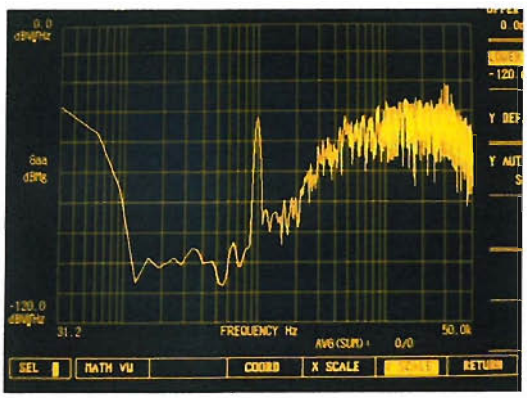

(h) fifth-order with 0.1g 1kHz sinusoidal input

FIGURE 7.21: Spectrum of the output bitstream measured by ADVANTEST R9211B FFT servo analyzer for high-order electromechanical ΣΔM.

7.4 Second PCB Prototype Experimental Results

The second PCB prototype is based on fully differential circuits. In a fully differential circuit, even though V_{x+} and V_{x-} may have different rising and falling slopes, the rising and falling edges of the differential signal V_{xd}=V_{x+} − V_{x-} are intrinsically symmetrical, as illustrated in Figure 7.22. Therefore, a fully differential circuit can get rid of inter-symbol effect on a ΣΔM [87]. To reduce the complexity of the second version PCB, the simple multi-feedback topology is used again.

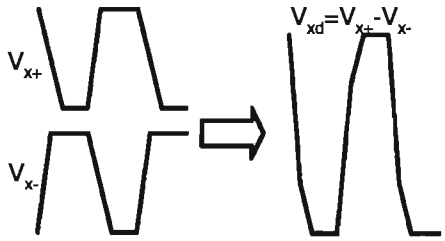

FIGURE 7.22: Inter-symbol effect on a fully differential CT ΣΔM.

Figure 7.23 shows the Pspice simulation of the output spectrum in a fifth-order CT electromechanical ΣΔM using fully differential circuits. The noise floor is below 50μV, while the noise floor of single-ended circuits (Figure 7.18) is about 0.5mV. The whole schematic of the fifth-order electromechanical ΣΔM is attached in Appendix 3. The simulation results are shown in Figure 7.24. The loop output noise floor is shown in Figure 7.24(a), while Figure 7.24(b) shows the output spectrum in response to a 0.1g, 1kHz sinusoidal input acceleration. Using the same test environment (Figure 7.20), the experimental results are shown in Figure 7.25. The output spectrum corresponds to a SNR of 90dB, in response to a 1kHz and 0.1g sinusoidal input acceleration. This is a considerable improvement compared with the first version single-ended circuits. These two pictures are only available after the Southampton fire. It can be seen that a dc component appears in the spectrum, which comes from a small offset from circuit blocks located after the demodulator and lowpass filter. Comparing Figure 7.25 with Figure 7.24, it can be seen the experimental results agree well with the simulation. Alternatively, as discussed in Chapter 2.4, it can be clearly seen that both the spectrum slope of the measurement results are 100dB/decade, which indicates that the control system is a fifth-order ΣΔM. These experimental results are preliminary due to the fabricated sensors were destroyed by the Southampton University fire. The noise floor is still little higher than expected due to the performance limitation of the sensor used for the prototype. Although spectrum averaging [23] can further reduce the noise floor and thus the harmonic distortion can be clearly shown, this is not available due to the performance limitation of the spectrum analyzer used in the project.

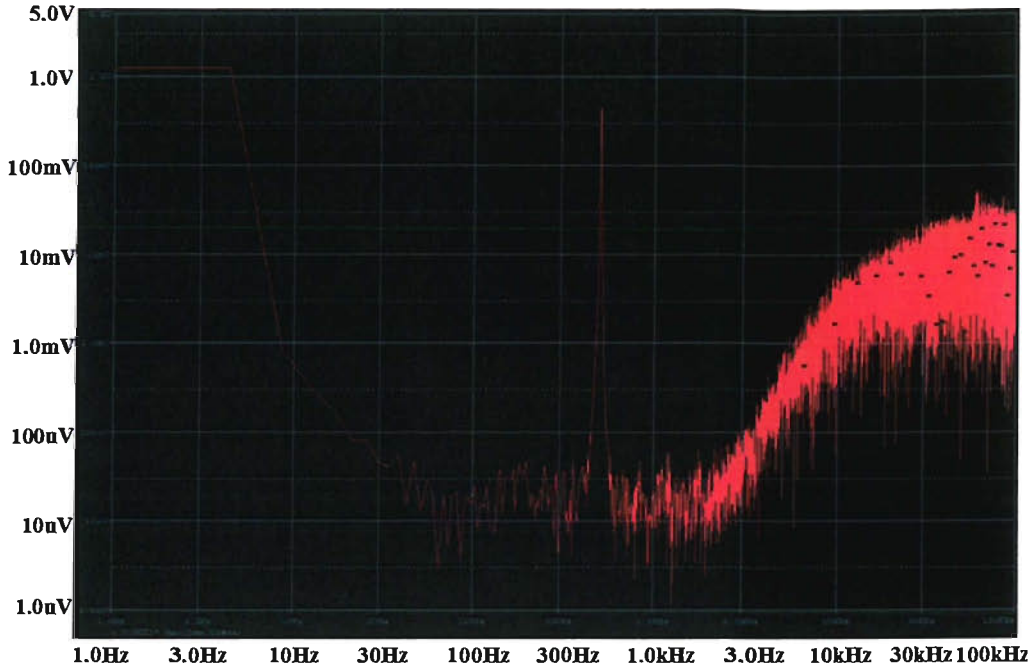

FIGURE 7.23: Pspice simulation: output spectrum of a fifth-order CT electromechanical ΣΔM using fully differential circuits.

7.5 Summary

A CT high-order electromechanical ΣΔM can get a similar performance as that of a DT high-order electromechanical ΣΔM using the same topology and gain coefficients. The extra loop delay is not a significant problem for a control system using a high-order ΣΔM if the sampling frequency is relatively low. Front-end circuits are analyzed, including the pickoff circuit and three demodulation circuits. Using available commercial components, a diode envelope was chosen to demodulate the 1MHz carrier signal in a PCB prototype. A CT fifth-order electromechanical ΣΔM was used for the PCB prototypes. Due to using a single-ended circuit topology, the experimental results of the first PCB prototype showed a SNR of about 70dB. While in the second PCB prototype, a fully differential circuit topology was adopted, measurements indicate that a SNR of 90dB in a 1kHz signal band was achieved. This measurement result agrees well with simulations of the fifth-order electromechanical ΣΔM.

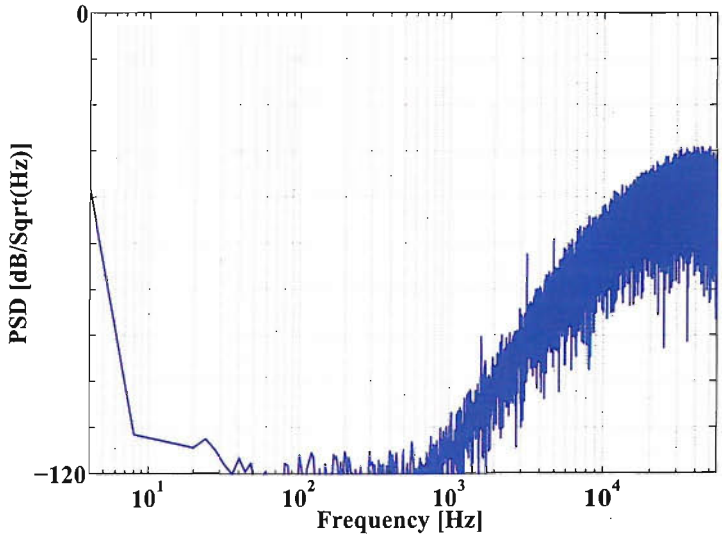

(a) A fifth-order noise floor (2nd version)

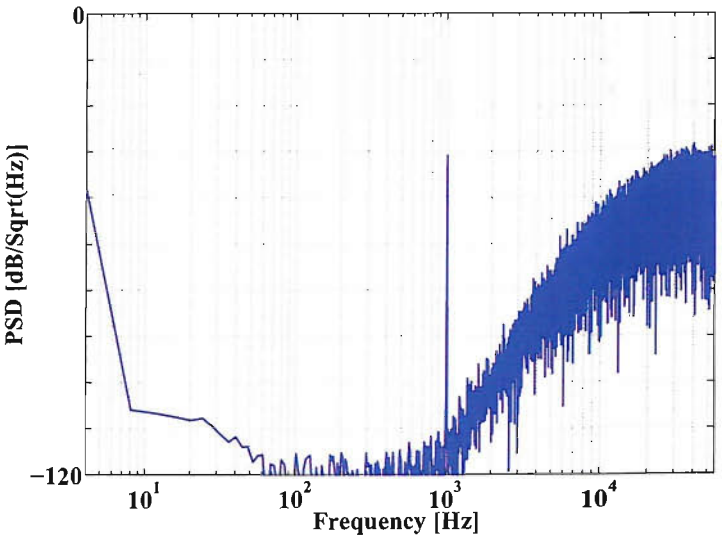

(b) A fifth-order with 0.1g, 1kHz sinusoidal input (2nd version)

FIGURE 7.24: Simulations: spectrum of the output bitstream of the fifth-order electromechanical ΣΔM (2nd version).

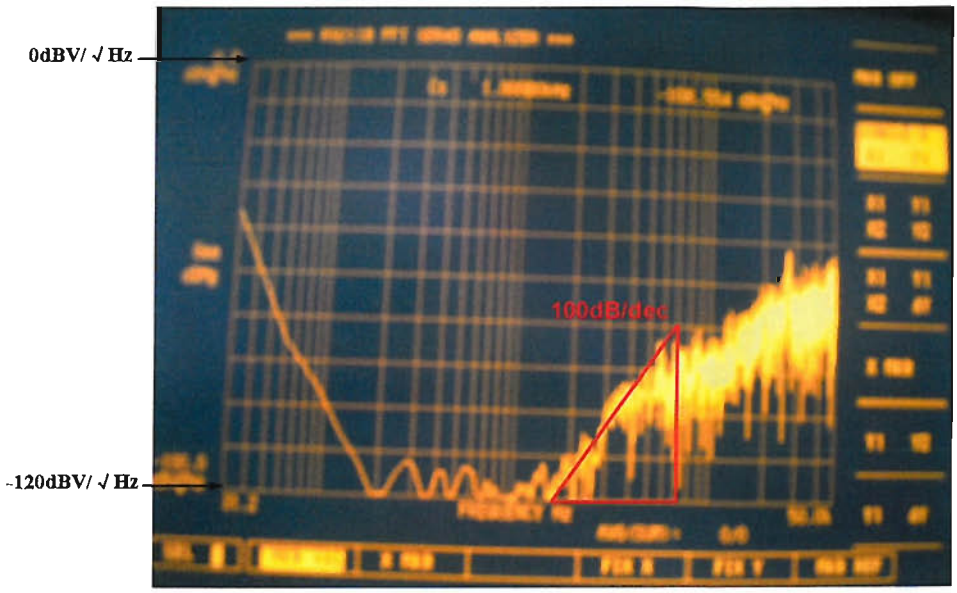

(a) A fifth-order noise floor (2nd version)

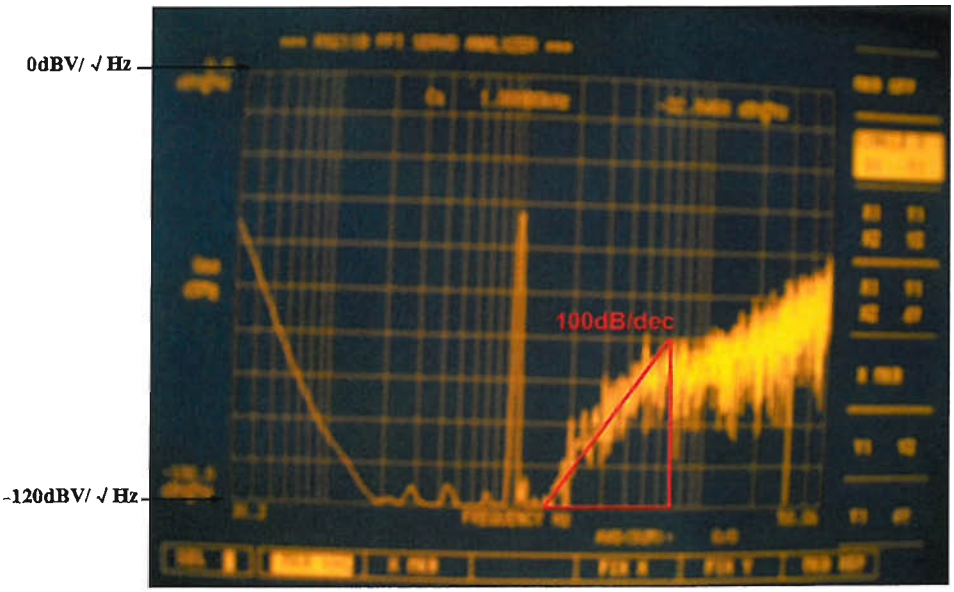

(b) A fifth-order with 0.1g, 1kHz sinusoidal input (2nd version)

FIGURE 7.25: The spectrum of the output bitstream measured by ADVANTEST R9211B FFT servo analyzer for the fifth-order electromechanical ΣΔM (2nd version).

Chapter 8

Microfabrication of A Prototype Accelerometer

8.1 Motivation

As the simulations done in Chapter 4 and the requirements for navigation/guidance applications, a very high performance sensing element is required to validate the design methodology of a high-order electromechanical ΣΔM. Quantization noise as discussed in 4.3, should have considerably lower noise floor than mechanical noise and electronic noise. In order to get a very large dynamic range (for example 100dB) of the control system, the critical parameter of the sensing element is the mechanical noise floor, which should be below $1\mu g/\sqrt{Hz}$ in a 1kHz bandwidth (for a full-scale input ±2g). However, there is no such high performance device commercially available. Another important issue for the control system using an electromechanical ΣΔM is high-order parasitic mechanical modes [10]. The sensing element is usually modeled as an ideal second-order mass-spring-damper system, which is characterized by a single resonant frequency. In fact, the dynamics of comb electrodes and springs result in high-order parasitic resonant frequencies. As investigated by Seeger [103], the parasitic modes should be above $f_s/4$ (f_s the sampling frequency of the quantizer) so that the mechanical sensing element acting as a noise-shaping filter does not disturb the operation of an electromechanical ΣΔM. Comb electrodes of a sensing element should be designed with short and therefore rigid finger electrodes. This leads to very high parasitic resonant frequencies, well above any frequencies of the feedback signal that potentially could excite the sense fingers and thus degrade the SQNR. A fully-differential structure of the sensor also helps to cancel microfabrication mismatches to first order. Additionally, to achieve a similar performance, the sampling frequency in a high-order electromechanical ΣΔM is much lower than that of a second-order loop, thus high-order loops have relatively higher immunity to the high-order parasitic modes of a sensing element than a second-order loop. Therefore, a high performance MEMS accelerometer is needed with the specific characteristics as discussed above.

8.2 Sensing Element Design and Analysis

8.2.1 Fully Differential Structure

A lateral single-axis accelerometer is designed with a fully differential structure. Figure 8.1 shows a schematic diagram of the fully differential sensing element.

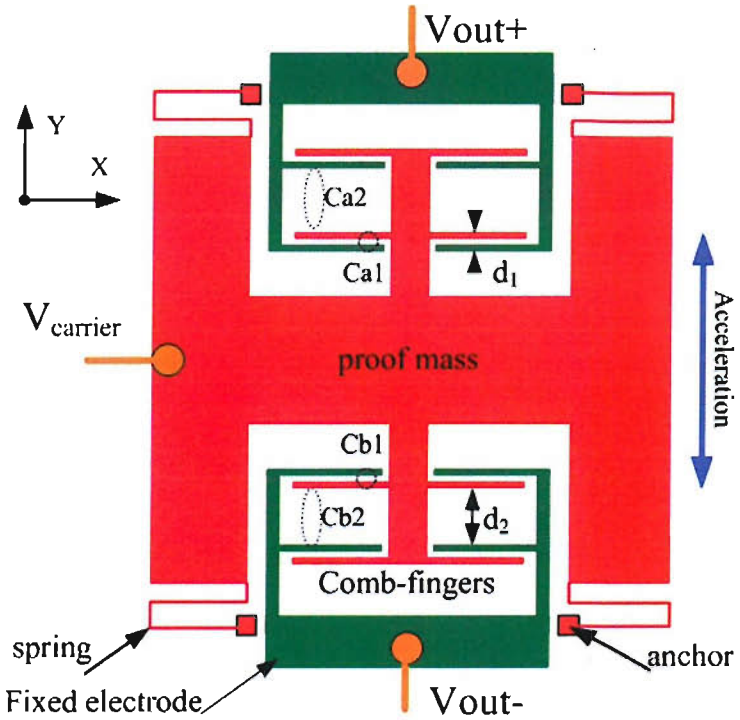

FIGURE 8.1: Schematic diagram of an accelerometer with a fully differential structure.

The fully differential accelerometer has two sets of capacitors (C_{a1} and C_{b1}, C_{a2} and C_{b2}) connected in series. The capacitor C_{a1} and C_{b1} have a nominal gap d_1 of $=3\mu$m while C_{a2} and C_{b2} have a gap of $d_2 = 30$ μm. An excitation voltage is applied to the common electrode - the proof mass, while the fixed electrodes are connected to two pickoff preamplifiers. The electrostatic force caused by the excitation voltage acts on the proof mass in symmetrically balanced directions and thus its effect is negligible. The layout is shown in Figure 8.2. The nominal capacitances at zero acceleration are calculated by:

$$C_{a1} = C_{b1} = N_{fingers} \cdot \varepsilon_0 \frac{A_{finger}}{d_1} = 1800 \times 8.85 \times 10^{-12} \times 60 \times 10^{-6} \times (60/3) = 19.12pF$$

$$C_{a2} = C_{b2} = N_{fingers} \cdot \varepsilon_0 \frac{A_{finger}}{d_2} = 1800 \times 8.85 \times 10^{-12} \times 60 \times 10^{-6} \times (60/30) = 1.912pF$$

It should be noted that the sensing capacitors C_{a1} and C_{b1}, C_{a2} and C_{b2} are in opposite arrangement, hence the capacitance changes in opposite direction when acceleration is applied.

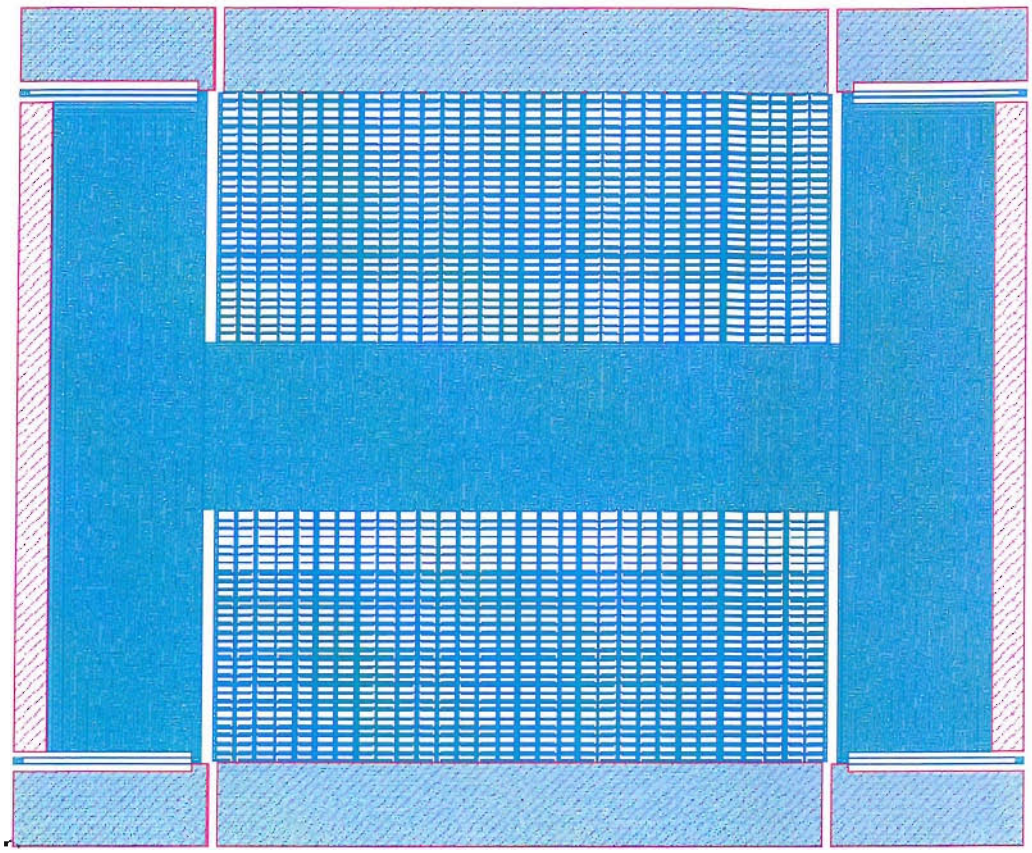

FIGURE 8.2: Layout of a fully differential microaccelerometer.

8.2.2 Spring Design

In order to design highly sensitive accelerometer, accurate predictions of the mechanical spring constant are needed. For simple suspensions the linear or first order, mechanical spring constant may be derived from basic beam bending equations relating deflection to loading. Under typical mechanical deflections experienced by accelerometers, this approximation of linear bending is appropriate. A folded beam structure is chosen for the spring design of this single-axis accelerometer, which has two folded beam springs, one on each side. The total spring constant of the microacclerometer is given by [53]:

$$k_y = \frac{24EI_y}{l^3} = \frac{2EtW^3}{l^3} \tag{8.1}$$

$$k_z = \frac{24EI_z}{l^3} = \frac{2Et^3W}{l^3} \tag{8.2}$$

where $E = 1.65 \times 10^{11} N/m^2$ is the Young's modulus, l represents the beam length, W the beam width and t the beam thickness. Figure 8.3 shows the structure of the spring, for the beam length l=800μm, thickness t=60μm, and width W=5μm, the spring stiffness

k_y=4.95 N/m is calculated by Equation 8.1. AutoSpring solver is the spring constant extractor of CoventorWare, which allows the extraction of multi-dimensional, non-linear spring behaviourfrom complex tether designs. The simulation shown in Figure 8.4 is done from first-order to fourth-order. In the range of deflection -1μm to +1μm, the stiffness constant is 1.25 N/m for one of four parallel springs, so the total K_y is 4 x 1.25=5 N/m, which agrees well with the analytical result.

FIGURE 8.3: Structure of the spring (1/4).

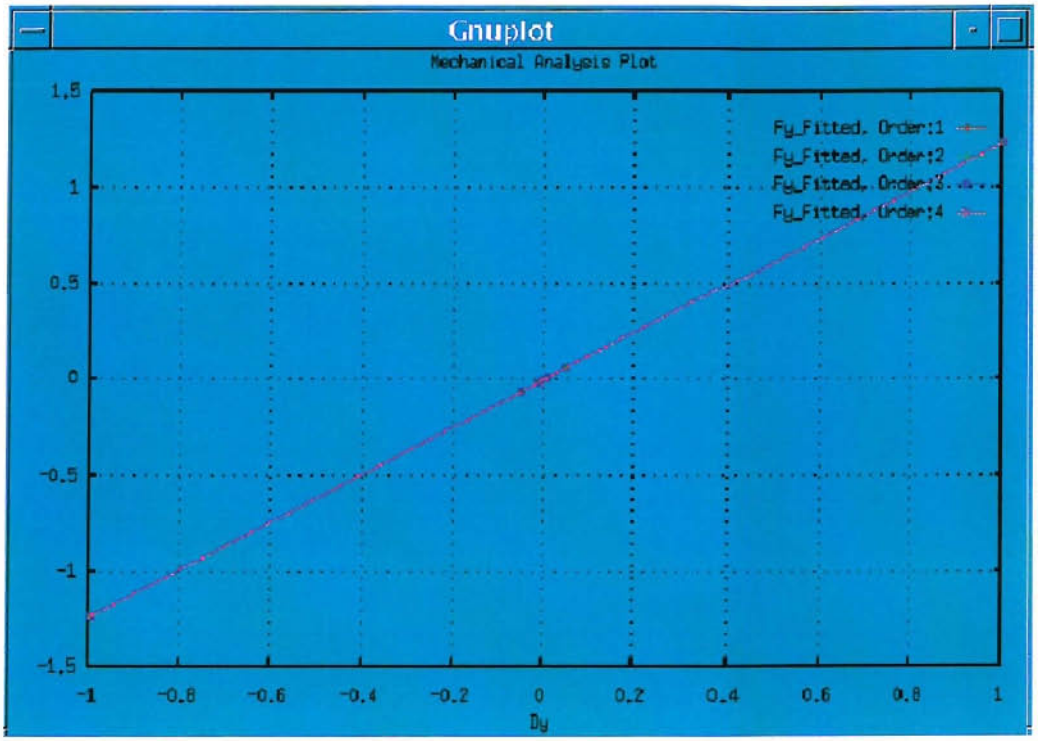

FIGURE 8.4: Mechanical spring simulated using the AutoSpring solver (CoventorWare).

8.2.3 Damping Optimization

The damping in a micromachined sensing element consists of both structural damping and viscous flow of gas within the structure region [104]. Since at typical operating pressures the structural damping component is orders of magnitude lower than gas damping, it can be ignored. The gas damping of a micro sensing element can be classified into a component due to Couette flow and a component due to squeeze-film damping. Couette flow is a viscous flow, which occurs when two plates slide parallel to each other under zero pressure gradients. An example of Couette flow may be found between the proof mass and the substrate during

motion of the proof mass. Typically this Couette force is an order of magnitude smaller than squeeze-film forces, and in many designs may be neglected. Squeeze-film damping occurs when the gap between two closely spaced parallel surfaces changes, it determines the dynamic behaviourof a micromachined sensing element. In the case of a rectangular plate ($L \times W$, $W \leq L$), the linearized Reynolds equation can be applied, the squeeze number, representing the compressibility of the squeeze film, is defined as [105]:

$$\beta = \frac{12\mu_{eff}L^2W}{P_0h_0^2} \tag{8.3}$$

where μ_{eff} is the air effective dynamic viscosity and will be defined below, L is the length of the rectangular plate, w is the width, P_o the ambient pressure, h_0 the mean film thickness and ω the oscillation frequency of the mass. The effective viscosity is defined as:

$$\mu_{eff} = \frac{\mu}{1 + 9.638\left(\frac{P_0}{P}K_n\right)^{1.159}} \tag{8.4}$$

where μ is the air dynamic viscosity, and the second term of the denominator is the correction term as function of the pressure (P is normalized pressure) and Knudsen number K_n. For large plates and thin gaps (i.e., $\beta \gg 0$), the gas acts as a compressible fluid since viscous effects at the plate edges trap air between the plates, the fluid does not move in response to the motion of the mass, but behaves as a spring. Small plates and wide gaps (i.e., $\beta \approx 0$) permit lateral motion of the gas, so the gas approximates incompressible viscous flow. Assuming ambient pressure at the edges (the edge boundary condition) the linearized Reynolds equation can be solved analytically for plates [106]. The damping coefficient d_a and spring stiffness k_a have been derived by Blech [105] and are provided below:

$$\begin{aligned} d_a &= \frac{64\beta P_0 A}{\pi^6 \omega h_0} \sum_{m,n=odd} \frac{m^2 + n^2/c^2}{(mn)^2[(m^2 + n^2/c^2)^2 + \frac{\beta^2}{\pi^4}]} \\ &= 0.8\frac{\mu_{eff}WL^3}{h_0^3} \sum_{m,n=odd} \frac{m^2 + n^2/c^2}{(mn)^2[(m^2 + n^2/c^2)^2 + \frac{\beta^2}{\pi^4}]} \end{aligned} \tag{8.5}$$

$$k_a = \frac{64\beta^2 P_0 A}{\pi^8 h_0} \sum_{m,n=odd} \frac{1}{(mn)^2[(m^2 + n^2/c^2)^2 + \frac{\beta^2}{\pi^4}]} \tag{8.6}$$

where m and n are odd integers and $c = W/L$, a geometry-dependent parameter.

The comb fingers in conventional capacitive micro accelerometer use long parallel plates as electrodes. In order to maximize the sensitivity of a capacitive accelerometer, the overlap length of comb fingers has to be kept long enough. However, the damping coefficient is very large and for high precision applications the sensors need vacuum packaging to lower the damping and to minimize the mechanical noise floor. There is a design trade-off between

the sensitivity and mechanical noise. From Equation 8.5, the relationship between the damping coefficient and the overlap length of comb fingers is cubic, or $d_a \propto W\,(L/h_0)^3$, squeeze film damping optimization can be realized by reducing the comb finger overlap area and increasing the number of parallel comb fingers to preserve the capacitance. For the design with W=60μm, L=60μm, c=1, the damping coefficient of the 1800 pair electrodes can be derived using Equation 8.5 as following:

$$\sum_{m,n=odd} \frac{m^2+n^2/c^2}{(mn)^2[(m^2+n^2/c^2)^2+\frac{\beta^2}{\pi^4}]} \approx \frac{c^2}{c^2+1}+\frac{2c^2}{9(c^2+9)} = 0.522 \tag{8.7}$$

Considering at standard atmospheric pressure (0.1013 MPa or 1atm) and temperature 300K (27^o), the dynamic viscosity of air is $\mu = 1.86 \times 10^{-5}$ Kg/(m·s), therefore

$\mu_{eff} = 0.895 \times 1.86 \times 10^{-5}$ Kg/(m×s),

$d_a = (1800) \times 0.8 \times 0.895 \times 1.86 \times 10^{-5} \times 60 \times 10^{-6} \times (60/3)^3 \times 0.522 = 6.007 \times 10^{-3}$ (N/m/s)

The *MemDamping* simulation of CoventorWare analyzes the frequency-dependent damping and spring characteristics of thin films of gas. Figure 8.5 shows a graph plotting the damping coefficient of 1800 pair comb fingers (each width 60μm, overlap length 70μm) as a function of frequency for the sensing element. The analytical result above matches well with the simulation for low frequencies. Additionally, both the analytical calculation by Equation 8.6 and simulation show the spring stiffness k_a are so small that can be neglected.

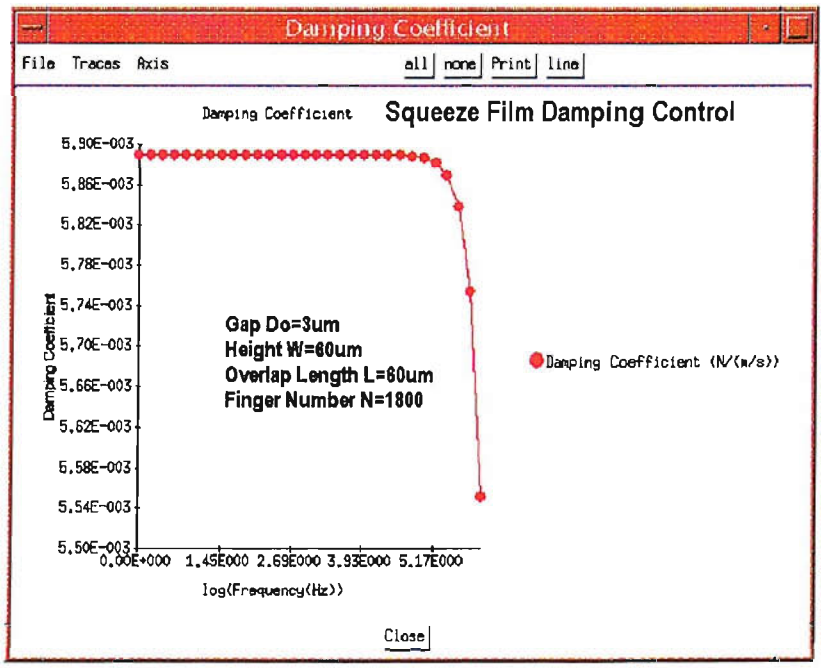

FIGURE 8.5: Squeeze-film damping simulated using the MemDamping Solver.

8.2.4 Modal Analysis

A modal analysis calculation computes the natural resonant frequencies of a mechanical structure at equilibrium, which define the frequency response of a sensing element. The system transfer function theoretically becomes infinite at the resonant frequency. These frequencies and their associated mode shapes represent the overall deformation of the mechanical structure oscillating at the modal frequency. The modal frequencies and shapes of a finite-element model can be calculated and visualized in CoventorWare through the MemMech solver. Because the modal analysis is performed on an undamped system, the amplitudes of these mode shapes do not indicate the actual amplitudes of the structure's motion and are thus normalized to a maximum deflection of 1 μm. The first mode is along the sensitive y-axis as shown in Figure 8.6, the resonant frequency is 323Hz. While the analytical result of the first mode is:

$$f_0 = \frac{1}{2\pi}\sqrt{\frac{k_y}{m}} = \frac{1}{2\pi}\sqrt{\frac{5N/m}{1.2\times 10^{-6}Kg}} = 325Hz \tag{8.8}$$

Figure 8.7 shows the second mode along x-axis, and its resonant frequency of 3.01kHz. Figure 8.8 shows the third mode along z-axis, and its resonant frequency of 3.96kHz. These modal frequencies are much larger than the first mode, resulting in low cross-axis sensitivity as expected.

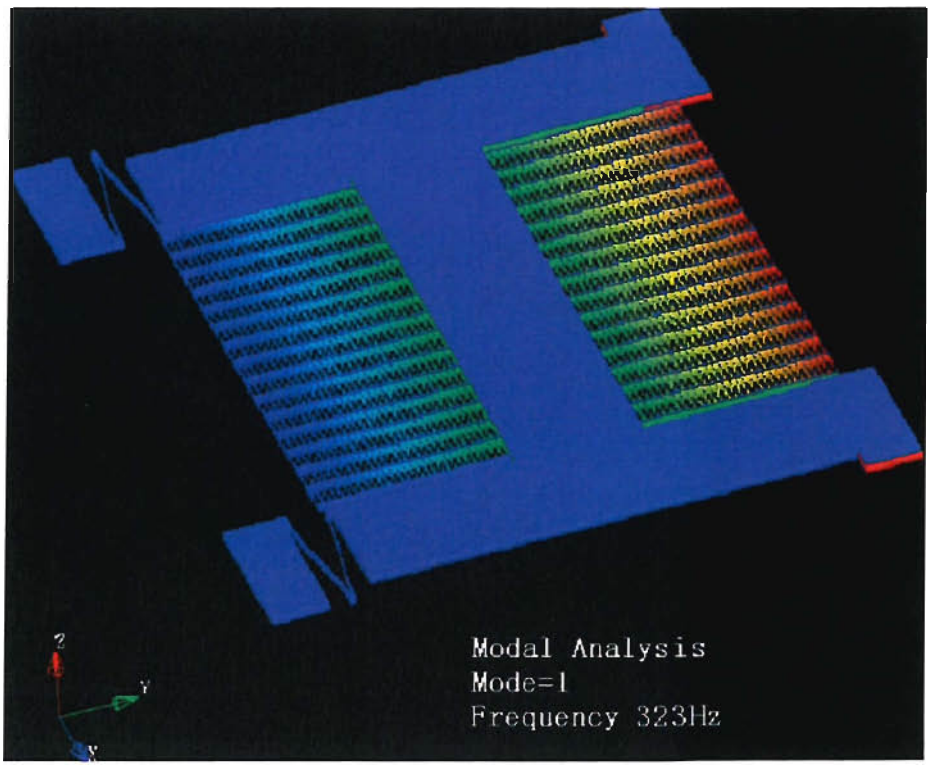

FIGURE 8.6: Modal analysis: mode=1, resonant frequency 323Hz.

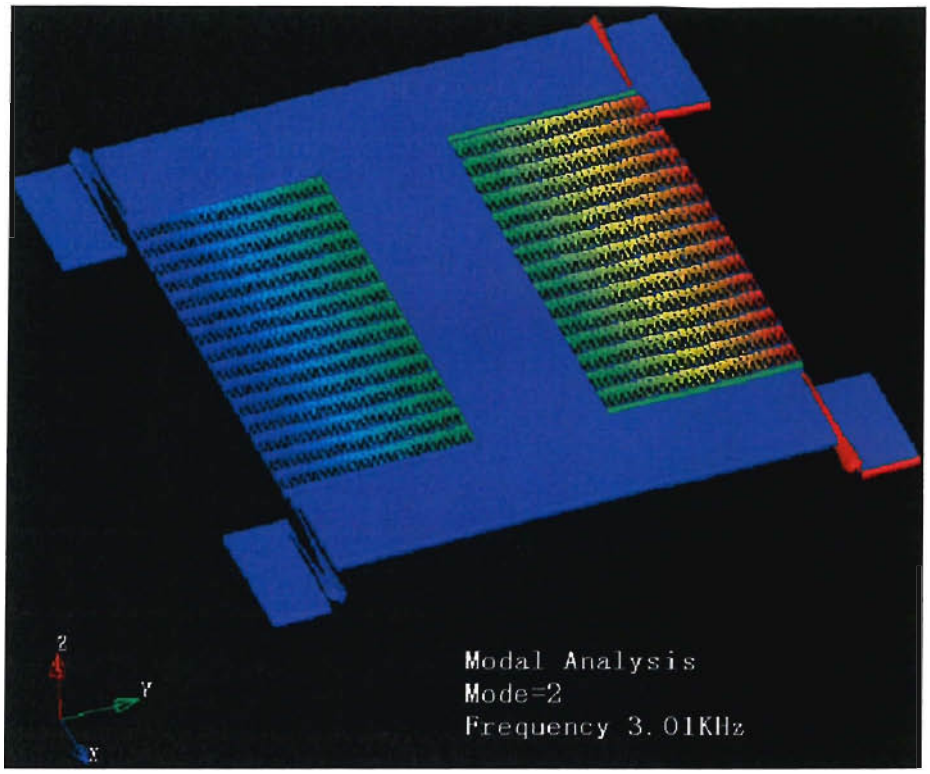

FIGURE 8.7: Modal analysis: mode=2, resonant frequency 3.01kHz.

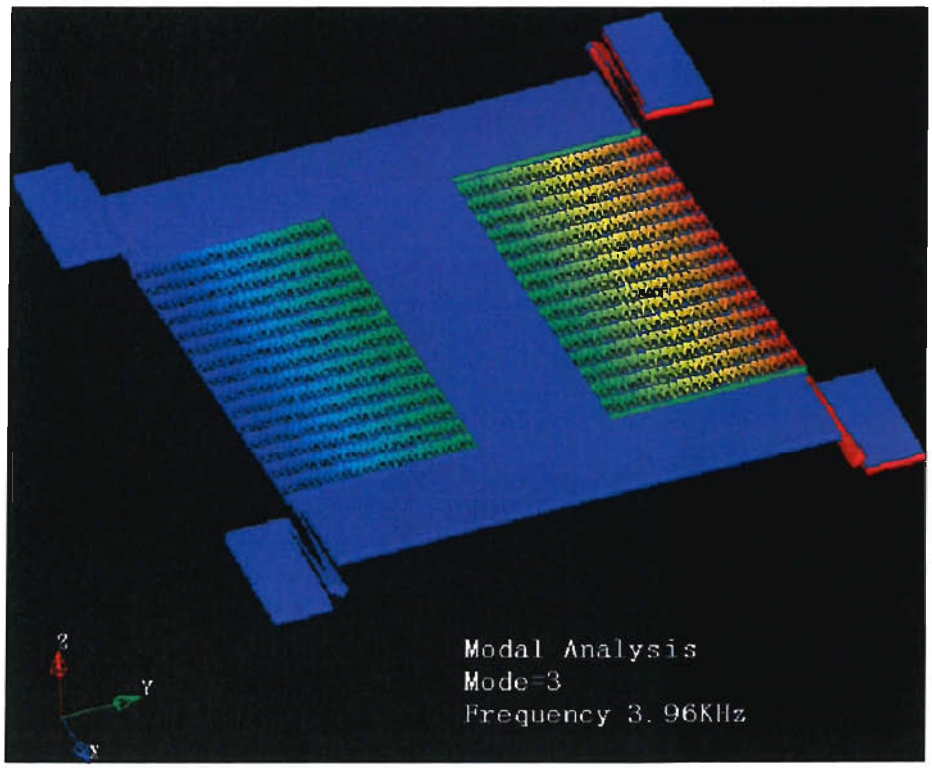

FIGURE 8.8: Modal analysis: mode=3, resonant frequency 3.96kHz.

8.2.5 Sensitivity and TNEA

The cross axis sensitivity is evaluated by specifying forces based body acceleration in X, Y and Z direction. From the displacement, the cross axis sensitivities for X-axis with respect to Y-axis can be calculated using the following equation [42]:

$$S_{a_x}^{a_y} = \frac{\Delta a_y/a_y}{\Delta a_x/a_x} = \frac{\Delta x_{1g}/(\Delta x_{2g} - \Delta x_{1g})}{\Delta y_{1g}/(\Delta y_{2g} - \Delta y_{1g})} \tag{8.9}$$

where $a_x = \frac{k_x \Delta x}{m}$ and $a_y = \frac{k_y \Delta y}{m}$. To determine the cross axis sensitivity, a two-stage simulation is performed by the MemMech solver of CoventorWare. First, 1g acceleration is applied both on the sense axis (y-axis) and the x-axis, simultaneously. Next, 2g acceleration is applied on x-axis while maintaining the 1g acceleration on y-axis. Figure 8.9(a) and Figure 8.9(b) show the deflections under these conditions. Using the similar conditions on y-axis and z-axis, Figure 8.9(c) and Figure 8.9(d) show the deflections under such conditions. Cross axis sensitivity for x- and z-axes are calculated using the equation above to be -70dB and -77dB, respectively.

The total static capacitance can be calculated by the *MemCap* of CoventorWare, which is the electrostatic solver that computes a charge matrix based on voltage conditions or a voltage matrix based on charge conditions, including the electric behaviourof lossy media. Figure 8.10 shows the capacitance of one array consisting 30 pair electrodes including fringe effects, the total static capacitance of 1800 pair electrodes is 60 x 4.721 = 28.32 pF, while analytic capacitance without fringe effects results in 21.03pF.

The static sensitivity of the accelerometer can be expressed as:

$$\mathbb{S} = \frac{dc}{da} = \frac{dc}{dx} \times \frac{dx}{da} = \frac{\varepsilon_0 A}{d_0^2} \times \frac{1}{\omega_r^2} = \frac{\varepsilon_0 \times A \times m}{d_0^2 \times k} = C \times \frac{9.8 \times m}{k \times d_0} (pF/g) \tag{8.10}$$

where ε_0=8.85e-12 is the permittivity of vacuum, A is the sensing area, m (1.2mg) the mass of the proof mass, k (4.95 N/m) the spring constant, and d_0 (3μ m) the gap between electrodes. The structure has a very high sensitivity $\mathbb{S}$=16.5 pF/g. The mechanical quality factor is calculated using Equation 2.4 to be 0.408, and the thermal noise equivalent acceleration (TNEA) can be calculated using Equation 2.11 to be 0.85 $\mu g\sqrt{Hz}$. Table 8.1 summarizes the parameters of the high-performance micro accelerometer.

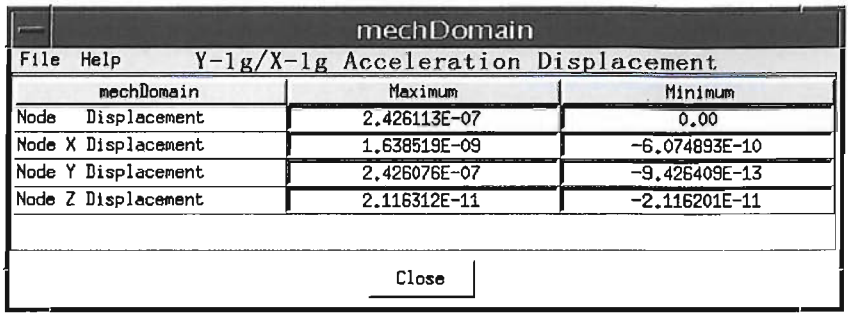

(a) input Y-1g/X-1g acceleration

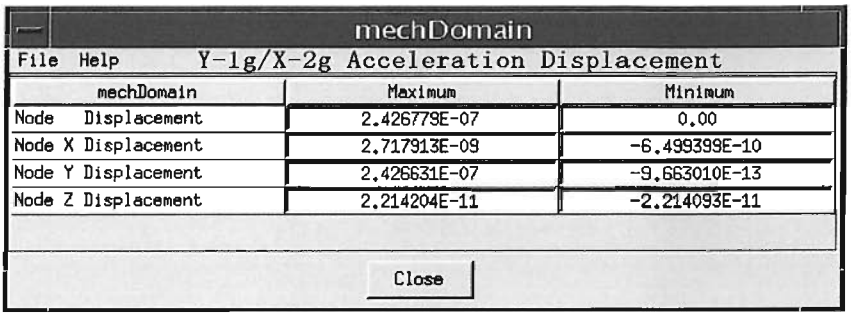

(b) input Y-1g/X-2g acceleration

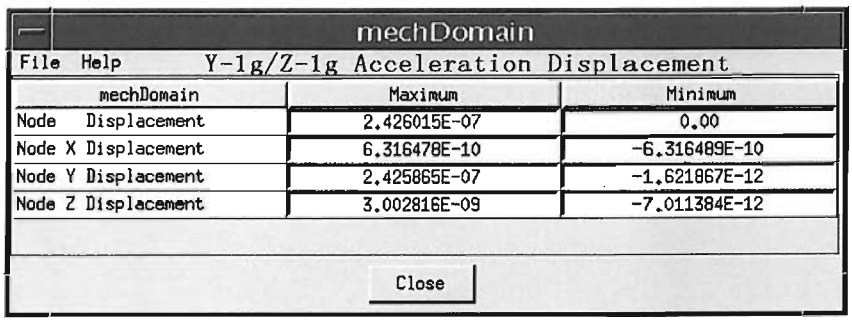

(c) input Y-1g/Z-1g acceleration

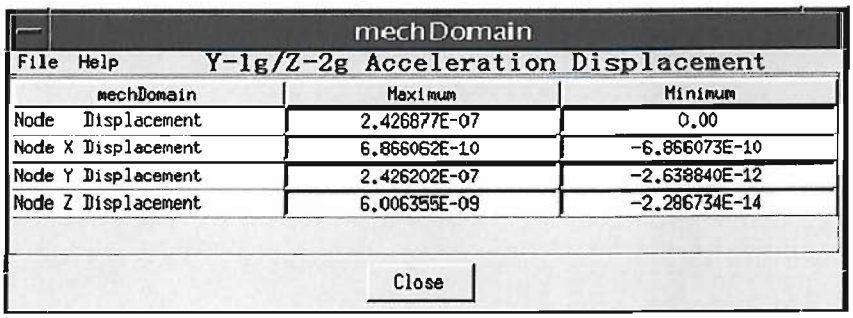

(d) input Y-1g/Z-2g acceleration

FIGURE 8.9: Cross sensitivity analysis, output displacement response to: (a) input Y-1g/X-1g acceleration; (b) input Y-1g/X-2g acceleration; (c)input Y-1g/Z-1g acceleration; (d) input Y-1g/Z-2g acceleration.

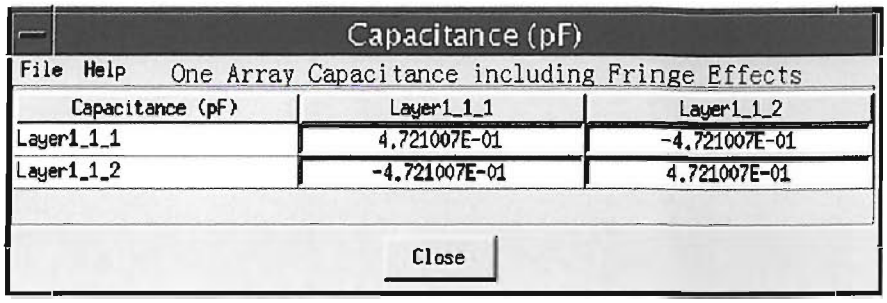

FIGURE 8.10: Capacitance including fringe effects (one array comb fingers=30).

Parameter	Value	Unit	Name
m	1.2	mg	*Mass of Proof Mass*
k_y	5	N/m	*Spring Stiffness*
b	0.006	Ns/m	*Damping Coefficient*
t	60	μm	*Thickness of Proof Mass*
L	70	μm	*Length of Comb Fingers (overlap 60μm)*
W	5	μm	*Width of Comb Fingers*
N	1800		*Number of Comb Fingers*
d_0	3	μm	*Sensing Gap Distance*
f_0	325	Hz	*Resonant Frequency(0.6% error from the MemMech solver)*
Q	0.41		*Quality Factor*
k_{xy}	-70	dB	*Cross Axis sensitivity (X-Y)*
k_{zy}	-77	dB	*Cross Axis Sensitivity (Z-Y)*
C_s	21.03	pF	*Static Sensing Capacitance*
$\mathbb{S}$	16.5	pF/g	*Static Sensitivity*
$TNEA$	0.85	$\mu g/\sqrt{Hz}$	*Mechanical Noise*

TABLE 8.1: Parameters of the μg micro-accelerometer

8.3 Fabrication Process

8.3.1 Silicon on Glass (SOG)

Fabricating the accelerometer using a silicon-on-glass process results in a low parasitic capacitance between the proof mass and the bottom nonconductive glass substrate. Furthermore, it is free of shear damping. By combining DRIE and anodic bonding, a large proof mass and very low stress can be achieved using single-crystalline bulk silicon. The residual stress is greatly removed compared with a poly-silicon surface micromachined process. The fabrication process is illustrated in Figure 8.11. The wafer parameters used in this process is summarized in Table 8.2. It requires three masks: the first is the recess mask for the Pyrex glass, the second is the structure mask, and the last is the metal contact pads for wiring. The fabricated sensor is shown in Figure 8.12(a). A local close-up view of parts of the electrode area and parts of the spring structure is shown in in Figure 8.12(b). The anodic bonding is shown in Figure 8.13. All these SEM pictures are preliminary fabrication results, the process was interrupted due to the Southampton University fire. The details of the fabrication process steps are described below:

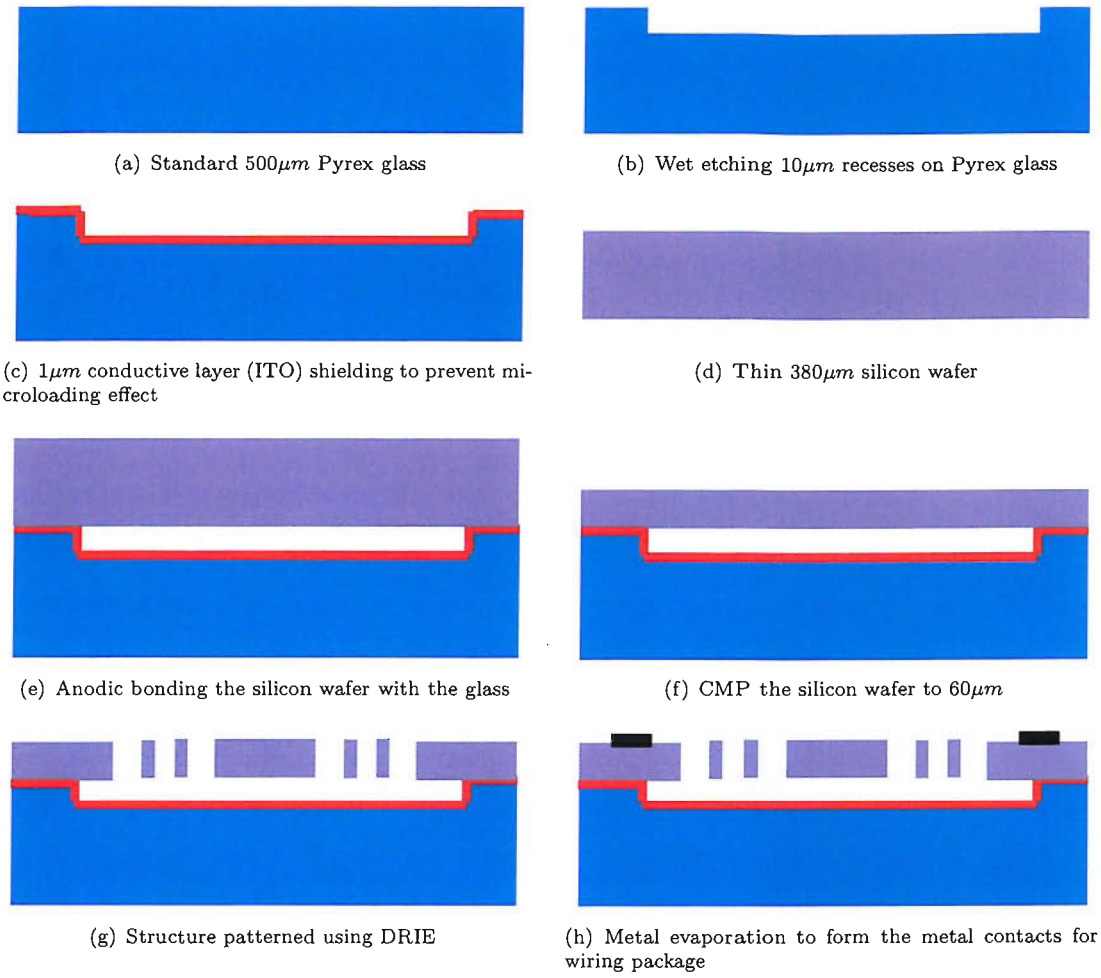

(a) Standard $500\mu m$ Pyrex glass

(b) Wet etching $10\mu m$ recesses on Pyrex glass

(c) $1\mu m$ conductive layer (ITO) shielding to prevent microloading effect

(d) Thin $380\mu m$ silicon wafer

(e) Anodic bonding the silicon wafer with the glass

(f) CMP the silicon wafer to $60\mu m$

(g) Structure patterned using DRIE

(h) Metal evaporation to form the metal contacts for wiring package

FIGURE 8.11: SOG fabrication process for the high performance accelerometer.

Size: $150mm$		
Type: N		
Orientation: $< 100 >$		
Resistivity: $0 - 0.1\ \Omega \cdot cm$		
Layer Name	**Thickness**	**Polished**
Silicon Layer	$380\mu m$	yes
Pyrex 7740 Glass Layer	$500\mu m$	N/A

TABLE 8.2: Wafer parameters of the SOG process.

1. The process uses a standard 7740 Pyrex glass (thickness $500\mu m$).

2. Glass recesses are etched $10\mu m$ deep using wet chemicals. The recess is located underneath the moving proof mass.

3. A $1\mu m$ conductive shielding layer is deposited on the glass recess area to prevent the microloading effects during DRIE. Microloading effect [107] is due to the different

etching rates for different high aspect ratio gaps. Without the conductive film the proof mass structure will have a non-uniform profile, especially for the thin fingers.

4. A thin $380\mu m$ silicon wafer is used for the structure.
5. Anodic bonding the silicon wafer with the standard Pyrex 7740 glass. Bonding voltage, temperature and time are 850V, 350°C and 120 mins, respectively.
6. A chemical mechanical polishing (CMP) process to thin the silicon wafer to $60\mu m$.
7. Silicon etching using DRIE (aspect ratio 20:1) to form the accelerometer structure.
8. Metal evaporation deposits metal to form contact pads for electrical wiring.

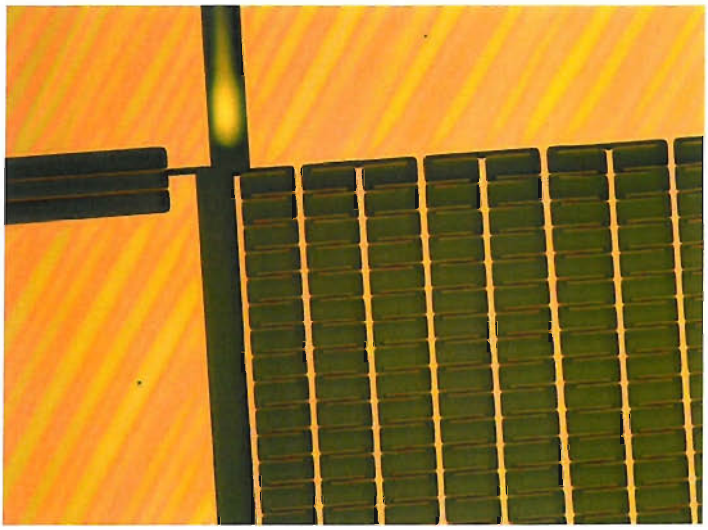

(a) A part of the electrode area

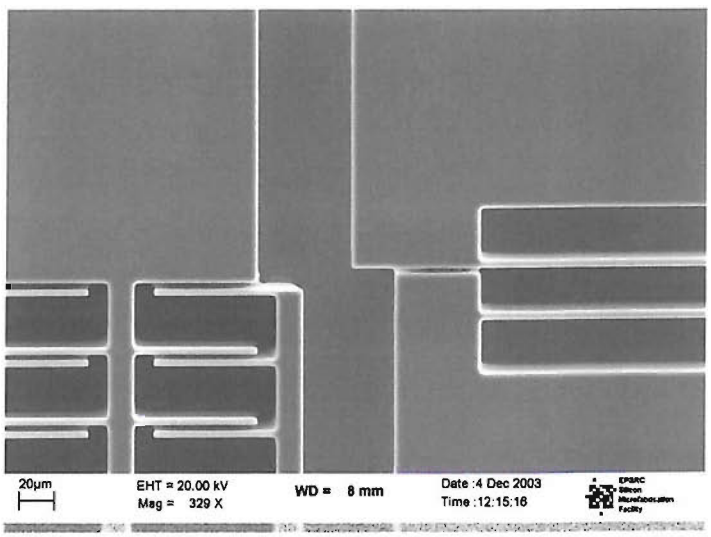

(b) A close-up view of part of the electrode area and part of the spring structure

FIGURE 8.12: SEM pictures of the fabricated sensor.

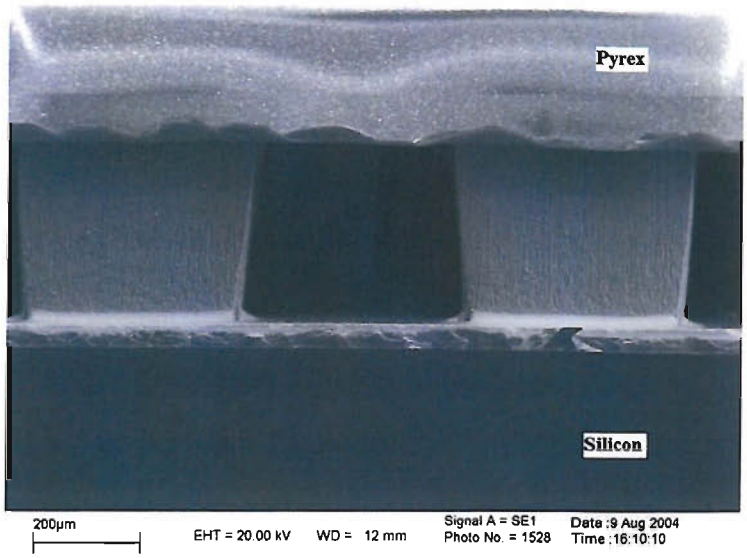

FIGURE 8.13: Anodic bonding (silicon wafer to Pyrex 7740 glass).

8.3.2 Silicon on Insulator (SOI)

In parallel, the sensor is also fabricated using SOI wafers. The specifications of the SOI wafer is shown in Table 8.3.

Size: $150mm$		
Type: N		
Orientation: $< 100 >$		
Resistivity: $0 - 0.1\ \Omega \cdot cm$		
Layer Name	**Thickness**	**Polished**
Device Layer	$50\mu m$	yes
Oxide Layer	$3\mu m$	N/A
Handle Layer	$600\mu m$	yes

TABLE 8.3: Wafer parameters of the SOI process

The minimum capacitor gap of the structure is also $3\mu m$. There are two masks (Front-side, Back-side) of the sensing element. Two plasma-etching steps and one wet-etching step are used. The fabrication process steps are shown in Figure 8.14 and described below:

1. DS-D0: Using the backside mask, a $20\mu m$ thick photoresist (SPR220-7) is patterned. The silicon under the proof mass is first removed from the backside of the wafer. Etching the handle silicon layer ($600\mu m$) all the way to the buried oxide layer using ICP DRIE for 200 minutes (etch rate $3\mu m$/min).

2. DS-D0: Then, the wafer is flipped. The front-side mask is patterned and aligned to alignment marks on the backside. A $2.2\mu m$ thick photoresist (SPR518) is used. The top layer is etched all the way through the thickness of the $50\mu m$ silicon device layer using ICP DRIE for 20 minutes (etching rate $3\mu m$/min).

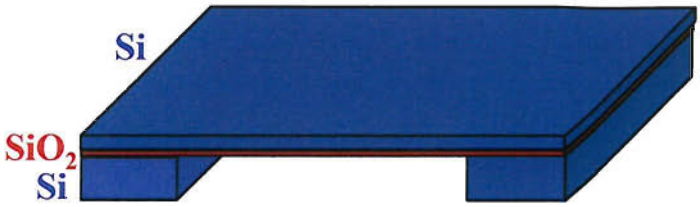

(a) Back side silicon DRIE etching

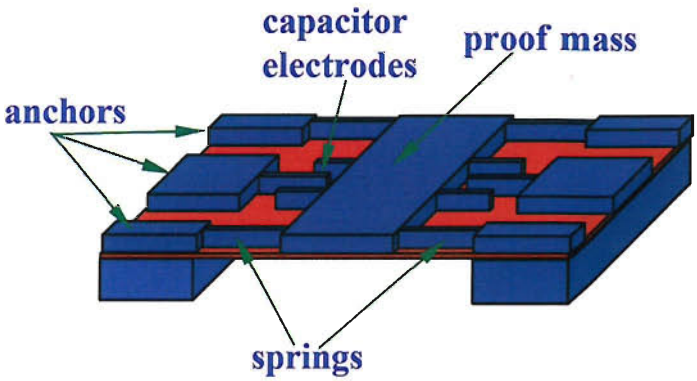

(b) Front side silicon DRIE etching

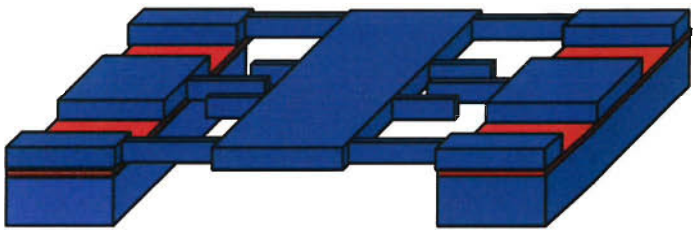

(c) Buried oxide etching and structure releasing

FIGURE 8.14: SOI fabrication process of the high performance accelerometer.

3. WH-E1: Strip $3\mu m$ SiO_2 buried oxide layer from wafer using 7:1 BHF wet etching.

4. ME-0X: Evaporating pure Al $1\mu m$ to form the wire pads for connecting electrodes to a IC package.

To get a successfully fabricated sensor using DRIE, it is necessary to use the features to get a uniform etching rate across the structure. The two fabrication processes were close to complete in the cleanroom facilities at the University of Southampton. However, due to the Southampton University fire last October, the cleanroom was destroyed, and thus the two fabrication processes were lost. However, the processes were re-started this February in Eindhoven. Concurrently, the device is also under fabrication in USA.

8.4 Summary

An accelerometer using a fully differential structure is designed. A large number of comb-fingers (1800) are used as sensing capacitors with short and therefore rigid finger electrodes. This arrangement leads to very high modal frequencies of the sensing element, which should be above $f_s/4$ for the operation of an electromechanical $\Sigma\Delta$M. The parameters (including the spring stiffness and damping coefficient) obtained using the CoventorWare simulation agree well with the analytical results. The sensor has a low mechanical noise floor, which is below a $1\mu g/\sqrt{Hz}$. The fabrication steps using a SOG process and a SOI process are given, and some preliminary fabrication results are shown.

Chapter 9

Conclusions

9.1 Conclusions

This work presents a design methodology of the control system for capacitive micromachined inertial sensors with a high-order single loop ΣΔM. By introducing electronic resonators, which generates complex pairs of zeros in the signal band, the QNTF's in-band mean value is further reduced which suppresses the total in-band quantization noise. Compared with a MF topology, a FF topology is suitable for low-voltage and low power applications due to its low integrator output swing. Monte-Carlo analysis on the sensitivity due to fabrication tolerances, including the sensing element and circuits, verified that a single loop ΣΔM has a better immunity to fabrication tolerances than a MASH ΣΔM. For high performance inertial sensors embedded in high-order ΣΔM, non-linear one-bit force feedback on the proof mass results in harmonic distortion in the signal bandwidth and thus reduces the SNDR. Using a displacement dependent feedback, a linearization scheme was put forward and the harmonic distortion is considerably suppressed. Although the pickoff stage still introduces non-linear effects (and thus a harmonic distortion in the signal bandwidth), its magnitude is relatively small. The noise components at different stages of the high-order electromechanical ΣΔM were analyzed, and electronic noise suppression at the pickoff stage was proposed based on the analysis. The mechanical quality factor Q of a sensing element also determines the different noise shaping properties. Electronic noise is not always detrimental in a ΣΔM, as it can behave as dithering to improve the linearity. In high-order electromechanical ΣΔMs, dead-zone and idle tones were greatly alleviated compared with a second-order ΣΔM.

For a micromachined vibratory gyroscopes, the sensing element is usually designed with a high quality factor Q, and hence can be treated as a resonator. Closed-loop sensors using a high-order bandpass ΣΔM as the control system have advantages over using a lowpass ΣΔM. Compared with a second-order ΣΔM loop, it provides much superior quantization noise shaping, which makes the quantization noise no longer the dominant noise source and further alleviates idle tones. Compared with a control system based on a high-order

lowpass ΣΔM, a high-order bandpass ΣΔM reduces the sampling frequency by about two orders of magnitude and has a wider and flat signal transfer function in the frequency range of interest. Two novel topologies of an eighth-order, bandpass ΣΔM are discussed and achieve a SNR ratio of about 100dB for typical parameter values for a micromachined sensing element and state-of-the art electronic components.

To get good resolution and linearity of capacitance variations, three demodulation methods were simulated. With available components, the diode envelope demodulation had the best performance. A prototype of a CT fifth-order electromechanical ΣΔM was built using SMT components in a six-layer PCB. The special issues in continuous-time ΣΔM were addressed, including clock jitter, inter-symbol effects and excess loop delay. The performance of the prototype with fully differential circuits was measured in real time by spectrum analyzers. The SNR of the prototype is about 90dB in a 1kHz signal band with a sampling frequency of 125kHz. These experimental results are preliminary due to the fabricated sensors were destroyed by the Southampton University fire.

A high performance micromachined accelerometer was designed with a fully differential structure. The in-plane sensor has a mechanical noise floor below $1\mu g/\sqrt{Hz}$, static sensitivity 16.5pF/g and a resonant frequency of 325Hz. Detailed FEM analysis were performed using CoventorWare to design these key parameters of the sensor. The fabrications using SOG wafers and SOI wafers were re-started after the fire at the University of Southampton.

9.2 Future Work

The goal of this research, in the long term, is to investigate how the performance of inertial sensors will be improved by incorporating them in a high-order ΣΔM. For the future, the following work should be addressed:

1. Finish the two parallel fabrication processes of the high performance accelerometer using SOG and SOI wafers. At present, the processes are re-started at Innos-Eindhoven, and at the same time the fabrication is underway at USA. Once prototypes are available, the open-loop performance will be tested to get accurate measurement of the frequency response, including high-order parasitic modal frequencies.

2. An ASIC implementation of a fifth-order ΣΔM using the multi-feedback topology with resonators. The target performance is 120dB (SNR) using a sampling frequency of 512kHz (equivalent to an OSR of 256 in 1kHz signal bandwidth). This is an EPSRC project based on the thesis.

3. Investigation of a multi-bit [63] high-order electromechanical ΣΔ M. The control system as shown in Figure 9.1 preserves the advantage of linearity of a one-bit electrostatic force feedback, gives a better stability margin and higher SQNR. The multi-bit

quantizer may be implemented by 10~12 bit flash ADC, and the quantization noise Q_1 is also shaped by the sensing element. While the electronic filter $H(z)$ can be of high-order to further reduce the noise Q_2 of the one-bit quantization. Moreover, $H(z)$ and the second quantizer are all in the digital domain, which can be implemented by a FPGA.

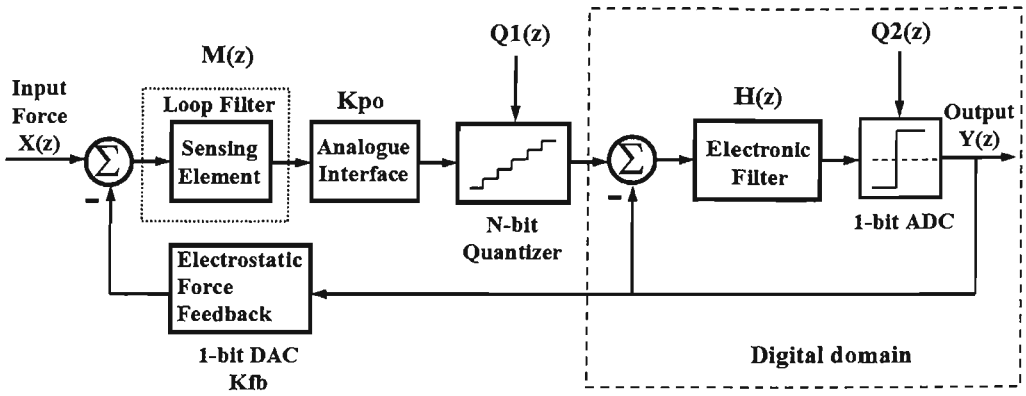

FIGURE 9.1: A multi-bit high-order electromechanical ΣΔM.

4. For a micromachined vibratory gyroscope, the work needs further investigation of the quadrature bandpass ΣΔM [108], [109] to cancel the quadrature error force due to fabrication imperfections. To get the correct information of the magnitude and phase of the quadrature error force, synchronous demodulation in I and Q channels will be performed, which apply an electrostatic feedback force to cancel the quadrature force along the sense direction without attenuation of the Coriolis force signal. This will lead to **all** digital force feedback on proof mass and also simplify the circuit design (shown in Figure 9.2).

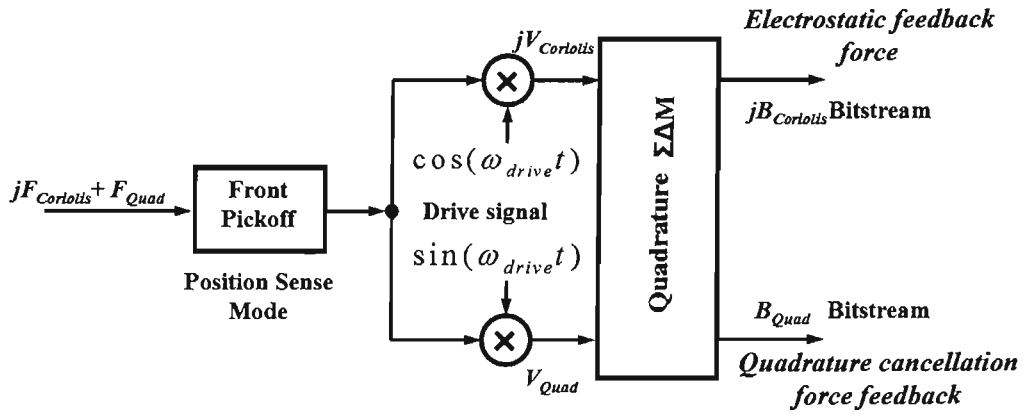

FIGURE 9.2: An electromechanical ΣΔM with quadrature force feedback cancellation.

5. Investigate the effects of high-order parasitic modal frequencies of a sensing element, as shown in Figure 9.3, on the stability and performance of a high-order electromechanical ΣΔM. So far, there is no effective solution to remove their effects only by electronic compensation techniques [10].

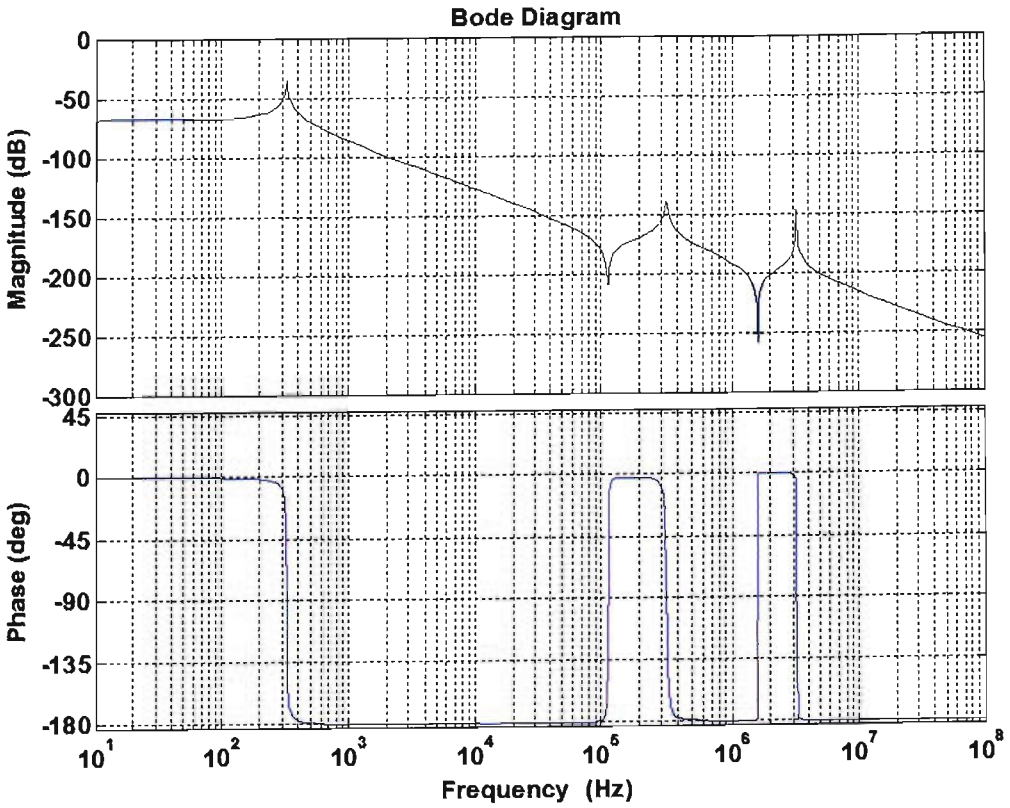

FIGURE 9.3: High-order parasitic modal frequencies of a micromachined sensing element.

Appendix A

MatLab Source Code for the PSD Simulation

```
% ************************************************************************
% Code is modified based on the work done by P. Malcovati [67] and R. Schreier [29].
% ************************************************************************
clear

t0=clock;
per0=8.85e-12;
perr=1;
area=6.5e-6 ;         %overlap electrode area
nomd=3e-6;           % nominal gap
m=9.7e-7;
b=0.2;
k=48.1;
vfb=1;
again=1;
cap=1e-12;
aaa=vfb/nomd;     % linearization factor
%aaa=0;             % without linearization
c_decop=2e-6;    % represents the decop capacitor of the charge amp circuit
k_of_fb=0.5*(per0*perr*area*vfb^2)/((nomd)^2); % electrostatic feedback
enoise=10e-9;     % input-referred white electronic noise PSD
% ************************************************************************
bw=1024;                % signal bandwidth
R=64;                     % OSR
Fs=R*2*bw;            % Oversampling frequency
Ts=1/Fs;
Tss=Ts;
N=128*1024;             % FFT samples number
nper=128;
Fin=nper*Fs/N;          % Input signal frequency (Fin = nper*Fs/N)
Ampl=0.5-pi/256;        % Input signal amplitude [V]
Ntransient=128;
delay=0.01*Ts;
desv=1e-4*Ts;
z0=0.9;
```

```
%
% kT/C noise and op-amp non-idealities
%
echo on;
Cf=5e-12;                    % Integrating Capacitance of the first integrator
alfa=(1e3-1)/1e3;          % A=Op-amp finite gain (alfa=(A-1)/A -> ideal op-amp alfa=1)
% alfa=1;
Amax=1.35;                 % Op-amp saturation value [V]
sr=1e6;                      % Op-amp slew rate [V/s]
GBW=5e6;                   % Op-amp GBW [Hz]
noise1=10e-6;               % 1st int. output noise std. dev. [V/sqrt(Hz)]
Δ=10e-9;                 % Random Sampling jitter (std. dev.) [s] (Boser, Wooley JSSC Dec. 88)
echo off;
Vref=1;
finrad=Fin*2*pi;           % Input signal frequency in radians
s0=sprintf('** Simulation Parameters **');
s1=sprintf('    Fs(Hz)=%1.0f',Fs);
s2=sprintf('    Ts(s)=%1.6e',Ts);
s3=sprintf('    Fin(Hz)=%1.4f',Fin);
s4=sprintf('    BW(Hz)=%1.0f',bw);
s5=sprintf('    OSR=%1.0f',R);
s6=sprintf('    Npoints=%1.0f',N);
s7=sprintf('    tsim(sec)=%1.3f',N/Fs);
s8=sprintf('    Nperiods=%1.3f',N*Fin/Fs);
disp(s0)
disp(s1)
disp(s2)
disp(s3)
disp(s4)
disp(s5)
disp(s6)
disp(s7)
disp(s8)
% ************************************************************************
% Open Simulink diagram first
% ************************************************************************
for span=1:50,
sim('SIMULINK MODEL', (N+Ntransient)/Fs);   % Starts Simulink simulation
% ************************************************************************
%   Calculates SNR and PSD of the bit-stream and of the signal
% ************************************************************************
%w=(blackman(N))';
w=hann(N);
%w=(rectwin(N))';
echo on;
f=Fin/Fs                  % Normalized signal frequency
fB=N*(bw/Fs)          % Base-band frequency bins
yy1=zeros(1,N);
yy1=bitstream(2+Ntransient:1+N+Ntransient)';
echo off;
ptot=zeros(1,N);
[snr,ptot,ps,pn]=calcSNR(yy1(1:N),f,fB,w,N,Vref);
% ************************************************************************
% Output
% ************************************************************************
figure(1);
```

```
92  clf;
93  semilogx(linspace(0,Fs/2,N/2), ptot(1:N/2), 'b');
94  hold on;
95  title('PSD of a 5th-Order Sigma-Delta Accelerometer')
96  xlabel('Frequency (Hz)')
97  ylabel('PSD (dB)')
98  axis([0 Fs/2 -160 0]);
99  grid on;
100 %hold off;
101 text_handle = text(floor(Fs/R),-40, sprintf('SNR = %4.1fdB @ OSR=%d\n',snr,R));
102 text_handle = text(floor(Fs/R),-60, sprintf('Signal Bandwidth =256Hz'));
103
104 figure(2);
105 clf;
106 plot(linspace(0,Fs/2,N/2), ptot(1:N/2), 'g');
107 grid on;
108 title('PSD of a 5th-Order Sigma-Delta Accelerometer')
109 xlabel('Frequency [Hz]')
110 ylabel('PSD [dB]')
111 axis([0 Fs/2 -300 0]);
112
113 figure(3);
114 clf;
115 spec=fft(yy1.*w)/(N/2);
116 semilogx(linspace(1,Fs/2,N/2), dbv(spec(1:N/2)), 'r');;
117 grid on;
118 title('Amplitude of a 5th-Order Sigma-Delta Accelerometer')
119 xlabel('Frequency [Hz]')
120 ylabel('Amplitude [dB]')
121 axis([0 Fs/2 -180 0]);
122 snr2=calculateSNR(spec(1:fB),nper);
123 text_handle = text(1000,-25, sprintf('SNR = %4.1fdB @ OSR=%d\n',snr2,R));
124 grid on;
125 hold off;
126
127 s1=sprintf('SNR(dB)=%1.3f',snr);
128 s2=sprintf('Simulation time =%1.3f min',etime(clock,t0)/60);
129 disp(s1)
130 disp(s2)
131
132 % ************************************************************************
133 % Histograms of the integrator outputs
134 % ************************************************************************
135 figure(4)
136 nbins=200;
137 [bin1,xx1]=histo(y1, nbins);
138 [bin2,xx2]=histo(y2, nbins);
139 [bin3,xx3]=histo(y3, nbins);
140
141 clf;
142 subplot(1,3,1), plot(xx1, bin1)
143 grid on;
144 title('First Integrator Output')
145 xlabel('Voltage [V]')
146 ylabel('Occurrences')
147 subplot(1,3,2), plot(xx2, bin2)
```

```
148 grid on;
149 title('Second Integrator Output')
150 xlabel('Voltage [V]')
151 %ylabel('Occurrences')
152 subplot(1,3,3), plot(xx3, bin1)
153 grid on;
154 title('Third Integrator Output')
155 xlabel('Voltage [V]')
156 %ylabel('Occurrences')
157 % ************************************************************************
158 % Input-output
159 % ************************************************************************
160 aa(span)=20*log10(10^((1-span)/7));
161 bb(span)=snr;
162 hold on
163 figure(5)
164 % plot(aa,bb,'--rs','LineWidth',2,'MarkerEdgeColor','k','MarkerFaceColor','g','MarkerSize',
165 plot(aa,bb,'kd');
166 axis([-160  0  -10  160])
167 grid on;
168 xlabel('Input Signal Power (dB)')
169 title('SQNR of 5th Order SDM Accelerometer')
170 ylabel('SQNR (dB)')
171 end
```

Appendix B

OrCAD Schematic of PCB Prototype (1st version)

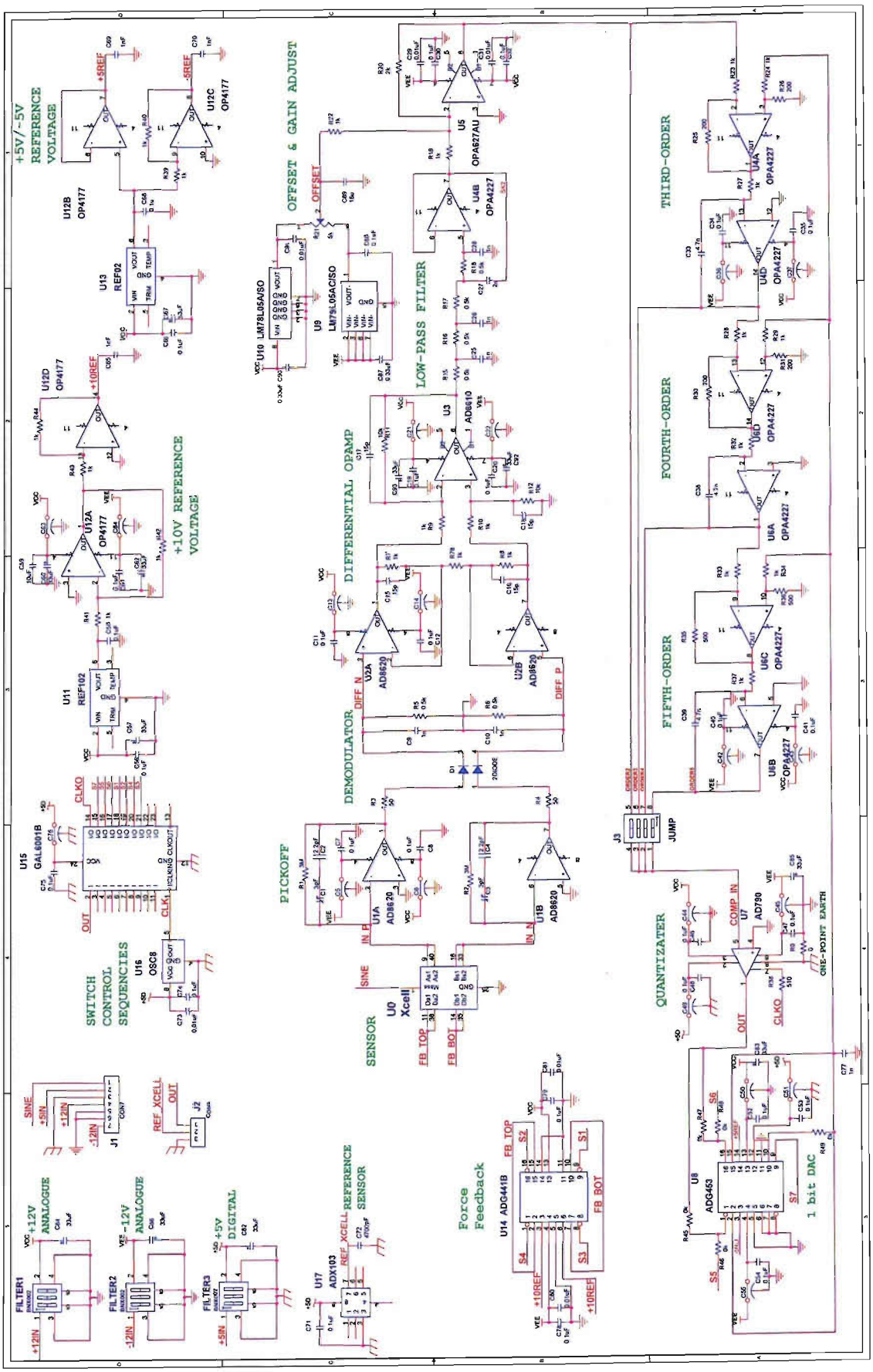
+5V/-5V REFERENCE VOLTAGE
+10V REFERENCE VOLTAGE
OFFSET & GAIN ADJUST
LOW-PASS FILTER
DIFFERENTIAL OPAMP
DEMODULATOR
PICKOFF
SENSOR
SWITCH CONTROL SEQUENCIES
QUANTIZATER
FIFTH-ORDER
FOURTH-ORDER
THIRD-ORDER
Force Feedback
1 bit DAC
REFERENCE SENSOR
ANALOGUE
DIGITAL
JUMP
ONE-POINT EARTH

Appendix C

Block Diagram of PCB Prototype (2nd version)

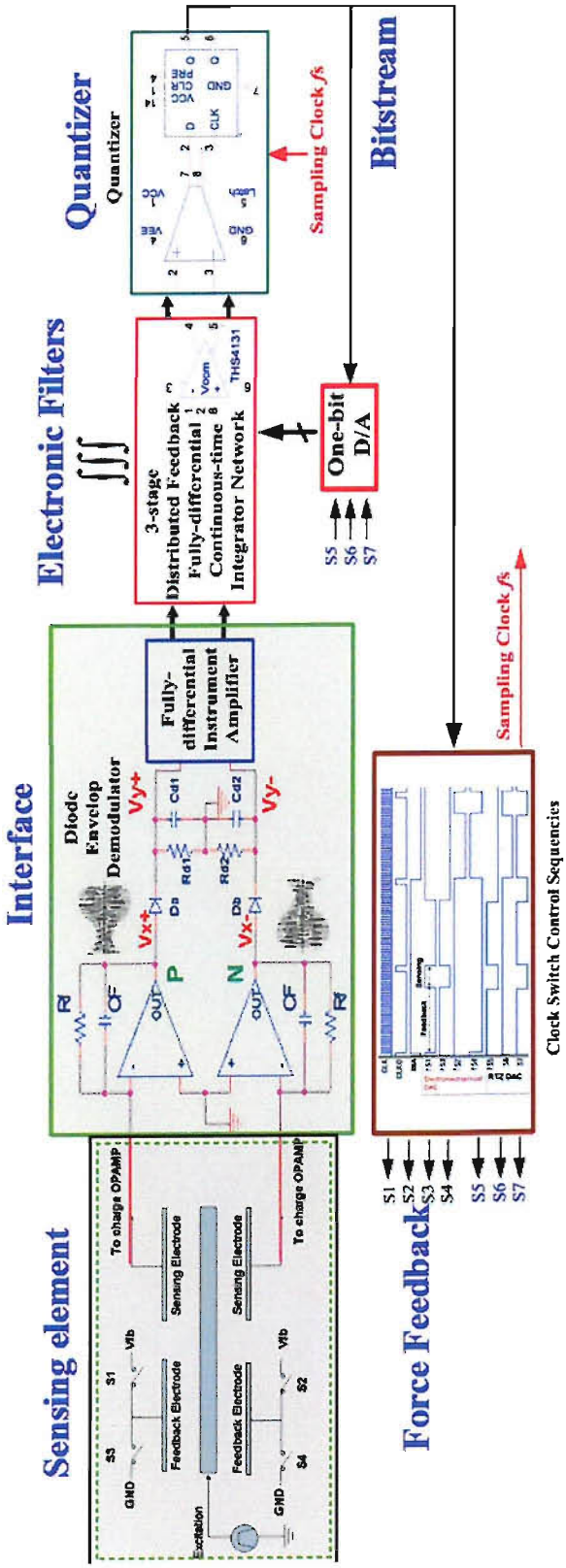
Quantizer
Quantizer
Sampling Clock fs
Bitstream
Electronic Filters
3-stage
Distributed Feedback
Fully-differential
Continuous-time
Integrator Network
One-bit
D/A
S5
S6
S7
Interface
Diode
Envelop
Demodulator
Fully-
differential
Instrument
Amplifier
Vy+
Vy-
Vx+
Vx-
P
N
Sensing element
To charge OPAMP
Sensing Electrode
Feedback Electrode
Excitation
GND
Vfb
S1
S2
S3
S4
Force Feedback
Sampling Clock fs
Clock Switch Control Sequencies
S1
S2
S3
S4
S5
S6
S7

Appendix D

OrCAD Schematic of PCB Prototype (2nd version)

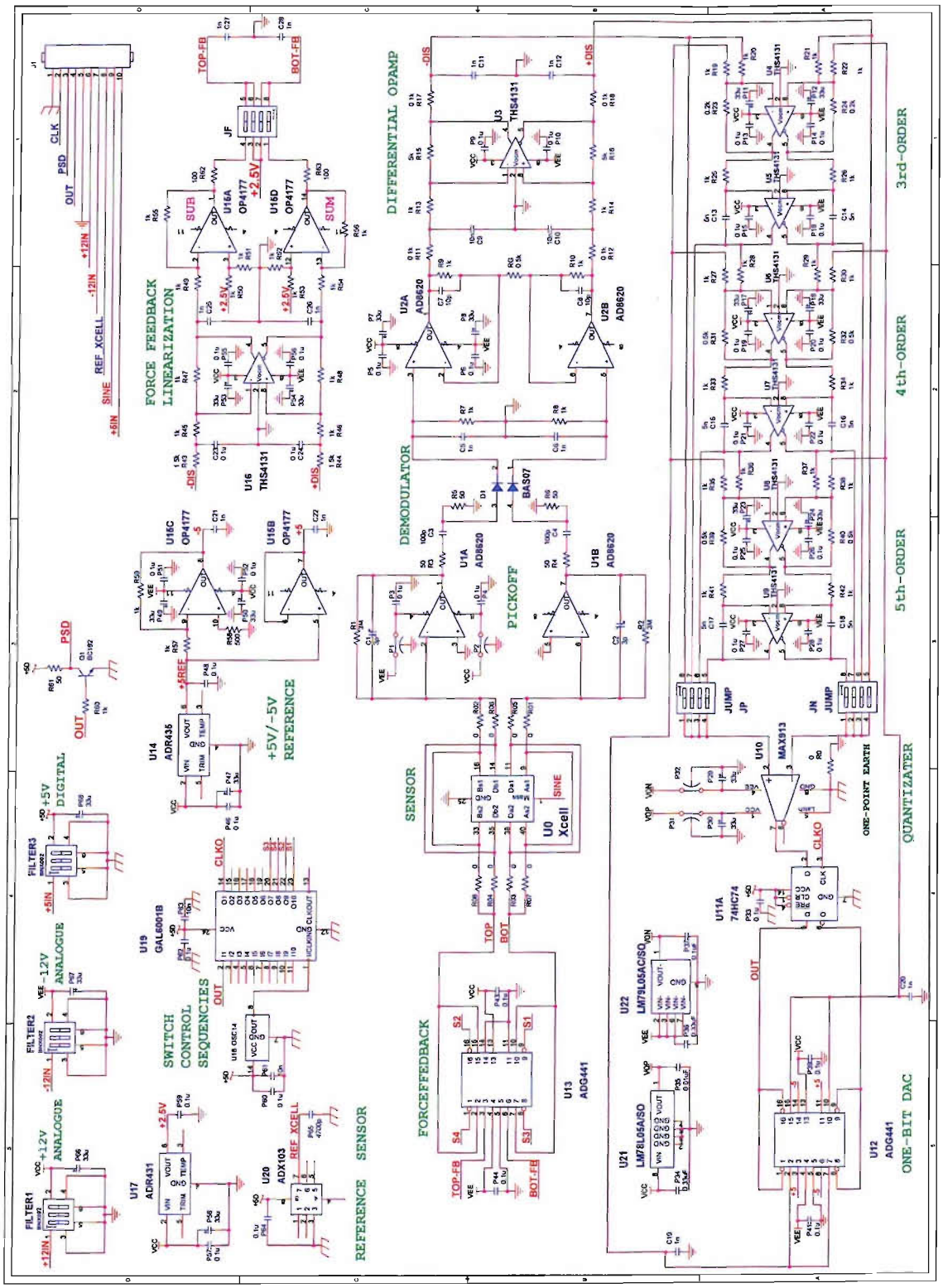
FORCE FEEDBACK LINEARIZATION
DIFFERENTIAL OPAMP
DEMODULATOR
PICKOFF
SENSOR
FORCEFEEDBACK
SWITCH CONTROL SEQUENCIES
REFERENCE SENSOR
+5V/-5V REFERENCE
3rd-ORDER
4th-ORDER
5th-ORDER
QUANTIZATER
ONE-BIT DAC
ONE-POINT EARTH
CLK
PSD
OUT
+12IN
-12IN
REF_XCELL
SINE
+5IN
TOP-FB
BOT-FB
SUB
SUM
THS4131
OP4177
AD8620
BAS07
ADR435
ADR431
ADX103
GAL6001B
MAX913
74HC74
ADG441
LM79L05ACISO
LM78L05ACISO
JUMP
JP
JN
TOP
BOT
Xcell

Bibliography

[1] L. M. Roylance and J. B. Angell, "A miniature integrated circuit accelerometer," in *IEEE International Solid-State Circuits Conference*, vol. XXI, Feb 1978, pp. 220 –221.

[2] W. Henrion, L. Disanza, M. Ip, S. Terry, and H. Jerman, "Wide dynamic range direct digital accelerometer," in *IEEE Solid State Sensor and Actuator Workshop*, Hilton Head Island, June 1990, pp. 153–157.

[3] C. Lu, M. Lemkin, and B. Boser, "A monolithic surface micromachined accelerometer with digital output," in *Digest of Technical Papers, 42nd ISSCC, 1995 IEEE International Solid-State Circuits Conference,*, Feb 1995, pp. 160–161.

[4] B. Boser and R. Howe, "Surface micromachined accelerometers," *IEEE Journal of Solid-State Circuits*, vol. 31, no. 3, pp. 366–375, March 1996.

[5] M. Lemkin and B. Boser, "A three-axis micromachined accelerometer with a CMOS position-sense interface and digital offset-trim electronics," *IEEE Journal of Solid-State Circuits*, vol. 34, no. 4, pp. 456–468, 1999.

[6] X. Jiang, F. Wang, M. Kraft, and B. E. Boser, "An integrated surface micromachined capacitive lateral accelerometer with $2\mu g/\sqrt{Hz}$ resolution," in *Solid-State Sensor, Actuator and Microsystems Workshop*, Hilton Head Island, June 2002, pp. 202–206.

[7] H. Kulah, J. Chae, and K. Najafi, "Noise analysis and characterization of a sigma-delta capacitive microaccelerometer," *IEEE Journal of Solid-State Circuits*, vol. 41, no. 2, pp. 352–361, Febuary 2006.

[8] T. Smith, O. Nys, M. Chevroulet, Y. DeCoulon, and M. Degrauwe, "A 15b electromechanical sigma-delta converter for acceleration measurements," in *IEEE 1994 International Solid-State Circuits Conference, ISSCC'94*, Feb 1994, pp. 160–161.

[9] T. Kajita, U.-K. Moon, and G. C. Temes, "A two-chip interface for a MEMS accelerometer," *IEEE Transactions on Instrumentation and Measurement*, vol. 51, no. 4, pp. 853–858, August 2002.

[10] V. Petkov, "High Order $\Sigma\Delta$ Interface for Micromachined Inertial Sensors," Ph.D. dissertation, Univ. of California (Berkeley), Spring 2004.

[11] M. Kraft, W. Redman-White, and M. E. Mokhtari, "Closed-loop micromachined inertial sensors with higher order ΣΔ modulators," in *Proc. 4th Conf. On Modelling and Simulation of Microsystems*, Hilton Head Island, March 2001, pp. 104–107.

[12] V. Petkov and B. Boser, "A fourth-order ΣΔ interface for micromachined inertial sensors," *IEEE Journal of Solid-State Circuits*, vol. 40, no. 8, pp. 1602–1609, August 2005.

[13] N. Yazdi, F. Ayazi, and K. Najafi, "Micromachined inertial sensors," *Proceedings of the IEEE*, vol. 86, no. 8, pp. 1640–1659, August 1998.

[14] M. Kuritsky, M. Goldstein, I. Greenwood, H. Lerman, J. McCarthy, T. Shanahan, M. Silver, and J. Simpson, "Inertial navigation," *Proceedings of the IEEE*, vol. 71, no. 10, pp. 1156–1176, Oct 1983.

[15] M.-H. Bao, *Micro mechanical transducers: pressure sensors, accelerometers, and gyroscopes.* Elsevier Science B.V., 2000.

[16] R. P. Leland, "Mechanical-Thermal Noise in MEMS Gyroscopes," *IEEE SENSORS JOURNAL*, vol. 5, no. 3, pp. 493–500, June 2005.

[17] H. Inose, Y. Yasuda, and J. Muradami, "A telemetering system by code modulation – delta-sigma modulation," *IRE Trans. Space Electronics and Telemetry*, vol. 8, pp. 204–209, Sept 1962.

[18] R. J. V. de Plassche, "A sigma-delta modulators as an A/D converter," *IEEE Trans. Circuits and Systems*, vol. 25, no. 7, pp. 510–514, July 1978.

[19] P. Aziz, H. Sorensen, and J. van der Spiegel, "An overview of sigma-delta converters," *IEEE Signal Processing Magazine*, vol. 13, no. 1, pp. 61–84, Jan 1996.

[20] R. J. D. Plassche, *CMOS Integrated Analog-to-digital and Digital-to-analog Converters.* Kluwer Academic Publishers, 2003.

[21] E. W. Weisstein, "Parseval's Theorem." [Online]. Available: http://mathworld.wolfram.com/ParsevalsTheorem.html

[22] Wikipedia, "Parseval's Theorem." [Online]. Available: http://en.wikipedia.org/wiki/Parseval's_theorem

[23] R. Schreier and G. C. Temes, *Understanding Delta-Sigma Data Converters.* Wiley-IEEE Press, 2004.

[24] S. Ardalan and J. Paulos, "Analysis of nonlinear behaviour in delta-sigma modulators," *IEEE Transactions on Circuits and Systems*, vol. 34, no. 6, pp. 593–603, June 1987.

[25] W. Lee, "A novel higher order interpolative modulator topology for high resolution oversampling A/D converters," Master Thesis, MIT, Cambridge, MA, June 1987.

[26] K.-H. Chao, S. Nadeem, W. Lee, and C. Sodini, "A higher order topology for interpolative modulators for oversampling A/D converters," *IEEE Trans. Circuits and Systems*, vol. 37, no. 3, pp. 309–318, March 1990.

[27] J. V. Engelen and R. J. D. Plassche, *Bandpass Sigma Delta Modulators: Stability Analysis, Performance and Design Aspects.* Kluwer Academic Publishers, Oct 1999.

[28] S. Norsworth, R. Schreier, and C. Temes, *Delta-Sigma data converters: Theory, Design, and Simulation.* IEEE Press, 1997.

[29] R. Schreier, "Delta Sigma Toolbox, MatLab File Exchange," 2000. [Online]. Available: http://www.mathworks.com/matlabcentral/fileexchange/loadFile.do?objectId=19&objectType=file

[30] L. Breems and J. H. Huijsing, *Continuous-Time Sigma-Delta Modulation for A/D Conversion in Radio Receivers.* Kluwer Academic Publishers, September 2001.

[31] O. Bajdechi and J. Huijsing, *Systematic Design of Sigma-Delta Analog-to-Digital Converters.* Kluwer Academic Publishers, 2004.

[32] S. Loeda, H. M. Reekie, and B. Mulgrew, "On the design of high performance wideband continuous-time Sigma Delta converters using numerical optimization," *IEEE Transactions on Circuits and Systems Part I: Regular Papers*, vol. 53, no. 3, pp. 1–1, March 2006.

[33] A. Yahia, P. Benabes, and R. Kielbasa, "Influence of the feedback DAC delay on a continuous-time bandpass $\Delta\Sigma$ converter," in *IEEE International Symposium on Circuits and Systems, ISCAS 2002.*, vol. 2, May 2002, pp. 648–651.

[34] K. Petersen, A. Shartel, and N. Raley, "Micromechanical accelerometer integrated with MOS detection circuitry," *IEEE Trans. Electron. Devices*, vol. 29, no. 1, pp. 23–27, January 1982.

[35] C. Enz and G. Temes, "Circuit techniques for reducing the effects of op-amp imperfections: autozeroing, correlated double sampling, and chopper stabilization," *Proceedings of the IEEE*, vol. 84, no. 11, pp. 1584–1614, Nov 1996.

[36] B. E. Boser, "Surface micromachning: an IC-compatible sensor technology," 1996. [Online]. Available: http://www-bsac.eecs.berkeley.edu/~boser/pdf/hotchips96.pdf

[37] F. Rudolf, A. Jornod, J. Berqovist, and H. Leuthold, "Precision accelerometers with μg resolution," *Sensors Actuators A: Physical*, vol. A21-A23, pp. 297–302, March 1990.

[38] G. Li, Z. Li, C. Wang, Y. Hao, T. Li, D. Zhang, and G. Wu, "Design and fabrication of a highly symmetrical capacitive triaxial accelerometer," *Journal of Microelectromechanical Systems*, vol. 11, no. 1, pp. 48–54, January 2001.

[39] Z. Xiao, M. Chen, G. Wu, C. Zhao, D. Zhang, Y. Hao, G. Zhang, and Z. Li, "Silicon micro-accelerometer with mg resolution, high linearity and large frequency bandwidth fabricated with two mask bulk process," *Sensors and Actuators A: Physical*, vol. 77, pp. 113–119, 1999.

[40] C. Iliescu and J. Miao, "One-mask process for silicon accelerometers on Pyrex glass utilising notching effect in inductively coupled plasma DRIE," *Electronics Letters*, vol. 39, no. 8, pp. 658–659, April 2003.

[41] N. Yazdi and K. Najafi, "An all-silicon single-wafer micro-g accelerometer with a combined surface and bulk micromachining process," *Journal of Microelectromechanical Systems*, vol. 9, pp. 544–550, Decemeber 2000.

[42] J. Chae, H. Kulah, and K. Najafi, "A hybrid Silicon-On-Glass (SOG) lateral micro-accelerometer with CMOS readout circuitry," in *The Fifteenth IEEE International Conference on Micro Electro Mechanical Systems*, Jan 2002, pp. 623–626.

[43] ——, "A monolithic 3-axis silicon capacitive accelerometer with micro-g resolution," in *The 12th International Conference Solid-State Sensors, Actuators and Microsystems, TRANSDUCERS '03*, Boston, MA, June 2003, pp. 81–84.

[44] N. Yazdi, K. Najafi, , and A. S. Salian, "A high-sensitivity silicon accelerometer with a folded-electrode structure," *Journal of Microelectromechanical Systems*, vol. 12, no. 4, pp. 479–486, August 2003.

[45] K.-H. Han and Y.-H. Cho, "Selfbalanced navigationgrade capacitive micro-accelerometers using branched finger electrodes and their performance for varying sense voltage and pressure," *Journal of Microelectromechanical Systems*, vol. 12, no. 1, pp. 11–20, Feb 2003.

[46] O. Gigan, H. Chen, O. Robert, G. Amendola, O. Francais, and F. Marty, "Fabrication and characterization of resonant SOI micromechanical silicon sensors based on DRIE micromachining, freestanding release process, and process, and silicon direct bonding," in *Nano and Microtechonology: Materials, Processes, Packaging, and Systems*, Melbourne, Australia, Decemeber 2002, pp. 194–204.

[47] M. Strohrmann, P. Bley, O. Fromhein, and J. Mohr, "Acceleration sensor with integrated compensation of temperature effects fabricated by the LIGA process," *Sensors Actuators A: Physical*, vol. 42, no. 1-3, pp. 426–429, April 1994.

[48] O. Kromer, O. Fromhein, H. Gemmeke, T. Khner, J. Mohr, and M. Strohrmann, "High-precision readout circuit for LIGA acceleration sensors," *Sensors Actuators A: Physical*, vol. 46, no. 1-3, pp. 196–200, January-February 1995.

[49] B. Borovic, A. Q. Liu, D. Popa, H. Cai, and F. L. Lewis, "Open-loop versus closed-loop control of MEMS devices: choices and issues," *Journal of Micromechanics and Microengineering*, vol. 15, no. 10, pp. 1917–1924, October 2005.

[50] C. Verplaetse, "Can a pen remember what it has written using inertial navigation? An evaluation of current accelerometer technology," 1995. [Online]. Available: http://xenia.media.mit.edu/~verp/projects/smartpen/

[51] J. I. Seeger, X. Jiang, M. Kraft, and B. E. Boser, "Parallel-plate driven oscillations and resonant pull-in," in *IEEE Solid-State and Actuator Workshop*, Hilton Head Island, June 2002, pp. 313–316.

[52] W. Yun, R. T. Howe, and P. R. Gray, "Surface micromachined, digitally force-balanced accelerometer with integrated CMOS detection circuitry," in *Technical Digest of the 1992 IEEE Solid-State Sensor and Actuator Workshop*, Hilton Head Island, June 1992, pp. 126–131.

[53] M. Lemkin, "Micro accelerometer design with digital feedback control," Ph.D. dissertation, Univ. of California (Berkeley), Fall 1997.

[54] X. Jiang, "Capacitive Position-Sensing Interface for Micromachined Inertial Sensors," Ph.D. dissertation, Univ. of California (Berkeley), Spring 2003.

[55] N. Yazdi and K. Najafi, "Performance limits of a closed-loop, micro-g silicon accelerometer with deposited rigid electrodes," in *Proceedings of the 12th International Conference on Microelectronics*, Tehran, Iran, October 2000, pp. 313–316.

[56] P. Malcovati, S. Brigati, F. Francesconi, F. Maloberti, P. Cusinato, and A. Baschirotto, "Behavioral modelling of switched-capacitor sigma-delta modulators," *IEEE Transactions on Circuits and Systems I: Fundamental Theory and Applications*, vol. 50, no. 3, pp. 352–364, March 2003.

[57] J. Wu and L. Carley, "A simulation study of electromechanical delta-sigma modulators," in *The 2001 IEEE International Symposium on Circuits and Systems*, vol. 2, May 2001, pp. 453–456.

[58] M. Kranz, S. Burgett, T. Hudson, M. Buncick, P. Ruffin, P. Ashley, and J. McKee, "A wide dynamic range silicon-on-insulator MEMS gyroscope with digital force feedback," in *Proceedings of the 12th International Conference on Solid State Sensors, Actuators and Microsystems (TRANSDUCERS '03)*, Boston,USA, June 2003, pp. 159–162.

[59] R. Oboe, R. Antonello, P. Carbone, E. Nunzi, E. Lasalandra, L. Prandi, and G. Spinola, "Design of a Delta-Sigma Bandpass Demodulator for a Z-Axis MEMS Vibrational Gyroscope," in *Proceedings of 2005 IEEE/ASME International Conference on Advanced Intelligent Mechatronics*, CA,USA, July 2005, pp. 238–242.

[60] J. Wu, "Sensing and control electronics for low-mass low-capacitance MEMS accelerometers," Ph.D. dissertation, Carnegie Mellon University, 2002.

[61] J. Wu, G. Fedder, and L. Carley, "A low-noise low-offset capacitive sensing amplifier for a $50\mu g/\sqrt{Hz}$ monolithic CMOS MEMS accelerometer," *IEEE Journal of Solid-State Circuits*, vol. 39, no. 5, pp. 722–730, May 2004.

[62] R. Baird and T. Fiez, "Linearity enhancement of multibit $\Sigma\Delta$ A/D and D/A converters using data weighted averaging," *IEEE Transactions on Circuits and Systems II: Analog and Digital Signal Processing*, vol. 42, no. 12, pp. 753–762, December 1995.

[63] N. Sakimura, M. Yamaguchi, and M. Yotsuyanagi, "Multibit delta-sigma architectures with two-level feedback loop using a dual-quantization architecture," *IEICE Trans. Electronics*, vol. E84-A, no. 2, pp. 497–505, Feb. 2001.

[64] H. Kulah, J. Chae, and K. Najafi, "Noise analysis and characterization of a sigma-delta capacitive silicon microaccelerometer," in *International Conference on Solid-State Sensors, Actuators and Microsystems (TRANSDUCERS'03)*, vol. 1, June 2003, pp. 95–98.

[65] T.-H. Kuo, K.-D. Chen, and J.-R. Chen, "Automatic coefficients design for high-order sigma-delta modulators," *IEEE Transactions on Circuits and Systems II: Analog and Digital Signal Processing*, vol. 46, no. 1, pp. 6–15, January 1999.

[66] R. Schreier, "An empirical study of high-order single-bit delta-sigma modulators," *IEEE Transactions on Circuits and Systems II: Analog and Digital Signal Processing*, vol. 40, no. 8, pp. 461–466, August 1993.

[67] P. Malcovati, "SD Toolbox 2, MatLab File Exchange," 2005. [Online]. Available: http://www.mathworks.com/matlabcentral/fileexchange/loadFile.do?objectId=7589&objectType=FILE

[68] J. Ruiz-Amaya, J. de la Rosa, F. Medeiro, F. Fernandez, R. del Rio, B. Perez-Verdu, and A. Rodriguez-Vazquez, "MATLAB/SIMULINK-based high-level synthesis of discrete-time and continuous-time $\Sigma\Delta$ modulators," in *Proceedings of the Design, Automation and Test in Europe Conference and Exhibition Designers Forum (DATE04)*, vol. 3, Feb 2004, pp. 150–155.

[69] F. Medeiro, *Top-down Design of High-performance Sigma-delta Modulators.* Kluwer Academic Publishers, January 1999.

[70] M. Neitola, "A Fully Automated Flowgraph Analysis Tool for MATLAB," 2006. [Online]. Available: http://www.mathworks.com/matlabcentral/fileexchange/loadFile.do?objectId=7224&objectType=file

[71] M. E. Mokhtari, "Advanced $\Sigma\Delta$M control systems for MEMS capacitive sensing accelerometers," Ph.D. dissertation, Univ. of Southampton (UK), Spring 2005.

[72] G. Franklin, J. Powell, and A. Emami-Naeini, *Feedback Control of Dynamic Systems*, 5th ed. Prentice Hall, 2005.

[73] J. Oizumi and M. Kimura, "Design of conditionally stable feedback systems," *IEEE Journal of Solid-State Circuits*, vol. 4, no. 3, pp. 157–166, Septemember 1957.

[74] A. Thomsen, D. Kasha, and W. Lee, "A five stage chopper stabilized instrumentation amplifier using feedforward compensation," in *Digest of Technical Papers of 1998 Symposium on VLSI Circuits*, June 1998, pp. 220–223.

[75] A. Thomsen, D. Kasha, L. Wang, and W. Lee, "A 110-dB-THD, 18-mW DAC using sampling of the output and feedbackto reduce distortion," *IEEE Journal of Solid-State Circuits*, vol. 34, no. 12, pp. 1733–1740, Decemember 1999.

[76] P. Cusinato, F. Pasolini, F. Stefani, and A. Baschirotto, "Saturation recovery technique for high-order bandpass switched capacitor $\Sigma\Delta$ modulators," in *The 8th IEEE International Conference on Electronics, Circuits and Systems*, vol. 2, Septemember 2001, pp. 1085–1088.

[77] A. Thurston and M. Hawksford, "Dynamic overload recover mechanism for sigma delta modulators," in *Second International Conference on Advanced A-D and D-A Conversion Techniques and their Applications*, July 1994, pp. 124–129.

[78] C. Dunn and M. Sandler, "Use of clipping in sigma-delta modulators," in *IEE Colloquium on Oversampling Techniques and Sigma-Delta Modulation*, March 1994, pp. 8/1–8/9.

[79] S. Brigati, F. Francesconi, P. Malcovati, and F. Maloberti, "A fourth-order single-bit switched-capacitor $\Sigma\Delta$ modulator for distributed sensor applications," *IEEE Transactions on Instrumentation and Measurement*, vol. 53, no. 2, pp. 266–270, April 2004.

[80] L. Breems, R. Rutten, and G. Wetzker, "A cascaded continuous-time $\Sigma\Delta$ Modulator with 67-dB dynamic range in 10-MHz bandwidth," *IEEE Journal of Solid-State Circuits*, vol. 39, no. 12, pp. 2152–2160, December 2004.

[81] P. Cusinato, F. Pasolini, F. Stefani, and A. Baschirotto, "Digital Technique for Instability Detection and Saturation Recovery in High-Order SC $\Sigma\Delta$ Modulators," *Analog Integrated Circuits and Signal Processing*, vol. 36, no. 1-2, pp. 7–19, July-August 2003.

[82] T. S. F. Rex T. Baird, "Stability Analysis of High-order Modulators for Delta-Sigma ADCs," in *1993 IEEE International Symposium on Circuits and Systems*, vol. 2, May 1993, pp. 1361–1364.

[83] Z.-M. Lin and W.-H. Sheu, "A generic multiple-feedback architecture and method for the design of high-order $\Sigma\Delta$ modulators," *IEEE Transactions on Circuits and Systems II: Analog and Digital Signal Processing*, vol. 49, no. 7, pp. 465–473, July 2002.

[84] (2006) Maxim integrated products. [Online]. Available: www.maxim-ic.com.cn/pdfserv/en/an/AN3642.pdf/

[85] J. Yeom, Y. Wu, and M. A. Shannon, "Critical aspect ratio dependence in deep reactive ion etching of silicon," in *International Conference on Solid-State Sensors, Actuators and Microsystems (TRANSDUCERS '03)*, vol. 2, June 2003, pp. 1631–1634.

[86] J. A. Cherry and W. M. Snelgrove, *Continuous-Time Delta-Sigma Modulators for High-Speed A/D Conversion: Theory, Practice and Fundamental Performance Limits.* Kluwer Academic Publishers, Oct 1999.

[87] S.Yan and E. Sanchez-Sinencio, "A continuous-time sigma-delta modulator with 88dB dynamic range and 1.1MHz signal bandwidth," *IEEE Journal of Solid-State Circuits*, vol. 39, no. 1, pp. 75–86, Jan 2004.

[88] Maplesoft, 2006. [Online]. Available: http://www.maplesoft.com/products/maple/index.aspx

[89] J. Cherry and W. Snelgrove, "Excess loop delay in continuous-time delta-sigma modulators," *IEEE Transactions on Circuits and Systems II: Analog and Digital Signal Processing*, vol. 46, no. 4, pp. 376–389, April 1999.

[90] O. Shoaei, "Continuous-Time Delta-Sigma A/D Converters for High Speed Applications," Ph.D. dissertation, Carleton University (Canadian), November 1995.

[91] N. Beilleau, H. Aboushady, and M. Louerat, "Systematic approach for scaling coefficients of discrete-time and continuous-time sigma-delta modulators," in *Proceedings of the 46th IEEE International Midwest Symposium on Circuits and Systems*, vol. 1, Dec 2003, pp. 233–236.

[92] B. J. Gallacher, J. S. Burdess, and K. M. Harish, "A control scheme for a MEMS electrostatic resonant gyroscope excited using combined parametric excitation and harmonic forcing," *Journal of Micromechanics and Microengineering*, vol. 16, no. 2, pp. 320–331, February 2006.

[93] C. C. Painter and A. M. Shkel, "Active structural error suppression in MEMS rate integrating gyroscopes," *IEEE Sensors Journal*, vol. 3, no. 5, pp. 595–606, October 2003.

[94] C. Acar and A. M. Shkel, "An approach for increasing drive-mode bandwidth of MEMS vibratory gyroscopes," *IEEE/ASME Journal of Microelectromechanical Systems*, vol. 14, no. 3, pp. 520–528, March 2005.

[95] A. Seshia, M. Palaniapan, T. Roessig, R. Howe, R. Gooch, T. Schimert, and S. Montague, "A vacuum packaged surface micromachined resonant accelerometer,"

IEEE/ASME Journal of Microelectromechanical Systems, vol. 11, no. 6, pp. 784–793, December 2002.

[96] J. C. Lotters, W. Olthuis, P. H. Veltink, and P. Bergveld, "A sensitive differential capacitance to voltage converter for sensor applications," *IEEE Transactions on Instrumentation and Measurement*, vol. 48, no. 1, pp. 89–96, Feb 1999.

[97] B. Schiffer, A. Burstein, and W. Kaiser, "An active charge cancellation system for switched-capacitor sensor interface circuits," *IEEE Journal of Solid-State Circuits*, vol. 33, no. 12, pp. 2134–2138, Decemeber 1998.

[98] J. Geen, S. Sherman, J. Chang, and S. Lewis, "Single-chip surface micromachined integrated gyroscope with $50^o/h$ Allan deviation," *IEEE Journal of Solid-State Circuits*, vol. 37, no. 12, pp. 1860–1866, December 2002.

[99] M. Tavakoli and R. Sarpeshkar, "An offset-canceling low-noise lock-in architecture for capacitive sensing," *IEEE Journal of Solid-State Circuits*, vol. 38, no. 2, pp. 244–253, Feb 2003.

[100] (2006) Analog devices. [Online]. Available: http://www.analog.com

[101] S. D. Senturia, *Microsystem Design.* Kluwer Academic Publishers, 2000.

[102] (2006) National instruments. [Online]. Available: http://www.ni.com

[103] J. I. Seeger, X. Jiang, M. Kraft, and B. E. Boser, "Sense finger dynamics in a $\Delta\Sigma$ force-feedback gyroscope," in *Proceedings Solid-State and Actuator Workshop, Hilton Head Island, SC.*, June 2000, pp. 296–299.

[104] T. Veijola, H. Kuisma, and J. Lahdenpera, "Model for gas film damping in a silicon accelerometer," in *International conference on solid-state Sensors and Actuators, Transducer'97, Chicago, USA*, June 1997, pp. 1097–1100.

[105] J. J. Blech, "On isothermal squeeze films," *Journal of Lubrication Technology*, vol. 105, pp. 615–620, Oct 1983.

[106] R. Darling, C. H. C, and J. Xu, "Compact analytical modelling of squeeze film damping with arbitrary venting conditions using Greens function approach," *Sensors and Actuators*, vol. A70, pp. 32–41, Oct 1998.

[107] M. Chabloz, J. Jiao, Y. Yoshida, T. Matsuura, and K. Tsutsumi, "A method to evade microloading effect in deep reactive ion etching for anodically bonded glass-silicon structures," in *The Thirteenth Annual International Conference on Micro Electro Mechanical Systems, MEMS 2000*, Jan 2000, pp. 283–287.

[108] J. Riches and N. Erdol, "Mismatch cancellation in quadrature bandpass $\Sigma\Delta$ modulators using an error shaping technique," *IEEE Transactions on Circuits and Systems II: Analog and Digital Signal Processing*, vol. 49, no. 2, pp. 73–85, Feb. 2002.

[109] R. Maurino and C. Papavassiliou, "Quadrature ΣΔ modulators with a dynamic element matching scheme," *IEEE Transactions on Circuits and Systems II: Analog and Digital Signal Processing*, vol. 52, no. 11, pp. 771–775, Nov. 2005.